Photonic and nanomechanical study for label-free monitoring of the fibrotic scar in spinal cord injury in mice

Clara Manesco

To cite this version:

Clara Manesco. Photonic and nanomechanical study for label-free monitoring of the fibrotic scar in spinal cord injury in mice. Human health and pathology. Université de Montpellier, 2023. English. NNT : 2023UMONS072 . tel-04578303

HAL Id: tel-04578303
https://theses.hal.science/tel-04578303v1

Submitted on 16 May 2024

THÈSE POUR OBTENIR LE GRADE DE DOCTEUR
DE L'UNIVERSITÉ DE MONTPELLIER

En Biophysique

École doctorale Information Structures Systèmes (I2S)

Unité de recherche UMR 5221 – Laboratoire Charles Coulomb (L2C) à Montpellier

Etude photonique et nano-mécanique pour le suivi sans marquage de la cicatrice fibrotique dans les lésions de la moelle épinière chez la souris

Présentée par Clara MANESCO
Le 18 décembre 2023

Sous la direction de Csilla GERGELY et Florence PERRIN

Devant le jury composé de

Serge MONNERET	Directeur de Recherche	Aix-Marseille Université	Rapporteur
Youri ARNTZ	Maître de Conférences - HDR	Université de Strasbourg	Rapporteur
Francesco PAVONE	Professeur	University of Florence	Examinateur
Christine DOUCET	Chargée de Recherche	CBS	Examinatrice
Virginie CALLOT	Directrice de Recherche	Aix-Marseille Université	Présidente du jury
Csilla GERGELY	Professeur	L2C	Directrice de thèse
Florence PERRIN	Professeur	MMDN	Directrice de thèse
Thierry Cloitre	Maître de Conférences	L2C	Co-encadrant

UNIVERSITÉ
DE MONTPELLIER

Etude photonique et nano-mécanique pour le suivi sans marquage de la cicatrice fibrotique dans les lésions de la moelle épinière chez la souris

**

Photonic and nanomechanical study for label-free monitoring of the fibrotic scar in spinal cord injury in mice

Faith is a fine invention

For Gentlemen who see!

But Microscopes are prudent

In an Emergency!

– Emily Dickinson

(1830-1886)

American poet.

Table of Contents

Acknowledgements

This thesis is the result of many pieces of work sewed all together with the help of people I would like to sincerely thank in the following lines.

First of all, I am grateful to Dr. Pierre Lefebvre for welcoming and hosting me in the Charles Coulomb laboratory and to Dr. Tangui Maurice for allowing me to work in the MMDN laboratory. It was a chance to be part of a project at the frontier between biophysics and neurobiology. This gave me the opportunity to see, understand and experience the distance, the bounds and the complementarity of these two fields.

I address my gratitude to my two supervisors, Pr. Csilla Gergely and Pr. Florence Perrin for the guidance, advices and support they provided to me. I would like to specially highlight their strong pragmatism that helped me to overcome my scientific and personal apprehensions. I am indebted to you both for allowing me to be a Ph.D. student on this collaborative project and for letting me access to cutting-edge microscopes and precious samples.

I also address my sincere acknowledgements to Dr. Serge Monneret and Dr. Youri Arntz for accepting to review my manucript, and more broadly, to all the jury members including Pr. Francesco Pavone, Dr. Virginie Callot and Dr. Christine Doucet, for their patience and goodwill concerning my thesis defense conditions.

I am particularly thankful to Pr. Jean-Noel Bacro from the Mathematics and Biostatistics department for his precious expertise and advices on the statistical tests and analysis.

I address special thanks to Dr. Liu Yuming for his prompt and precise answers and for the relevant advices he gave to me about CurveAlign preprocessing.

My grateful thoughts are also going to Dr. Marta Martin and Dr. Thierry Cloitre for their constant support and expertise all along the thesis. Marta, thank you for the huge work you provided on AFM during this project, for your advices and for the priceless good mood and gentleness you showed each time. Thierry, your vast knowledge and patience are commendable. I hope I could make the best use of the complete and pertinent explanations you shared with me.

I was very fortunate to work with two amazing colleagues who enriched my Ph.D. experience and who made me considerably grow as a scientist. First, I am truly grateful to Dr. Béla Varga. Béla, you taught me so many things during my first year of Ph.D. with open-mindedness, good spirit and energy. I would probably never thank you enough for all your time, patience and professionalism.

I will keep in mind the rigorousness, the sense of detail, the pedagogy and the satisfaction of doing science by you side. These moments built solid scientific values in me. Secondly, I address my deep gratitude to Dr. Oscar Saavedra who joined the team at a crucial moment and who breathed new life in the protocol elaboration. Thank you Oscar for this detailed-orientated vision of yours that helped me to approach the experimental set up with more awareness. From now, I will never blindly trust software anymore. Thank you also for the practical and positive conversations we had, for your diligent work on this project. And most of all for your great kindness and honesty which was a tremendous support for me and, without doubt, one of the main reasons I brought my thesis to a conclusion.

I would like to also offer my special thanks to Dr. Yannick Gerber for the valuable time we shared together on immunohistochemistry experiments, for his patience when teaching me how to collect the samples, and for all the advices he provided to me. Thanks Yannick for your pedagogics skills, your professionalism and your positive temper. My thanks are also extended to all IBN team, Ph.D student and interns, Jean-Christophe, Clarisse, Clémence and Nacéra for the quality of the samples preparation. I am very grateful to all of you for your time and your thoroughness that were essential to carry out my imaging experiments.

My experience at the lab was particularly delightful thanks to my colleague Dr. Bruno Robert. Bruno, you are one of the most gentle and affable person I've ever met. It was a pleasure to share the office with you, to have all these unhealthy but vital sugar breaks together, to be able to talk about science, career or personal life with the same sincerity. Thank you for this daily optimistic spirit of yours. I also want to express my acknowledgement to Joshua de Lizaraga who provided a considerable help for the MPM data acquisitions and analysis during his internship. Many thanks Josh, for your generosity, your humor and your optimistic energy that were essential parts of my well-being at work. I wish you good luck for your Ph.D. journey and hope it will bring you all the satisfaction you deserve. A special thank is finally going to our other interns, Thomas Fressoz whom detailed work on AFM bibliography was very appreciable to apprehend the various studies about stiffness in central nervous system, and Safa Mostefaoui for her meticulous and dedicated skills in the stiffness evaluation.

The Ph.D. adventure was not evidence at the first sight but it sprung during the enlightened experiences I had in research after my master graduation. I would like to address here a special and respectful regard to Pr. Inger Andersson from BMC at Uppsala University who offered me an unforgettable experience in her lab, to Pr. Tetsuya Takakuwa from the Graduate School of Medecine at Kyoto University for his professional guidance and for the high-end project he entrusted me, and to Dr. Emmanuelle Le Bars from I2FH Platform at CHU St Eloi in Montpellier for providing me my first internship in biomedical imaging and for giving me a durable taste for the research field.

The last acknowledgement section is dedicated to the people who are my primordial balance between professional and personal investments. I address my faithful gratefulness to my friends who showed an amazing empathy and understanding of how delicate and absorbing a Ph.D. project could be, especially to Seb for his constant support and for all the restful moments we shared, to Chloé and Julie for their long-term friendship and for their kindness, and to Amel, Amandine, Claire and Orianne who experienced the doctoral work before me and whom useful advices kept me focus on my goals. An immense and everlasting gratitude is sent to my dear friend Yuliana who, despite of her own challenges, always found time for our precious conversations. Her unwavering support was and still is an essential strength for me. My deepest affection is going to my family for their patience and unconditional love, no matter my professional plans or projects. I am sincerely grateful also to my in-laws for their tremendous support during my thesis completion. Finally, I express my invaluable gratitude and trust to my partner, Guillaume, who never failed in supporting me all these years leniently and with maturity. Thank you, Guillaume, for all your honest and constructive critics about science or soft skills that enabled to reach the best inside of me. Thank you for believing in me even when I doubted, thank you for your active role in many of my personal achievements.

This work was supported by the MUSE I-Site priority theme “Feed-Protect-Care” and by the CPER-BNIF Bioimaging Nanofoundry for the microscopes and imaging experiments and by the patients’ organization “Verticale” (To Pr. Perrin and Dr. Gerber) for the samples providing.

Publications and Scientific communications

Publications

2023

Manesco, C., Saavedra-Villanueva, O., Martin, M., de Lizaraga, J., Varga, B., Cloitre, T., ... & Gergely, C. (2023). Organization of collagen fibers and tissue hardening: Markers of fibrotic scarring after spinal cord injury in mice revealed by multiphoton-atomic force microscopy imaging. *Nanomedicine: Nanotechnology, Biology and Medicine*, 102699.

Scientific communications

2021

- *COST* Mar 2021, Web-Conference: University of Utrecht, The Netherlands and University of Gothenburg, Sweden. ⟨hal-03463478⟩ **Poster presentation.**

Manesco, C., Varga, B., Gerber, Y., Cloitre, T., Fernandez, M. M., Gergely, C., & Perrin, F. (2021, March). Non-linear optical imaging and atomic force measurements to monitor spinal cord injury in mice and non-human primates. In *COST*.

- *Spring School les Houches*, May 2021, Les Houches, France. ⟨hal-03463502⟩ **Communication in Congress.**

Manesco, C., Varga, B., Cloitre, T., Fernandez, M. M., Gerber, Y., Perrin, F., & Gergely, C. (2021, May). Multimodal imaging approach for optical label-free readout of spinal cord injury. In *Spring School les Houches*.

- *PhysBio*, Jun 2021, Paris-Saclay, France. ⟨hal-03463535⟩. **Oral presentation and poster.**

Manesco, C., de Lizaraga, J., Varga, B., Cloitre, T., Martin-Fernandez, M., Gerber, Y., ... & Gergely, C. (2021, June). Label-free imaging techniques for monitoring spinal cord injury: from pathophysiology to therapeutic strategies in mice. In *PhysBio*.

- *MiFoBio – Functional Microscopy for Biology*, Nov 2021, Presqu'ile de Giens, France. ⟨hal-03463551⟩ **Poster presentation.**

Manesco, C., de Lizaraga, J., Varga, B., Cloitre, T., Fernandez, M. M., Gerber, Y., ... & Gergely, C. (2021, November). Multimodal label-free imaging approach to monitor spinal cord injury in mice. In *MiFoBio–Functional Microscopy for Biology*.

2022

- *SPIE Europe Neurophotonics*, Apr 2022, Strasbourg, France. **Oral presentation.**

Manesco, C., de Lizaraga, J., Varga, B., Cloitre, T., Martin, M., Gerber, Y., ... & Gergely, C. (2022, May). Monitoring spinal cord injury in mice with a multimodal label-free imaging approach. In *Biomedical Spectroscopy, Microscopy, and Imaging II* (p. PC1214409). SPIE. https://doi.org/10.1117/12.2621206

Abbreviations and Glossary

Abbreviations (alphabetic order):

AIS: ASIA (American spinal injury association) impairment scale

AFM: atomic force microscopy

CNS: central nervous system

CSF1-R: colony-stimulating factor 1 receptor

CSF: cerebrospinal fluid

CSPGs: chondroitin sulfate proteoglycans

E: Young's modulus

ECM: extracellular matrix

F-D curve: force-distance curve

FS-AFM: Force spectroscopy AFM

FFT: fast Fourier transform

fMRI: functional magnetic resonance imaging

FP: FingerPrint algorithm

GFAP: glial fibrillar protein

eGFP: enhanced green fluorescent protein

GM: grey matter

H&E: Hematoxylin and Eosin

HS: hemisection

IF: immunofluorescence

IHC: Immunohistochemistry

MDM: monocyte-derived macrophage

MMP: matrix metalloproteinase

MPM: multiphoton microscopy

2PEF: two-photon excited fluorescence

PET: positron emission tomography

PLR: path length ratio

PM: photomultiplier

ROI: region of interest

SCI: spinal cord injury

SHG: second harmonic generation

SNR: signal-to-noise ratio

WM: white matter

Glossary (alphabetic order):

Activated astrocytes/microglia: activation occurs after an injury, when homeostasis is perturbed. Astrocytes and microglia in a homeostatic state become activated with modifications in size and shape that help their migration to the injury site.

*Biomarker***:** specific targets (cells, molecules, structures) that are related to significant changes in clinical observations.

Confocal microscopy principle: a pinhole, inserted in the microscope set up, blocks the light from outside the focal plane providing a better contrast.

Fibrillar collagen: collagen pattern representing the most common type of collagen. It involves the cleavage of the N and C terminal sequences by specific proteinases and the assembly of procollagen into cross-striated fibrils by lysyl oxidase action, shaped into a cylindrical structure. Eventually, collagen fibrils associate into heterotypic fibers (fibril-bundles). Its specific structure allows SHG to occur.

Fibrotic scar: part of the glial scar composed of an astrocytic bound directly located around the lesion site (also called the lesion core).

Fluorochromes: fluorescent tag (exogenous sources) to target the structures of interest within a tissue. The fluorescent signal produced can be detected with fluorescence microscopy.

Force-distance curve: typical curve obtained with AFM in force spectroscopy mode. It represents the distance wandered by the tip and the deflection (bending of the cantilever when interacting with the sample) induced by forces.

Hemisection model: spinal cord injury model in animal where an incision is performed, usually with microscalpel or scissors, and affects only half of the spinal cord. Various types of hemisection exist such as dorsal, ventral and lateral. Lateral hemisection preserves one side of the spinal cord maintaining some functions in the animal.

Histopathology: the examination of microscopic changes in biological tissues and cells in various pathological states.

Immunohistochemistry/Immunofluorescence: most widely protein detection techniques relying on the antigen/antibody complex (a specific antibody matches specific antigen in the tissue). Immunohistochemistry uses enzymatic labels (as peroxidase) while immunofluorescence uses a fluorescent tag.

Inelastic interaction: light absorption phenomena leading to light emission based on fluorescence (as in two-photon fluorescence 2PEF) or based on structural properties of the samples (as in Second Harmonic Generation SHG) as well as to vibrational signatures of the molecules measured by spectroscopy (Raman spectroscopy).

Ipsilateral side: name of the side injured, in a lateral hemisection model. The spared part is called the contralateral side.

Label-free imaging: imaging technique relying on the direct interaction between the light and the targeted biological system and that do not need external staining of the sample.

Mechanobiology: the study of the effects of physical forces and mechanical properties at different scales (proteins, cells and tissues).

Multimodal imaging: combination of various imaging techniques (labeling or label-free), to bring complementary information and help to address a more accurate diagnosis or treatment.

Non-centrosymmetric structures: crystals lacking inversion symmetry. Few non-centrosymmetric biological structures exist, the main being fibrillar collagen, microtubules and myosin in sarcomere.

Secondary injury: classification of spinal cord injury phases. Its time-line depends of the species and SCI model used. It follows the physical trauma (the primary injury) and can last 6 months post injury. It includes many scarring events such as neuroinflammation, excitotoxicity and the glial scar formation.

Young's modulus extraction: Young's modulus (or elasticity modulus, in Newton, describing the stiffness of the sample) can be calculated by fitting a specific portion of the force-distance curve to a theoretical model (usually the Hertz model for biological sample). It can be obtained for each pixel of the acquisition grid and an elasticity map can be computed from it.

List of Figures

I- Generalities and objectives of the thesis

II- Materials and Methods

III- Results and discussion

General conclusion and perspectives

Appendix

List of Tables

Abstract

Spinal cord injuries (SCI) are part of the most impactful pathologies in the central nervous system (CNS). They can induce dramatic physical and psycho-social effects for the patients, associated with a consequent impact on the health care system. When an injury occurs, it induces a cascade of events disturbing the surrounding structures and cell populations, and includes the formation of a glial scar. This scar is composed of various cell populations such as activated microglial and astrocytes. Fibroblasts are producing collagen with the support of reactive astrocytes and are involved in the fibrotic process. The glial scar is a dense chemical and physical barrier with dual effects on the recovery. No curative treatment is currently available. However, promising pharmaceutical approaches have been developed through the transient depletion of microglia using a GW2580 treatment, an inhibitor of CSF1R receptor that specifically regulates the proliferative part of microglial cells.

The exploration of collagen in the glial scar formation has raised poor attention comparing to the interest in microglia and astrocytes roles. Fibrillar collagen as collagen I is well known in common wound healing processes occurring in the rest of the body following alteration of ECM, and is defined by a supramolecular organization in cross-striated fibril shaped into a cylindrical structure and eventually associated into fibers. This assembly leads to unique optical properties that can be directly monitored by non-linear optical measurements (NLO), such as Second Harmonic Generation (SHG), without special sample preparation and without any exogenous labeling. As SHG is a coherent signal that depends on the polarization of the incident laser by performing Polarization-resolved SHG (P-SHG) collagen fibers arrangement at a supramolecular level can be assessed related to the fibrils nature (related to their symmetry profiles).

The global approach we proposed in our work was to exploit the potential of NLO optics in detecting and characterizing fibrillar collagen in SCI (using Multiphoton microscopy to visualize simultaneously 2-photon excited fluorescence and SHG signals) in a mouse model and to correlate the obtained structural information to the biomechanical behavior of the tissue via micro/nano-indentation force measurements with Atomic Force Microscopy (AFM). Collagen fibers exhibited by their SHG signal were characterized with two methods: CurveAlign software dedicated to collagen fibers analysis in biological samples and a home-build Fingerprint algorithm written in MATLAB establishing an analysis pipeline more adapted to our study. We eventually generated a skeleton map of the fibers to extract relevant metrics such as the fibers' density, tortuosity and orientation at local level (calculating the circular variance of the local orientation) or at global level (calculating the statistical entropy). Our multimodal label-free imaging approach was thus dedicated to reveal and monitor

lesion biomarkers deduced from the fibrotic structure and the elasticity of injured spinal cord tissues after various time-points post-injury and to investigate the potential effect of a pharmacological treatment with GW2580 at 6 weeks post injury.

The SHG signal exhibited by fibrillar collagen enabled to specifically monitor it as a biomarker of the lesion. An increase in collagen fibers density and the formation of more tortuous fibers overtime from 1 week to 6 weeks post-injury was observed. P-SHG measurements revealed both fibrils symmetry types (cylindrical and trigonal) at all the time-points post injury. Nano-mechanical investigations revealed a noticeable hardening of the injured area from 1week post injury, correlated with collagen fibers' formation.

These observations indicate the concomitance of important structural and mechanical modifications during the fibrotic scar evolution following a spinal cord injury in mice.

Résumé

Les lésions de la moelle épinière (LME) font partie des plus graves maladies du système nerveux central (SNC). Elles peuvent induire des effets physiques et psycho-sociaux dramatiques chez les patients, associés à d'importants coûts pour le système de santé. Lorsqu'une lésion advient, une cascade d'évènements est enclenchée perturbant les structures et populations cellulaires à proximité. Ces perturbations ont notamment pour conséquence la formation d'une cicatrice, la cicatrice gliale. Elle est constituée de diverses populations cellulaires telles que les formes activées de microglies et d'astrocytes. Les fibroblastes qui produisent du collagène sous l'action d'astrocytes participent au processus fibrotique. La cicatrice gliale constitue une dense barrière physique et chimique dont les effets sont à la fois bénéfiques et délétères. Aucun traitement curatif n'existe à l'heure actuelle. Cependant, des thérapies pharmaceutiques ont été développées, notamment par la déplétion transitoire de la microglie en utilisant le GW2580, un traitement qui inhibe le récepteur CSF1R impliqué dans la partie proliférative des cellules gliales.

Le rôle du collagène dans la formation de la cicatrice gliale a été peu exploré en comparaison de ceux de la microglie et des astrocytes. Le collagène fibrillaire tel que le collagène de type I est bien connu dans les processus de cicatrisation classiques, suite à une altération de la matrice extracellulaire (MEC). Le collagène fibrillaire se caractérise par une organisation supramoléculaire en fibrilles striées regroupées en une structure cylindre pour finalement être associées en fibres. Cet assemblage lui confère des propriétés optiques uniques qui peuvent être directement détectées par des mesures d'optique non-linéaire (ONL) telle que la génération de seconde harmonique (GSH) sans qu'une préparation spéciale ou un marquage exogène de l'échantillon soit requis. De plus, la GSH étant un signal cohérent qui dépend de la polarisation du laser incident, des mesures de GSH résolue en polarisation (P-GSH) peuvent être menées afin de déterminer l'arrangement supramoléculaire des fibres de collagène associé à la nature des fibrilles (elle-même associée à la symétrie).

L'approche globale que nous avons proposée était d'exploiter le potentiel de l'ONL pour la détection et la caractérisation du collagène fibrillaire (utilisant la microscopie multiphotonique pour visualiser simultanément la fluorescence par excitation à deux photons et le signal GSH) dans un modèle murin de LME, et de corréler les informations structurales obtenues avec le comportement biomécanique du tissu, déterminé par microscopie à force atomique (MFA) en mesurant les forces appliquées lors de micro-nano indentations. Les fibres de collagène observables grâce à leur signal en GSH ont été caractérisées via deux méthodes successives : avec le logiciel CurveAlign spécifiquement dédié à

l’analyse des fibres de collagène dans les échantillons biologiques, et avec un algorithme codé au sein de l’équipe basé sur le « Fingerprint algorithm » pour une analyse plus adaptée à notre étude. Un « squelette » de fibres a été généré par cet algorithme nous permettant d’extraire des métriques pertinentes caractérisant les fibres présentes dans la lésion telles que la densité de fibres, leur tortuosité, ainsi que leur orientation à un niveau local (calculant la variation circulaire de l’alignement local) et à un niveau plus global (calculant l’entropie statistique). Notre approche d’imagerie multimodale sans marquage a donc eu pour but de révéler et suivre des biomarqueurs issus de la structure fibrotique et de l’élasticité de tissus de moelle épinière lésée à différent temps après lésion, et d’évaluer le potentiel effet d’un traitement au GW2580 à 6 semaines post lésion.

Le signal GSH émis par le collagène fibrillaire nous a permis de l’identifier comme biomarqueur de la lésion. Une augmentation de la densité de fibres ainsi que la présence de fibres plus tortueuses ont été observées entre 1 et 6 semaines post lésion. Les mesures en P-GSH ont révélé la présence de deux types de symétrie des fibrilles (cylindrique et trigonal) à tous les temps après lésion. L’étude des propriétés nano-mécaniques a montré un durcissement notable de la zone lésée à partir d’une semaine post lésion, certainement corrélé à la formation de fibres de collagène.

Ces observations indiquent la concomitance d’importantes modifications structurales et mécaniques au cours de l’évolution de la cicatrice fibrotique suite à une LME chez la souris.

General Introduction

It is nowadays assumed that microscopes and more generally imaging technologies access elements and structures commonly “unseen”. However, this assumption has not always been taken for granted, and more precisely, the determinant role of imaging in characterizing biological samples has become evident only some decades ago. We can mention Rosalind Franklin and her X-ray diffraction studies, which revealed the double-helix structure of DNA (1953) and, on a more current topic, June Almeida who first described the structure of the coronavirus (1967) using electron microscopy; these two relevant examples highlight the need of specific imaging techniques in order to reveal specific targets.

Indeed, imaging technologies have become unavoidable in scientific research to observe biological samples at level of proteins, cells and tissues. The real challenge of “bringing to light” the structure of interest in a complex biological process or disease has led to the advent of various imaging techniques. Some of them are involving labeling methods, relying on chemical affinities between a tag and the molecule of interest. Others are called “label-free”, relying on the direct interaction between the light and the targeted biological system. Labeling techniques are well-known and commonly used practices but still considered operator-dependent and time-consuming. On the other hand, label-free imaging technologies are at the forefront of the research since no external staining perturbing the system is needed. However, it would be reductionist to claim that label-free investigations could replace the staining approach in terms of reliability, time-consumption and reproducibility. Both methods have their advantages and limitations, but more importantly, they are targeting different properties of the sample. To that degree, it can be suitable to combine both of them, in a so called multimodal imaging, to bring complementary information and help to address a more accurate diagnosis or treatment. For example, multimodal imaging approaches has been particularly relevant in the field of histopathology, which is the microscopic analysis of tissues aiming to identify disease and characterize them. The visualization of biomarkers in pathological tissues through imaging has become increasingly important in monitoring disease apparition, evolution or recovery. In that context, biomarkers are defined as specific targets (cells, molecules, structures) that are related to significant changes in clinical observations (Frank & Hargreaves, 2003). Protocols for imaging are relevantly established in a way to identify biomarkers; in that way, they can be precursor tools in drug selection that further increases therapeutics strategies efficiency, and even leads to clinical translation of the treatment. Clinical protocols based on labeling has been thence routinely combined with quantitative assessments performed with label-free techniques in the investigations of cancers or neurodegenerative disease. Among the labeling techniques, Hematoxylin and Eosin (H&E) staining – discriminating cells nuclei and proteins – and some immunohistochemistry (IHC) techniques – those relying on tagged specific antibodies tags to target proteins and provide specific contrast – remain at the present the gold standard methods for visualizing a target component. When using a fluorescent tag, the IHC contrast is usually directly observed through a fluorescence microscope and can be followed by slides digitalization into a tissue data bank. Computing these data enables a Computer Aid Diagnosis, which consists in different processing steps (segmentation, feature selection and quantification) to identify and evaluate components in a tissue (Cicerone & Camp, 2018). Co-registered multimodal label-free imaging can eventually complete the labeling approach by addressing two types of interactions: linear interactions through light refraction for example, and non-linear interactions. The late case refers to the behavior of light in non-linear media implying that the polarization density P depends non-linearly on the electric field. Such phenomena are observed at very high light intensities and lead to light emission based on fluorescence (as in two-photon fluorescence 2PEF) or based on structural properties of the samples (as in Second Harmonic Generation SHG), as well as to vibrational signatures of the molecules measured by spectroscopy (Raman spectroscopy). Other label-free techniques assessing mechanical behaviors, as atomic force microscopy (AFM), or radiology approaches allowing *in vivo* imaging such as magnetic resonance imaging (MRI) or positron emission tomography (PET), are also commonly used to explore pathological states.

The multimodal approach has become increasingly valuable for studies in neurosciences. The establishment of translational imaging models is fundamental to investigate neurological disorders in a pre-clinical context due to the difficulty to access human central nervous system (CNS). Current micro and macro-imaging procedures have been designed to carry out the investigations in small animals, non-human primates, healthy human volunteers and patients (Wong et al., 2009). These procedures mainly include: i) radiolabelling, for example of dopamine antagonist receptor imaged with PET in patients with Parkinson's disease (Niccolini et al., 2014), ii) functional MRI generating mechanism-related maps to monitor therapeutic strategies in spinal cord injury (SCI), for example in patients with acute cervical spinal cord injury (Haefeli et al., 2017), iii) the combination of Raman spectroscopy with labeling to characterize, for example, Alzheimer disease using biological media (as blood, CSF and urine) from patients (Khan et al., 2018) or Raman combined with other non-linear optical techniques for example in a SCI hemisection model in rats (Galli et al., 2012), iv) blood flow monitoring in CNS lesions, and v) mechanical assessments on healthy or injured CNS tissues, for example in rats with AFM (Moeendarbary et al., 2017).

Among all the diseases evoked, spinal cord injuries (SCI) are probably one with the most long-term impairments and care costs, despite the fact that they rarely cause death. A major point of interest in SCI is the formation of the glial scar, mainly composed of two cells populations: astrocytes and microglia, which eventually migrate to the injury site and create a boundary between the healthy and injured parts. Several microglia, especially the amoeboid cells, are also found within the lesion. The resultant chemical and physical barrier has both beneficial and adverse roles by: partly stopping the injury propagation on one hand, but also participating in the failure of the axonal regeneration and recovery process on the other hand (Alizadeh et al., 2019). The scar is composed of an astrocytic bound directly located around the Iesion site (called the lesion core or fibrotic scar) and of a dense heap of activated microglia (called microglial scar). The formation of the glial scar has been widely investigated in terms of cell-related events and modifications based on microglia, astrocytes or monocytes-derived macrophages roles. Surprisingly, less interest was dedicated to the implication of collagen in the scarring occurrence and evolution, despite the fact that fibrillar collagen has a well-known and key role in common scar and fibrosis formation (Reish & Eriksson, 2008; Thomas & Somenek, 2012). In the same vein, the existing collagen descriptions in SCI are mostly focused on collagen type IV, present in basal lamina (Klapka & Müller, 2006), while fibrillar collagen (such as type I) is poorly studied in this context. Investigating the process of collagen fibers' formation by the scar with appropriate imaging tools can provide valuable information on their role in the lack of spontaneous axonal regeneration after an injury.

The basic vision of our work was to combine appropriate imaging approaches, especially label-free techniques, to study traumatic SCI on excised tissues with the aim to identify and characterize relevant biomarkers of the scar formed at the injury site. To this purpose, we've worked on a lateral hemisection (HS) model in mice where only half of the spinal cord is affected. We assessed the relevant structural and morphological signature of the injured spinal cord tissue, as well as the nanobiomechanical behavior of healthy and injured spinal cord (SC) tissues at cellular level. As tissue stiffness is a regulator of neuronal growth (Benzina et al., 2013), tissue elasticity measurements could help understanding why adult mammalian axons do not regenerate spontaneously after injury. Therefore our investigations were based on two main imaging techniques: i) the non-linear multiphoton microscopy (MPM) enabling to retrieve on the same sample two images comporting different information, and ii) force measurements via AFM. MPM measures first SHG that occurs only in the presence of non-centrosymmetrical structures (such as fibrillar collagen), and secondly the 2PEF signal of the tissue components based on their genetically modification to express enhanced green fluorescence protein (eGFP) specifically in microglia and monocyte-derived macrophages.

The glial scar was explored with these two techniques at different time-points post lesion to monitor structural and elasticity (Young's modulus) modifications of the tissue. The SHG signal was determinant to evidence the presence of fibrillar collagen specifically located at the injury site, which subsequently led us to the characterization of collagen fibers formation in time: at 72hours post injury (hpi), 1week, 2 weeks and 6 weeks post injury (wpi). We started our observations at 1wpi based on the fact that the glial scar is already formed at this time-point (Wanner et al., 2013), even if it is still evolving up to several months after injury. According to our first qualitative investigations, our hypothesis was that the collagen fibers and their extension could undergo modifications in time, with less collagen expressed before 1wpi and more collagen after. We further performed polarization dependent measurements of the SHG signal. This step aimed to assess the preferential orientation of the collagen bundles at the different time-points and access their structure at supramolecular and tissue levels. The hypothesis was that the properties of the fibers could also vary in time and that the fibers orientation and/or their straightness could become a relevant indicator of the scar evolution at a specific time-point. Image and data analysis was performed using two methods: i) CurveAlign software (Liu et al., 2020) dedicated to collagen fibers analysis in biological samples, as a first approach to extract relevant fibers metrics, and ii) a home-build Fingerprint algorithm (FP) (Kovesi, s. d.; Lin Hong et al., 1998) written in MATLAB, to overcome some limitations of CurveAlign and establish an analysis pipeline more adapted to our study. Additionally, immunohistochemistry was also carried out in order to confirm the type of collagen detected in the lesion. Since SHG specifically targets fibrillar collagen types, we've used collagen type-I and type-II antibodies for these studies. AFM force spectroscopy measurements were performed at the same post-lesion time-points as for MPM acquisitions to map the elastic properties of the excised spinal cord tissues, addressing both the grey and white matters and the injured (lesion) parts of the tissue. We expected to observe a difference in the elasticity of the grey and white matter since they have different structures, and also to observe a change in the elastic properties of the lesion part that could thereafter be correlated with our MPM observations. We similarly started to investigate the effect of a treatment (pharmacological transient depletion of microglia/macrophage proliferation in mice that underwent SCI) in an additional 6wpi group.

The present manuscript is structured in the following chapters:

- **Chapter I**. **Generalities and objectives**. This part first gives some global elements about I.1) Spinal cord injury (the context, the physiopathology, the glial scar, the lesion models) in order to introduce the disease and the samples involved in this study. As the glial scar characterization in our work was mainly performed through the evaluation of collagen fibers properties, the second part of Chapter I is dedicated to I.2) Collagen presentation (the composition, collagen types and their optical properties) to make the bridge between the structure we observed and the imaging techniques we've used. The last part covers a literature review on I.3) Imaging spinal cord injuries and presents a state of the art on the modalities used to image SCI until now. A more detailed description of MPM, the SHG signal and AFM force measurements is presented in this section to provide basic knowledge and the physical principles of the used techniques. The Chapter I ends with a short section to clearly state the specific objectives of our work and the choice of the methodology to bring innovative information.

- **Chapter II. Materials and Methods**. This second chapter presents the concrete strategies we've applied to study the scarring process. It starts with the presentation of the II.1) biological samples: the mouse SCI model, the histological preparations, followed by the two immunohistochemistry approaches we performed to identify the type of collagen. The next section focuses on II.2) the multimodal approach we designed: the MPM and SHG set up on one side, and the AFM acquisitions on the other side. The last part of Chapter II is dedicated to II.3) image and data analysis, describing the two methods of processing we've developed and the statistical tests we applied to evaluate significance. The global aim of Materials and Methods is to show the coherence between the biological question and the physical approaches we've customized to address SCI.

- **Chapter III. Results and discussion**. This part presents the experimental results we've obtained, starting with III. 1) Preliminary studies we have conducted at 1wpi including axial and longitudinal sections. A comparison with uninjured spinal cord samples is also presented at this point. The second section III.2) shows the qualitative approach including the collagen type identification with immunohistochemistry, the direct visualization of fibrillar collagen at the injury site with MPM and SHG at different time-points and the evaluation of collagen extension. The following section of Chapter III addresses the III.3) collagen fibers investigation at supramolecular level trough the polarization curves, followed by fiber-level assessments performed by computing relevant metrics, with CurveAlign in a first step and with the Fingerprint algorithm in a second time, pointing out the complementarity of both techniques for our study**.** The last section of the chapter is dedicated to present the III.4) elastic properties of the tissue in the SCI context, via force measurements performed by AFM. A discussion part has been included at the end of each results section in order to comment and confront our findings with other studies.

Conclusion and perspectives. This final and summarizing part aims to remind the starting point of the study, the adequacy of the methods rolled out to reveal and characterize a suitable biomarker of the glial scar and the experimental results obtained in this context. A complementary section ends the manuscript, presenting the perspectives of the current work, namely the relevance of employing a vibrational spectroscopy imaging method, the broadband coherent anti-stokes Raman spectroscopy (BCARS) for the exploration of spinal cord injury, as well as some ongoing investigations in MPM and AFM.

CHAPTER I

-

GENERALITIES AND OBJECTIVES OF THE WORK

I . Generalities and objectives of the work

I.1. Spinal Cord injuries (SCI)

I.1.1. Context: incidence, causes and outcomes

Spinal cord injury (SCI) is a singular type of injury among the other neurological disorders. It can lead to devastating physical and psychosocial effects for the patients and to a huge impact on the health care system. The International Spinal Cord Society (ISCoS) estimated, in a report from 2011, that the global prevalence of SCI varies from 239 to 1009 cases per million population, with incidence rates specific to the geographic areas: 39 per million in the United States, 35 per million in Canada, 16 per million in Western Europe and 15 per million Australia (Cripps et al., 2011). Complementary information from this report states that the SCI incidence tended to increase over the years in North America, apparently associated with an increase in violence-related SCIs (18%). This increasing is higher than the one observed in Western Europe or Australia.

From an etiological view, most of the SCI cases (90 %) are traumatic and less have non-traumatic causes. A more detailed definition of traumatic SCI is given by the National SCI Database in North America as a "*traumatic lesion of neural elements in the spinal cord resulting in temporary or permanent sensory and/or motor deficit*" (Stover et al., 1999). Autonomic deficits can also occur after a trauma. To this extend, the following diseases and causes are not comprised in the late definition and are considered as non-traumatic SCI: developmental and congenital anomalies, inflammation (for example, multiple sclerosis), ischemia (cord stroke), pressure on the cord due to expanding lesions such as abscess or tumor (Paddison & Middleton, 2014), affections of the intervertebral disc, lesions to nerve roots and cancer nor vascular diseases. Traumatic SCI are due to various causes and display different occurrence, depending on the geographic location, as presented in *Figure 1*. Traffic accidents (implying mainly motor vehicle crashes) are the leading SCI cause over years in most countries (40 to 50%), followed by falls (29%) in work-related situations or at elderly people over 60 years. Violence-related SCIs were increasing in the late 90s before to display an overall decrease after 2000 (to 14%). Sport-related SCIs represent also a noticeable part of SCI causes especially in young patients, even if their proportion has significantly decreased in the past years (to 8%) (Y. Chen et al., 2013). The male-female ratio for SCI is 2:1, with a higher risk to be affected during adolescence for women and during early and late adulthood for men.

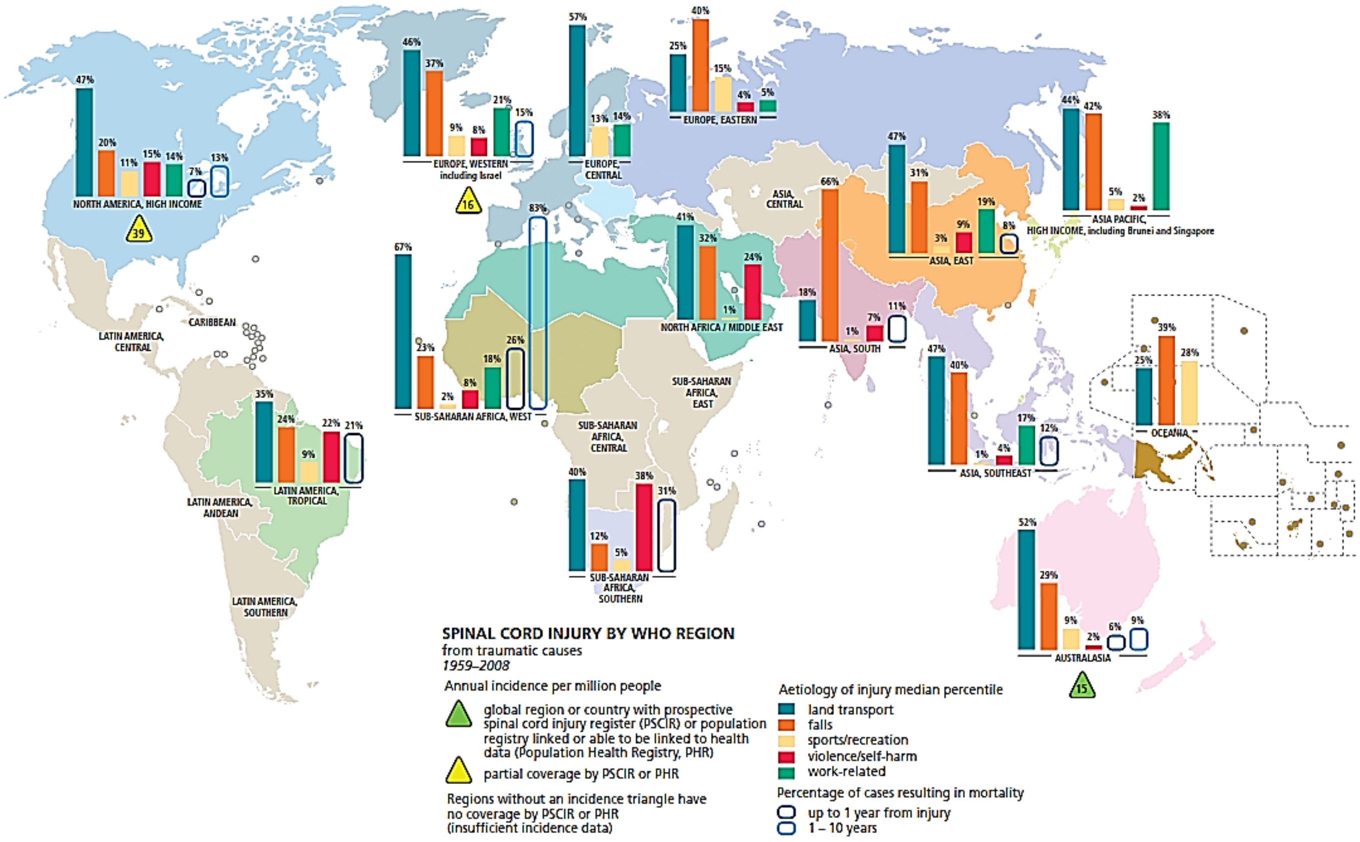

Figure 1 : Global mapping of spinal cord injury from traumatic causes by World Health Organization (WHO) region 1959–2008 From (Cripps et al., 2011).

The clinical consequences of SCI mostly depend on the severity of the lesion (complete or partial lesion) and also on the level of the injury (rostro-caudal axis). Outcomes may consist in the loss (complete or partial) of sensory and/or motor functions that are located caudal to the level of the injury. In other words, lesions located at the thoracic level can induce paraplegia while cervical lesions may lead to tetraplegia. The affection of the cervical level, more specifically at C5 level, is the most common one (50%), followed by thoracic (35%) and lumbar (11%) regions. For the majority of patients, that survived after a SCI, the most represented categories in the United States since 2010 are thus partial tetraplegia (46%), then complete (21%) and partial paraplegia (20%). The complete tetraplegia has the lowest occurrence (13%) (Merritt et al., 2019). Consequently, the life expectancy and quality of the patient significantly depends on the injury level and the spared tissues. Ultimately, the level of the injury and the severity of the symptoms imply significant costs including cares for the patient at the hospital (surgery, hospitalization), and at home (nursing and pharmacy), with an estimation of $2.35 million per SCI patient for a life-time (Hachem et al., 2017). An overview of the SC level-dependent motor impairments and the lifetime cost associated to the injury localization and severity is illustrated in *Figure 2*.

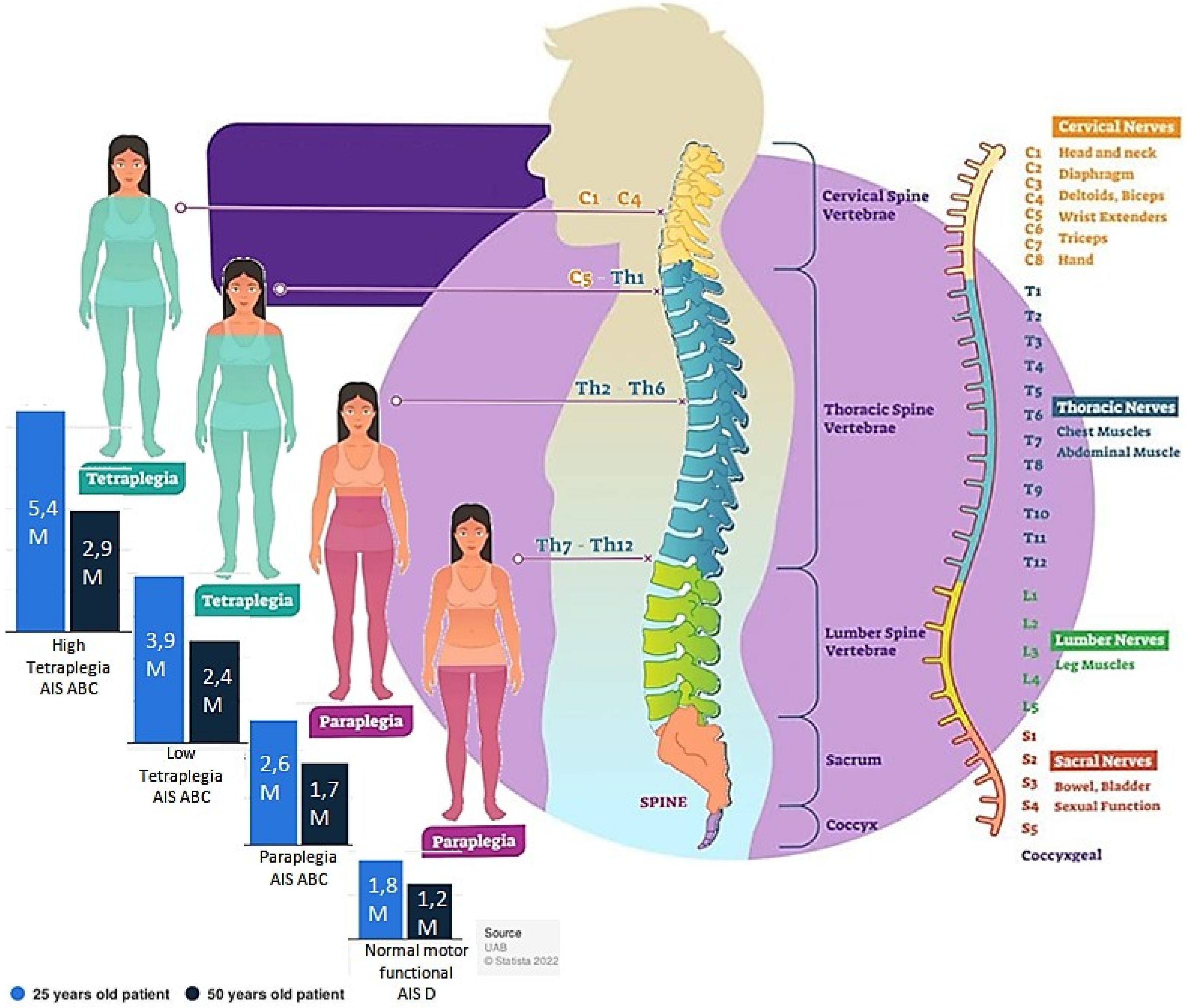

Figure 2: SC level-dependent functions with paralysis extension after SCI and lifetime costs (in Million $) related of injury severity using AIS classification (ASIA impairment scale, a clinical scale that classifies the completeness of the injury from A for total injury to E for normal motor functional).

Because of its meaningful impact on patient’s life (daily comfort, social interactions, school and work access) and in society expenses, SCI has raised a high awareness in terms of prevention and lifelong care. The main current therapeutic strategies involve non-pharmacological methods as surgery or rehabilitation that decompress and stabilize the injury, pharmacological protocols to improve the axonal conduction (using fampridine for example), neuroprotective approaches (inhibiting Nogo-A protein for example) and cell-mediated repairing using stem cells (Baptiste & Fehlings, 2007). With no standard and efficient curative treatment, the importance of novel therapeutic strategies in SCI has become crucial. Reaching this goal is patently related to a better understanding of the physiopathology underlying the injury event. On this wise, the next section aims to present the knowledge we have about the steps of the glial scar formation.

At this point, it is important to mention that accessing human spinal cord tissue, and especially injured tissues with specific time-points after the lesion, is a very difficult process. The histological studies in Human are thus very rare and only nine have been reported in a recent review (Perez et al., 2021). Most of these studies mainly involve MRI and behavioral protocols and do not afford evident conclusion about the glial scar in Human. For this reason, the human spinal cord anatomy described below is given as a reference (a comparison with a mouse model is given in part I.1.3 dedicated to the SCI animal models) and the occurring events after injury are presented through various studies conducted mainly in animals (the animal model is specified for each example).

I.1.2. Anatomy and physiopathology

I.1.2.1. Healthy spinal cord in Human

The human healthy spinal cord is part of CNS, extends caudally and is protected by the vertebral column. It is surrounded by meninges composed of three membranes: the dura mater, arachnoid and pia matter (Nógrádi, 2006). The spinal cord is made of two structures: the grey matter (GM), composed by the bodies of neuronal cells and glial cells, and the white matter (WM) containing oligodendrocytes (glial cells which produce myelin) and myelinated axons, elongated and orientated along the rostro-caudal axis that allow to connect the brain to specific parts of the periphery and *vice versa*. The WM is organized in specialized bundles of axons, forming ascending and descending tracts, which transmit sensory or motor information. In the spinal cord (contrary to the brain), the GM is surrounded by WM. A schematic view in *Figure 3* shows axial sections at different levels of the spinal cord as well as the different cell populations in CNS (a clinical view of human spinal cord is provided in the appendix section).

I.1.2.2. Spinal cord injury (clinic and animal models)

When an injury occurs to the spinal cord, it induces a complex cascade of events that eventually modifies structures and functions within and around the injury site. Changes in the spinal cord caused by an injury are divided into two steps, referred as primary and secondary injuries, with processes that occur in different phases. The timing of these phases varies depending on the model. Even in Human, no real consensus for the timing has been reached so far. One example of classification in Human is provided by Ahuja and colleagues (Ahuja et al., 2017): the immediate phase is related to the first and immediate traumatic event, the early acute phase for events occurring less than 48h after the injury, subacute phase for those from 48h to 14 days, the intermediate phase, up to 6 months, and the chronic phase for events occurring or lasting more than 6 months post injury.

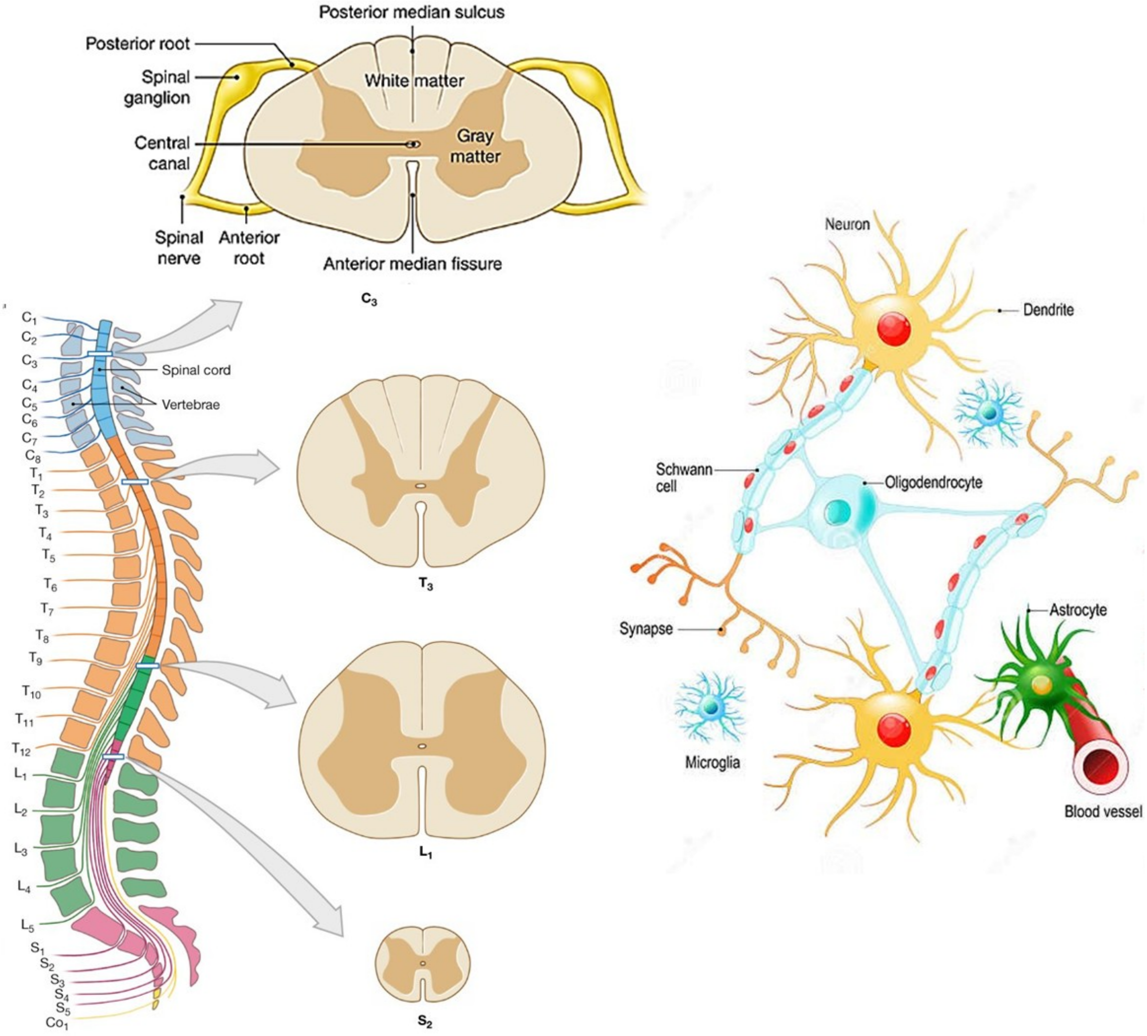

Figure 3 : Anatomy of the spinal cord in Human (healthy state). On the left, the spinal cord division into 7 cervical, 12 thoracic, 5 lumbar and 5 sacral vertebrae with axial views at different levels (C3, T3, L1 and S2). On the right, schematic of the different cell populations. Modified from https://www.studocu.com/en-us/document/university-of-wisconsin-madison/human-anatomy and https://stock.adobe.com/ch_fr/images/neurons

I.1.2.2.1. The primary and secondary injuries (from immediate to intermediate phases)

The primary injury is the physical trauma. It can result in many types of lesions, as for example the compression, contusion or the section (partial or complete, even if the late case is very rare) of the spinal cord. At the specific focal point of the trauma, the nervous tissue is destructed and the immediate consequence concerns both GM, WM and also blood-vessels, with the destruction of neurons and oligodendrocytes, along with vasculature disruption causing primary ischemia and hypoxia in human (Ahuja et al., 2017). In some cases, the blood-brain barrier is also disrupted.

The secondary injury follows the primary lesion. It induces hemorrhagic necrosis as well as new chain-reaction processes that worsen the initial damage. At this point, the spinal cord swells, that may cause the cease/alteration of blood flow regulation, as well as secondary ischemia. The hypoperfusion initiated in GM finally reaches the WM and creates a spinal shock. During the acute phase, the defensive immunity response rolls a chain of processes which contributes to the neuroinflammation. We can mention the migration of activated agents (neutrophil cells, microglial cells and macrophage-derivated monocytes or MDM) and chemical release, especially of glutamate which is mainly involved in excitotoxicity by deregulating intracellular calcium and producing free radicals. As a time-line example in mice, compression and contusion models have shown two waves of activation for neutrophils release that peak at 3 and 14 days post injury, while activated microglia and MDM peak from 4-7 to 14 days post injury (it is now commonly accepted that there is a few infiltration of MDM from the periphery in mice). For comparison, microglial release in Human also peaks within days but depicts a slower decrease than in rodents (for review, see Perez et al., 2021). The neuroinflammation is one of the processes that lead to the loss of cells integrity of neurons and worsen oligodendrocytes alteration. The release of cytokines and chemokines, (with the noticeable release of TNF-α cytokine inducing the recruitment of T-lymphocytes) is another aspect of inflammation. This release has dual effects, mainly damaging in the neurodegeneration activation, as in Wallerian degeneration reported in rodents (Forgione & Fehlings, 2013).

Another considerable event is the formation of a scar, called the glial scar. Since our study is aimed to monitor this specific structure, more detailed related explanation is provided in the following section.

I.1.2.2.2. The Glial scar

The glial scar formation begins even within second after the injury in mice, when microglial cells start to migrate towards the injury site (to partly form the scar). The scarring formation continues during the secondary injury and maturates in the chronic phase. It is a multifactorial process involving various cell populations such as: reactive astrocytes, macrophages, oligodendrocytes precursor cells (OPCs), pericytes, fibroblasts and microglia (Alizadeh et al., 2019).

Reactive astrocytes (or scar-forming astrocytes, which are hypertrophied astrocytes), OPCs and pericytes (located in the parenchyma far from the lesion in some SCI models) migrate directly to the injury site and associate with the extracellular matrix (ECM) around the injury epicenter (Soderblom et al., 2013). The ECM proteins such as fibronectin, collagen and laminin are produced by fibroblasts (infiltrated from compromised meninges). The resulting scar formation is mainly induced by glial fibrillary acid protein (GFAP) upregulation, related to the level of activation of astrocytes (GFAP is overexpressed by activated astrocytes that eventually form the astrocytic border of the scar and surround the lesion site) and is called fibrotic scar or lesion core (Z. Li et al., 2021). As discussed previously, the characteristics of this fibrotic scar formation varies among species and the SCI models used. One noticeable observation can be done about the overall astrocytic response which seems to be slower in Human than in other animal models (including non-human primates) (Perez et al., 2021). Concerning fibroblastic processes, the fibroblasts proliferate and aggregate in the injured area, in both contusion and hemisection models in mice, but peak differently at 7 days post injury (Soderblom et al., 2013) and at 14 days post injury (Göritz et al., 2011) respectively. In both cases, the fibrotic scar matures within 14 days post injury (Z. Li et al., 2021) and consequently limits the extension and the inflammation from the injury to the spared parts. Despite of this initial and protective action, the dynamic maturation of the fibrotic scar during the chronic phase leads to an over regulation of chondroitin sulfate proteoglycans (CSPGs) in the ECM. This step inhibits the axonal regeneration, as illustrated in an hemisection model in mice (Dias et al., 2018) as well as cell differentiation in rodents, monkeys and Human (Alizadeh et al., 2019). More specific investigations has been done on both scar-forming astrocytes (Yang et al., 2020) and on fibroblasts to explore the dual role of the glial scar. Astrocytic modulation as well as fibroblasts regulator factors have been targeted as therapeutic strategies to reduce the scar formation and promote regeneration (for fibroblasts related processes, see review of (Z. Li et al., 2021)).

The other cell population highly involved in glial scar formation is microglia. Normally present in the spinal cord under a homeostatic state form (with a thin and elongated shape), microglia becomes activated when an injury occurs. In that case, the cells become bigger and rounded in order to efficiently migrate to the injury site; they are called ameboid microglia. The microglial activation is caused by resident and infiltrating inflammatory cells which produce and release cytokines and chemokines. During the first two weeks following the injury, as presented through a study in a contusion model, microglia highly proliferates and migrates to the injury site (Bellver-Landete et al., 2019). It locates right between infiltrating cells and astrocytes to create a glial border, inducing the subsequent astrocytes proliferation and the fibrotic scar formation by the release of microglia-derivated factors (such as IGF-1 for example). Similarly to astrocytes, microglial has a dual role, leading to neuroprotective effects and repairing during the first week after injury (Bellver-Landete et al., 2019) together with prejudicial consequences by participating in the secondary lesions formation (as reviewed in (David & Kroner, 2011; Yuan & He, 2013)) and by producing various pro-inflammatory mediators called proteolytic enzymes (such as matrix metalloproteinases in Human and rodents for example (Pang et al., 2021)). In that context, and even if exact microglia implication in neuroinflammation, tissue protection or recovery is not clear, complete depletion of microglial cells after an injury has been described to compromise glial scar formation, to increase immune cells infiltration as well as to reduce locomotor recovery (Bellver et al., 2019). Interestingly, when investigating the transient depletion of microglia proliferation in a hemisection model in mice with a pharmacological approach that targets CSF1R receptor (the membrane receptor of microglia insuring their proliferation, differentiation and survival), results concomitantly show that a treatment of 1-week duration with a CSF1R inhibitor (called GW2580) promotes motor recovery (Poulen, Aloy, et al., 2021) while prolonged treatment is no beneficial (Poulen, Bartolami, et al., 2021). After maturation, the glial border reaches a stabilized but dynamic form where activated microglia and macrophages (dedicated to phagocytosis of the neural debris), together with neutrophils and OPCs, are located in the lesion epicenter while astrocytes form a cellular barrier surrounding the lesions site. *Figure 4* is presenting a schematic of both forms of the glial scar, in the acute and chronic phase, in adult mammalians.

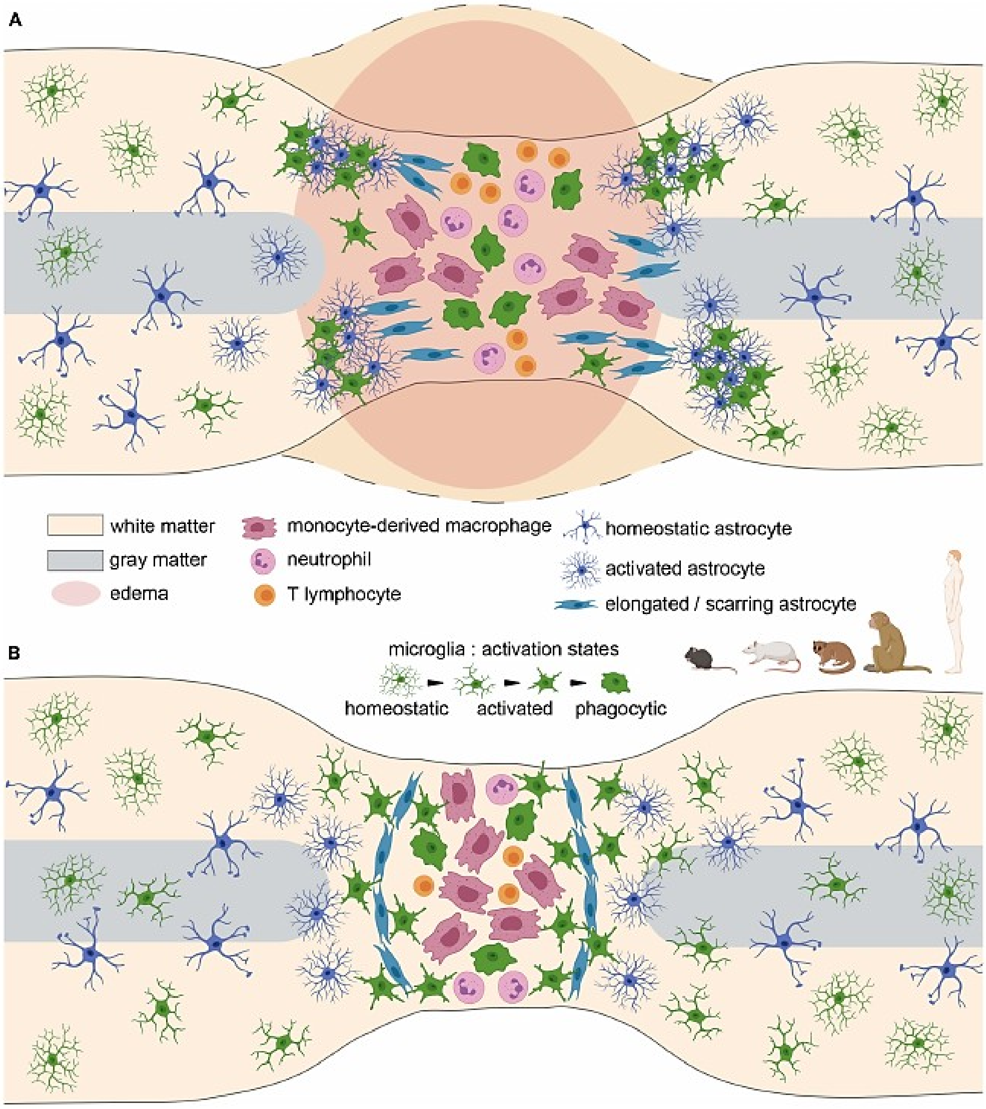

Figure 4: Glial scar formation in rodents and primates. In (A), the acute phase with cellular infiltration, reactivity, proliferation, and edema at the lesion site. In (B) Glial scar stabilization at the subacute/chronic stage, from (Perez et al., 2021).

During the chronic injury phase, the dynamic of the glial scar and the secretion of CSPGs by the astrocytes represent the main issue for the neuronal regeneration. Various strategies targeting CSPGs signaling pathways (as for example the neuronal transmembrane receptors LAR and PTPσ) have been attempted for axonal regrowth in SCI mice models (review in (Sami et al., 2020)).

I.1.2.2.3. The chronic phase

After the damaging and defensive processes that confront each other after the immediate injury, a chronic phase is reached when the scar is formed. Beside the deleterious effects of the glial scar during this period, some other persistent events are impactful and can be related to long-term impairments. Among these, a persistent demyelination (perturbation of myelin structure and function) or abnormal endogenous remyelination mechanisms have been reported to overall contribute to axonal degeneration and has been correlated to altered oligodendrocytes remyelination in various SCI animal models (review of (Alizadeh et al., 2015)). Following this assumption, clinical strategies have been developed targeting remyelination in SCI through, for example, induced pluripotent stem cells transplanting approaches (Alizadeh et al., 2015). Interestingly, a more recent study in a contusive model in mice has demonstrated that, even if oligodendrocytes myelination is required for myelin regeneration after SCI, it is not mandatory for locomotor recovery (Duncan et al., 2018)). More rarely, the astroglial scarring during the chronic phase have been associated with fluid-filled cystic cavities formation in rats or human followed, in some cases, by syrinx apparition (cavities containing CSF within the spinal cord) (Ahuja et al., 2017).

To have an overall remark on the pathophysiology of the SCI, the glial scar is part of the lesion healing process that exists in adult mammals, the other process being the regeneration ability that still prevails in lower vertebrates and developing higher mammals (Gu et al., 2015). Nonetheless, neuronal regeneration exists in adult mammalians and neuroplasticity is an important factor to examine for recovering considerations. Thus, it is important to underline that glial scar should not be confused with more classical scars (or fibroblastic scars) which are made of dense material deposition (mainly collagen) (Norenberg et al., 2004). A section is specifically dedicated to collagen implications in both fibroblastic and glial scar in part I.3 Collagen: roles and optical properties. Finally, studies of the glial scar formation in human SCI have shown a relatively mild process compared to rodents, mainly due to different astrocytic mechanisms that do not create, in most of the observations, an impermeable barrier in human (Perez et al., 2021). Despite the differences between species, the most relevant method to understand such a complex biomedical problem as SCI remains the animal model. In the last section of Spinal cord injuries generalities, a summary of animal models used for SCI is provided with a focus on the section model.

I.1.3. SCI animal models

A good SCI model should be relevant for the pathological processes occurring after an injury, and able to produce the different degree of lesion severity. Besides, it should be reproducible and easily available (Alizadeh et al., 2019). However, in most of the cases, experimental models fail to be translated into a clinical application. That is why it is crucial to carefully chose and design the protocol according to the underlying pathological question. Small rodents are the most frequently used because of the cost and ease of experimentation comparing to the other SCI models such as primates (lemurs, monkeys) and larger non-primates models (cats, swine). Among rodents, rats have a closer similarity of physiopathology with human SCI than mice (Alizadeh et al., 2019). To go further, it is known that larger mammals have the potential to lead to more effectiveness in treatment translation to clinics due to the closer resemblance in CNS anatomy with Human than rodents (Nardone et al., 2017) Mice and humans share similarities in functional and electrophysiological mechanisms but also many anatomical differences such as cord size and subarachnoid space and vasculature. Larger models present more comparability with humans in terms of spinal canal dimensions or vasculature (Weber-Levine et al., 2022). The size does not reflect the spinal cord organization or the best compatibility; for example, pigs can be larger than primates but less relevant for humans. An anatomical comparison between species through axial sections (lumbar-sacral region) is provided in *Figure 5 a.* As we have worked with a mouse model, axial sections (cervical, thoracic and lumbar regions) from mice are also provided in *Figure 5 b,* as well as sagittal and coronal (longitudinal) views *in Figure 5 c.*

That being said, both rodent and larger mammal models have their advantages and drawbacks, especially when it comes to mimic the variety of lesion occurring in human ((Zhang et al., 2014). Moreover, results are not comparable between different lesion models (Basso et al., 2006). Compression and contusion models are the closest to clinical cases: the first model reproduces a compression of the spinal cord after a dislocation or fracture that can happen in car crashes or sports, and the second model induces a shock on the spinal cord with a weight that can mimic SCI fights-related.

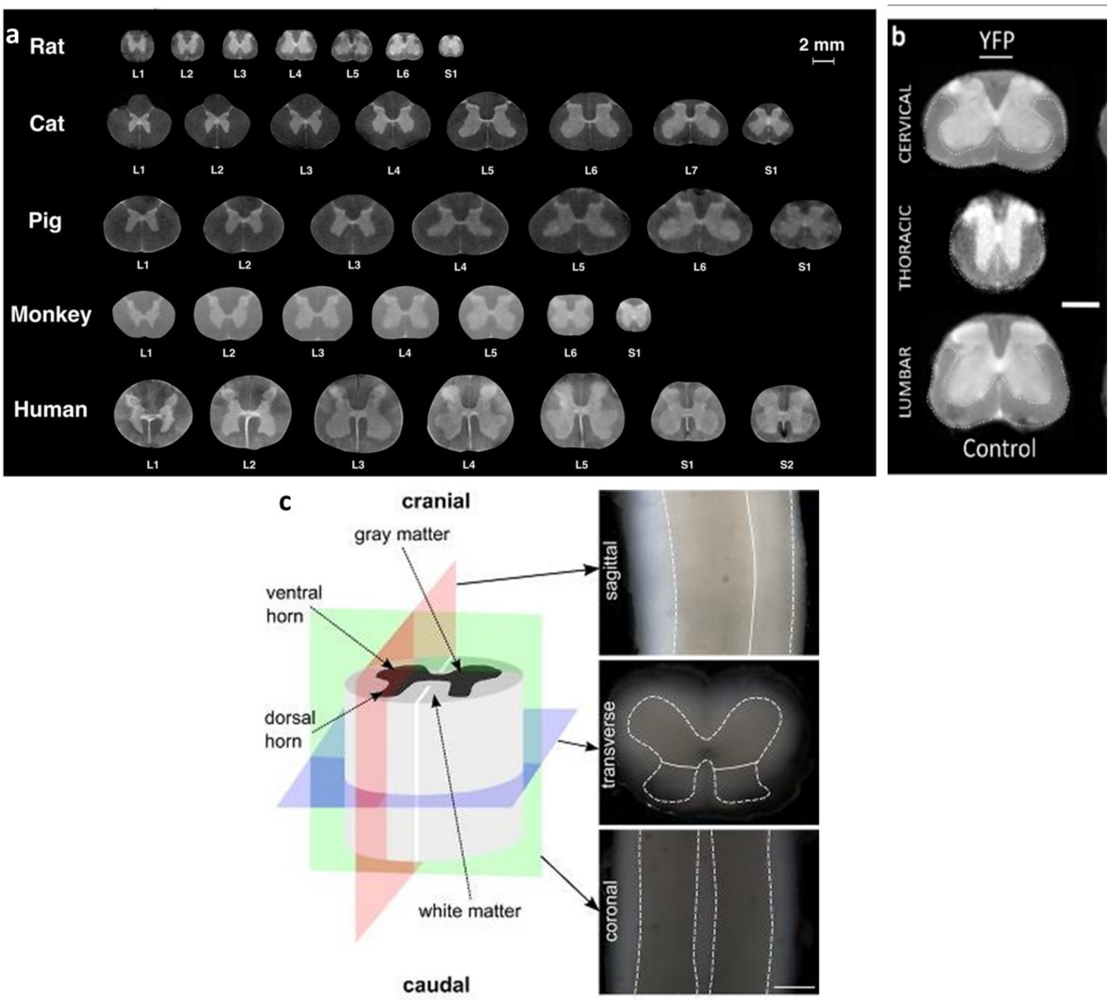

Figure 5: Spinal cord segments comparison between species. In a, MRI images of spinal cord segments L1-S1 of rats, cats, pigs, monkeys and humans (from (Toossi et al., 2021)). In b), MRI images of spinal cord segments from cervical, thoracic and lumbar regions of control mice, scale bar is 1 mm (modified from (Gatto et al., 2018)). In c) Schematic of the three anatomical planes of spinal cord in mice (red for sagittal, blue for transverse or axial and green for coronal or longitudinal), with the corresponding representative slices, scale bar is 500 µm (from (Koser et al., 2015)).

Section models allow producing a clear and complete lesion in the spinal cord, and are partially related to SCI induced by stab-wound cases (Cheriyan et al., 2014). In this model, the section can affect the whole spinal cord (transection) or only half of it (hemisection, with various types: dorsal, ventral, lateral…). The incision is performed with a microscalpel or scissors and can reach specific bundles of fibers in the spinal cord which thus lead to controlled impairments implications (motor or sensitive). In the hemisection case (HS), the surrounding environment is less impacted (less tissue disruption) than in transection with more neuroplasticity opportunities such as interspinal conduits sprouting (axons from the spared part are spreading their connections to the injured part). The injured side is called ipsilateral side.

The lateral HS approach has the valuable feature of preserving one side of the spinal cord which maintains bladder (in the long run, not after the injury) and intestinal functions in the animal, and gives also the opportunity to investigate the lesion characteristics and evolution in comparison with the spared part. *Figure 6* depicts HS model in rat, with the lesion located on the right side.

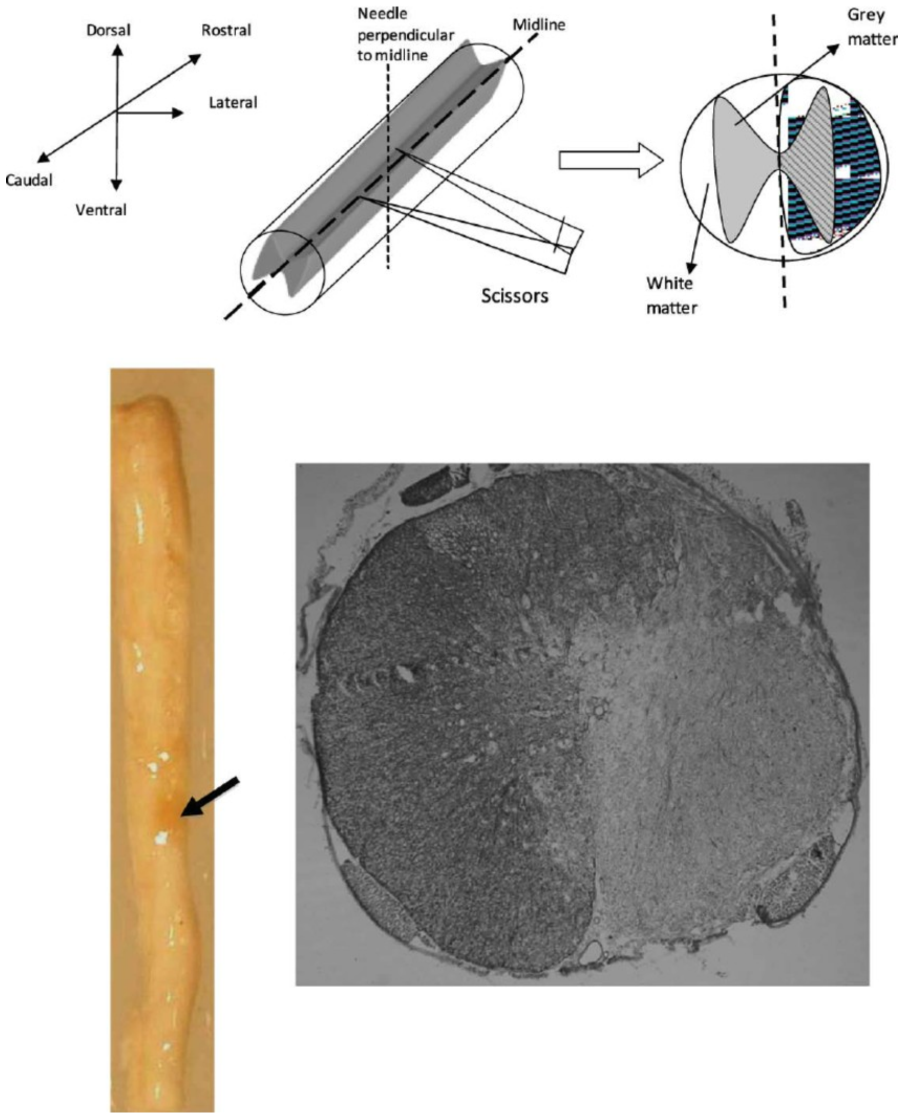

Figure 6: SCI hemisection model in rat. The upper part presents a schematic of how the injury is performed on the right side of the spinal cord, with an associated axial scheme of a half injured spinal cord. The two following images provide different views of the injury: on the left, a picture is showing an entire spinal cord, the black arrow indicates the injured portion. On the right, an optical image of a SC axial section is showing the tissue disorganization on the lesion side (right) while the spared part keeps its integrity. Adapted from (Saxena et al., 2011).

After presenting some key numbers and physiopathology phases in SCI, the next part reviews relevant examples where labeling and label-free imaging methods have been employed to investigate the lesion evolution.

I.2. Imaging spinal cord injury

Various imaging techniques have been developed to explore the cellular and the physiological changes that induce neurological diseases in the CNS, and specifically in the spinal cord. Consistently with our multimodal imaging protocol, the presented techniques will cover Immunohistochemistry (IHC) and its combination with fluorescence [confocal fluorescence and two-photon microscopy (2PEF)], and non-linear signals such as Second Harmonic generation (SHG), as well as Atomic force microscopy (AFM) for mechanical properties probing.

I.2.1. Gold standard method: staining and immunolabeling through fluorescence microscopy (1-photon and 2-photon microscopy).

Histopathology is the examination of microscopic changes in biological tissues and cells in various pathological states. This method has been used for centuries with constant improvements and is commonly applied in the clinical field. For diagnosis, histopathologists examine patients' biopsies that were processed with histological staining before microscope observation. The staining procedure is composed of five main steps: i) the sample fixation that retains the chemical properties while hardens the tissue in prevention for sectioning, and is usually performed through perfusion or immersion with formaldehyde fixatives, ii) the processing, mainly through dehydration that removes water using ethanol followed by hydrophobic clearing solutions, and resins addition to enhance the samples cutting, iii) the embedding (with or without paraffin depending on the cases) to extract the cellular structure, iv) the sectioning: preparation of sections with required thickness for slide mounting, and v) the staining itself (Alturkistani et al., 2015). As staining is an irreversible process, inducing modifications in tissue penetration and potentially in cellular integrity, freezing (when no paraffin is used) or removing paraffin after staining is recommended to reduce degradation of the cellular components. The stained slide can be directly observed with a microscope or be converted into a digital image, to further investigation with special software for qualitative and quantitative analysis. It can be assisted with Computer Aid Diagnosis (CAD) for a better image processing. The slide digitalization comes together with benefits (clearer view and availability of data, more precise and assisted assessments, cost-efficiency) and drawbacks (loss of 3-dimensionality, accessibility) (Hussein & Raad, 2015).

The staining itself has undergone improvements over the years. Routinely used dyes include: hematoxylin eosin (H&E) where the nuclei is stained in blue by hematoxylin and the basic components as cytoplasm or collagen are stained in pink for eosin, Golgi stain (for neuronal fibers) or Toluidine blue (Musumeci, 2014). The advanced techniques include: immunohistochemistry (IHC), an immunological labeling comporting enzymatic or fluorescent (immunofluorescence IF) stains. In IHC, different enzymatic labels are employed as peroxidase or alkaline phosphatase. In IF, fluorescent tagged antibodies can be typically used to provide an image contrast of proteins with a diagnosis interest. These targets are mostly functional proteins, as cell surface markers or soluble and structural proteins (Cicerone & Camp, 2018). With its high specificity in detection, IHC/IF helps to understand mechanisms underlying disease apparition. Moreover, simultaneous IHC/IF labeling can be performed to image many proteins at the same time. The method yet has also drawbacks: the accessibility of the proteins within the tissue and the efficiency of the immunolabeling action between the tagged antibody and the target, as well as the variability of labeling and compatibility problems that can occur with several stains (including background fluorescence coming from auto-fluorescent structures that can interfere with IHC) (Cicerone & Camp, 2018). *Figure 7* is showing a summary of the staining routine protocol with examples of H&E and IHC/IF (fluorescent tag) in kidney fibrosis explorations.

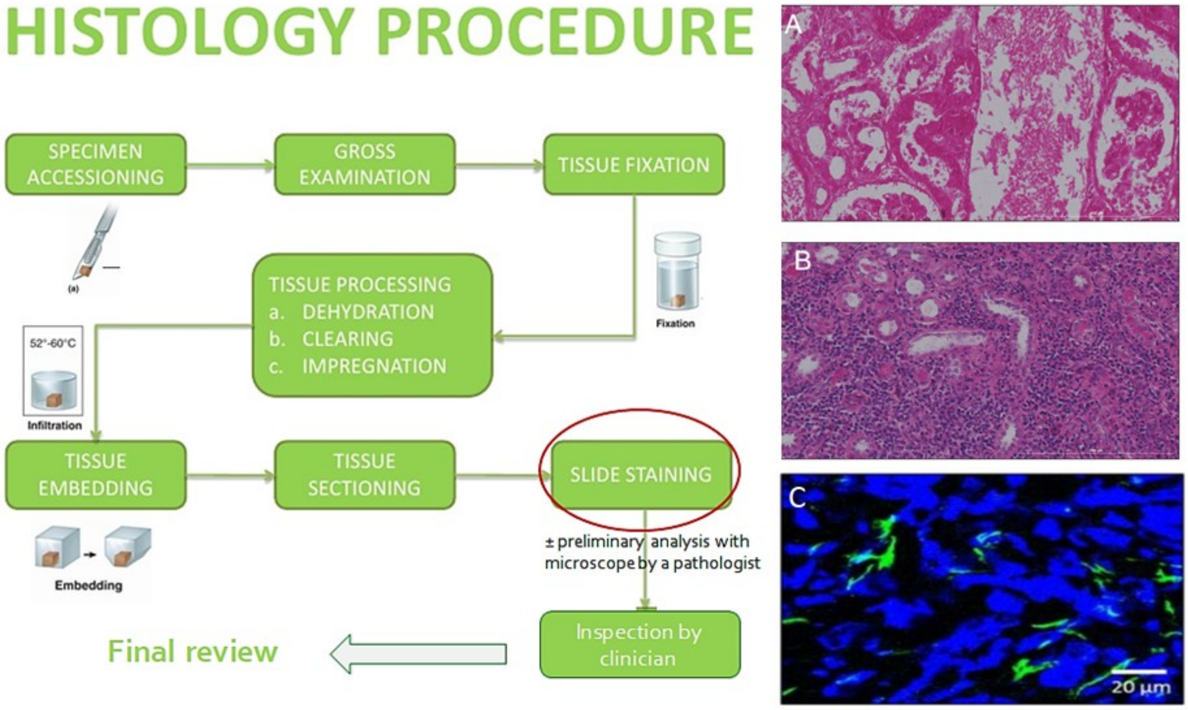

Figure 7: The different steps in a routine procedure of tissues preparation (left) modified from: https://www.slideshare.net/Medimeas/histology-procedure. Staining (right) in kidney: H&E in (A) normal state and in (B) chronic nephritis (fibrosis), from https://www.biotek.com/resources/application-notes/hematoxylin-and-eosin-stained-tissue/.and IF (C) for α-SMA in green (tag targeting activated fibroblasts), from (Kitano et al., 2017).

Overall, the IHC procedure is longue (from hours to days) and the interpretation is often user-dependent (when no quantitative analysis is additionally performed).

Imaging methods based on fluorescence can be used for the observation of components that have been previously labeled with a specific fluorescent tag to target the structures of interest. These tags are also called fluorochromes and are exogenous sources that need to be brought into the original sample. Auto-fluorescent molecules also exist (as flavin and NADH) called also endogenous sources. The advanced techniques in fluorescence microscopy include confocal and two-photon fluorescence microscopy, for in depth 3D cell and tissue imaging. In classical one-photon fluorescence 1PEF, the sample is excited with a visible light and a photon (with a certain energy E=hv) is required to bring the fluorescent molecule from the fundamental state to the excited state. To return to the ground state, the molecule emits one photon with a lower energy (or at a higher wavelength) than the energy of the absorbed light. The efficiency of the emission is given by the fluorescence quantum yield ($N_{\text{photons emitted}} / N_{\text{photons absorbed}}$). Consistently, a good fluorochrome needs to have a good quantum yield (0.8 or 0.9) together with a short lifetime in the excited state (3 ns) and a low photobleaching (which is the irreversible destruction of an excited fluorochrome in presence of oxygen reactive components). Commonly used fluorochromes are fluorescein, DAPI, Green fluorescent protein (GFP) or Texas-Red. In 1PEF microscopy, a pinhole is necessary in the microscope set up, to block the light from outside the focal plane and provide a better contrast; this is the confocal microscopy principle. Conversely to one-photon fluorescence, in multiphoton microscopy (MPM), the sample is excited with a near infrared laser which allows non-linear (NL) phenomena to occur (the non-linear processes is developed in SHG section). The most frequently used NL method is two-photon excitation microscopy (2PEF), where 2-photons with the same energy (E= hv/2 for each photon) are absorbed by the molecule to reach the excited state, with the help of an intermediate “virtual state” after the absorption of the first photon (Batista, 2018). This absorption can only occur for high intensities, at the focal point of the laser and allows a very good excitation confinement in the laser focal point. The signal here is varying as the square of the excitation intensity and this dependency is allowing the 3D localization of 2PEF signal (Pena, 2006). Along with this noticeable advantage, MPM leads to a better depth penetration than 1PEF (~ 500 nm to 1.5 mm) due to less diffusion of the excitation light and less background, to reduced photobleaching due to the confined excitation, and to endogenous contrast. Finally, MPM allows the combination of various contrasts (endogenous, exogenous fluorescent, other NL processes) for observing the various optical properties of the tissue components.

Figure 8 is illustrating the difference in light confinement between 1PEF (at the focal point and along the excitation beam) and 2PEF (only at the focal point) microscopy and the related Jablonsky energy diagrams.

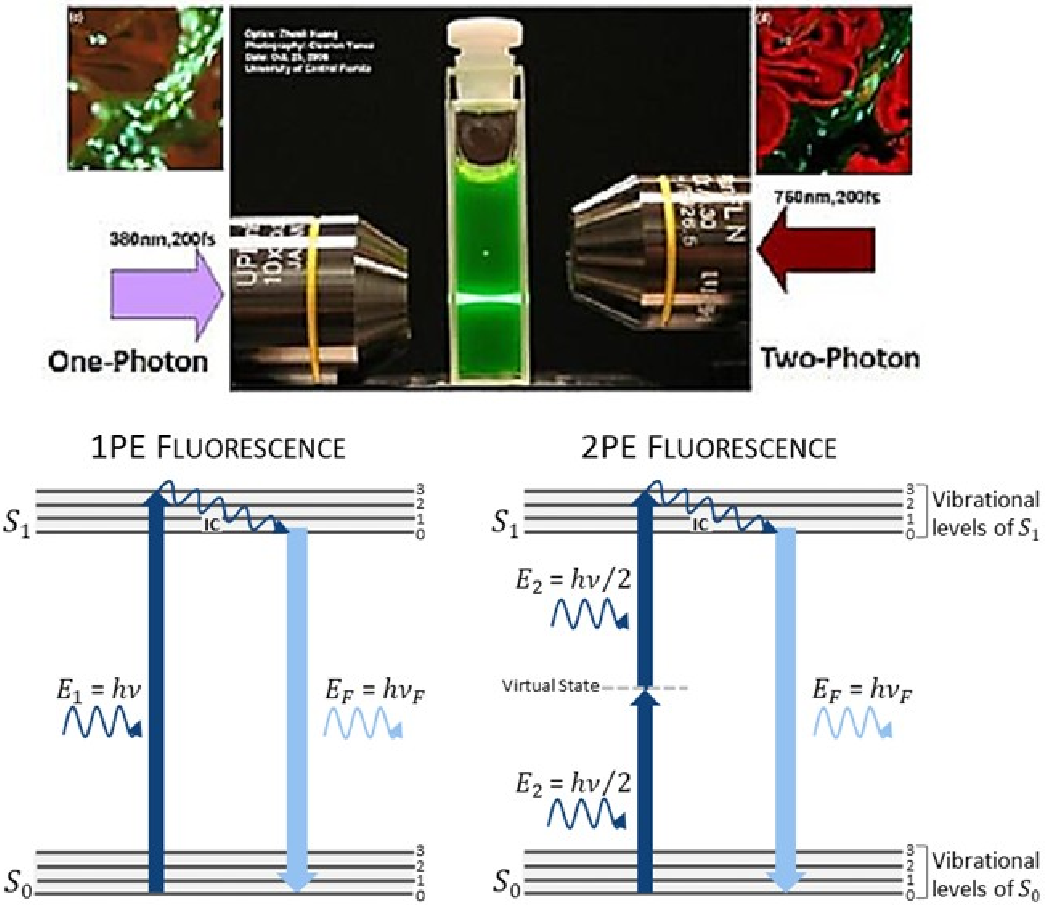

Figure 8: 1-photon and 2-photon microcopy principles showing the difference in light confinement from (Huang et al., 2011) and in Jablonsky energy diagrams from (Batista, 2018).

Staining, IHC/IF and fluorescence microscopy consist together in a gold standard method that have been employed for years in SCI to visualize labeled targets. For example, to assess the effect of a CSF1-R inhibitor treatment in mice and non-human primates, staining techniques as luxol fast blue, neutral red staining and IHC have been combined (Poulen, Aloy, et al., 2021). Staining has also been widely used to validate observations coming from label-free imaging. For example, toluidine blue staining has been performed together with MRI in a HS model in mouse to evidence the lesion area extension on the same spinal cords (Noristani et al., 2018). In combination with Raman spectroscopy, H&E has been correlated to spectral plots to assess a treatment by comparing healthy, injured and mice groups treated with low-level laser therapy (treatment for cutaneous wounds)(Gong et al., 2018). Raman has also been employed to illustrate pathological processes at different time-points post injury in a contusion rat model (J. Li et al., 2019). Specific spectroscopy investigations have been performed on myelin sheaths with CARS (that excites the CH_2 bonds present in myelin lipids) to investigate the demyelination process, combined with immunolabeling of cells nuclei (Fu et al., 2008) or of Ranvier nodes components (Shi et al., 2011). CARS has also been recently used to compare spinal cord myelin in different species (Poulen, Gerber, et al., 2021) as well as after SCI in mice and non-human primates to assess GW2580 treatment effects on myelinated fibers (Poulen, Aloy, et al., 2021). *Figure 9* is presenting the contrasts one can reach with various staining methods, including toluidine blue, H&E, and IF, carried out in SCI (HS model in mice and contusion model in rat).

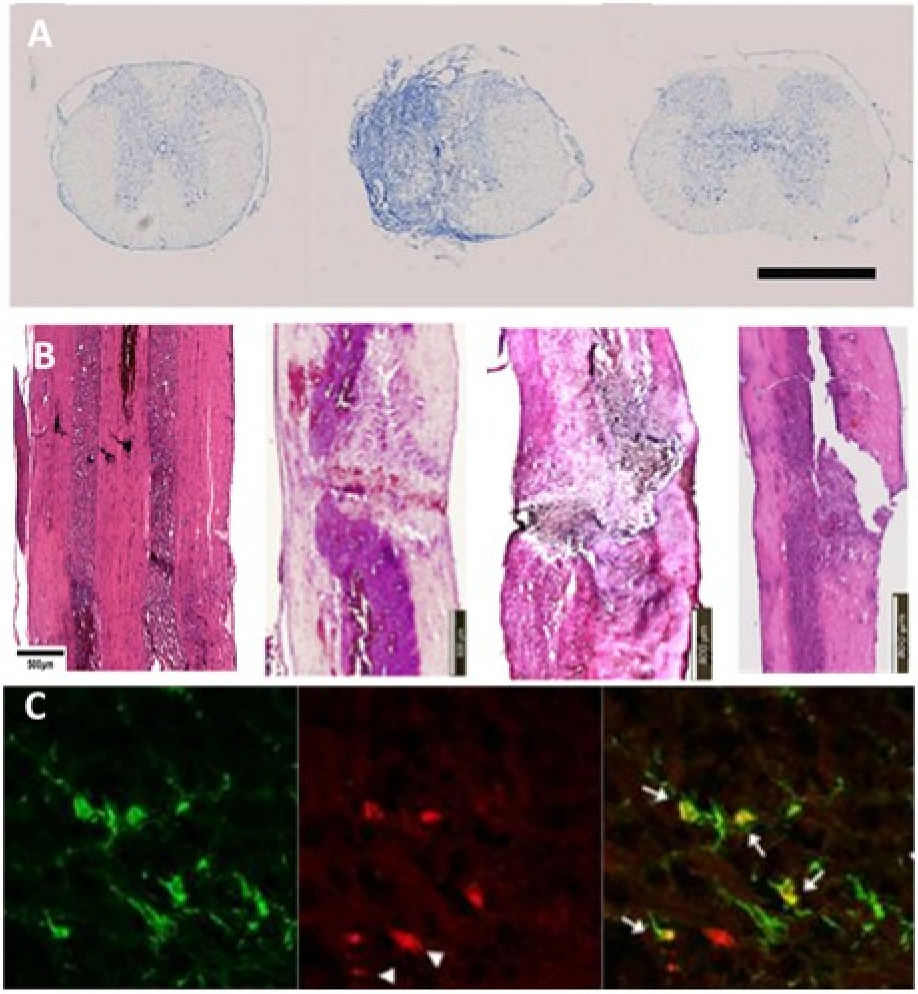

Figure 9: Staining and immunolabeling in SCI. In (A) Toluidine blue staining of SC axial sections after a hemisection (HS) in mice, in (from left to right) rostral, lesion and caudal locations, scale bar = 1mm, from (Gerber et al., 2018a)*. In (B) H&E staining on longitudinal sections of (from left to right) healthy SC, from (Gong et al., 2017), and at different times post-injury in a contusion model in rats: 1-DPI, 7-DPI and 14-DPI, from (J. Li et al., 2019). In (C), eGFP expressed in microglia (green), IF of proliferating cells (red) and merged (yellow) in HS in mice, scale bar= 10 µm modified from (Gerber et al., 2018a).*

Immunostaining and particularly IF, visualized through 1PEF and 2PEF, can be integrated with other non-linear imaging techniques to: i) bring validation from a well-established method, ii) target more specific structures and properties in the same imaging protocol, iii) investigate the relation between different factors involved in SCI to reach a better understanding of underlying mechanisms related to the pathological state. To this extend, MPM has become a widely used label-free minimally invasive method. Indeed, 2PEF imaging can be associated with further non-linear contrasts, such as Second Harmonic Generation (SHG) for neuronal repair or fibrotic scar formation (Galli et al., 2012) and Third Harmonic Generation (THG) an interface-sensitive microscopy used to image myelin and neurons (Farrar et al., 2011). The next section concentrated on SHG, which has been widely exploited in our study for collagen characterization. Elements of theory about non-linear processes, SHG in non-centrosymmetric structures and polarization-resolved SHG (P-SHG) are provided in a first place. Some applications in SCI are briefly discussed at the end of the section. As SHG has been used in SCI mainly for fibrillar collagen investigations, more precise examples are given in the I.3 Collagen part, at section I.3.2 Collagen in SCI.

I.2.2. Second Harmonic generation (SHG)

I.2.2.1. Non-linear (NL) processes

In nonlinear optics, or NLO, the optical properties of the material are modified in the presence of an intense electromagnetic field as for example in a laser beam. To apprehend these modifications, we consider the polarization density (dipole moment per unit volume) first in linear optics: when a light interacts with a sample, it generates a polarization density P linearly dependent on the applied electric field strength E, and the relation can be described as follows:

$$P(t) = \varepsilon_0 \chi^{(1)} E(t) \tag{1}$$

where the proportionality constant $\chi^{(1)}$ is the linear susceptibility tensor and ε_0 is the permittivity of a free space . $\chi^{(1)}$is related to relative permittivity ε_r and to the refractive index of the medium n, by:

$$\chi^{(1)} = \varepsilon_r - 1 \tag{2}$$

$$n= \sqrt{\varepsilon_r} \tag{3}$$

$\chi^{(1)}$ is describing the intrinsic optical properties such as: the optical index, the linear absorption (1PEF for example), the birefringence and light scattering for example (Rao, 2012).

In NLO, P is expressed as a power series in the field strength as:

$$P(t) = \varepsilon_0 \, [\chi^{(1)}E(t) + \chi^{(2)}E^2(t) + \chi^{(3)}E^3(t) + \cdots]$$

$$\equiv P(t) = P^{(1)} + P^{(2)} + P^{(3)} + \cdots$$

$$\equiv P(t) = P^{(1)} + P^{(NL)} \tag{4}$$

where $\chi^{(2)}$ and $\chi^{(3)}$ are known as the second-order and third-order susceptibility tensors, respectively. A description of the $\chi^{(2)}$ components is detailed in part I.2.2.3 Polarization-resolved SHG. These tensors indicate the degree of polarizability of a dielectric material. In general, these two quantities depend on the frequencies of the applied field, but we will always work with the assumption that the medium response is instantaneous, so we consider them constant (Boyd, 2008). Consequently, referring to equation (4), $P^2(t) = \varepsilon_0 \, \chi^{(2)}E^2(t)$ is the second-order polarization and $P^3(t) = \varepsilon_0 \, \chi^{(3)}E^3(t)$ is the third-order polarization. $P^2(t)$ is varying quadratically with the electric field and can only occur in non-centrosymmetric structures, which are basically crystals lacking inversion symmetry. Indeed, liquids, gases and many crystals are centrosymmetric structures and cannot generate second-order polarization. Few non-centrosymmetric biological structures yet exist, the main being fibrillar collagen, microtubules and myosin in sarcomere. In such structures, second-order processes can happen such as Second Harmonic Generation (SHG) (described further). Conversely to $P^2(t)$, $P^3(t)$, specifically $\chi^{(3)}$, can occur in both centro and non-centrosymmetric structures and describe third-order linear processes such as stimulated Raman scattering and Third Harmonic Generation (THG). The typical values of $\chi^{(2)}$ and $\chi^{(3)}$ in condense matter are $1{,}94 \times 10^{-12}$ m/V and $3{,}78 \times 10^{-24}$ m²/V², respectively (Boyd, 2008). The most common way to describe NLO phenomena is to consider the expression of $P(t)$ and to combine it with Maxwell's equations in a source-free medium (Rao, 2012). The resulting equation is presented under the following form:

$$\nabla^2 E(t) = \frac{n^2}{c^2}\frac{\partial^2 E}{\partial t^2} = \frac{1}{\varepsilon_0 c^2}\frac{\partial^2 P^{NL}}{\partial t^2} \tag{5}$$

with n, the refractive index of the medium (related to equations (2) and (3)) and c, the velocity in light in vacuum $c = \frac{1}{\sqrt{\mu_0 \varepsilon_0}}$ μ_0 is the free-space magnetic susceptibility.

Though the first observations of NL phenomena were reported in 1941, NL optics truly started with the advent of the first lasers which allowed to observe SHG phenomena in 1961 (Boyd, 2008) . SHG is a second-order coherent process, depending on the polarization of the laser beam and inducing a high directional signal (Hanrahan et al., 2020).

Alongside 2PEF, SHG can be recorded on the same sample with MPM following an excitation with high intensity (10^6-10^{14} W/cm^2). Such intensities can be reached only by lasers, mainly in pulse mode. While 2PEF is based on the absorption of the light energy that breaks the coherence between the resulting emitted photon and the excitation photon(s), SHG is the non-linear diffusion of the light and, no absorption occurs. SHG process is based on a two-photon excitation process, as in 2PEF, but no excited state is properly reached; only virtual transitions happen. The resulting photon has a higher energy than one single excitation photon, but has precisely twice the frequency 2ω (and half the wavelength) compared to the excitation light, while the emitted 2PEF signal is shifted to red wavelengths. The coherence in SHG is kept between the excitation and the emitted photons, and the atomic modifications are varying quadratically with the strength of the electric field $E(t)$. As a result, the intensity of SHG signal increases as the square of the intensity of the excitation beam. *Figure 10* is presenting differences between 2PEF and SHG with Jablonsky energy diagrams and corresponding emitted photons wavelengths. An example of the specific excitation of different tissue components with both signals is also provided *Figure 10 D*).

As a second-order phenomenon, the requirement for SHG occurrence is to have a non-centrosymmetric medium, composed of polarizable electrons between a donor group and acceptor group at molecular level (Pena et al., 2005) that act as dipoles when excited by an electromagnetic field. An SHG signal is generated only if these dipoles irradiate in phase with the excitation light. SHG is also sensitive to the distribution and orientation of the dipoles in the focal volume (Mostaço-Guidolin et al., 2017). For an effective collection of the forward emitted SHG, the numerical aperture (NA) should be carefully chosen since it depends on the illumination angle (i.e. the directionality of the incident light). For NA<0.8, $\theta_{peak} = 1/\sqrt{2}\,\theta_{NA}$ with θ_{peak} the angle of maximum SHG signal and θ_{NA} the illumination angle (Hanrahan et al., 2020). Phase dependency and directionality are developed in the following section I.2.2.2 SHG in non-centrosymmetric structures.

I.2.2.2. SHG in non-centrosymmetric structures

Non-centrosymmetry, i.e. lacking inversion symmetry, is a necessary condition for SHG signal to occur. If we consider the interaction between an incident light with a ω frequency and one molecule acting like a dipole (a scatterer), the symmetry of the molecule is an important parameter to consider: in a symmetric molecule, the electrons can start to oscillate at the same frequency ω and the dipolar moment is equal to 0. The emitted signal thus has the same frequency ω as the excitation light. Such interaction is called Rayleigh scattering.

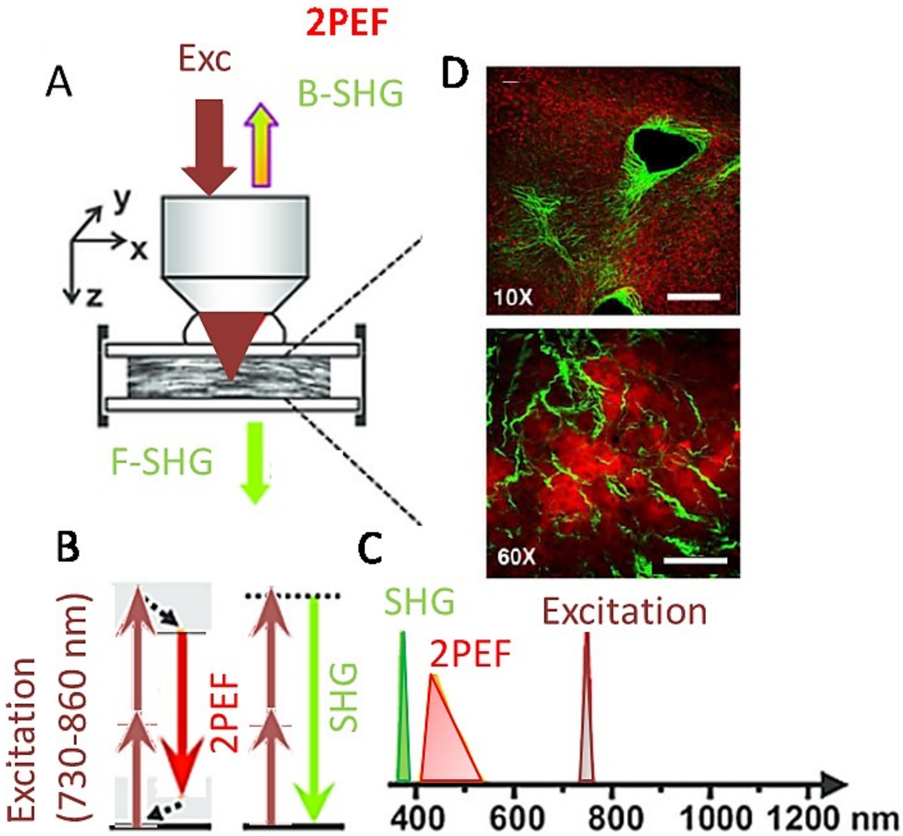

Figure 10: Non-linear processes: (A) Emission of 2PEF (red) and SHG (green) in the forward (F-SHG) and in the backward (B-SHG) directions. (B) Jablonsky energy diagrams of 2PEF and SHG. (C) Excitation and emitted wavelengths are presented along the wavelengths axis (in nm), A,B and C modified from (Aptel et al., 2010). (D) Simultaneous 2PEF (red pseudo-color) and SHG (green pseudo-color) imaging in human fibrosis liver, showing the typical tissue autofluorescence and fibrillar collagen, respectively. With 10x (up) and 60x (down), scale bars are 250 and 60 µm, modified from (Gailhouste et al., 2010).

In the case of a non-symmetric molecule, the electrons do not respond symmetrically to the excitation and the dipolar moment is not null; as a result, the emitted frequencies are a combination of the initial ω frequency, plus other frequencies at 0 or 2ω. The latter frequency is the one representing the harmonic scattering of the light (Pena, 2006). Most of SHG applications target several molecules organized together within a structure; in structures with high molecular arrangement, the harmonic scattering is coherent and constructive interferences occur. Eventually, sufficient signal is produced to be detected. On the contrary, in not perfectly arranged structures, the scattering is incoherent and the resulting signal depends on the number of radiating molecules.

That is the reason why, even if a structure is non-centrosymmetric, it also needs a well-defined molecular arrangement. If it does not fulfill both conditions, the structure won't produce enough SHG signal to be observed, as for example in DNA (Rao, 2012).

Another crucial point to consider is the directionality of the dipoles and more precisely their orientation: dipoles orientated in the same direction induce constructive interferences while dipoles orientated in opposite directions (antiparallel) lead to destructive interferences. The dipole orientation is related to the phase mismatching factor Δk. In order SHG generation to happen, the following condition must be fulfilled:

$$\Delta k = k_{2\omega} - 2k_{\omega} \tag{6}$$

with k_{ω} and $k_{2\omega}$ the wave vectors of the incident beam and of the emitted wave with a double frequency, respectively (Hanrahan et al., 2020). If the phase matching is perfect, $\Delta k = 0$, the emitted signal propagates in both forward (F) and backward (B) directions. However, in biological tissues, non-perfect matching is the most frequent case encountered. If a collimated laser is used to excite the sample, SHG propagation is in the same direction as the excitation beam (Pena, 2006). When a focused laser beam is used, SHG propagates with an angle θ with respect to the incident light, along two symmetric lobes (Moreaux et al., 2000). In addition, the size of the scattering structure must be considered (forward emission dominates if the scattering structure is large compared to the excitation wavelength) (Zipfel et al., 2003). Usually, SHG is predominantly emitted in the forward direction and it is therefore collected in transmission. For small structures (size smaller or equal to SHG wavelength) backward emission becomes equivalent to forward emission and is therefore epi-collected. *Figure 11* is summarizing the directionality in SHG generation. Overall, the coherence of SHG leads to an anisotropic signal and to the 3D observation of the tissue at a micrometric level (Pena, 2006).

The directionality of the dipoles has a great impact on SHG generation. All at once, the directionality of the incident beam plays also a key role in the characterization of the non-centrosymmetrical structures detected. Varying the polarization of the excitation light can leverage the susceptibility tensor to reveal supramolecular organization parameters such as the symmetry. The next section will develop the components of the $\chi^{(2)}$ and its relation with the laser beam polarization.

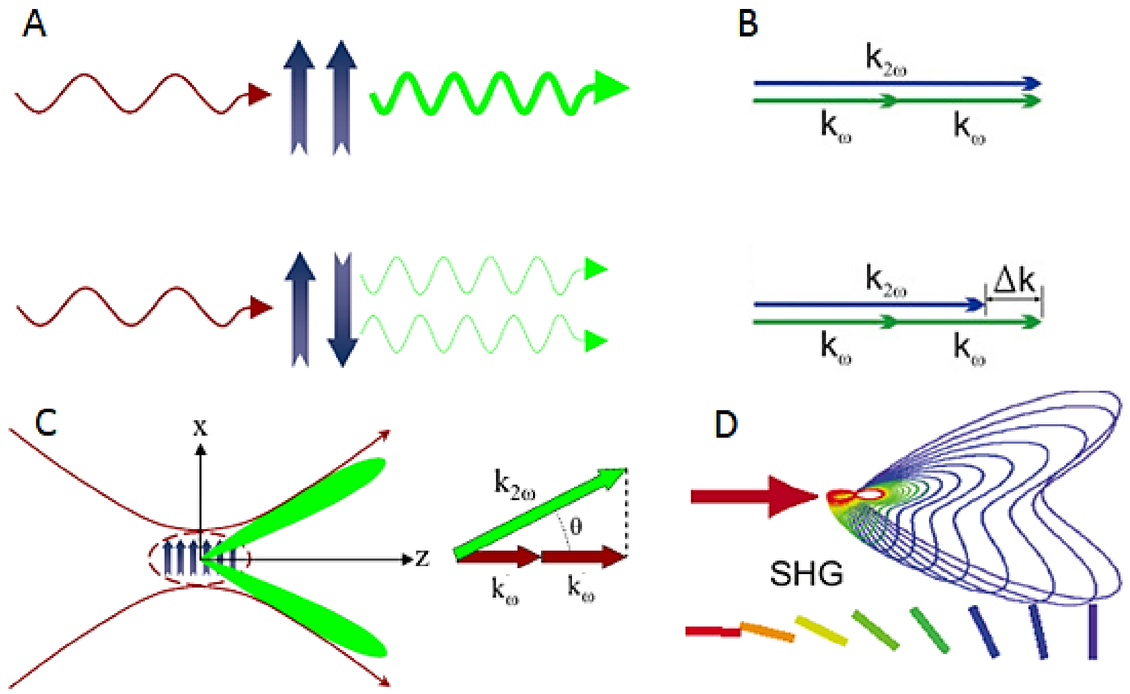

Figure 11: Dipoles directionality in SHG generation. In (A), dipoles orientation in the same direction (up) induces SHG signal, while antiparallel orientations (down) result in destructive interferences and null SHG signal. In (B) phase matching conditions in a perfect matching case (up) where $k_{2\omega}$ the wave vector with double frequency is equal to k_ω the wave vectors or the incident beam, and (down) a common case in tissues with a phase mismatch factorΔk. In (C), the radiation directionality in the case of a focused beam where the emission wave is orientated with an angle θ against the optic axis. In (D), the radiation pattern depending on the dipoles orientation against the optic axis. Sources: (A) and (C) modified from (Pena, 2006), (B) from (Kumar et al., 2018), and (D) from https://kcci.virginia.edu/shgthg (Accessed on 19 June 2022).

I.2.2.3. Polarization-resolved SHG (P-SHG)

The polarization of the incident light can be tuned to extract valuable structural parameters of the non-centrosymmetric system. In classical SHG imaging, the laser excitation is polarized circularly while in polarization-resolved SHG (or P-SHG), the SHG signal is collected in function of the orientation of a linearly polarized laser. The relation between the SHG intensity and the polarization of the incident beam can be described as follows (Cisek et al., 2021):

$$I_{SHG} \propto \chi^2 : E . E \tag{7}$$

with: . the tensor product, E is the intensity and also the polarization of the electric field of the incident laser and χ^2 is the second-order susceptibility tensor we presented earlier. In this equation, we can observe that the intensity of the SHG signal is dependent on the supramolecular structure, the orientation of the scatterers (these information are contained in the term χ^2) and on the intensity and polarization of the incident light (Cisek et al., 2021). To further describe the components of the tensor, we start from the expression of the electric field radiated at 2ω that can be decomposed into two components: E_s (perpendicular to the incidence plane) and E_p (parallel to the incidence plane (Pena, 2006):

$$E_s \propto\ f_{s,p}\, E^2{}_p(\omega) + g_{s,p} E^2{}_s(\omega) + h_{s,p}\, E_p(\omega) E_s(\omega) \qquad (8)$$

with $f_{s,p}$, $g_{s,p}$ and $h_{s,p}$ the 6 components of the tensor χ^2. The tensor components are usually measured in laboratory coordinate system with the IJK/XYZ indices, where the sample is located in the X-Z plane and the laser excitation beam is propagating along Y-axis. When considering 2D polarimetry, the laser is focused on the X-Z plane and only six components of the tensor can be extracted. We can further write the previous$f_{s,p}$, $g_{s,p}$ and $h_{s,p}$ tensor components according to the coordinate system: $\chi^{(2)}_{XXX}, \chi^{(2)}_{XXZ}, \chi^{(2)}_{XZZ}, \chi^{(2)}_{ZXX}, \chi^{(2)}_{ZZX}$ and $\chi^{(2)}_{ZZZ}$, with $\chi^{(2)}_{XXZ} = \chi^{(2)}_{XZX}$ and $\chi^{(2)}_{ZZX} = \chi^{(2)}_{ZXZ}$ in the SHG generation (Golaraei et al., 2019). According to these second-order susceptibility tensor elements, the 3D orientation of the structures within the sample can be expressed in six different equations for each component, in relation with the polarization angle of the excitation beam α. The six equations won't be provided here, but an example can be shown for $\chi^{(2)}_{ZXX}$:

$$\chi^{(2)}_{ZXX} = cos\alpha\, cos\delta\, \left[\chi^{(2)}_{ZZZ} - 2\chi^{(2)}_{XXZ} - \chi^{(2)}_{ZXX}\right) cos^2\alpha\, sin^2\delta + \chi^{(2)}_{ZXX}] + \chi^{(2)}_{XYZ}\, \sin(2\alpha)\, sin\delta \qquad (9)$$

In this specific case, the term $\chi^{(2)}_{XYZ}$ is a chiral component. There are also non-chiral components, often used for symmetry assessments. To compute symmetry properties in fibrillar collagen, for example, the Kleinman symmetry ($\chi^{(2)}_{ZXX} /\ \chi^{(2)}_{XXZ} = 1$) is assumed, together with a cylindrical C6v symmetry. This leads to the consideration of the ratioρ=$\chi^{(2)}_{ZZZ}/\chi^{(2)}_{ZXX}$, which is the SHG anisotropy, and to the extraction of the angle δ, which is the in-plane projection of the collagen fibers orientation (Cisek et al., 2021). Additionally, SHG intensity can be plotted in function of the angle of polarization. The obtained polarization curves, have thus a specific profile related to the supramolecular structure and the symmetry of the emitters: straight fibrils bundles are associated with a cylindrical symmetry while wavy fibrils have trigonal symmetry. A balance between symmetry can subsequently be calculated depending on the tissue state (Mercatelli et al., 2020). In some tissue investigations (such as in tendons), attenuation or birefringence can interfere with P-SHG and do not allow symmetry parameters recording (Gusachenko, 2014).

To close the presentation of SHG principle, advantages and drawbacks of the method are provided in Table 1.

Table 1: Second harmonic generation, advantages and drawbacks

Advantages	Drawbacks
Good depth penetration (500 µm to 1.5 mm)	Cost and set up montage
Light confinement in the focal point	Relevant only for specific structures
Reduced photobleaching and phototoxitcity	Some supramolecular parameters unattainable depending on the tissue
Excellent contrast for intrinsic asymmetric molecules	
χ^2 variation in function of scatters supramolecular arrangement, density and orientation; various characterizations with one parameter	
3D visualization due to signal coherence	
Phase information about radiation pattern	

In the SCI context, SHG has been mainly used to investigate demyelination and fibrotic scar formation through analysis of fibrillar collagen. Examples concerning the latter point are detailed in part I.3.3.3 Collagen in SCI, especially in Galli and colleagues work (Galli, 2018) which is currently the main study on fibrillar collagen observation and quantification in SCI using SHG. Collagen has been also explored in healthy spinal cord (Cheng et al., 2019; Liao et al., 2016) where SHG signal was mainly originated from nerve axons and *dura matter*. Demyelination, often studied with CARS, has also been investigated using the SHG signal sensitivity to detect the membrane potential associated with myelinated fiber changes after an injury (X. Chen et al., 2012). Observing nerve regeneration, SHG has been associated with 2PEF to detect cell-matrix interaction in the fibrotic scar after a treatment based on chondroitinase (Huang et al., 2011). *Figure 12* illustrates the SHG signal of the myelinated nerve fibers in a healthy spinal cord in rats.

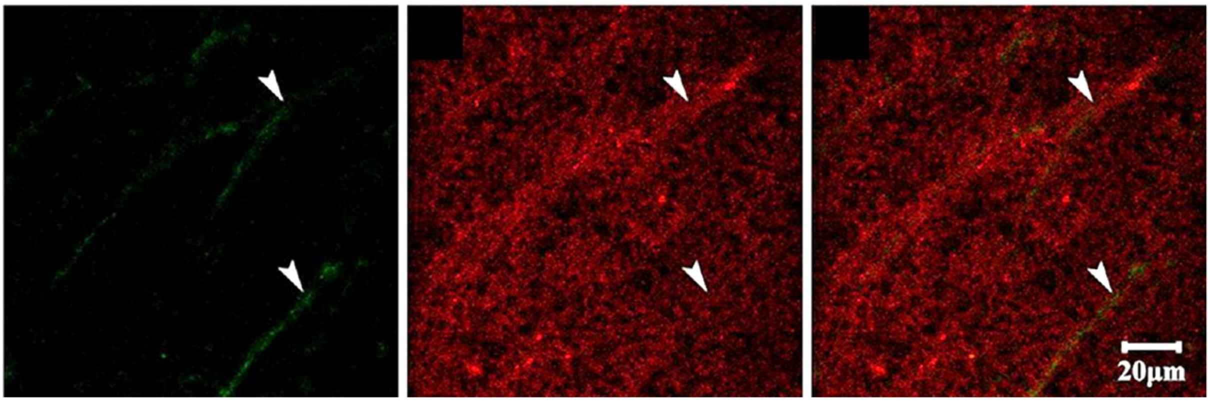

Figure 12: Non-linear imaging in the lateral column in a healthy spinal cord in rats. From left to right: SHG signal (green) emitted by the myelinated nerves fibers (arrows), 2PEF (red) emitted by granules surrounding the cytoplasm nuclei, and merged image of both signals, from (Liao et al., 2016).

I.2.3. Atomic Force Microscopy (AFM)

Mechanobiology is studying the effects of physical forces and mechanical properties at different scales (proteins, cells and tissues) monitoring cell division and differentiation, signaling, phenotypic changes or pathological processes (Krieg et al., 2019). Among the scanning probe microscopy family, the most widely used is Atomic Force Microscopy (AFM). Since its development in the 80's by Binning, Quate and Gerber, AFM has made a huge contribution to the investigation of biological systems, since it can operate in various environments such as aqueous media, and in physiological conditions, with no required staining. Moreover, it provides sub-nanometer resolution and measurements of sub-picoNewton forces (Churnside et al., 2012) and allows to probe structural and functional parameters underlying the cell structural integrity (Gavara, 2017). Even if strong improvements have been reached in terms of set up variety for biological research, such as combination with epi-fluorescence, or temperature-controlled fluid cells, the main principle of AFM is still quasi unchanged: a cantilever (micrometrical dimensions) ended by a sharp (nanometric) probe is taken close to the sample to probe its topography with a very high signal to noise ratio, which allows for example the detection of single proteins in the cellular membrane (Krieg et al., 2019). The technique is based on the measurement of the bending of the soft cantilever due to the interaction forces between the sharp tip and the sample surface. Despite the apparent simplicity of the technique, several points must be considered to relevantly address the scientific question, to define the protocol relatively to the sample probed, and to further process the recorded data.

One crucial point is the choice of the nanometric tip as the tip size (typically with a radius less than 10 nm) is related to the lateral resolution of AFM. The tip is machined at the end of a flexible macrometric cantilever (characterized by its spring constant) itself built in a silicon or silicon nitride macroscopic chip. When the tip interacts with the sample surface, the cantilever acts as a lever and bends, or is deflected. The deflection can be followed by a laser focused on the cantilever end that is eventually reflected and detected on a quadrant photodiode. All the slight changes in the cantilever position can thus be monitored by a constant feedback that maintains the tip near the sample, usually at a constant distance. More precisely, when deflection changes occur, the photodiode moves in a way that the difference between the output photovoltage from the top and bottom of the quadrant diode is equal to 0. The movement of the cantilever induced by piezoelectric changes and the cantilever bending are happening perpendicularly to the sample surface (Gavara, 2017). The tip approach also depends on the chosen mode that provides various parameters along topography such as: the sample elasticity, the friction or adhesion forces (Varga et al., 2018). *Figure 13 f)* is showing AFM principle and main measurements.

When monitoring the mechanical properties of the sample, the force spectroscopy mode is used when the tip is gently indented into the sample and the applied force is measured. The horizontal position of the cantilever is not varying, only the vertical movement and the related deflection are recorded. The distance wandered by the tip and the deflection induced by the forces are represented in a force-distance (FD) curve. At least one FD is recorded for each pixel of the probed area. Apart from the FD curve, relaxation or creep can also be calculated by various tip movements following the indentation. *Figure 13 a)* is providing a scheme of the mechanical properties' measurements. *Figure 13 b)* is presenting a FD curve, composed of four different steps: I) the tip is still far from the surface, and starts to approach the sample, II) the tip touches the sample, III) the cantilever starts to deflect in contact with the surface until reaching the trigger force defined in the protocol. The whole blue curve from I) to III) is called the approaching curve. By fitting the approaching curve with the appropriate theoretical model, the stiffness of the sample (given by elasticity modulus, or Young's modulus (E) can be determined. IV) After a certain time, the tip is eventually withdrawn from the sample. Various binding parameters such adhesion force or strength of the binding can be extracted from the retraction curve (red curve). The maximal adhesion is provided by the difference between the starting point and the minimum recorded force (Varga et al., 2018).

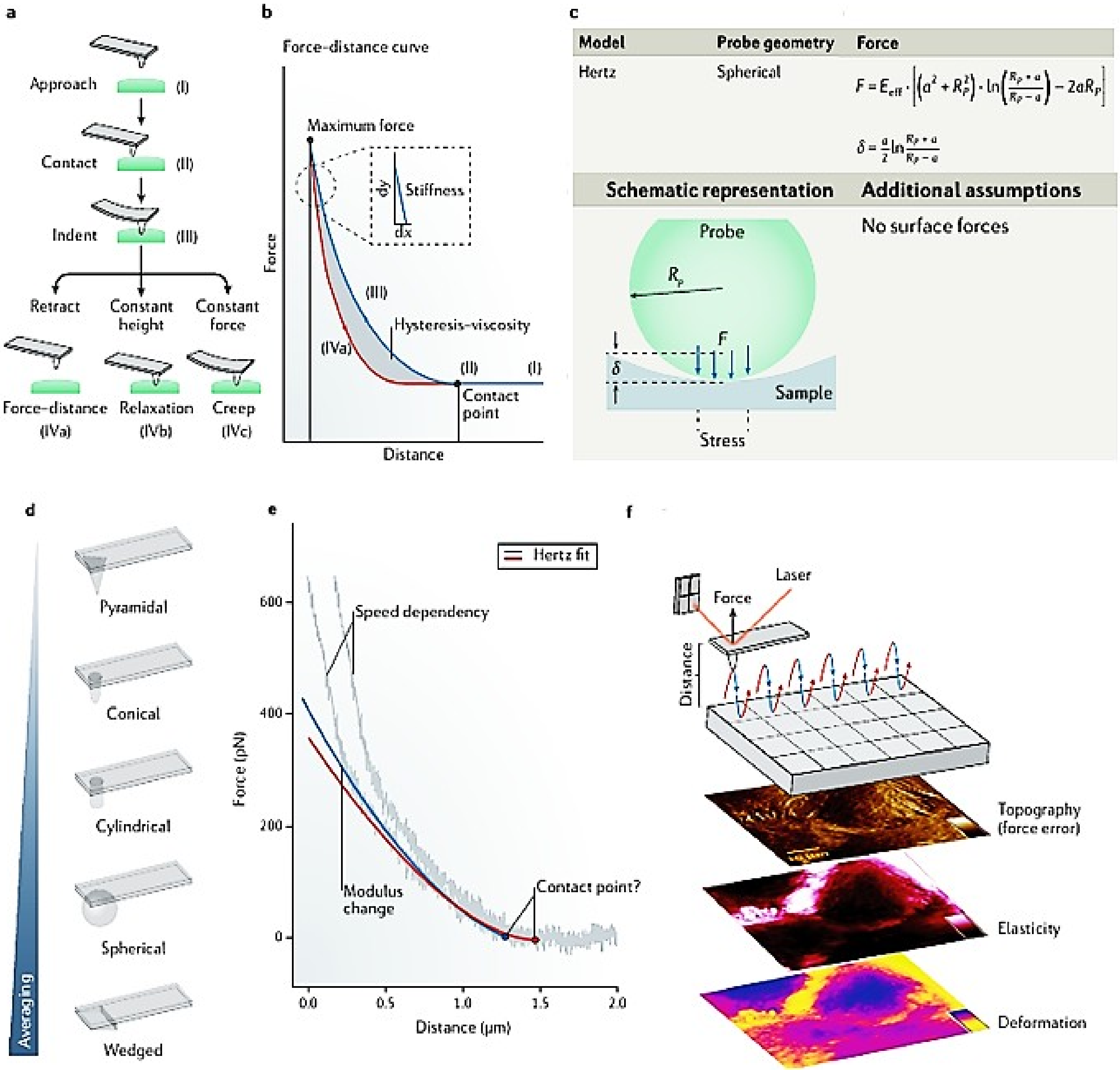

Figure 13: Imaging the mechanical properties of biological samples with AFM. In (a) mechanical properties study with tip indentation into the sample; in (b) a typically recorded Force-Distance (FD) curve with I) the tip is far from the surface, II) the tip touches the surface, III) the cantilever start to deflect until the trigger point is reached. The blue curve is the approach curve. IV) The tip is retracting until its initial position; in (c), Extraction of Young's modulus in relation of the model chosen (Hertz) and the tip geometry (spherical); in (d), various tip geometries, the larger the probe, the more averaging over the probed area; in (e), Force-curve fitting with a Hertz model to extract Young's modulus, and in (f), AFM principle with its various outputs on biological samples. Modified from (Krieg et al., 2019).

Extraction of the Young's modulus E from the "stiffness portion" of the FD curve enables to characterize the elastic properties that are crucial in a living system to respond and adapt to external stresses. This extraction depends on the theoretical model chosen for fitting the curve, together with the shape of the tip. Using cylindrical and spherical probes eases the estimation of the elastic properties for biological samples comparing with pyramidal probes. Also, the number of discrete measurements must be sufficient to obtain proper results, as the measurements are more or less averaged over the area (Krieg et al., 2019). *Figure 13 d)* is showing the impact of the average, depending on the tip shape. Among the theoretical models, the Hertz model is the most widely used for the FD curve fitting, and the relation between the loading force (F), the Young's modulus (E) and the indentation depth $\delta$is given by the following equations in the case of a spherical tip:

$$F = E_{eff}.\left[\left(a^2 + R_p^2\right).\ln\left(\frac{R_p+a}{R_p-a}\right) - 2aR_p\right] \tag{10}$$

$$\delta = \frac{a}{2}\ \ln\frac{R_p+a}{R_p-a} \tag{11}$$

with $R_p$the probe radius (spherical tip), and a the contact radius between the probe and the surface as illustrated in *Figure 13 c).* Though the model has several assumptions such as the sample being linearly elastic, no surface forces occurring and indention depth being less than 10%, it is the one the mostly used for biological samples (Gavara, 2017). Young's modulus can be thus generated in each pixel of the acquisition grid. The subsequent elasticity maps can be computed, revealing the nano-mechanical properties of the sample. Other maps can be also generated from this kind of probing, such as height (topography) or adhesion maps.

AFM has been presented here as a gold standard method to investigate mechanical properties of biological samples, as long as the acquisition protocol and fitting parameters are correctly defined. AFM applications in the SCI context have significantly increased in the past years in order to evaluate the elasticity of the injured area, on fixed or fresh tissues, and on various lesion models. A summary table with the models, the AFM parameters and the main conclusions of AFM studies performed in SCI is provided in the Results Chapter, at the AFM results section. Here, only some relevant applications are briefly discussed. First, GM and WM mechanical properties have been evaluated on fresh SC tissues from healthy mice, with an IHC labeling to link the stiffness to the underlying cellular structures (Koser et al., 2015). The results suggested that GM is stiffer than WM in all the anatomical planes, with a higher heterogeneity within GM than in WM. Moreover, the stiffness distribution was found to be correlated with the orientation of axons and other cellular components such as cell nuclei. Interestingly, in a study performed by Cooper and colleagues (Cooper et al., 2020) in sham mice models (uninjured mice), the authors did not find any difference between GM and WM stiffness. Moreover, as they compared two tissue preparations: fresh tissue (adapted from Koser and colleagues study) and snap-frozen preparation (frozen but not fixed tissue), no stiffness difference was found between the two methods. In another study carried out in cervical hemisection in rats (Domínguez-Bajo et al., 2019), the authors compared fresh and fixed tissues, and found in both cases that GM was stiffer than WM (with higher E values in fixed samples).

These examples of converse conclusions suggest the importance of experimental methods in stiffness assessments (including tissue preparation, lesion model or statistics analysis). In a work of Moeendarbary and colleagues (Moeendarbary et al., 2017) performed on fresh SC injured tissues in a crush injury model in rats, healthy GM matter is reported to be stiffer than WM, and a softening of the tissue is observed on the lesion area. In addition, this softening is positively correlated with gliosis markers such as glial intermediate filaments or extra cellular matrix (ECM) protein markers like collagen type IV. Cooper and colleagues (Cooper et al., 2020) observed the effects of contusion SCI on SC stiffness in chronically injured mice and found that scars are stiffer than healthy tissue. Another study has reported the evolution of the stiffness from different locations near to the injured area to far away locations (Baumann et al., 2020), in snap frozen tissues in a chronic HS model in rats. The conclusions suggested a decreased Young's modulus that is propagating away from the lesion core, correlated with changes in the tissue composition. *Figure 14* depicts the AFM imaging protocol along the spinal cord section, and the associated Young's moduli.

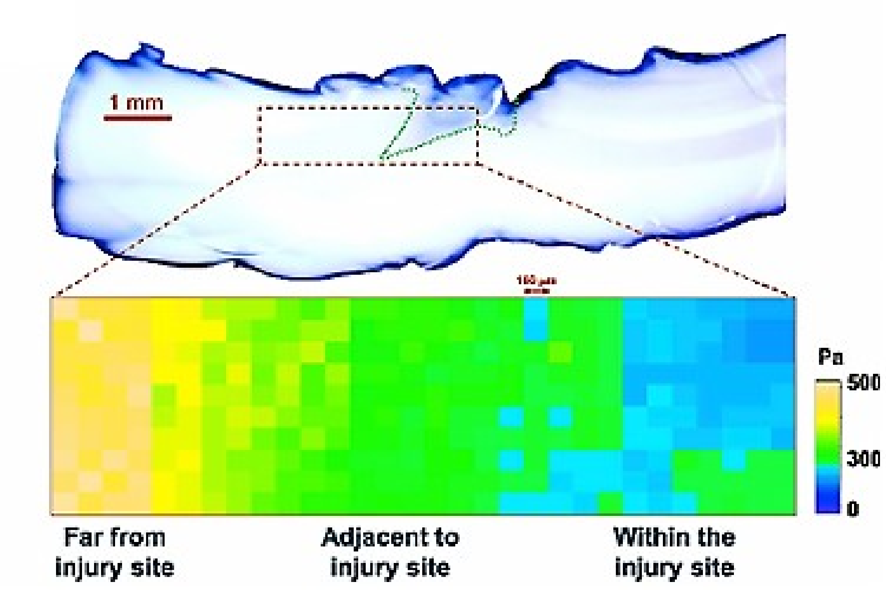

Figure 14: AFM mapping in injured spinal cord tissues. The Young's moduli were recorded and averaged in two different areas: around the injury site (within and adjacent) and far from the injury site. From (Baumann et al., 2020).

This review of some imaging techniques using labeling (IHC) or label-free (2PEF, SHG and AFM) followed by a global view of their application in SCI suggests the richness of a potential combination of acquisitions sources to target different properties of the sample. Some of these properties are related to the fibrotic part of the glial scar, and more specifically to the collagen. The next part thus concentrates on collagen description and characterization by imaging label-free techniques. The latest point in the collagen observation mainly focuses on techniques that have been described earlier (MPM-SHG and AFM).

When it comes to collagen investigation, numerous studies just denominate the protein by "collagen" without specifying which type is concerned. However, the optical properties of collagen highly depend on its type and its supramolecular organization in fibers. In addition, the role of fibrillar collagen in the formation of the astrocytic part of the glial scar is poorly investigated in comparison to the role of non-fibrillar collagen IV. The scope of the following paragraphs is a short literature review on imaging techniques enabling to visualize and characterize collagen.

I.3. Collagen: roles and optical properties

Collagens are the most abundant proteins in mammals (almost 30% of total protein mass). They belong to the family of extra cellular matrix (ECM) proteins and participate actively in ECM remodeling, a process that directly shapes tissues and maintains them healthy. Therefore, collagens have a decisive role in the structural integrity of tissues during growth, morphogenesis, and in the healing process after a wound injury or after tumors genesis (Myllyharju, 2004). Collagens have a crucial role also in cell processes including: cell adhesion, signaling and migration. There are more than 1300 mutations in collagen, characterized by 23 genes of the 42 human genes coding for collagen, with at least 28 types of collagen defined in vertebrates as type I-XXVIII. 19 proteins are formally defined as collagens, at least 4 additional collagen polypetide chains, and more than 15 proteins with collagen link domains (Myllyharju, 2004). Collagen mutations are leading to various hereditary disorders and alterations in ECM remodeling, and can induce cancer or fibrosis-related disease. The diagnosis and monitoring of these diseases has been greatly improved due to valuable imaging targeting fibrosis visualization. The next sections provide: i) a global view of ECM involvement in tissue repair and the level of collagen implication, followed by ii) a description of collagen composition and its variety of structures, iii) disorders due to abnormal collagen deposition specifically in ECM remodeling failure, and iv) some relevant examples where fibrosis-related disease have been investigated with label-free imaging techniques.

I.3.1. Global view of tissue integrity, repair and collagen involvement

The healthy shape of cells and tissues is supported by the interactions between more than 200 glycoproteins and ECM components including mainly collagens, integrin, fibronectin, and proteoglycans. *Figure 15* is showing a global view of ECM composition. Additionally to its static scaffolding role, the multiple repeating domains and motifs of ECM constituents allow cell adhesion, migration and binding to growth factors, and can affect cell differentiation and death. On the other hand, cells also actively take part in ECM remodeling (Arseni et al., 2018).

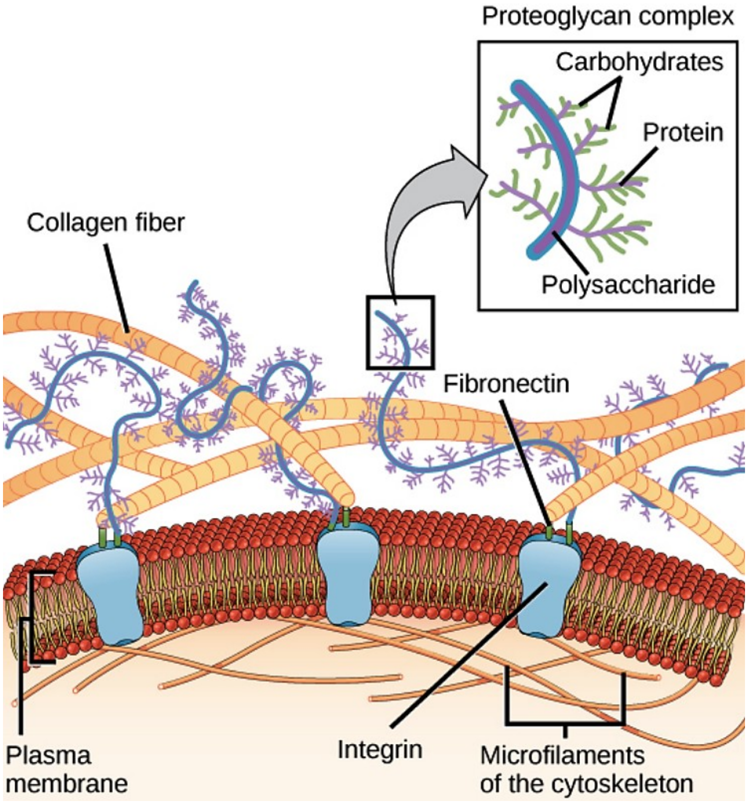

Figure 15: Extracellular matrix composition. The extracellular matrix is connected to the surrounding cells by proteins called integrins, anchored in the plasma membrane and linked to microfilaments of the cytoskeleton. Proteins in the extracellular matrix include collagen fibers, proteoglycans and also fibronectin. Fibronectin acts as a bridge between the matrix proteins and the integrins. All together, these components ensure the structural integrity of the tissue. Image credit: OpenStax Biology from: https://www.khanacademy.org/science/ap-biology/cell-structure-and-function/membrane-permeability/a/the-extracellular-matrix-and-cell-wall, accessed on August, 2022.

The ECM is present under two forms: the interstitial matrix and the basement membrane, differing in location and composition as presented in *Figure 16 a)* and having distinctive functions. The interstitial matrix is implied in cells connections within the stroma which insures the structural integrity of tissues. It is composed of hyaluronic acid, various fibrillar collagens types, elastin and fibronectin. The amount of each component varies between the types of tissue, and also at micrometric scale within the same tissue. The basement membrane is encountered at the surface of epithelial cells, muscle cells and adipocytes, and is mainly composed of collagen IV and laminins. Laminins are proteins composed of α, β and γ chains organized in cross-shapes structures that can combine into different types (as laminin-G type with a calcium-binding site highly involved in cellular receptors and extracellular ligands). The basement membrane and the cells are strongly bound to each other, and this binding is primordial for cell polarity in epithelium, and for further homeostatic maintaining processes (Winkler et al., 2020).

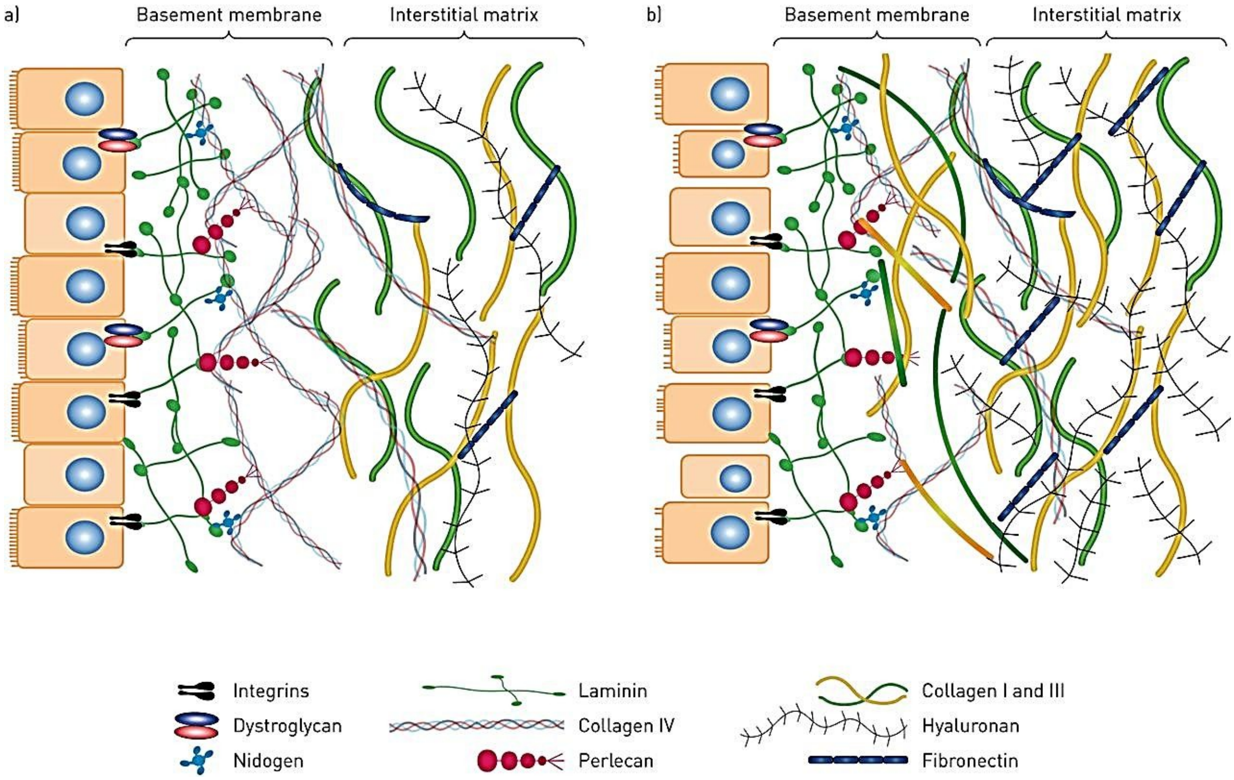

Figure 16: Illustration of interstitial and basement membrane composition in a) healthy state and b) after a fibrotic disease in lung. From (Hussell et al., 2018).

Collagen and elastin are part of the fibrous proteins, collagen being the most abundant of both, and elastin providing the elasticity in various tissues such as arteries, lung, cartilage or skin. Conversely to the strength provided by collagen, elastin (first produced as tropoelastin which forms elastic fibers via fibrillin bindings) brings a higher extensibility to the fibers due to its composition rich in hydrophobic domains. Being tensile and extensible at the same time, elastin allows the tissue to return back to its original shape after a mechanical stress. This property is called viscoelasticity (Winkler et al., 2020). Fibronectin is a dimer form of two fibronectin monomers, bounded together through disulfide bridges. It contains a large amount of binding sites for various biomolecules as integrins or collagens. The association of fibronectins and fibrils is a key factor for cells anchoring in matrix fibers. The remodeling of the interstitial matrix and the basement membrane is a defensive process that happens after a trauma, implying a large cascade of consequences in cell signalization or mechanical behaviors, and involving more than 700 proteins. It can lead to cells deregulation in producing an excessive amount of ECM and eventually cause inflammation, fibrosis and tumor genesis (Wynn, 2007). The basement membrane is less affected by the changes than the interstitial matrix, and provides a stable organization in compartments to the tissue. *Figure 16 b)* is showing an example of remodeling after a pulmonary fibrosis, depicting the massive deposition of fibrillar collagens (types I and III).

Generally speaking, ECM has a key role in mechanical maintaining, in cells or tissues anchoring, and it also furnishes growth factors and cytokines for healthy tissues development. ECM remodeling, also called fibrotic healing, basically results in non-functional tissues, composed of fibroblasts that will synthesize a new-formed fibrillar collagen deposition. This formation is commonly referred to as scar tissue or fibroblastic scar. The fibrotic healing is one of the two existing repairing process, the other being the regenerative healing, or regeneration. In regeneration, the new replaced cells are similar to the damaged one and no scar is formed. *Figure 17* is illustrating the two types of healing and the different mediators involved. When the fibrotic healing is out of control, it becomes a deleterious process, such as fibrosis and can result in a definitive scar (Wynn, 2007).

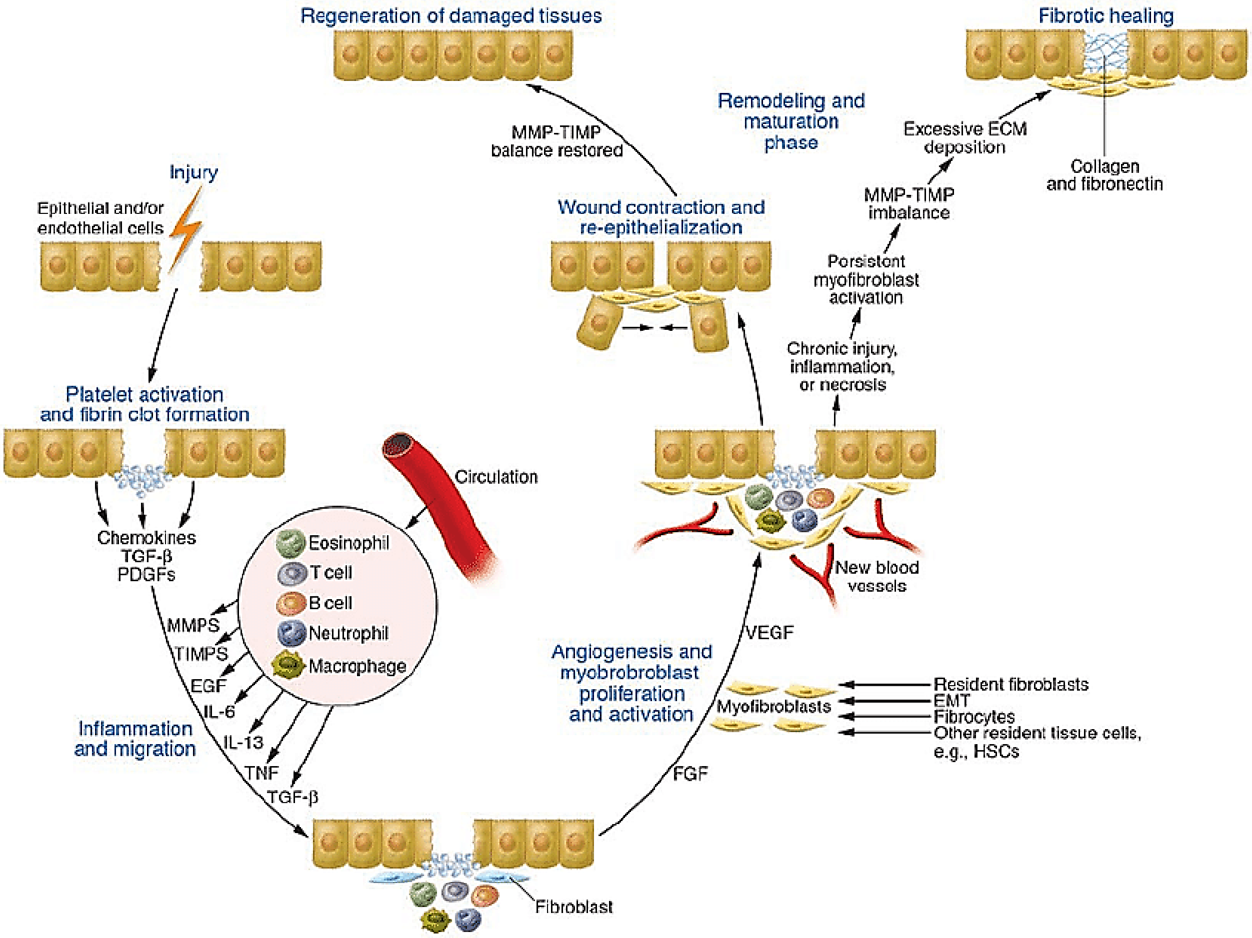

Figure 17: Wound healing process leading to two ways of healing: the regeneration of damaged tissues and the fibrotic healing implying collagen and fibronectin deposition. Legend adapted from (Wynn, 2007).

As a key component of ECM, collagen can significantly affect the fibrotic healing and can lead to fibrosis in case of failure in ECM remodeling. A better understanding of collagen composition and variety can thus help to apprehend malignant processes.

I.3.2. Biology of collagen

I.3.2.1. The triple helix structure

The basic subunits of collagen are the polypeptide α-chains, which are varying in size from 662 to 3,000 amino acids (Ricard-Blum, 2011). Collagen molecules are composed of three α-chains and contain at least one domain with repeating Gly-X-Y sequences of each constituent chain (Myllyharju, 2004). The three α-chains can be identical in some collagens and form homotrimers with three similar α1-chains (for example in collagen type II), or be different and therefore form heterotrimers such α1α2 or α1α2α3 (for example collagen type IX). Collagen type I is present under a heterotrimer form ($\alpha 1_2 \alpha 2$) but can also be found under a homotrimer form (Brown & Timpl, 1995). All together, collagen types have 38 distinct α-chains. The three chains of a molecule are coiled into a left-handed helix and aligned along the same axis to finally form a triple helix, also called procollagen. The helix is stabilized by the presence of the Gly-X-Y sequence with glycine every third position. The sequence is necessary to pack the coiled structure, most of the time by high content of proline and hydroxyproline in X and Y positions (X-Y components may be different). This sequence provides a rod shape to the helix, but it can also present imperfections which cause a considerable flexibility at molecular level. Interchain hydrogen bonds and electrostatic interactions are also important elements in the stabilization. *Figure 18* is showing a global picture of collagen, from the molecular organization in amino acid chains to the assembly in fibers.

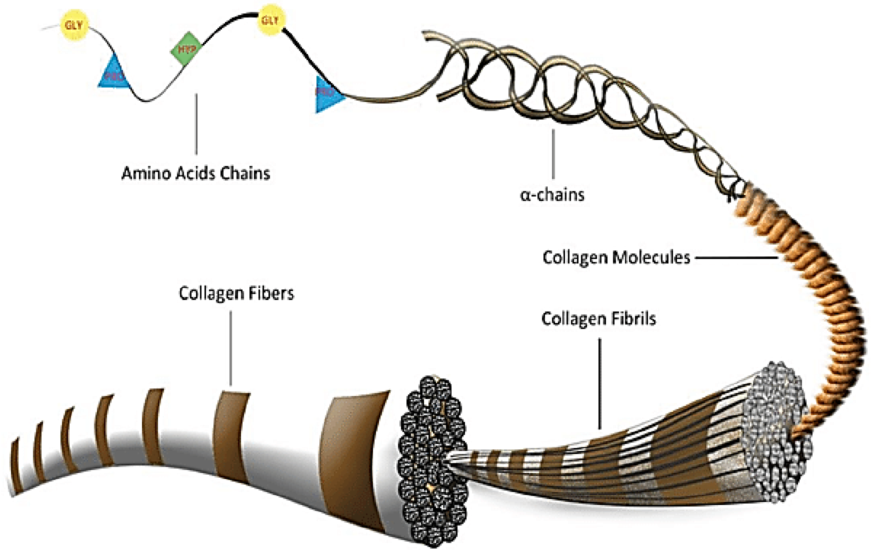

Figure 18: Four level structuration of collagen in fibers. The amino acids chains, composed of glycine, proline and hydroxyproline, are coiled together in a triple helix structure composed of three α-chains to form the collagen molecules. Eventually, collagen molecules will assemble together into fibrils and form the collagen fiber. From (Lin et al., 2019).

The variety of collagens types is essentially due to the diversity of assembly patterns that take place after various post-translational modifications. More precisely, the transcription of collagen gene in the fibroblast nucleus and the translocation of pre-procollagen within intracellular space are followed by the synthesis of the α-chains and the triple helix formation. The last stage requires several modifications including: i) hydroxylation within the endoplasmic reticulum, through collagen hydroxylases and glycotransferases (Myllyharju, 2004) especially the 4-hydroxyproline of which role is crucial in raising the thermal stability of the triple helices (Brown & Timpl, 1995), ii) procollagen chains assembly with N-glycosylated residue, iii) intramolecular and intermolecular disulfide bonds formation, and iv) the subsequent binding to heat shock protein 47 (HS47) a chaperon that also highly stabilizes the triple helix (Ricard-Blum, 2011). The newly synthesized collagen is then translocated into the extracellular medium where procollagen molecules are finally assembled together.

Figure 19 is depicting the different stages of collagen formation from the transcription within the nucleus to the extracellular space translocation.

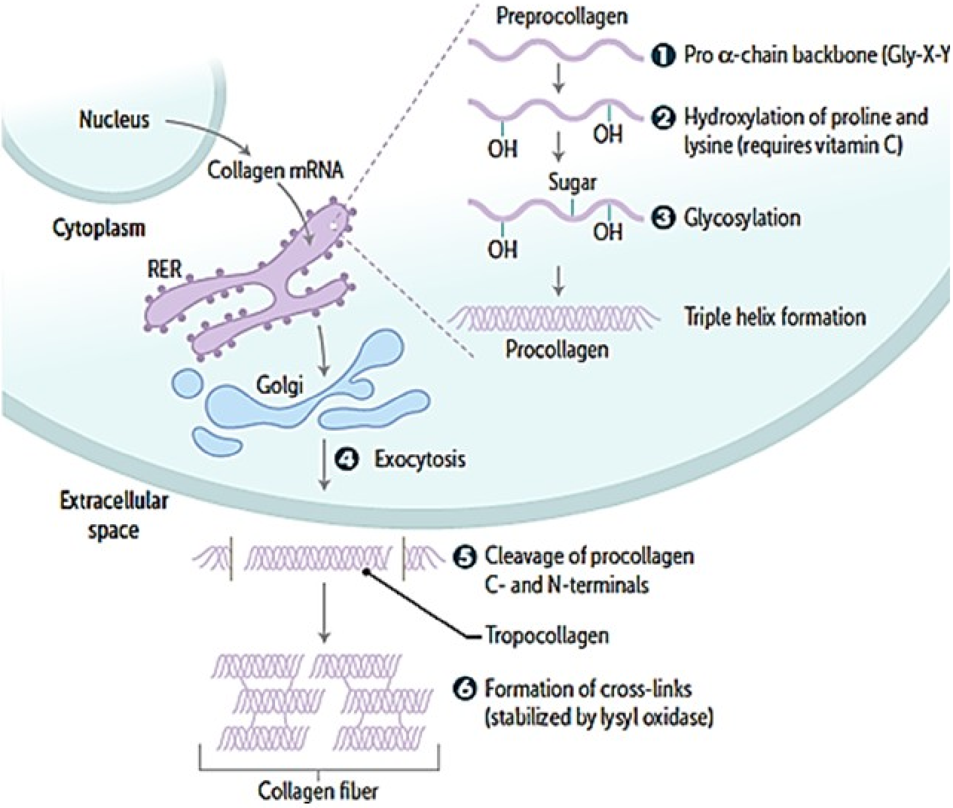

Figure 19: Collagen synthesis and assembly in a fibroblast. After collagen gene transcription in the nucleus, pre-procollagen chains are coiled together in the endoplasmic reticulum after hydroxylation and glycosylation stages. Procollagen molecules translocate then through the Golgi complex before reaching the extacellular space where there are assembled together in fibers, from "First Aid for the USMLE Step 1" usmlematerials.net. accessed on August 2022.

I.3.2.2. Collagen types classification

More than 28 types of collagens have been identified and further classified in four categories, depending on the assembly of their procollagen chains in the extracellular space: in fibrils, networks, beaded filaments and anchoring fibrils. The fibrillar collagen pattern forming the fibrillar collagen types such as collagen I, involves the cleavage of the N and C terminal sequences by specific proteinases. Procollagen molecules are then assembled into cross-striated fibrils by lysyl oxidase action, and are shaped into a cylindrical structure. Eventually, collagen fibrils associate into heterotypic fibers (fibril-bundles) i.e. composed of several collagen types associated together. For example, collagen I associates with collagen III, V and XII, mainly in skin or in cornea (for collagen I-V association), or collagen II associates with types IX and XI, in cartilage (J. W. Wu et al., 2010). The diameter of collagen fibrils can reach 500 nm or more and the banding pattern has a periodicity of around 65 nm (Ricard-Blum, 2011). One distinctive fibrils formation is collagen XXVII assembly that is non-striated, with fibril diameters of 10 nm (Plumb et al., 2007). Another pattern of interest for our study is the network-forming collagen type IV. This type is made of several formations of tetramers and NC1 dimers (assembled though the NC1-domain and probably stabilized by the action of methionine), as well as two molecular isoforms composed of $\alpha1_2$ α2 and $\alpha5_2\alpha6$ chains (Vanacore et al., 2005). Conversely to fibrillar collagens, collagen IV does not assemble into tight fibrils, certainly due to the numerous interruptions in its triple helix domain. Additional assemblies include the fibril-associated collagen with interrupted triple-helices (FACIT) as collagen type IX, hexagonal networks as collagen VIII and X types present in Descemet’s membrane and in hypertrophic cartilage, beaded filaments and anchoring fibrils as collagen VI and collagen VII respectively, with a special function of collagen VII in epidermis-dermis connection(Ricard-Blum, 2011). Depending on the location in the body, the collagen type is not necessarily displaying the same structure. For example, collagen XVI in skin is associated with fbrillin-1, while in cartilage it is included in bands of collagens II and XI. *Figure 20* is summarizing the collagen types and their associated formations, as well as the genes that encode their genesis.

The diversity of collagen forms and their classification is reflected at different scales, from the variety in the Gly-X-Y sequence to the diversity of α-chains combination and the pluralistic collagen molecular assemblies. However, this high diversity also implies the possibility of many mutations or deregulations, leading to beneficial effects on one hand (more flexibility of the molecule for example), to various pathological manifestations on the other hand such as excessive amount of collagen production. The collagen degradation is then an important process in maintaining the right balance in the ECM deposition.

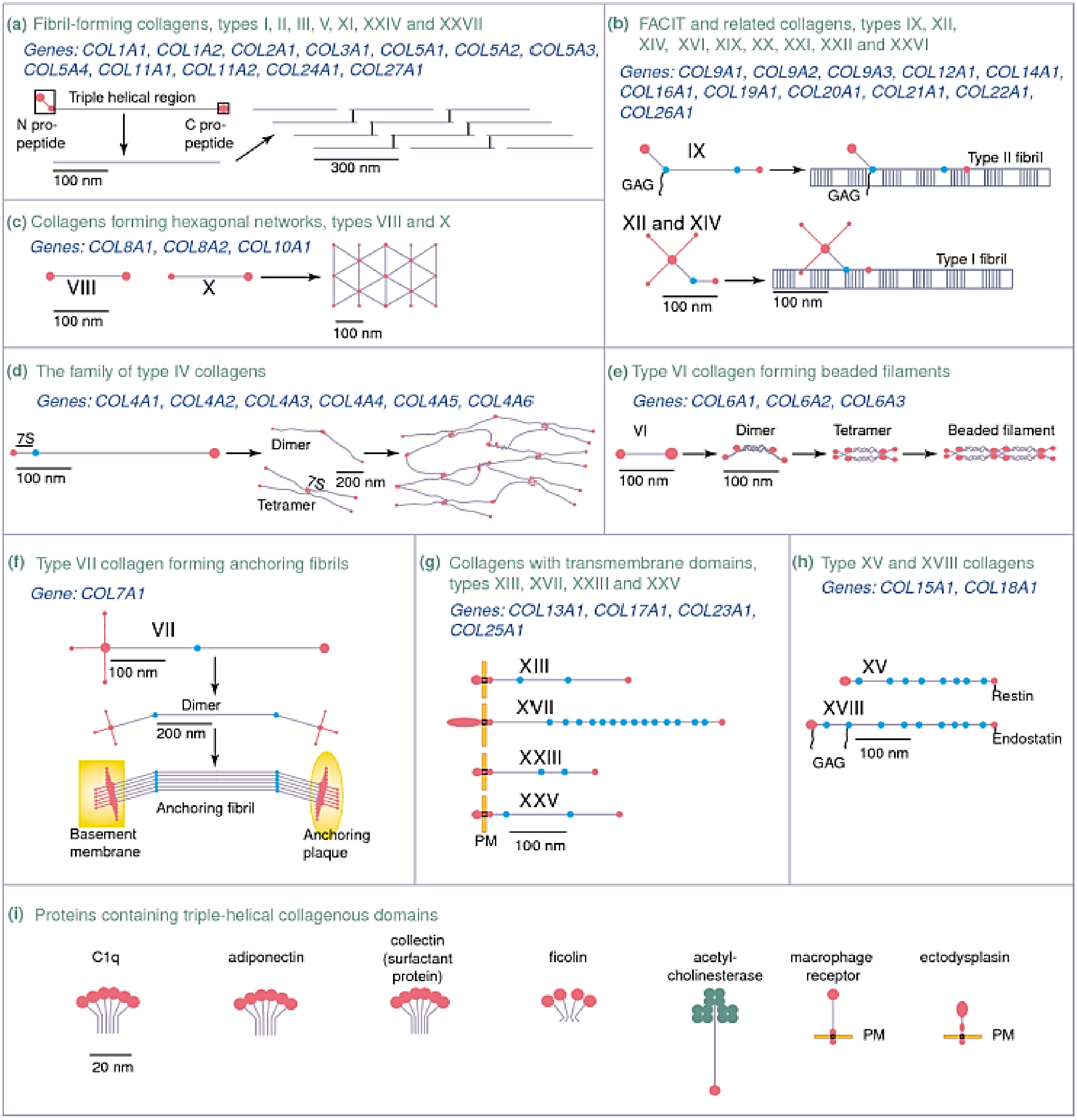

TRENDS in Genetics

Figure 20: Collagen types classification into nine subfamilies according to their supramolecular assembly. Related genes are also indicated for each subfamily. From (Myllyharju, 2004).

It involves proteases, aimed to break the ECM fibrils, and matrix metalloproteinases (MMPs) such as collagenases and stromelysins. MMPs cleave collagen fibrils into one-quarter and three-quarter fragments that are subsequently degraded and digested by cystein cathepsins (Arseni et al., 2018). Sheddases are enzymes that also degraded membrane collagens by specifically releasing their ectodomain as soluble forms (Ricard-Blum, 2011). Finally, the ECM proteinase inhibitors called tissue inhibitors of metalloproteinases (TIMPs) are regulating the global ECM degradation in function of the amount already produced.

I.3.3. Imaging collagens in disease

ECM remodeling alterations are due to protease mutations and can induce a high number of diseases as fibrosis, cancer or skin disorders. Mutations in collagen genes, encoding structural elements of the ECM, can also lead to hereditary disorders. Genetic disorders are associated with an altered collagen structure or are due to an excessive degradation of collagen while fibrosis is related to an excessive ECM production and the loss in the capability to degrade collagen structures (Arseni et al., 2018). The genetic disorders won't be detailed here, but briefly, the majority of the mutations have been identified in only six of the 42 collagen genes. They mainly concern the substitution of glycine, which further stops the folding of the helix and its stabilization (Ricard-Blum, 2011). The mutations currently identified are related to inherited disease implying skeletal malformations and skin fragilities (as osteogenesis imperfect and Ehlers-Danlos syndrome), as well as muscular disabilities (as Bethlem myopathy-1).

The study of ECM malignant processes in fibrosis or cancer requires the characterization of collagen in various conditions and models. Along genetics and chemical studies, imaging protocols have been increasingly developed to visualize and extract relevant collagen properties that discriminate diseased states. The choice of the imaging technique depends on the targeted parameters: qualitative (presence/absence of collagen, organization, collagen type identification) or quantitative metrics (fiber orientation, anisotropic/isotropic fibers ratio). Histopathology using a labeling approach such as IHC has been a common method for cancer diagnosis as it helps to identify the collagen presence. But it tends to be limited for precise quantitative assessments, specifically because it depends on the epitope accessibility to the antibody and the efficiency of the reaction between both. The advantage of using label-free imaging techniques in this context is that fibrillar collagens assembly lends optical properties that can be directly detected by non-linear optic measurements such as SHG, with small intrinsic background and without any exogenous labeling or heat damaging effects on the sample. This approach can be further combined with other label-free methods such as auto-fluorescence imaging or AFM, and even confronted to IHC to enrich the sources of acquisitions, as previously discussed in part I.2.I.

The following paragraphs present some investigations of collagen in tumor and fibrosis-related disease, pointing out the relevancy of SHG imaging in fibrillar collagen characterization. The last section covers the collagen implication in SCI, to compare the glial scar formation to the other fibrotic processes.

I.3.3.1. Collagen in tumor and fibrosis-related disease

There are four main processes that govern ECM remodeling. If only one of these steps is modified, the cascade of consequences will be complex due to the wide variety of cell populations and functions related to ECM binding and signaling (Winkler et al., 2020). Remodeling starts with the deposition of new ECM that directly changes the composition and quantity of pre-existing ECM. It is followed by biochemical and mechanical modifications of the global ECM, and by a degradation step involving proteolytic factors. The reorganization itself is then driven by force-induced processes that affect the alignment of the fibers and create passages for cells circulation. In cancer, this remodeling serves its own genesis and metastasis. Indeed, the tumor modifies the chemical and physical properties of ECM and even remodels it in organs located far away from its original occurrence, favoring metastasis. The modifications of ECM in cancer induce pro-tumorogenic activations with the release of hyaluronan, and an increased deposition of ECM components, especially fibrillar collagen. This fibrillar collagen increase leads to a fibrotic phenotype of the interstitial matrix (called desmoplasia) characteristic of some cancers as breast cancer (Winkler et al., 2020). The organization of the interstitial matrix passes from curly and parallel-orientated collagen and elastin fibers (depicting a healthy state) to linear and perpendicular orientated fibers (scarring state) (Verhaegen et al., 2012). This reorganization promotes the tumor development and more generally speaking the tumor growth by pro-tumor signaling in cancer cells, invasion through the basal membrane, migration within the stromal matrix and vascularization leading (Muschler & Streuli, 2010; Winkler et al., 2020). The other major consequence of ECM remodeling is the occurrence of fibrosis, and its associated fibroproliferative disease such as cardiovascular disease, macular degeneration, pulmonary fibroses or systemic sclerosis.

There is no current treatment targeting directly the fibrotic process in cancer. For that reason, increased interest has been devoted to disrupt the tumor or the fibrosis promoting cascade. In the review of Wynn (Wynn, 2007), the author is discussing the different factors that could be considered as fibrogenesis biomarkers. For example, the correlation between the inflammatory and the fibrotic processes has been reported, through the action of macrophages related to the ECM degradation that could lead to reversible fibrotic process in liver fibrosis. Another interesting hypothesis is coming from the upregulation of myofibroblasts by infectious agents and by the overexpression of TGF-β which is stimulating the whole ECM production. Finally, angiogenesis and fibrogenesis have been investigated together and results suggest that vascular remodeling is related to endothelial progenitor cells interactions or is occurring in successive vessels disruptions that enhance the global fibrotic phenomenon. Targeting ECM-modified enzymes or cell-ECM interactions by inhibiting, for example, the angiogenesis process could thus be a promising approach for limiting fibrogenesis. In this context, the monitoring of fibrillar collagen as a fibrogenesis biomarker has raised a high interest to complete the therapeutics strategies. Fibrillar collagen can be targeted with staining methods such as IHC or Masson's trichrome stain to visualize the fibrotic fibers in blue as illustrated in *Figure 21*.

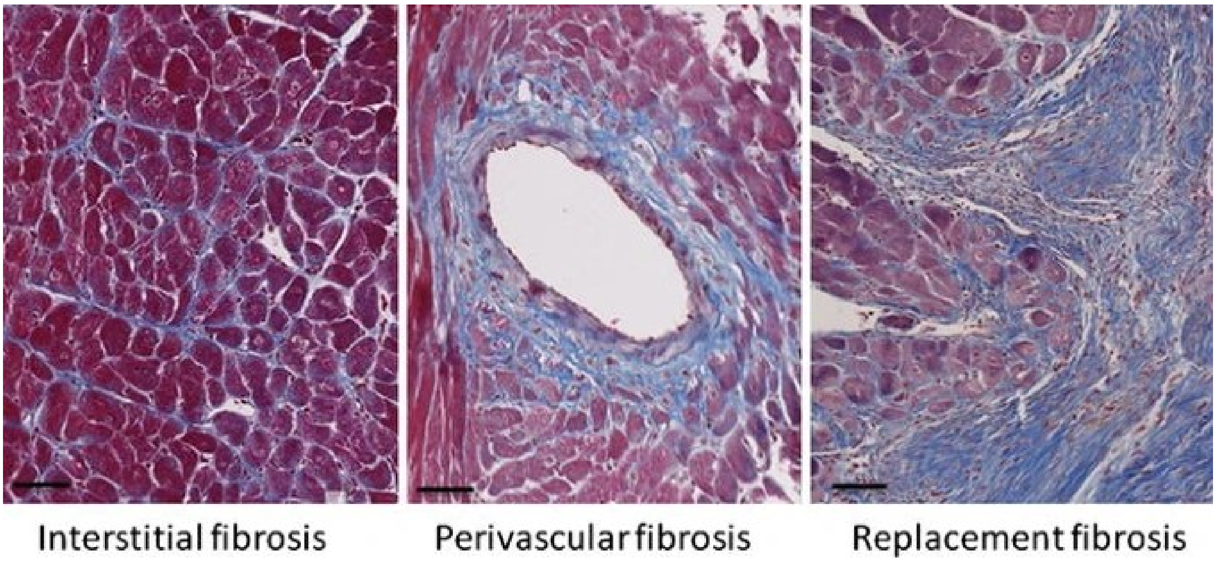

Figure 21: Cardiac tissue from mouse stained with Masson's trichome stain, evidencing the cardiomyocytes in red and fibrotic fibers (collagen) in blue. Interstitial and perivascular are presented, together with a replacement fibrosis that occurs in the myocardium after infarction. From (Piek et al., 2016).

SHG is also a valuable imaging technique to observe fibrillar collagen since it specifically targets its supramolecular organization in fibrils and does not require any labeling.

I.3.3.2. Collagen imaging with SHG

As described in part I.2.2, SHG is a non-linear process that occurs in non-centrosymmetric structures. In fibrillar collagen type I,II or III for example, the molecular organization into cross-linked fibrils confers to collagen fibers the non-centrosymmetric properties that allow SHG occurrence. The high anisotropy, due to the tight alignment of repeated structures in the triple helix, and the packing into fibrils which leaves some intra-molecular gaps enhance the SHG signal (P. Xu et al., 2004). The signal generated then propagates along the excitation beam, with almost 90% of the propagation in the same forward direction as the excitation beam in the case of collagenous tissue (Mostaço-Guidolin et al., 2017). Due to the presence of peptide bonds within procollagen α-chains, one fiber will have a permanent dipole moment (alignment of the positive charges in the same direction and of the negative charges in the opposite direction) and act as a single dipole of which radiation is in every direction, except perpendicularly to the incident beam (a single fiber is radiating both forward and backward, while fibers bundles radiation is mainly forward) (Cicchi et al., 2013). SHG depends on the polarization of the incident laser, and varying this parameter provides information about collagen orientation as shown in *Figure 22*.

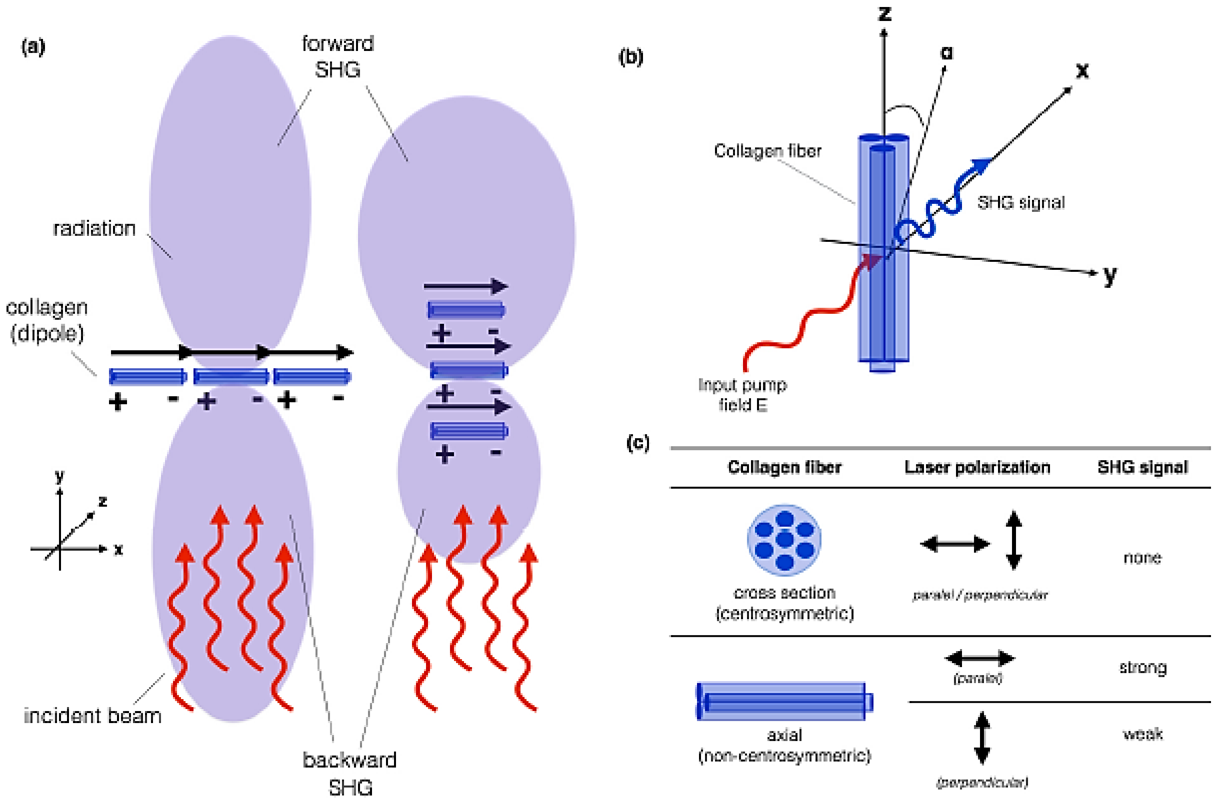

Figure 22: SHG signal generation in collagen fibers (a) representation of SHG signal radiation pattern due to the permanent dipole in collagen fibers, (b) geometrical arrangement in collagen fibers and SHG signal propagation, and (c) SHG signal intensity depending on laser polarization. Figure and legend adapted from (Mostaço-Guidolin et al., 2017).

Collagen fibers have been widely imaged with SHG in many tissue types, in both healthy and diseased states, due to the high specificity of the SHG signal. Fibrillogenesis and the size of a single fiber have been monitored and calculated using SHG, because of the high sensibility of the technique (Bancelin et al., 2012, 2014). *Figure 23* presents some examples of SHG acquisitions in healthy organs or in collagen gel pointing out the high variability of collagen fibers, their abundance and shape, depending on the tissue and species.

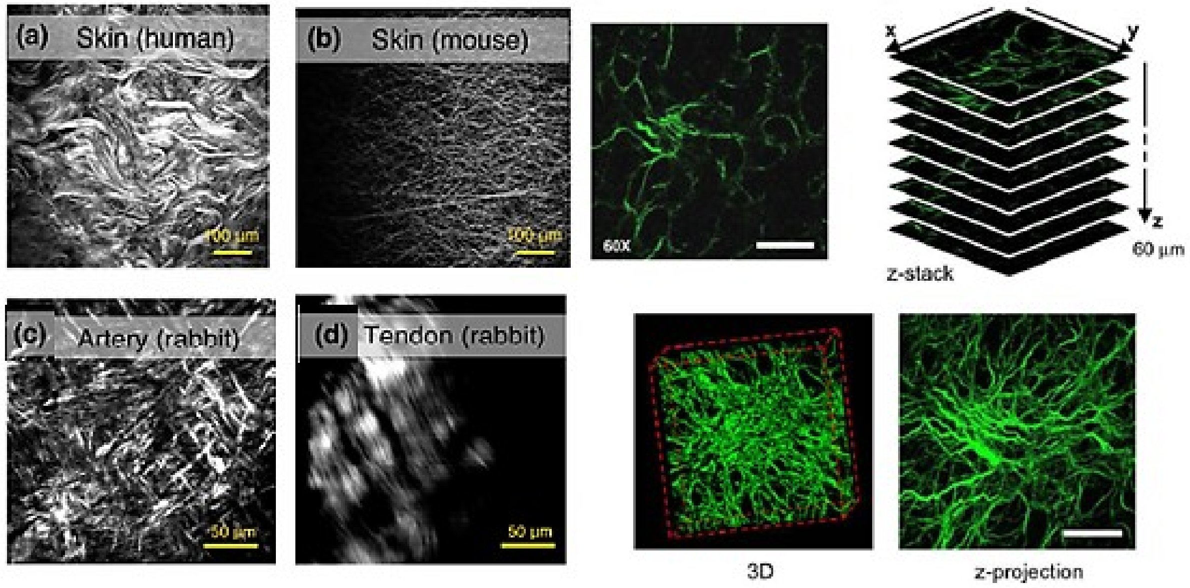

Figure 23: SHG signal imaging of collagen networks in various organs and species (left) Legend adapted from (Mostaço-Guidolin et al., 2017), and (right) SHG stack acquisitions with mid-depth visualization, z-stack, 3D reconstruction and z-projection in human fibrotic liver (collagen pseudo-colored in green). Adapted from (Gailhouste et al., 2010).

Fibrillar collagen can be characterized with SHG at different scale-levels: i) at molecular level, exploiting the polarization dependency of the molecular organization and performing P-SHG to obtain the SHG non-linear optical susceptibility d_{22} and the second order susceptibility tensor $\chi^{(2)}$, ii) at supramolecular level (collagen fiber-bundle scale), using P-SHG or circular polarization to obtain the straightness of the fibrils or the prevailing supramolecular symmetry, as well as statistical approaches as Grey Level Co-occurrence Matrix (GLCM) to analyze texture patterns, and iii) at tissue structure level, using scoring fibers areas as the Second-harmonic to Autofluorescence Ageing Index of Dermis (SAAID scoring method) (Cicchi et al., 2013), tumor-associated collagen signatures (TACS) (Provenzano et al., 2006) and fibrosis-SHG index (Gailhouste et al., 2010) or performing Fast Fourier transform (FFT) to obtain the orientation of the fibers via the anisotropy/isotropy ratio.

At molecular level, d_{22} was significant for tumorous and normal tissue with almost twice as low values for tumors, in the range of 0.08-0.11 pm/V (Hompland et al., 2008). $\chi^{(2)}$ is defined by the methylene group of proline and hydroxyproline residues in the α-chain and its calculation assumes that collagen has a cylindrical symmetry (Cicchi et al., 2013). In that context, $\chi^{(2)}$has been used to evaluate the peptidic helical pitch angle (the orientation of peptide and methylene groups relatively to the helical z-axis) and to further discriminate collagen I and collagen II types (Cicchi et al., 2013). It also allows calculating the balance between cylindrical and trigonal symmetry at a supramolecular level (symmetry of the fibrils bundle composing a fiber), related to the polarization curves obtained, for example, in breast cancer as illustrated in *Figure 24* (Mercatelli et al., 2020). Polarization curves (SHG intensity in function on the incident light angle) depicts two typical symmetry profiles: trigonal when the curve has one hump, or cylindrical when the curve has two humps (Mercatelli et al., 2020)

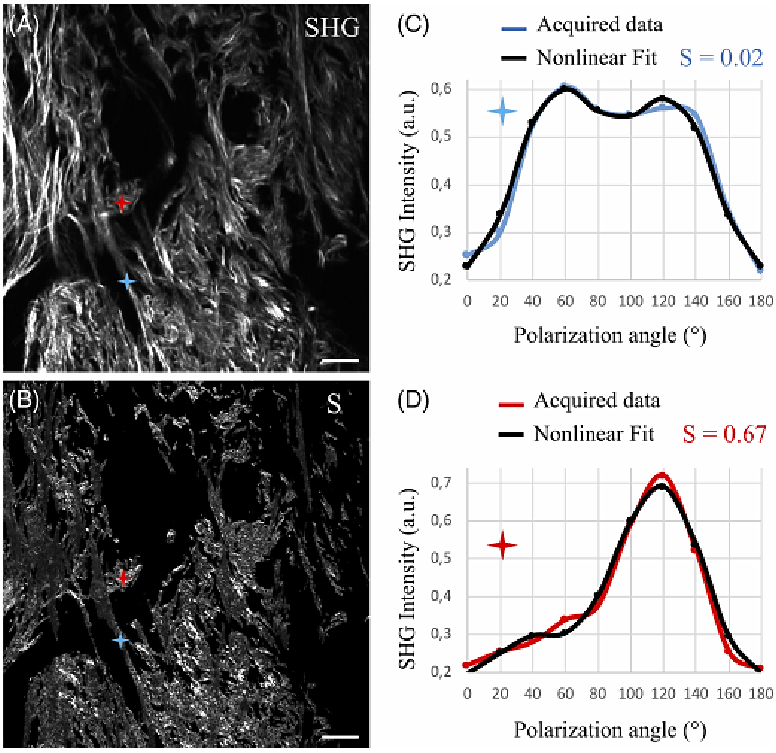

Figure 24: (A) P-SHG images are acquired in breast cancer and (B) the corresponding symmetry maps are indicating the prevailing of cylindrical or trigonal symmetry, associated with the polarization curves profiles for straight fibrils (blue cursor) in (C) and wavy-like fibrils (red cursor) in (D). Legend adapted from (Mercatelli et al., 2020).

At tissue level, quantitative imaging approaches have been developed in the recent years to measure the orientation and contents of collagen fibers observed through SHG, such as structure tensors, fibers analysis plugins like Orientation J (Fiji) or CT-Fire method (based on Curvelet Transform) dedicated to individual fiber tracking and fiber parameters extraction (Pijanka et al., 2019). CT-FIRE method is described in more details in the Material and Methods chapter. Common parameters studied for collagen fibers characterization are: the fibers orientation (alignment), their diameter, length, width, density, the number of branch points and metrics for networks characterization (reviewed by de Vriès and colleagues (de Vries et al., 2023)).

FFT or discrete FFT are relevant in calculating collagen fibers directionality by performing analysis of the spatial frequency of image pixel intensity (Sander & Barocas, 2009). The frequencies distribution allows characterizing the image texture by calculating the dominant fiber orientation, as well as the anisotropy (by ellipse fitting the power spectrum) and to extract the angular fiber distribution (from the magnitude) (Pijanka et al., 2019). In the ellipse fitting, higher values are expected along directions which are orthogonal to fibers directions, with an elliptic shape in well-aligned fibers patterns, in comparison of random orientations where the shape is circular (Cicchi et al., 2013). Collagen orientation can also be evaluated with image level analysis, and anisotropy/isotropy ratio can be calculated to estimate the regularity of collagen fiber orientation (Ling et al., 2017). Interestingly, Cicchi and Ling studies are resulting in controversial observations about the orientation signature depending of the organ studied. In Cicchi paper, healthy skin dermis is depicted as a well-aligned fibers pattern and keloid/diseased state as a randomly orientated one, while in Ling paper, the investigation of prostate cancer showed that malignant samples are highly aligned along one single direction when normal samples are more randomly organized. Provenzano and colleagues study supports the latest statement of high collagen alignment in malignant tissues, suggesting that collagen fibers relative to mammary tumors reorganize into a radial alignment (probably sustained by proteolytic cleavage) that helps local cell invasions (Provenzano et al., 2006).

Even if the high specificity of SHG signals concern all the fibrillar collagen types, it has been reported that at equal concentrations and same excitation intensity, the SHG signals of collagen types II and III are significantly weaker than SHG signal of collagen I (Lutz et al., 2012). As expected, the network of collagen type IV does not exhibit any SHG signal, due to the centrosymmetrical arrangement of the procollagen molecules within its structure. Fibrillar collagen types' visualization is provided in *Figure 25*.

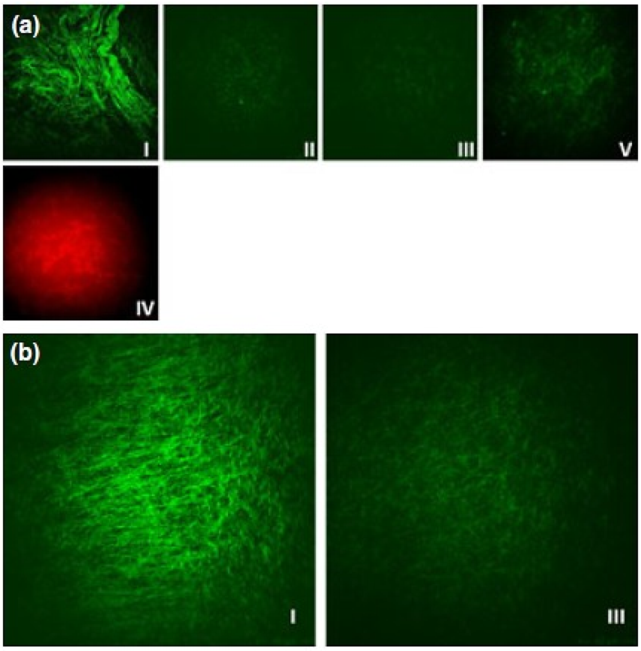

Figure 25: Collagen I, II, III and V (fibrillar) and IV (network forming) types by MPM laser scanning microscope. In green pseudo-color, the SHG signal by fibrillar collagen types. In red pseudo-color, the autofluorescence of collagen type IV (as this type does not generate any SHG signal). Legend adapted from (Lutz et al., 2012).

A clear difference is observed between the high collagen I SHG signal and other types weaker signals and SHG absence for collagen IV. The specificity of SHG signals for fibrillar collagens can be verified by comparing SHG images to the ones obtained with IHC, which is known to efficiently discriminate between many types of collagens. Immunolabeling, fluorescence microscopy and SHG has been performed together, for example in fibrotic mouse kidneys to monitor both collagen I and IV types, collagen I being specifically located in the adventitia of the artery and collagen IV specifically in basal lamina neighboring the artery. The immunolabeling results confirmed the expected locations of both collagen I and IV, and demonstrated colocalization between SHG signal and anti-collagen I immunolabeling, while SHG signal does not colocalize with anti-collagen IV immunolabeling (Strupler et al., 2007). Similar observations have been obtained for fibrillar collagen in liver fibrosis, comparing normal and cirrhotic states and targeting collagen types I, III and IV. As shown in *Figure 26*, colocalization between the two-photon excited fluorescence (TPEF) and SHG was observed for the labeled collagen I and III, but not for collagen IV (Gailhouste et al., 2010).

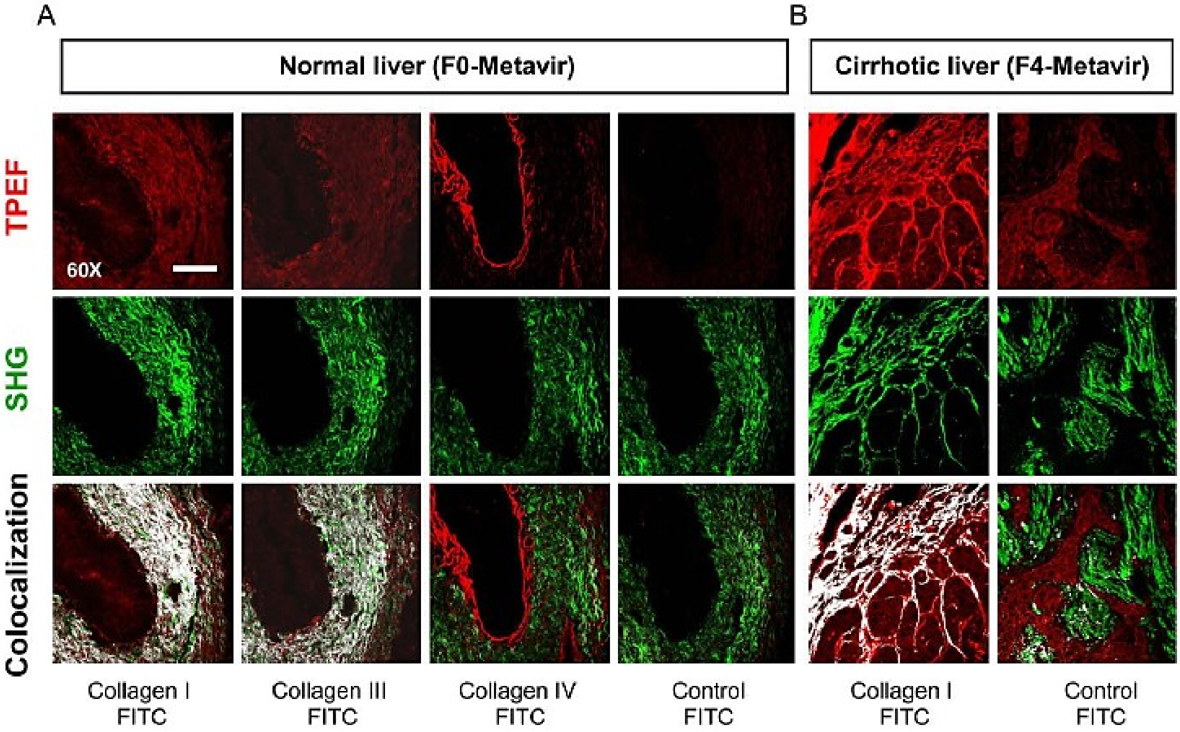

Figure 26: Immunohistochemistry assays of collagen I, III and IV combined with SHG. Immunolabelling is imaged by TPEF (red) in (A) normal liver and (B) cirrhotic liver and associated SHG images (green) are provided in the same area. Colocalization is also displayed (white). Laser excitation: 25 mW with 810 nm wavelength; 60x objective; Scale bar: 50 lm. Conversely to collagens I and III (located in adventitia) , collagen IV (located in basal lamina) is not showing colocalization with SHG. SHG signal is therefore specific method to underscore fibrillar collagen in normal and cirrhotic states. Legend adapted from (Gailhouste et al., 2010).

The difference in SHG signal for collagen I and collagen IV comes from their supramolecular structure. SHG being a coherent signal, it is related to the crystalline order in collagen fibrils, and is absent in the centrosymmetrical arrangement in collagen IV (Strupler et al., 2007). The assembly of collagen IV domains (mainly without any cleaving, in contrast to fibrillar collagen) through lysine aldehyde-derived linkers makes the matrix insoluble, and its meshing with laminin in the basement membrane creates a hermetic barrier allowing the screening of charge-dependent structures, but it is not tight enough to exclude large proteins (Klapka & Müller, 2006). Even if collagen I and IV do no present the same behavior in SHG microscopy, surface SHG can be used to study chiroptical effects in both collagen types (Pena et al., 2005). Indeed, at the surface of an isotropic layer of chiral molecules, due to the absence of inversion symmetry in these molecules, the centrosymmetry is broken. Consequently, surface SHG can occur in collagen type IV and chiroptical effects can be identified in relation of the type of chirality (Pena et al., 2005). P-SHG measurements have been performed on thin layers of collagen I and IV, resulting in a difference in chiral enhancement in SHG signal intensity between the two types (enhancement from collagen I being higher than from collagen IV), but similar values have been obtained for the molecular hyperpolarizability of both collagens (Pena et al., 2005).

I.3.3.3. Collagen in SCI

The diseases presented previously and the related implications of fibrillar collagen only concerned the fibrotic scarring in common tissues and organs. In CNS and specifically in SCI, the glial scar formation was described in part I.1.2.2.3, and it has been showed that its investigation was mainly conducted through the prism of astrocytes and microglial roles. Even if the fibrotic process is not necessarily the same within CNS and in skin for example, ECM components such as fibroblasts are still implicated when interacting with astrocytes to form the fibrotic scar (Z. Li et al., 2021). Interestingly, the collagen type involved in the SCI fibrotic scar that has been the most described so far is not fibrillar collagen, but collagen type IV. Indeed, collagen type IV has long been considered as one of the major components within the fibrotic scar tissue (Klapka & Müller, 2006) and remains the most investigated collagen in the glial scar, especially with IHC in various models (Hermanns & Reiprich, 2001; Streeter et al., 2020). The amount of studies concerning collagen IV is too wide to be completely reviewed here, but one relevant illustration coming from Streeter and colleagues study (Streeter et al., 2020) on a hemi-crush model in C57/BL6 mice is provided in *Figure 27*. Collagen IV properties have also been explored in order to understand how it interacts with the other scar components or how it influences the axonal regeneration. It has been shown that collagen properties are not endogenously inhibiting the axonal regrowth after an injury, but it is rather the influence of molecules in the environment that bind to collagen meshwork and modulate its abilities towards axonal regrowth inhibition (Tonge et al., 1997). Interestingly, some subgroups of axons have been reported to penetrate the fibrotic matrix, and to co-localize with MMPs (Kassar-Duchossoy et al., 2001), even if the majority of axons cannot regrowth and lead to a failure in functional recovery. The expression of ECM remodeling and degradation after an injury is different from normal SC state, and similarly to commons scars, collagen IV deposition enhances fibrosis which limits the axonal regeneration (Stoll & Müller, 2006). Similarly, therapeutics targeting the inhibition of collagenous scarring improve the axonal regrowth (Onose et al., 2009). Finally, mechanically collagen IV (and other ECM matrix components) has been correlated with a softening of the injured area in a crush lesion model in rats (Moeendarbary et al., 2017).

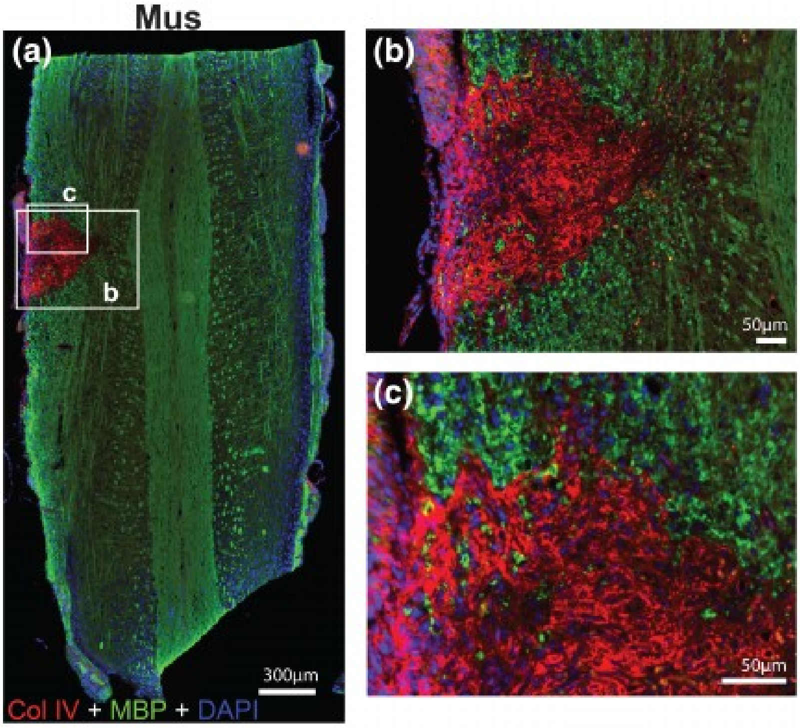

Figure 27: Glial scar components staining at 4 weeks post-injury: collagen IV (red), myelin basic protein (green) and DAPI (blue), on longitudinal cervical spinal image (a), with high magnification images of the lesion epicenter (b,c). Figure and legend adapted from (Streeter et al., 2020).

Despite of the collagen IV prevailing in fibrotic scar characterization, the interest in SHG for fibrillar collagen exploration in the SC or SCI has started to slightly increase in the past few years (Hubertus et al., 2022). Some recent studies based on MPM reported that SHG signal was mainly coming from fibrillar collagen I and nerve fibers in relation with astrocytes hypertrophia in SCI tissue in rats (X. Chen et al., 2021) and that SHG allowed the recognition of collagen type I in the fibrotic scar in a crush model in mouse through an intervertebral window (W. Wu et al., 2022). Interestingly, in two studies investigating contusion models in mice (Horiuchi et al., 2015) or rats (Liao et al., 2019), SHG signal emitted by collagen was observed in dura or pia matter respectively, but not directly in the injury site.

A previous work (Huang et al., 2011) exploring collagen in SCI with 2PEF and SHG, detected collagen in the fibrotic scar in a transection model in rats, but the authors referred to collagen type IV as scar component and not collagen type I. In the mentioned examples, collagen I was identified with SHG, but was not further investigated and properly quantified. There is yet one major study that has clearly defined and characterized collagen type I in SCI, conducted by Galli and colleagues (Galli et al., 2018). In their work, the authors explored the effect of an alginate hydrogel on the glial scar at two post injury time-points in rats (28 and 154-days post-injury). To this extend, they identified collagen type I with SHG and quantified it with SHG-scoring and fibers orientation analysis (with Directionality tool in Fiji). SHG imaging was combined with fluorescence microscopy and with CARS for myelin observation. The main results pointed to a morphological difference of the scar between untreated and treated groups: dense collagen was filling the lesion in control group while only thin layers around cysts were observed in treated rats. Differences in collagen fibers orientation were also reported: fibers with large angles to the longitudinal axis in control groups and clear alignment of the fibers with the treatment. All together, the observations evidenced a correlation between collagen fibers and axons alignments, suggesting that collagen I does not intrinsically inhibit axonal growth, despite of the global impediment in neuronal regeneration induced by the glial scar. This statement matches with Tonge and colleague’s previous conclusions (Tonge et al., 1997). Figure 27 depicts the main conclusions of Galli’s study about collagen fibers scoring and orientation assessed in a control and treated group.

A few studies also investigated fibrillar collagen type I in SCI with Western-blot and IHC/IF approaches or by quantifying genes expression. The expression and role of collagen I was studied in a contusive SCI model in rat, evidencing collagen I with Western-blot and collagen mRNA quantification at 4 weeks post injury, as well as the specific location of collagen I around blood vessels, that could imply its role in angiogenesis (Okada et al., 2007). In another study, the relation between astrocytic scar formation and collagen I was investigated, showing a high expression of collagen I during scar formation through the integrin-N-cadherin pathway (Hara et al., 2017). Blocking the interaction between reactive astrocytes and collagen I led to abortion of astrocytic scar formation and to a better axonal regeneration. The study of Anik and colleagues (Anik et al., 2011) combined the exploration of both collagen I and IV types with an IHC analysis in a spinal cord ischemia re-perfused injury model in rat. They found that both collagen types were present after 24h of perfusion, and that their expressions were related to an increase in TIMP-2 level which probably inhibits MMPs action.

Finally, we can mention the specific investigation of fibrillar collagen type III and of collagen type IV with IHC in a transection model in rats, showing that both collagens are massively deposited in regions of spinal cord injury corresponding to axonal growth failure, but they do not contribute directly to this failure (Weidner et al., 1999).

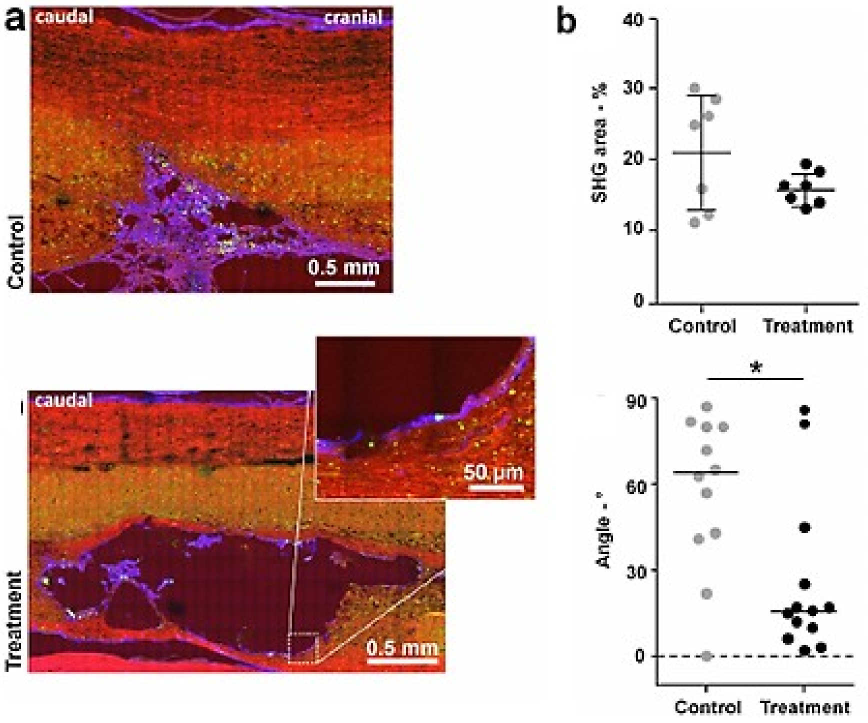

Figure 28: (a) Multimodal label-free images of longitudinal sections of non-treated (up) and treated (down) rats groups at 154 DPI with: CARS: red, TPEF: green and SHG: blue, with a magnified zone in treated group. (b) Quantification of tissue area covered by SHG-active collagen at 154DPI(up) and evaluation of collagen fibers direction at 28 and 154 DPI. Figure and legend adapted from (Galli et al., 2018).

To summarize the collagen observations in SCI, even if the main interest has been dedicated to collagen IV, there are promising results on the significant implication of fibrillar collagen in astrocytic scar formation. Above all, only few explorations of fibrillar collagen in SCI in rats or mice have been specifically conducted through SHG imaging so far.

I.3.3.4. Other techniques to investigate collagen

SHG imaging can routinely be combined with 2PEF, usually to colocalize IHC with SHG signal. 2PEF can also be used to investigate fluorescence lifetime of collagen autofluorescence in correlation with SHG acquisitions. It has been found *in vitro,* that the reduction of crosslinking in collagen assembly led to an increase in SHG signal together with the decrease of fluorescence lifetime. The explanation could be that reduced crosslinking affects the space between collagen fibrils of a single fiber, and this space changing is subsequently influencing the SHG signal (Lutz et al., 2012). Apart from SHG-fluorescence combinations, some other label-free techniques have been commonly employed to detect and characterize collagens, such as X-rays, ultrasounds, MRI, AFM or Raman spectroscopy. For example, AFM monitoring combined with SHG imaging of thin collagen films has highlighted the fact that pre-determined characteristics of the collagen films (exposing the films at various experimental conditions) can influence the collagen non-linear optical properties and thus be used as pathological models (Stylianou et al., 2011). Another SHG-AFM study was conducted by Hase and colleagues (Hase et al., 2021) applying FT to perform collagen fibers orientation analysis in a tendon injury animal model, correlating FT-SHG parameters to the Young’s modulus of the same samples. An emerging technique to assess mechanical properties of collagenous tissues is Brillouin micro-spectroscopy that has been used together with SHG and Raman micro-spectroscopy to evidence the relation between the collagen supramolecular structure and the mechanical behavior of corneal lamellae (Mercatelli et al., 2019). A study using Raman micro-spectroscopy has revealed distinct spectral signatures for type I and IV collagens and the spectral markers of the skin (in dermis, epidermis and epidermis/dermis junction) have been identified (Nguyen et al., 2012). Finally, SHG has also been employed in combination with light-sheet microscopy to target fibrillar collagen and investigate its synthesis in lung fibroblast 3D cell cultures (Hanrahan et al., 2020).

The aim of the entire collagen section was to underlie the importance of fibrillar collagens in ECM remodeling and show examples on how dysfunctional collagens can induce pathological states. Moreover, fibrillar collagens have a very specific assembly pattern that confers them nonlinear optical properties, detected by SHG imaging. SHG has been widely used in fibrillar collagens characterization with the extraction of various metrics that were identified as biomarkers in malignant processes, such as cancers.

I.4. Objectives of the work

The glial scar process, while scarcely investigated with label-free techniques (2PEF, AFM and spectroscopy), has aroused poor attention in SHG imaging. The low number of studies using SHG imaging to investigate SCI comes probably from the fact that one of the main components of interest remains collagen type IV, which does not generate any SHG signal. In comparison, fibrillar collagen (especially type I) is well-known for its implication in fibrotic scarring after wound-injuries or in tumors, and possesses a structure that is specifically related to SHG signal generation. As far as we know, there is only one major work performed by Galli and her colleagues (Galli et al., 2018) where fibrillar collagen I is clearly defined and quantified (by SHG scoring and fibers orientation) in SCI at 2 different time-points post injury. Their study also involves a multimodal approach including 2PEF, SHG and CARS. The area of fibrillar collagen investigation is thus left quasi unexplored, especially with a more precise longitudinal investigation and further characterization from a biomechanical point of view. The global aim of our work is precisely to exploit the potential of SHG in detecting and characterizing fibrillar collagen in SCI (using MPM), and to combine the information obtained from collagen nonlinear optical properties to the biomechanical response of the tissue, measured with AFM. Our multimodal label-free imaging approach is thus dedicated to monitor the structure and the elasticity of injured spinal cord tissues in mice, and to investigate the potential effect of a pharmacological treatment.

The specific objectives of our study are:

- Set up an experimental pipeline for MPM-SHG acquisitions conforming to the biological sample, the injury model and the biophysical questions addressed. This approach includes establishing the relevant acquisition parameters (stacks, mosaic and polarization-dependent imaging).
- Evaluate the structural modifications induced by a hemisection of the spinal cord in a mouse model, at different time-points after lesion, using MPM microscopy associated to SHG imaging. The MPM is dedicated to 2PEF imaging which allows the visualization of microglial cells (fluorescent in our mouse model) and the positioning on relevant locations on the spinal cord. SHG allows the specific detection of fibrillar collagen fibers and their monitoring at different states of the tissue.
- Define a valid protocol for SHG data analysis, based on the extraction and the quantification of collagen fibers in a tissue where they are normally absent, but they gradually develop post-injury. For this purpose, two methods have been successively availed: i) the software CurveAlign (Liu et al., 2020) based on CT-FIRE (originally developed and used for collagen in cancer tissues) to detect individual fiber and extract some fiber-level parameters in a first approach, and ii) a

home-developed Fingerprint algorithm to refine our image processing and address fiber metrics more relevant to SC tissue and our data.

- Monitoring the mechanical properties of the tissue, in the lesion area, around and far from the lesion (in spared parts) using AFM microscopy to compare the elasticity of injured and spared parts at different time-points after injury. There is a growing consensus on the major role played by tissue biomechanics in the rodent SC in physiological condition and following injury since in pathological condition drastic mechanical changes underlie tissues remodeling.
- Evaluate the potential effect on the structural and mechanical properties of the injured SC of a treatment with GW2580 known to induce a transient pharmacological depletion of the microglia and macrophages. For that purpose, we've included in our studies also samples from a treated group and compared it with a non-treated group at the same time post injury.

As a perspective of our work, we have initiated complementary investigations with MPM and AFM as well as acquisitions with fast Raman spectroscopy (Broadband Coherent Anti-stokes Raman spectroscopy or BCARS) to obtain the chemical fingerprints of the tissue components and of the treatment.

CHAPTER II

-

MATERIALS AND METHODS

II . Materials and Methods

II.1. Biological samples and immunolabeling

To investigate the structural and mechanical properties of the spinal cord scar tissue, we performed a T9 lateral hemisection (HS) in a transgenic mouse model. Tissues were prepared and collected for *ex vivo* analysis: immunohistochemistry, immunofluorescence and multimodal imaging acquisitions with MPM and AFM.

II.1.1. Animals and lesion model

The experiments were done according to the European legislative, administrative and statutory measures for animal experimentation (EU/Directive/2010/63 of the European Parliament and Council) and the ARRIVE guidelines. The study was approved by the local ethic committee (n◦ 36), by the Veterinary Services Department of Hérault, and the French Ministry of National Education Higher Education and Research (authorization n◦ 34118). All the efforts were made to reduce the number of animals and their suffering.

II.1.1.1. Animals - Mice

CX3CR1$^{+/eGFP}$ transgenic mice were used. They express enhanced green fluorescent protein (eGFP) downstream of the Cx3cr1 promoter (Jung et al., 2000). The eGFP protein is thus expressed in resident CNS myeloid cell line such as microglial and circulating peripheral monocytes. Mice obtained from the Jackson Laboratory (Bar Harbor, ME, USA) were maintained on a C57BL/6 background. Only heterozygote females CX3CR1$^{+/eGFP}$ were used for this work. We analyzed the same samples as those used in a previous study (Poulen, Aloy, et al., 2021). Tissues were collected at different time-points in the acute, subacute and chronic phases: 24h, 72h (hpi), 1 week, 2 weeks, 4 weeks, 6 weeks and 12-weeks post-injury (wpi).

II.1.1.2. Spinal cord injury and post-operative cares

3-months old female mice were anaesthetized with 3-4% isoflurane (Vetflurane®, Virbac, France). Anesthesia was then maintained with a 1-2 % isoflurane mixed with 1L/min oxygen flow rate during the surgery and eye gel was applied to the cornea. The lesion model consisted in a lateral spinal cord hemisection at thoracic 9 level (T9), on the left side of the spine, from the center of the spinal cord to the periphery. It was performed with a micro knife [10315-12, Fine Science Tools (FST)]. To overcome sphincter disability induced by the lesion, bladders were emptied manually twice a day until the full recovery of the sphincter control. Such injury at T9 level led to paralysis without affecting the respiratory functions; as the left side was injured, it induced left hind limb paralysis. Monitoring of the mice was conducted during 1 hour after surgery sphincter. Bodyweights were monitored before surgery, and daily until the spinal cord processing to assess the global state of the mice.

II.1.2. Treatment

Additional investigations were performed at 6wpi on a group receiving a GW2580 oral treatment (6wpiT) as previously described (Poulen, Aloy, et al., 2021): the treatment with GW2580 began right after the surgery, lasting 1 week. Mice within the control group were fed with a standard rodent chow (A04, maintenance diet, SAFE diet, AUJY, France) and mice in the treatment group were fed with the same diet but including 0.1% GW2580 (corresponding to 150mg/kg per day per animal, LC Laboratories, Woburn, USA).

II.1.3. Tissues preparation for *ex vivo* analysis

The fixation step aimed to preserve tissue integrity and was carried out through an intracardiac perfusion protocol. Animals received an intra-peritoneal injection of a lethal dose of tribromoethanol (500 mg/kg, Sigma-Aldrich Darmstadt,Germany). Once the thoracic cage was opened, the diaphragm was sectioned and the mice were perfused intracardially via a needle attached to the peristaltic pump. The needle was inserted into the left ventricle, and the right atrium was sectioned in order to stop blood flow back to the heart. Mice were first intracardially perfused with 40 mL of cold phosphate buffer saline (PBS) at pH=7.2 in order to chase out all the blood in the body and avoid clots formation, followed by fixative paraformaldehyde (PFA) 4% (Sigma Aldrich).

To remove the spinal cord from the backbone, surrounded tissues were taken away then each vertebra starting from the cervical level was cut with curved scissors and removed. The spinal cord was detached from the vertebral column and post-fixed with the same fixative during 2h. The samples were then frozen and immerged in a 30% sucrose solution. They were subsequently placed in molds and covered with Tissue-Tek O.C.T ™ compound that solidifies and protects the samples once frozen. The molds were eventually placed at -80°C before being conserved at -20°C for the cutting step. All the cryosections were collected at -20°C on Superfrost Plus© slides using a cryostat (Microm HM550, Thermofisher Scientific, Waltham, MA, USA).

Axial or longitudinal sections were collected at different thickness ranges defined for optimal imaging acquisitions depending on each experiment (thickness range from 14-µm for axial sections to 30-µm for longitudinal sections). *Figure 29* is illustrating the collection of both axial and longitudinal sections.

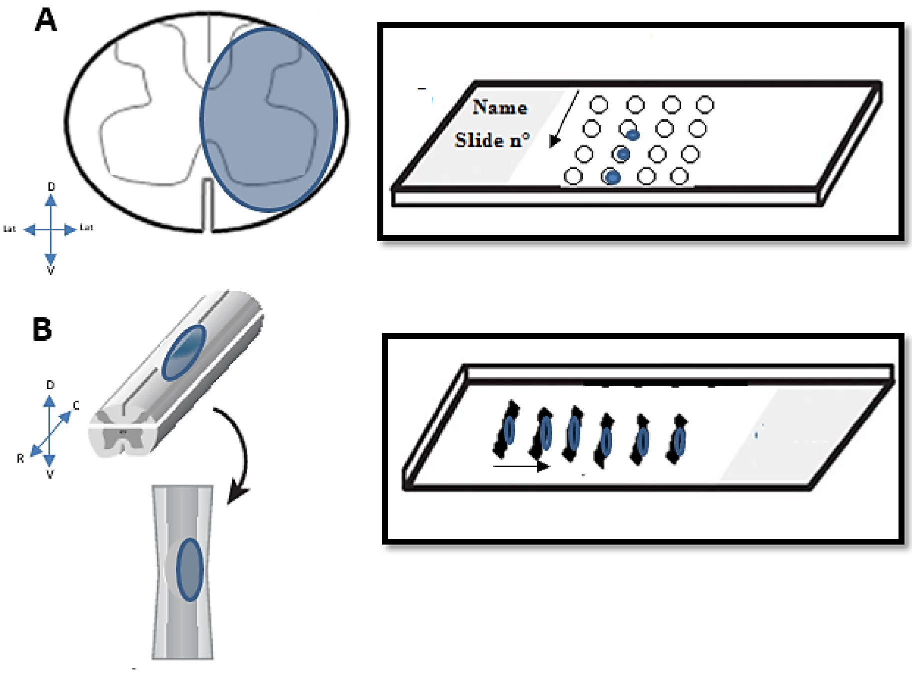

Figure 29: Schematic of the spinal cord sections collection. (A) Axial view of a spinal cord with a lesion presented on the right (blue circle). The axial sections were collected from rostral to caudal. The arrows indicate the way of collection on the slide. The lesion is visible at the thoracic level. Axial sections were collected from a 1 cm segment of the spinal cord centered on the lesion site (630µm intervals between each section along the rostro caudal axis) (B) Longitudinal view of the injured spinal cord. Longitudinal sections were collected along the dorso-ventral axis. Thus, the lesion is visible on all the sections (150µm intervals between each section along the dorso-ventral axis).

II.1.4. Labeling

Immunolabeling was performed after spinal cord injury with: i) immunofluorescence IF, to evidence the presence of collagen I and collagen IV in preliminary observations and to co-localize IF signal with SHG (for collagen I) at different time-points on longitudinal sections, using both Alexa 594 (for confocal microscope observations) and Alexa 633 (for co-localization in MPM) , and with ii) IHC (peroxidase staining) to evidence and monitor collagen I and IV on longitudinal sections at different time-points post injury, to better discriminate between both collagen types and visualize their expression over time.

In our work, we used anti-collagen I and anti-collagen IV primary antibodies to target specifically collagen I and collagen IV within the fibrotic scar:

- rabbit anti-collagen I (Abcam, Cat#ab21286; sequence available here: https://www.uniprot.org/uniprot/P02452)
- rabbit anti-collagen IV (Abcam, Cat#ab6586; sequence available here: https://www.uniprot.org/uniprot/P02462)

These antibodies have already been used successfully in mice (Y. Li et al., 2020; Streeter et al., 2020).

II.1.4.1. Immunofluorescence (IF)

Collected spinal cord sections were first washed 10 min in PBS to remove the remaining OCT and then incubated in citrate buffer (pH6, at 37°C) for 2 hours. The sections were subsequently incubated 20 min in a solution of lysine and then washed twice in 0.1 M PBS. To block the non- specific binding site, the slides were incubated for 1.5h at room temperature with a blocking buffer (0.1 M PBS containing bovine serum albumin (BSA, 1%, Sigma Aldrich, Gilligham, UK) and Triton X-100 (0.1%, Sigma Aldrich, Gilligham, UK)). Then, the sections were incubated with the primary antibody: rabbit anti-Collagen I (Abcam (ab21286), 1:100) and rabbit anti-Collagen IV (Abcam (ab6586), 1:200) for 48h at 4°C. Sections were rinsed with 0.1 M PBS 3x10 min and were placed in Alexa 594 or 633 conjugated anti-rabbit antibodies (1:1000; Vector Laboratories, Burlingame, USA and Millipore Bioscience Research Re- agents, Massachusetts, USA) diluted in blocking buffer during 2h. The slides were rinsed during 30 min in PBS, mounted by applying cover slips using fluorescent mounting medium (DAKO, Denmark), and dried overnight. Negative controls (without primary antibody incubation) were carried out for each staining, and showed no coloration. Details about the samples number are provided in the corresponding imaging sections.

II.1.4.2. Peroxidase staining

In that case, secondary antibodies are conjugated with the peroxidase enzyme and when combined with diaminobenzine (DAB), the reaction induces a brown precipitate.

For peroxidase staining, we performed the same first steps as for IHC (PBS washing, incubation in citrate buffer and subsequently in a lysine solution) until the second PBS washing step. After the rinsing, the sections were placed for 10 min in hydrogen peroxide ($H2O2$, 1% diluted in 0.1 M PBS, Sigma Aldrich, Gilligham, UK) followed by 1.5h incubation in the blocking buffer, and by the primary antibodies incubation for 48h at 4°C. Then, the sections were rinsed with 0.1 M PBS 3x10 min and incubated in the peroxidase-conjugated secondary antibody (Jackson Immunoresearch, Stratech Scientific Ltd., Soham, UK) dilluted 1:500 for 2h, at room temperature. A subsequent rinse with 0.1 M Trizma base saline (TRIS) during 3 ×10 min was performed, and the Vector DAB (3,30-Diaminobenzidine) kit (DAB Substrate Kit; Vector Labs, Burlingame, CA, USA; H-2200) was used to visualize the product of the peroxidase reaction. The reaction was stopped with a rinse in 0.1 M TRIS for 3 × 10 min. A dehydration was then performed on the sections, using increasing concentrations of ethanol (70, 80, 90% and absolute) and finally cleared with by xylene for 15 min each. Finally, slides were mounted by applying cover slips using Eukitt (Sigma Aldrich, Gilligham, UK), removing air bubbles, and dried overnight. Negative controls showed no coloration. Images were acquired and analyzed using NDP view software (NanoZoomer Digital Pathology System, Hamamatsu, Hamamatsu city, Japan). Peroxidase staining observations were carried out on 22 and 30- µm thick longitudinal sections at 24-hpi, 72-hpi, 1wpi, 2wpi, 4wpi and 6wpi (with and without treatment). A maximum of 3 mice were used (2 slides with 3-sections/mouse).

A scheme illustrating both labeling methods is provided in the appendix section. *Figure 30* is summarizing the methodology to obtain the biological samples and Table 2 is presenting details about the samples (section type, time-points) involved in each imaging modality.

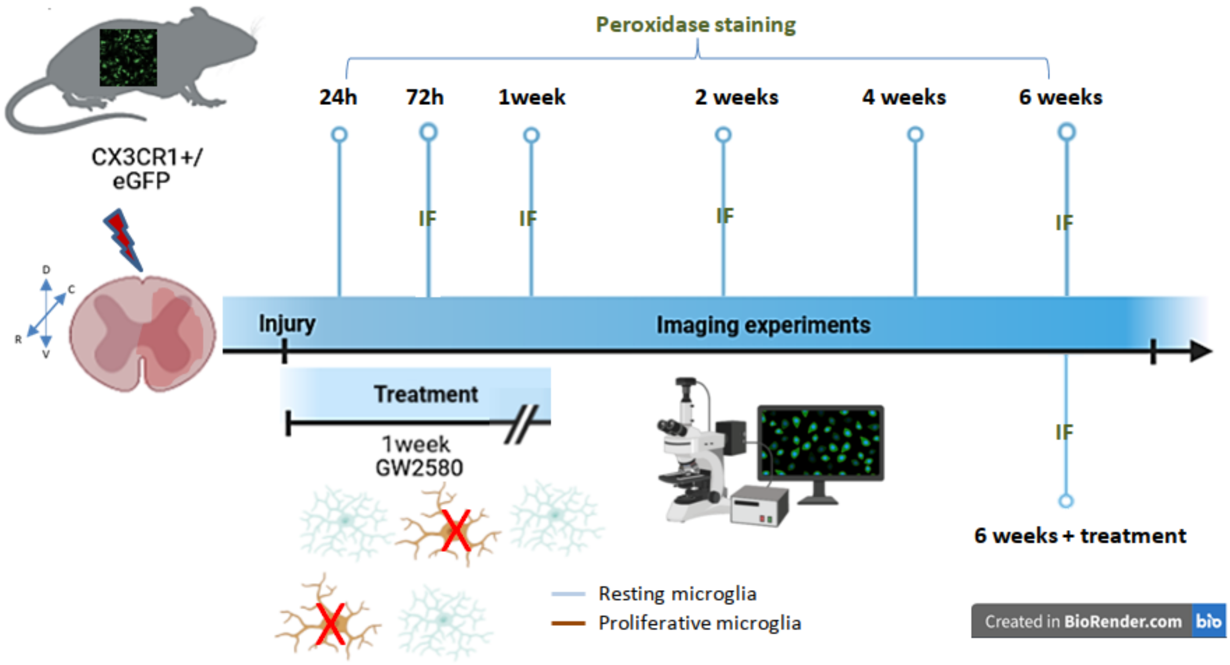

Figure 30: SCI mouse model, treatment and time-points for the imaging acquisitions. Lateral hemisection was conducted in CX3CR1$^{+/eGFP}$ mice, resulting in paralysis of the ipsilateral hindpaw. Spinal cords were collected at different time-points and labeled for imaging experiments (the labeling is indicated in green). A scheme of the treatment effect is also provided: GW2580 inhibits the proliferation of microglia. It was administrated immediately after the injury, during 1 week. Spinal cords were collected 6wpi for treatment assessments.

Table 2: Animals and samples per time-point and condition

Experiment	**Type of section**	**Time-point (total number of mice/time point)**	**Number of slides/mouse - sections /slide**
Peroxidase staining (collagen I and IV) - qualitative analysis	Longitudinal	24-hpi **(2);** 72-hpi **(2)** ; 1wpi **(2)**; 2wpi **(2)**; 4wpi **(2)**, 6wpi **(2)**; 12wpi **(2)**; 6wpi NT **(4);** 6wpi + TT **(3)*** ***Number of mice/collagen type**	2 slides – 3-5 sections
Immunofluorescence (Alexa594) - preliminary observations	Axial Longitudinal	1wpi **(2)** 1wpi **(1)**; 6wpi **(2)**	4 slides – 1-2 sections 3 slides – 2 sections
Co-localization Immunofluorescence (Alexa633) with SHG signal	Axial Longitudinal	1wpi **(2)** 72-hpi **(1)**; 1wpi;**(1)** 6wpi **(1)**	3 slides – 2 sections 3 slides – 2 sections
MPM acquisitions-preliminary observations	Axial Longitudinal	1wpi **(1)** 1wpi **(2)**	6 slides – 4-5 sections 1 slide – 2 sections
MPM acquisitions – quantitative analyses	Longitudinal	72-hpi **(3)** ; 1wpi **(3)**; 2wpi **(3)**; 6wpi NT **(3)**; 6wpi + TT **(3)**	3 slides (no SHG signal) ; 2 slides – 1-2 sections; 2 slides – 1-2 sections ; 3 slides – 2-3 sections; 2 slides -1 section
AFM acquisitions-preliminary observations	Axial Longitudinal	1wpi **(3)** 1wpi **(2)**	2-4 slides – 3 sections 1 slide – 2 sections
AFM acquisitions – quantitative analyses	Longitudinal	72-hpi **(3)** ; 1wpi **(3)**; 2wpi **(3)**; 6wpi NT **(3)**; 6wpi + TT **(3)**	3 slides – 2-3 sections; 2 slides – 1-2 sections; 2 slides – 1-2 sections ; 3 slides – 2-3 sections; 2 slides -1-2 sections

II.2. Imaging protocols

II.2.1. Confocal fluorescence microscopy

Morphometric fluorescent photographs were obtained with Alexa 594 for qualitative observations, using laser scanning inverted (Leica SP5, Mannheim, Germany) and (Zeiss 5 Live Duo, Oberkochen, Germany) confocal microscopy, with TexRed contrast to reveal the expression of collagen filaments (type I and IV) and discriminate it from eGFP contrast which evidences microglia in CX3CR1 transgenic mice. 448 × 335 μm^2 images were taken adjacent to the lesion center and reconstruction of the sections was performed using the Carl Zeiss LSM-710-NLO software.

The acquisitions were conducted on 14-µm thick axial sections at 1wpi (2 mice) and on 22 and 30-µm thick longitudinal sections at 1wpi and 6wpi (a maximum of 2 mice per time-point, with 3 slides per mouse containing 2 sections).

II.2.2. Multiphoton (MPM) setup and acquisitions

II.2.2.1. Setup

The combined 2PEF/SHG imaging was carried with a home built multiphoton microscope, based on an upright scanning microscope (SliceScope, Scientifica Ltd, UK) equipped with a galvanometer scan head (MP-2000, Scientifica) and using a Nikon 16x long working distance water immersion objective (CFI75 LWD-16x-W, NA=0.8, Nikon, Japan). The schematic setup of the MPM is presented in *Figure 31*. The samples were excited at 780 nm by a femtosecond Ti:Sapphire laser (Tsunami, Spectra - Physics, USA) in pulsed mode (operating in the 760-900 nm wavelength range) at 80 MHz frequency. The polarization of the beam was controlled by a combination of achromatic plates. The 2PEF was epi-collected through the objective, filtered by a dichroic mirror and specific band-pass filters (details below) and then detected by a photomultiplier PM. The SHG signal was collected in transmission through a 1.4-NA water-immersion condenser (U-AAC, Olympus, Japan), also filtered and detected by a PM.

II.2.2.1.1. Signal collection

Our experimental setup allowed the simultaneous collection of: i) the low auto-fluorescence of the sample to image the whole tissue (low emission on a large wavelength range), ii) the endogenous microglial fluorescence due to eGFP (emission peak: 510 nm), iii) the IF of specific structures labeled with Alexa633 (emission peak: 647 nm), and iv) the SHG signal (emission: 780/2= 390 nm) generated in non-centrosymmetric structures (as collagen fibers). To allow such a collection, 2PEF signal was filtered by a 735 nm long-pass dichroic (FF735-Di02, Semrock, USA), a 750nm short-pass filter (FESH0750, ThorLabs Inc, USA), a 450nm long-pass filter (62-942, Edmund Optics Ltd, UK).

SHG signal was filtered by a 482 nm long-pass dichroic mirror (86-331, Edmund Optics, Ltd, UK), a 550nm short pass filter (84-708, Edmund Optics, Ltd, UK) and a 447 nm high-performance band-pass filter (NT 48-074, Edmund Optics, Ltd, UK).

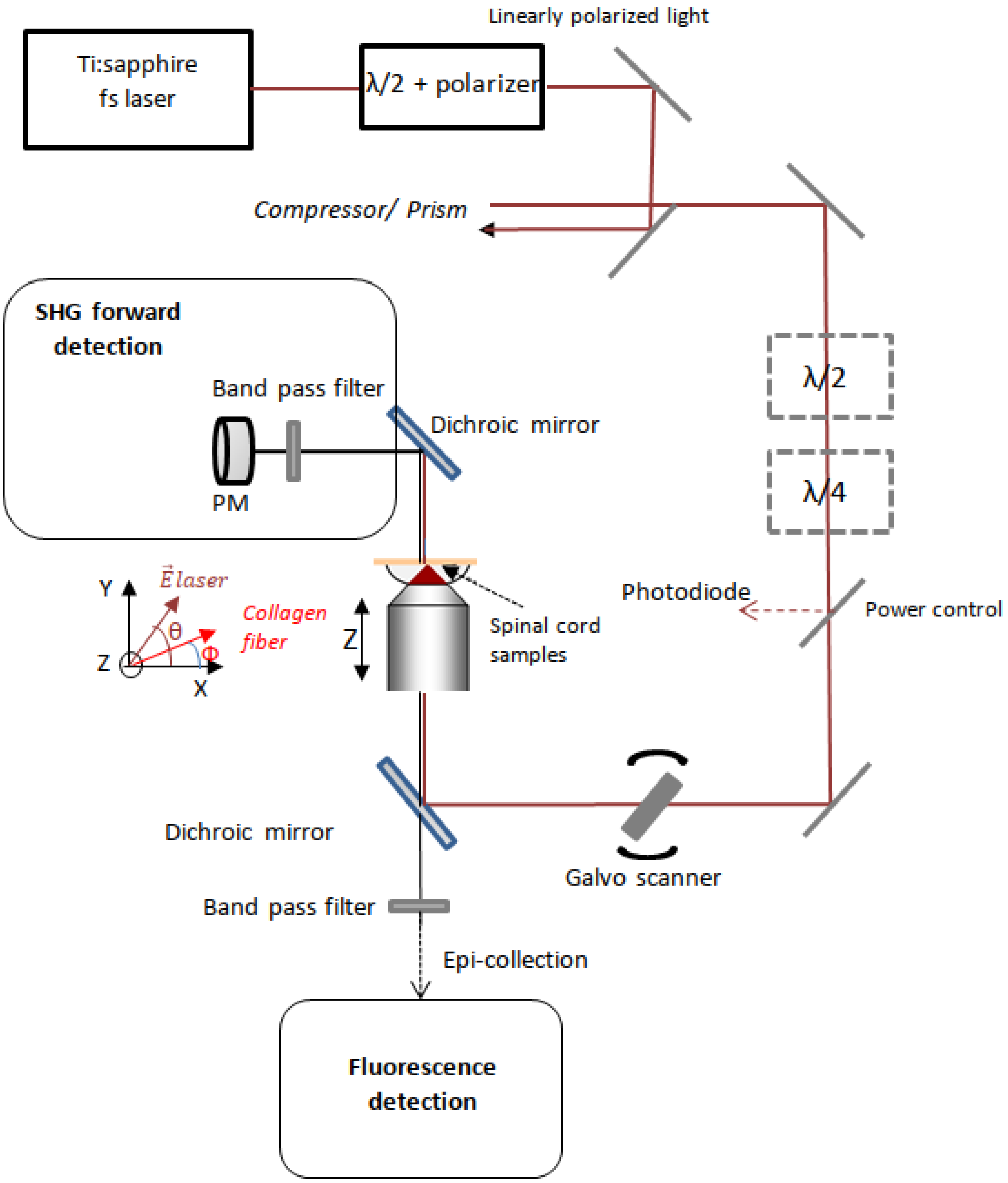

Figure 31: Multiphoton microscope setup. The sample was excited with a laser beam (brown line) in pulse mode (fs pulse duration) and the signal emitted was detected i) in epi-collection for 2PEF and ii) in transmission (forward detection) for SHG. The power applied on the sample was monitored with a photodiode for eventual laser drift corrections. For collagen supramolecular assessments, the linearly polarized light was controlled with λ/2 and λ/4 plates. Acquisitions were also performed with circular polarized light using a λ/4 plate.

In our protocol, Alexa 594 and Alexa 633 were the chosen fluorochromes emitting fluorescent signal when excited with the appropriate excitation wavelength. Alexa 633 was chosen specifically for co-localization within the MPM setup as it was easier to excite in 2PEF than Alexa 594 and its emission wavelength did not interfere with the SHG signal. The spectral excitation and emission profiles of Alexa 594 and Alexa 633 are shown in *Figure 32*.

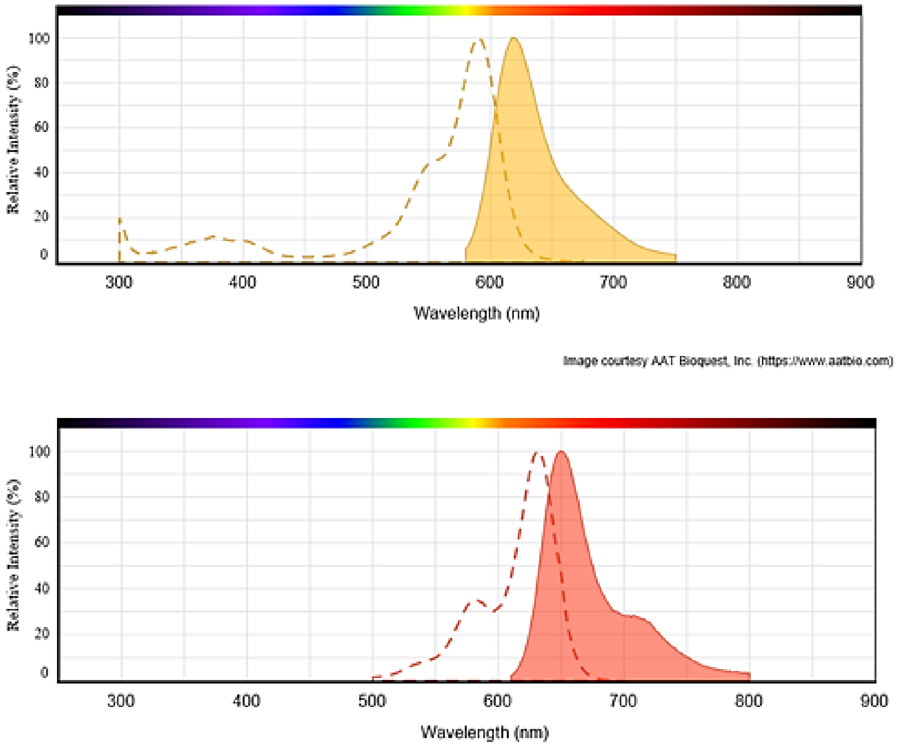

Image courtesy AAT Bioquest, Inc. (https://www.aatbio.com)

Image courtesy AAT Bioquest, Inc. (https://www.aatbio.com)

Figure 32: Excitation and emission spectra of Alexa 594 (up) and Alexa 633 (down). Alexa 594 exhibits red fluorescence with maximum excitation at 590 and emission at 618 nm, while Alexa 633 exhibits far red fluorescence with maximum excitation at 632 and emission at 647 nm. From: https://aatbioquest.blogspot.com/2017/02/the-spectra-of-alexa-fluor-dyes.html Accessed on June 25 2022.

After passing through the filters, the signals reached the detectors (photomultipliers PM). Our setup included 2 PMs (one for each signal): R928P (Hamamatsu, Japan) for 2PEF and a high sensitivity GaAsP photomultiplier (H7422P, Hamamatsu, Japan) for SHG. These PMs can be used for photons counting mode but here we used them in analog mode (C. Xu et al., 2013). The PMs' voltages were defined at the start of the acquisition and were kept constant all along the session.

II.2.2.1.2. Beam power and polarization control

As discussed in the introduction chapter (I.2.2.2, pages 45-47), due to the coherence of the SHG signal, its intensity depends on several parameters. These parameters are mainly the intensity (or the power) and the polarization of the excitation beam, as well as the relative orientation and position of all the scatterers contained in the probed volume and contributing to the signal of a single pixel (Pena, 2006). In our case, the dipoles are arranged starting from the triple helix of the collagen molecule, to fibrils and finally in fibrils bundles to form collagen fibers. Furthermore, the assessment of collagen fibrils bundles (related to the polarization curves) implies a fine control of the incident beam direction.

In our setup, the power injected in the microscope was kept constant by an achromatic λ/2 plate followed by polarizer (Glan prism). The half-wave (λ/2) plate rotated the incident linearly polarized light before it reached the polarizer, and thus modulated the beam fraction transmitted. Besides, the power was controlled in real-time to correct potential power drifts that could happen during long imaging sessions (lasting hours). To limit the photobleaching events on the sample, a shutter was added right after the laser and opened only for the image acquisition (shutters were also placed before the PMs).

The laser beam’s polarization was controlled using a combination of achromatic half-wave (λ/2) and quarter-wave (λ/4) plates mounted on rotary stages. The rotary stages allowed a fine control of the incident beam linearly polarized direction (with a 20° step) and P-SHG images were acquired for polarization curves plotting. A λ/4 wave plate was also used to change the linear polarization of the incident light into circular polarization, for mosaic acquisitions. In that case, we could detect all the collagen fibers directions no matter their orientation (Pena, 2006).

II.2.2.1.3. Other elements

The other elements in the MPM setup included the compressor (which compensated for group delay dispersion and insured that short pulses are reaching the sample), and also two galvanometric mirrors (Galvo scanner) allowing to scan the sample with the laser beam in the x,y plane (perpendicular to the beam propagation direction which is along axis z). Eventually, the beam passed through a dichroic mirror and was focused on the sample trough the objective. The software related to the MPM setup (Labview program) controlled the opening and closing of the shutters, the definition of the acquisitions parameters and the launching images’ acquisitions (software interface is provided in the appendix section).

II.2.2.2. Samples

Preliminary MPM studies were conducted on 14-µm thick axial (1 mouse) and 22-µm thick longitudinal (2 mice) sections at 1wpi. IF/SHG co-localization was performed first on axial sections at 1wpi (2 mice), and on longitudinal sections at 72-hpi, 1wpi and 6wpi for qualitative observations with one mouse per time-point (3 slides per mouse containing 2 sections). Large mosaic reconstructions were performed on longitudinal sections at 72-hpi, 1wpi and 6wpi (with and without treatment), with 3 mice per time-point (3 sections/mouse).

SHG quantitative assessments were carried out on 22-µm and 30-µm thick longitudinal sections at 72-hpi, 1wpi, 2wpi and 6wpi (with and without treatment). 3 mice were used per time-point with 3 slides maximum per mouse containing maximum 3 sections. The time-points batches were processed simultaneously, as well as the 6-weeks batches with and without treatment, to steer clear of experimentation bias.

The slides were maintained in Petri dishes before and after MPM imaging in a 0.1M pre-sonicated PBS solution. The sections were checked under a bright field microscope to locate the injured area and the spared grey and white matters.

II.2.2.3. Imaging parameters

II.2.2.3.1. Resolution and Z-stack

Tissues imaging requires a large field of view, a good resolution, together with a long distance work (Oheim et al., 2001). Therefore, we used a CFI75 LWD-16x-W water immersion objective with a 0.8 NA, a long working distance of 3.0 mm and a field of view of 2mm, conferring a good image quality in combination with confocal microscopy. The resolution of the microscope can be theoretically expressed by the following equations (Rao, 2012):

$$r_{xy} = \frac{0.7\lambda_{em}}{NA} \tag{12}$$

$$r_z = \frac{2{,}3\ \lambda_{em} n}{NA^2} \tag{13}$$

With r_{xy} lateral resolution and r_z axial resolution, λ_{em} the emission wavelength, n the refractive index of the medium, and NA the numerical aperture. Typical values obtained for our setup, with NA=0.8 and λ_{em}= 400 nm, were a resolution in x, y of 0.35 µm, whereas the resolution in z is 2µm.

Z-stack images were recorded in a window of 432x432 µm^2, at 1024x1024 pixels resolution, with a 2 µm Z step (enough according to the z resolution calculated above). A motor moved the objective head with a 50-100 nm precision.

The images were acquired at the injury site (ipsilateral side, on the border, where high SHG was detected) with an averaging of 6 images per plain to improve the signal-to-noise ratio (SNR) and to gain time.

P-SHG polarization stacks were obtained with an incident polarization angle Θ ranging from 0° to 180° with 20° step, as illustrated in *Figure 33*. The data were subsequently processed for supramolecular (polarization curves) and tissue level (CurveAlign and the Fingerprint algorithm) characterization.

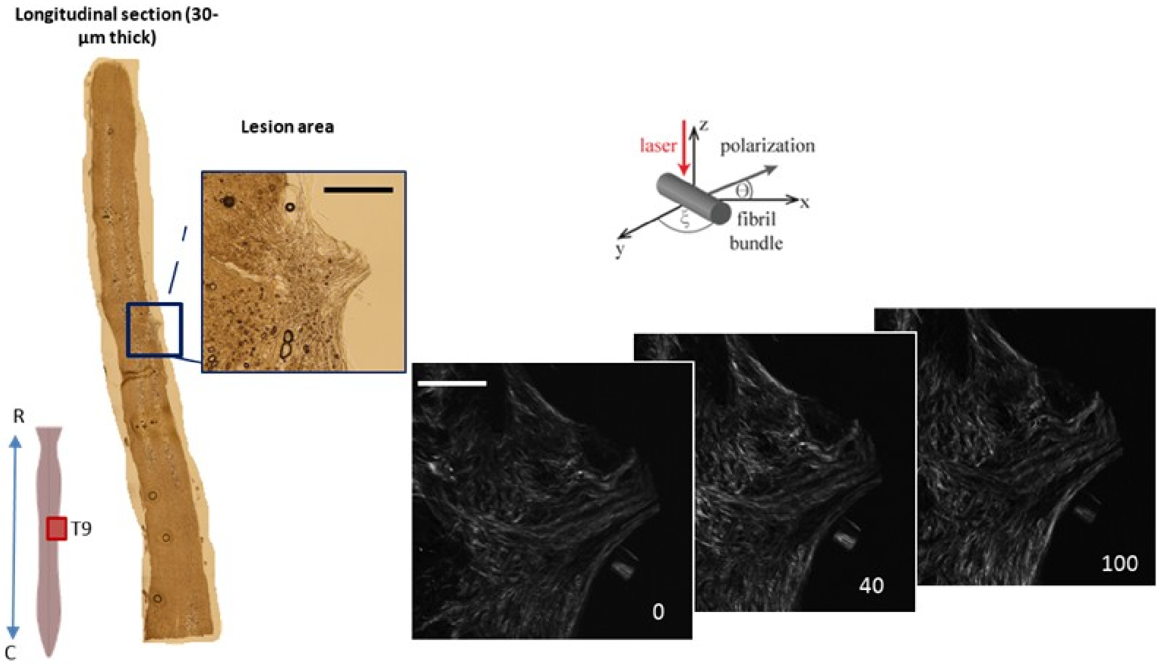

Figure 33: P-SHG z-stacks acquisition. After locating the lesion on the spinal cord (blue square) with optical microscopy, P-SHG stacks were acquired (15 z-stacks, to cover the sample thickness, 6 images per stack) with varying incident beam angle (from 0° to 180° with a 20° step). Here examples are provided for incident polarization angle Θ= 0, 40 and 100°. Scale bars: 167 µm (black), 100 µm (white).

II.2.2.3.2. Mosaic

To estimate the collagen fibers spatial extension, large mosaic images were recorded by stitching tiled images. These mosaic images covered the whole samples section around the injury site until no SHG signal was detected when scanning the rostro-caudal axis, as illustrated in *Figure 34*.

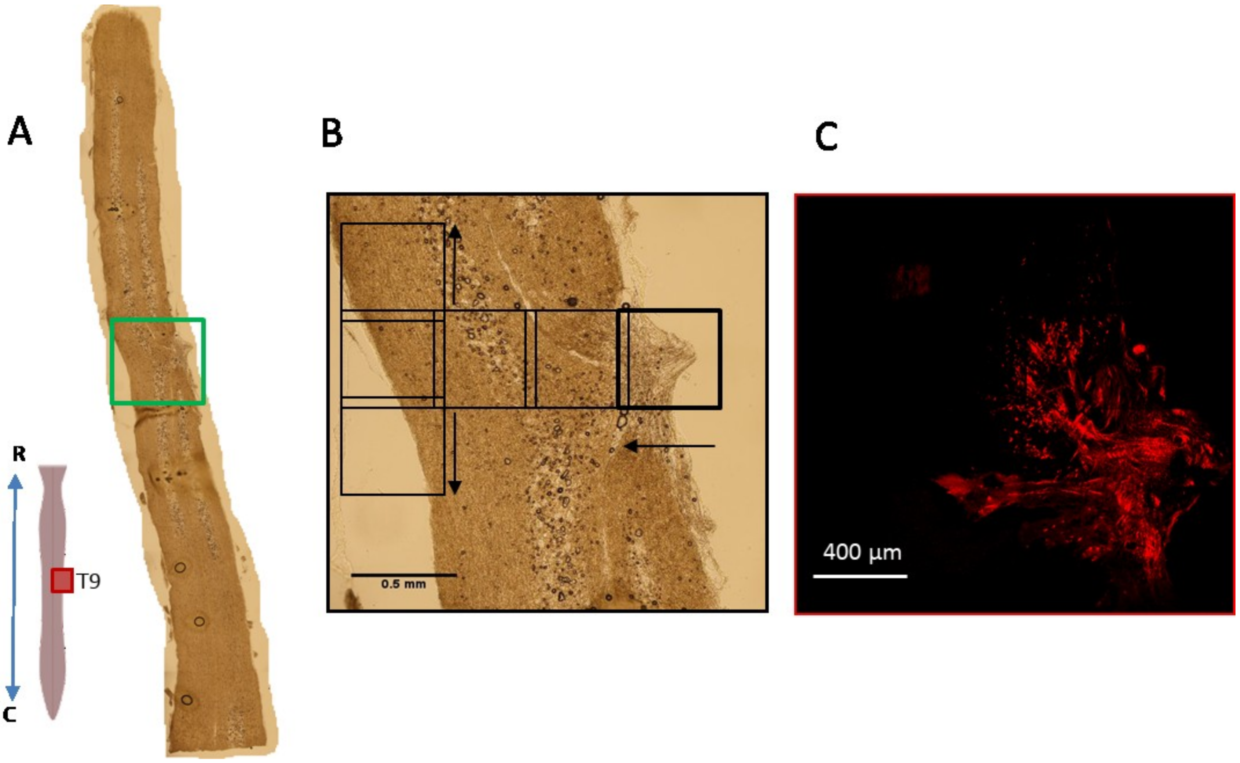

Figure 34: Mosaic acquisition. A. Bright field image of a spinal cord (longitudinal section) where the injury area is presented on the right. The acquisition area is highlighted by the green square. B. The enlarged area within the green square. For SHG mosaic acquisitions, tills (black squares) of 432x432µm² were measured. C. An example of collagen fibers extension after mosaic reconstruction (SHG signal in pseudo-color red).

Stacks were observed first to locate the optimal depth for imaging (generally the middle level) and the final acquisition at the chosen plain (no stack acquisition here) was an average of 30 images to improve the SNR. The tiled images were subsequently processed with Fiji (ImageJ, Grid collection/stitching plugin) to reconstruct the whole imaged area (Schindelin et al., 2012).

II.2.3. AFM-FS acquisitions and analysis

AFM measurements aimed to assess the mechanical properties of the excised spinal cord tissues in distinct regions (GM, WM and injury site) and to investigate the evolution of these properties at different time-points post-injury. AFM force-spectroscopy measurements were performed using an Asylum MFP-3D head coupled to a Molecular Force Probe 3D controller (Asylum Research, Santa Barbara, CA, USA) and combined with an inverted optical microscope (Zeiss Axiovert 200/Olympus ix-71) for positioning on the sample and for optical image acquisitions.

II.2.3.1. Tip characteristics

The choice of the probe is essential for accurate force curves measurements. Spherical probes have been reported to ease elasticity measurements on biological tissues (Krieg et al., 2019) and have already been used for measurements on spinal cord slices. This kind of probe can be obtained, for example, by gluing polystyrene beads using ultraviolet glue to the top of the cantilevers (Baumann et al., 2020; Moeendarbary et al., 2017). In our protocol, we used a 2-µm radius spherical colloid built-in probe cantilevers with a nominal spring constant of 200 pN/nm, length of 450 µm, width of 50 µm, and resonance frequency of 16 kHz (Biosphere B2000-CONT, S/N: C2521399, NanoTools). The detailed characterization of the tip is provided in Table 3. The spring constant of the cantilevers was determined using the thermal noise method available within the MFP-3D software.

II.2.3.2. Samples and indentation

Preliminary observations were made on fixed 14-µm thick axial sections (3 mice) and on 22-µm thick longitudinal sections (2 mice) at 1wpi. AFM-FS time-course acquisitions were performed on 22-µm and 30-µm thick longitudinal sections at the same time-points as for P-SHG experiments: 72-hpi, 1wpi, 2wpi, 6wpi (with and without treatment). 3 mice were used per time-point (maximum of 3 slides/mouse containing 3 sections). AFM imaging was performed prior to P-SHG for optimal mechanical characterization of the tissues. The slides were maintained in Petri dishes before and after AFM imaging in a 0.1M pre-sonicated PBS solution.

The validity of the theoretical model fitting (elasticity maps calculation with Hertz model fitting), the indention has to be maintained at less than 10 % of the height of the sample. Samples' thickness was chosen accordingly to this condition and a maximum loading force of 25 nN was applied in our measurements, as showed in *Figure 35-B*, corresponding to a maximal indentation depth δ of 1 µm.

The indentation depth can also be calculated accordingly to the following formula: $\delta = z - d$, with d the cantilever deflection and z the piezo translation after contact (Moeendarbary et al., 2017). In combination with the equation (11) presented in part I.2.3, the contact radius a in our case could be further evaluated at 0,77 µm.

Other conditions are: $a/h<<0.1$ with h, the slice thickness, which was valid in our case (0.035 for 22-µm thick and 0.026 for 30-µm thick) and $0.2Xa/R<0.2$ with R, the radius of the tip (Moeendarbary et al., 2017), also valid here, with a result of 0.08.

Table 3: biosphere B2000-CONT tip technical data

AFM tip	
Shape and material	Sphere - Diamond-like carbon
Sphere size	2 µm
Height	15 µm (10-15 µm)
Setback	15 µm (5-25 µm)
AFM cantilver	
Shape	Beam
Force Constant	0.2 N/m
Resonance Frequency	13 kHz
Length	450 µm
Width	50 µm
Thickness	2 µm

Additionally, the chosen thickness eased the location on the tissue and the discrimination between GM and WM (illustrated in the appendix section).

A point to mention here is that our work did not aim to obtain the effective absolute Young’s modulus values, as we imaged fixed samples and the elastic properties were not those of fresh tissues. Fresh tissues are difficult to obtain and to process, especially during the spinal cord removal where the injured parts can easily be damaged without fixation. Nevertheless, the study of the variation of Young’s moduli in different areas of the SC could be still a relevant parameter to investigate if aimed to monitor the elastic properties of the tissues at different time-points post-injury.

II.2.3.3. AFM-FS acquisitions parameters and analysis

The force measurements were carried out in PBS buffer, at room temperature and with the following parameters: a set point of 0,200 V (the strength interaction between the tip and the surface), integral gain of 2.5 (strength of the feedback), force distance of 4 µm and velocity of 10µm/s. The force-volume experiments were performed on a grid of 20x20 points over a region of 60x60 µm^2 (*Figure 35-A*) in different area: injury site, grey matter (GM) and white matter (WM) with 3 to 10 experiments per area type. FD curves were recorded at each point as a function of the loading force applied by the tip (maximum 25 nN), generating height maps of the sample topography. The recorded AFM-FS data (*Figure 35-B*) were used to determine the Young's modulus (E) of the tissue (*Figure 35-C*) using the Hertz contact model (Johnson, 1982). Histograms of the distribution of Young's moduli were fitted with a Gaussian function (*Figure 35-D*) to obtain the mean E value of the probed area in different locations on the spinal cord. Eventually, surfaces of the samples with an elasticity color code were generated for qualitative assessments, prior to quantitative comparisons (*Figure 35-D*).

Young's modulus values were subsequently overall normalized to bring all values into the range [0,1] for a simpler visualization before comparison as follows:

$$\bar{E} = \frac{E_i - E_{min}}{E_{max} - E_{min}} \tag{14}$$

With, E_i the average Young's modulus generated from each elasticity map, $\bar{E_\imath}$ the normalized average of Young's moduli for this map, E_{max} and E_{min} are respectively the maximum and minimum Young's moduli found over all the measurements. E_{max} = 167.0 kPa and E_{min}= 0.35 kPa.

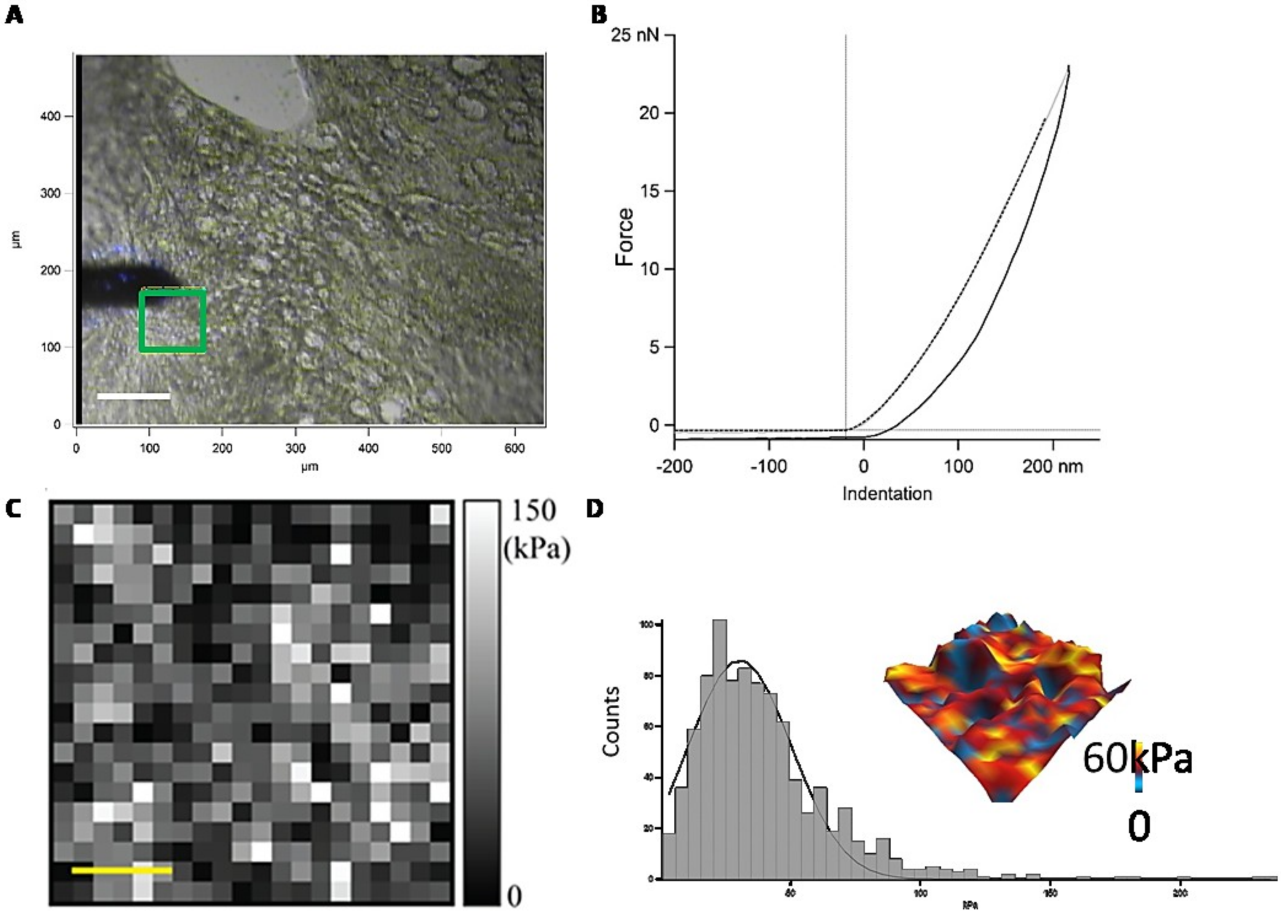

Figure 35: AFM-FS acquisitions. A. Bright field image of the sample showing the AFM tip and the acquisition area (square of 60x60 µm²) at the injury area. B. Typical force-distance curve fitted with the Hertz model. C. Elasticity map of a scanned area (20x20 points). D. The histogram of Young's moduli was fitted with a Gaussian function to obtain the main value. Inset: height map with an elasticity color code. Scale bars are: 80 µm in A and 15 µm in C.

II.3. MPM images processing and metrics extraction

P-SHG measurements were first aimed to assess the supramolecular organization of collagen fibrils bundles in relation with the evolution of the lesion. By plotting the polarization curves (SHG signal versus polarization angle) we could describe the fibrils profiles (straight or wavy-like) at each time-point post-injury based on a previous work (Mercatelli et al., 2020). Further data analysis for tissue level assessments was performed with two different methods. The first one was an open-source software named CurveAlign (Liu et al., 2020), initially dedicated to characterize collagen fibers in cancers, which allowed us to extract a first set of fiber metrics. To improve the detection and characterization of collagen fibers within our spinal cord tissue samples, we secondly developed a custom-made code written in MATLAB (MathWorks Inc.) based on the Fingerprint enhancement algorithm (Kovesi, s. d.; Lin Hong et al., 1998).

II.3.1. Polarization curves

We looked at the supramolecular structure of the collagen fibrils (cylindrical symmetry for straight bundles and trigonal symmetry for wavy-like ones) detected in the SHG image within the lesion at different time-points post-injury including the treated group. Our approach was meant to properly identify both profiles in a selection of fibers and to qualitatively assess their presence.

First, the fibers were contoured in ImageJ (Schindelin et al., 2012) with the ROI manager (*Analyze > Tools > ROI Manager)* targeting single fibers that appeared at specific polarization angles. Fibers exhibiting the same SHG intensity no matter the angle were probably part of a thick bundle containing several collagen fibrils, summing their response, hence the signal that was not sensitive to the polarization changes. To visualize only fibers/bundles sensitive to the polarization angle, a subtraction was performed between two projection images (maximum projection of the whole Z-stack) obtained at 0 and 100° (angles chosen in preliminary investigations, *Figure 36-A*). The most visible fibers or bundles in the resulting image (*Figure 36-B)* were the ones parallel to the light polarization and a set of them were manually delineated as regions of interest (ROIs). The ROI masks were then applied on the raw SHG data obtained at different polarization angles (*Figure 36-C)*, after co-registering the image plains with the subtraction image to avoid the misplacement of the mask.

SHG intensity values within the ROIs were measured for all Z-stack plains (no projection here) using Multi Measure plugin (from Bob Dougherty Stack-Sorter plugin, version 10:11, 2002, 2005, Optinav) with *ROI manager*> More>>Multi Measure. Finally, the ROIs' intensity from the central plain was plotted into a polarization curve. The profile of the polarization curves allowed us to discriminate between two types of fibers either consisting of an assembly of straight/aligned fibrils or wavy/disordered fibrils and to evaluate the relative abundance of each fibril type.

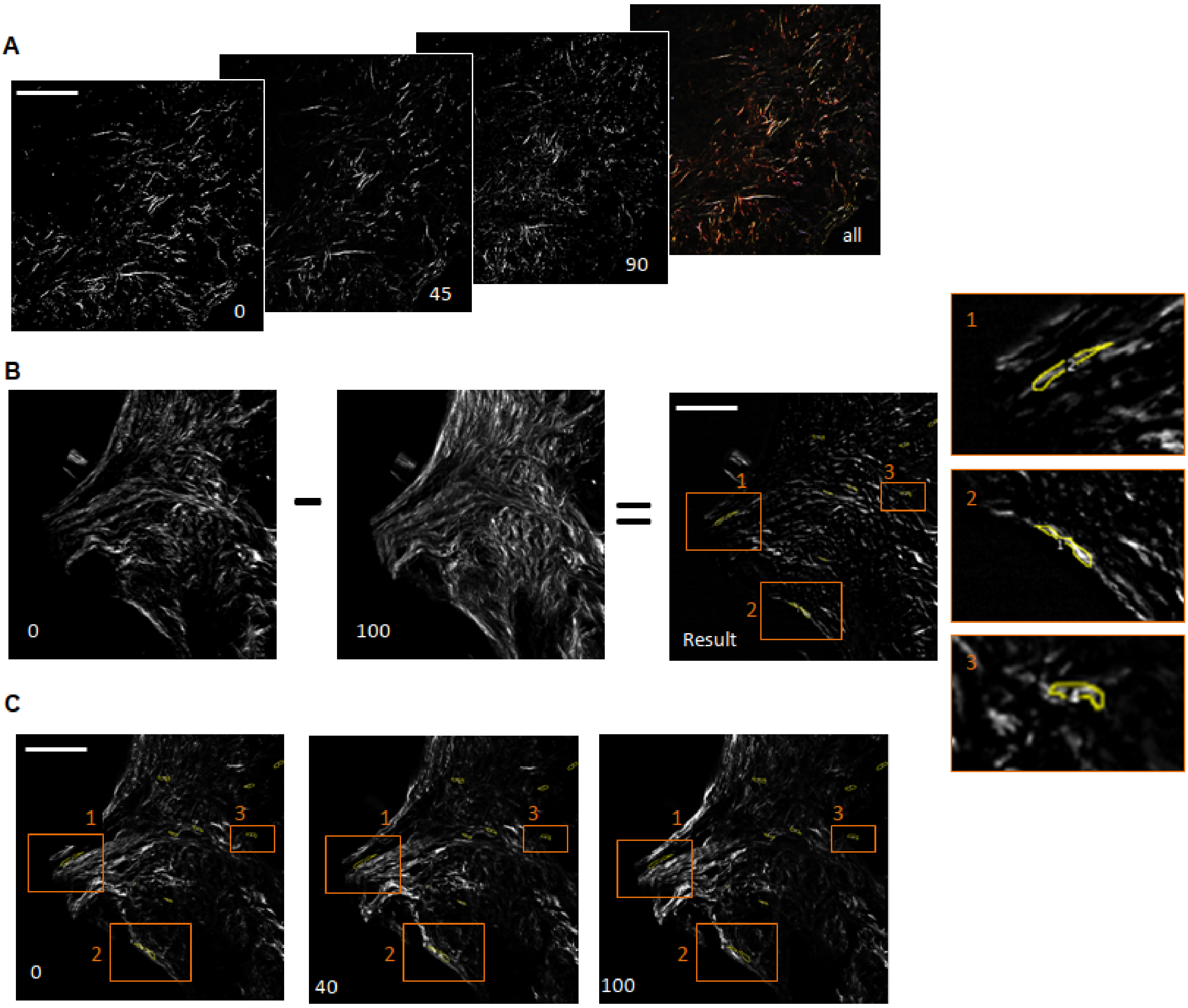

Figure 36: Fiber selection for plotting the polarizations curves. In (A), preliminary P-SHG images at different polarization angles (45°step), from left to right: 0°, 45°, 90° and composite image (0°: blue, 45°: yellow, 90°: red). Collagen fibers are sensitive to the light polarization and are visible if they are parallel to it. More clear changes were observed between 0 and 90° than between 0 and 45°. In (B), the fibers were selected on a resulting image by subtracting the SHG image obtained at 100° to the one at 0° (maximum projection of whole Z-stack). The mask of the selected ROIs was defined on the resulting image; examples of 3 ROIs (yellow contouring) are zoomed on the right (orange squares). In (C), the ROIs mask was applied on the raw P-SHG images (on each plain), here showed for 0°, 40° and 100°, with the same example ROIs as in (B). Scale bar is 100 µm.

Further we performed a quantitative analysis of the SHG images to measure the content and the orientation of the collagen fibers observed by extraction of relevant fiber metrics. We've used the Curvelet Transform (CT) algorithm implemented in the open source software CurveAlign as CT-FIRE (Bredfeldt et al., 2014). The CT-FIRE method allows to identify and track individual fiber and to calculate fiber metrics as their length, their diameter, their number and their orientation (Pijanka et al., 2019). The next section presents briefly the principle of CT as well as an overview of how CurveAlign is working, through examples from our study.

II.3.2. CurveAlign principle and pipeline

II.3.2.1. Curvelet Transform (CT)

The curvelet transform, also called multiresolution geometric analysis (MGA), is defined as a multiscale directional transformation following the review of Ma and Plonka (Ma & Plonka, 2010) and can exploit the regularity of curvilinear structures such as edges, lines or curves. It comes from the wavelet method traditionally used for point singularities (discontinuities) and based on dilated but area-fixed windows (Ma & Plonka, 2010). However, wavelets fail to represent the geometric properties of the structures and cannot efficiently work for line singularities. Ridgelets for straight lines and then curvelets for curved edges (Candès et al., 2006) have been proposed as an answer to wavelets weakness to describe curvilinear elements which are highly anisotropic and sensitive to the directionality. The difference in the results obtained, for example in image denoising between wavelets and curvelets thresholding, is illustrated in *Figure 37*, where we can see how curvelet thresholding is less noisy and the feature edges are better defined than in the wavelet method.

The building and the identification of lines, curves and edges in an image is called a sparse representation (in 2D). Here, "sparseness" for an image means a compact description of such an image in a transformation domain (Fadili & Starck, 2009). The first generation of curvelets consists in considering a partition of the original image and applying a ridgelet transform to the sub-parts. At sub-scales, the edges could be considered as straight lines. Despite the advantages of this first approach, a second generation of curvelets has followed with a lower redundancy and a simpler indexing structure. This index includes only three parameters to define the objects of interest: the scale, the orientation (the angle) and the position (Fadili & Starck, 2009). The scale is set at 2^{-j}, the orientation noted θ_l is defined as the equi-spaced sequence of rotation angles, with $\theta_l = 2\pi \cdot 2^{-\lfloor j/2 \rfloor} l$ (l is an integer between 0 and 2π), and the position is noted $x_k^{i,j} = R_{\theta_l}^{-1}(2^{-j}k_1, 2^{-\frac{j}{2}}k_2)$ with R_{θ_l} the rotation by θ_l radians, and k= (k_1, k_2) the sequence of translation parameters.

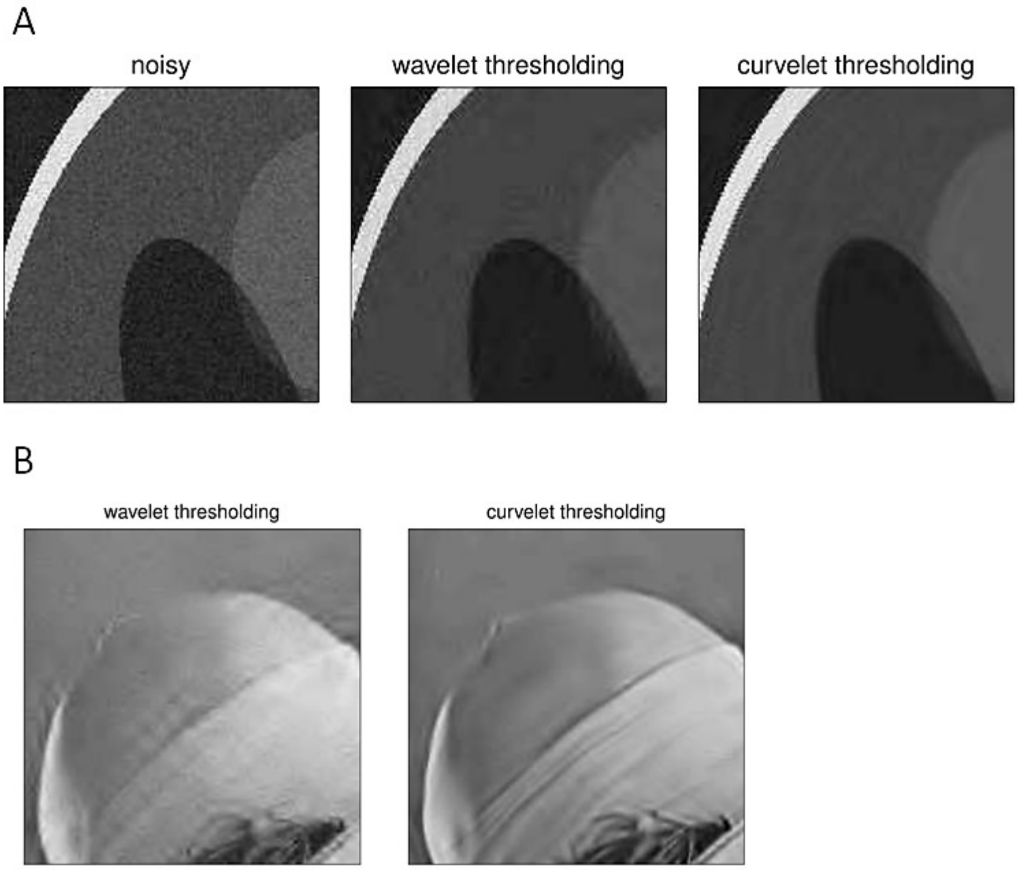

Figure 37: Difference between wavelets and curvelets thresholding. The two transformations are applied in (A) on a zoomed area of a phantom and in (B) on a photograph-like image. In both cases, the curved edges are more clearly identified with the curvelet method. Adapted from Emmanuel Candès "Lecture 2: Curvelets", available on: www.crm.umontreal.ca/Imagerie06/pdf/montrealLecture2.pdf

The waveform φ_j, considered as an initial curvelet or "mother" curvelet, can be expressed in the Fourier domain with its Fourier transform $\hat{\varphi}_j$ as follows (Fadili and Starck, 2010):

$$\hat{\varphi}_j(r,\theta) = 2^{-\frac{3j}{4}} \widehat{w}\ (2^{-j}r)\hat{v}\,(\frac{2^{\left\lfloor \frac{j}{2} \right\rfloor \theta}}{2\pi})\ . \tag{15}$$

With $\widehat{w}$ and $\hat{v}$, the radial and angular windows, respectively. The curvelet variation describes the translation and rotation of the initial curvelet φ_j:

$$\varphi_{j,l,k}(x) = \varphi_j\ \left(R_{\theta_l}\left(x - x_k^{j,l}\right)\right). \tag{16}$$

If the frequency ν is continuous, the curvelets coefficients of the $f(x)$ data are defined by the equation:

$$c_{j,l,k} := \langle f, \varphi_{j,l,k} \rangle = \int_{\mathbb{R}^2} \hat{f}(\upsilon)\hat{\varphi}_j(R_{\theta_l}\upsilon)e^{ix_k^{j,l}\cdot\upsilon}d\upsilon, \tag{17}$$

and simplified for the curvelet representation in the special domain as:

$$c_{j,l,k} := \langle f, \varphi_{j,l,k} \rangle = \int_{\mathbb{R}^2} f(x)\overline{\varphi_{j,k,l}(x)dx} \tag{18}$$

In this context, curvelets are following a parabolic scaling relation stating that, at the scale considered 2^{-j}, each object has an envelope aligned along a ridge (length $2^{-j/2}$ and width 2^{-j}) (Candès et al., 2006).

Figure 38 is showing the curvelet representation according to the parabolic scaling, the location and the orientation. The Cartesian equivalence can further be obtained followed by an implementation for discrete data.

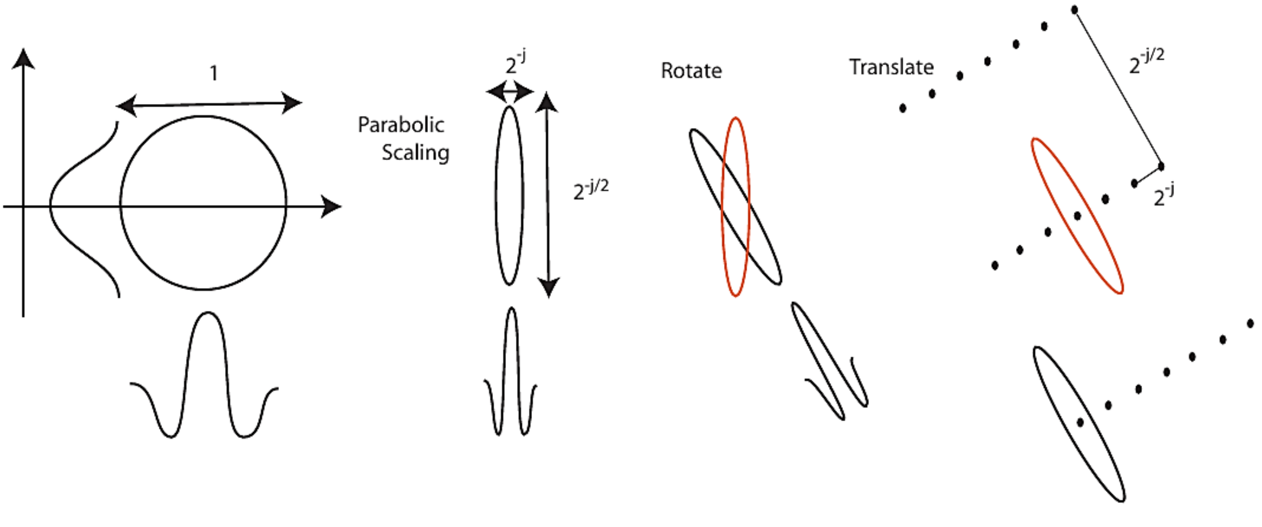

Figure 38: Curvelets characterization by three parameters: the scale (following a parabolic scaling relation), the location and the orientation (rotation, translation). From Emmanuel Candès "Lecture 2: Curvelets", available on www.crm.umontreal.ca/Imagerie06/pdf/montrealLecture2.pdf

More explanations are available in the previously cited studies (Candès et al., 2006; Fadili & Starck, 2009).

The Curvelet transformation (CT) allows the identification of structures like fibers and has been implemented in the software CurveAlign for the specific characterization of collagen fibers.

II.3.2.2. CT-FIRE and Curve Align

CurveAlign is an open-source software that was initially developed (Bredfeldt et al., 2014; Liu et al., 2017; Pavone & Campagnola, 2013) as a quantitative tool to determine the collagen fibers orientation relative to a tumor boundary. Further, it was complemented with a fiber extraction tool, the CT-FIRE based on the CT for individual fiber identification and analysis.

Pre-processing is an essential step before importing the images into CurveAlign. This step is described below, followed by data analysis. Our P-SHG data were pre-processed in ImageJ in order to remove the background and enhance the fibers contrast prior to their identification and characterization.

II.3.2.2.1. Pre-processing in Image J

Images were pre-processed in batches. A batch corresponded to all the data for one mouse. Below are provided the steps for the acquisition of one image at a given polarization angle.

The full Z-stack was first merged into a single image with Fiji (ImageJ, version 1.52g, on Windows 10), averaging the intensity over all images. The resulting image was converted into an 8-bit type following the recommendation for CurveAlign inputs and auto-contrasted using *Adjust>Brightness-Contrast>Auto* function. This function changes the default grey values into an 8-bit image, (0 the minimum and 255 the maximum displayed pixel values) by adjusting brightness and contrast, taking the image's histogram as a reference. To avoid oversaturated pixels, the *Auto* function was applied only once. The relevance of auto-contrasting for CurveAlign analysis is illustrated in *Figure 39*.

A background subtraction was then performed with *Process>Subtract Background* using a "rolling ball" algorithm based on Sternberg's paper (Sternberg, 1983). This algorithm assesses a local background value for each pixel by averaging values over a sphere located around the pixel, and this local value is then subtracted from the original image. According to the plugins recommendations, the radius should at least have the size of the largest object in the image that is not part of the background. After preliminary tests with CT-FIRE, we set the radius ball at 25 pixels to efficiently detect the fibers at all the time-points (an example is provided in the appendix section). After the pre-processing, we further analyzed our data with CT-FIRE first, and then with CurveAlign using the CT-fibers mode.

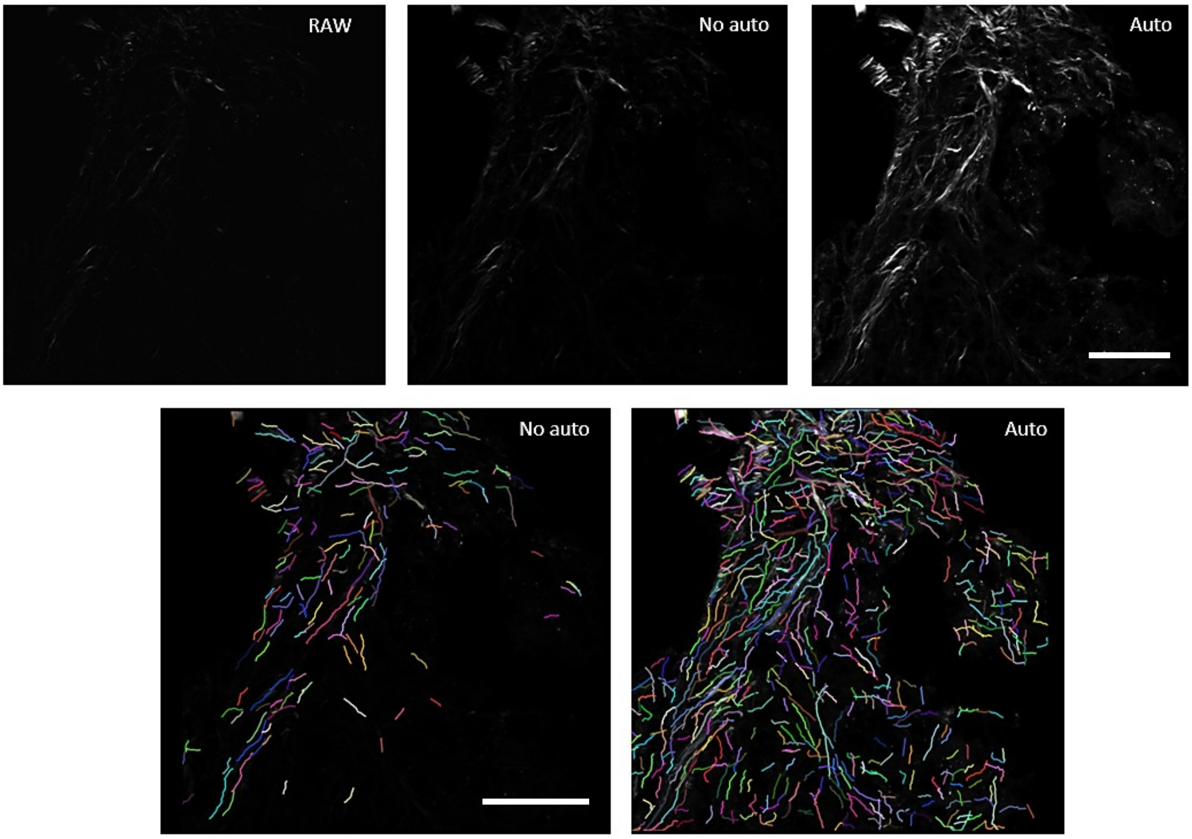

Figure 39: Auto-contrasting for fibers visualization enhancement. The raw data (only the central plain is presented here) image is showed in comparison with an 8-bit average image (8-bit conversion recommended on: https://eliceirilab.org/software/ctfire/ct-fire-faq/), without and with auto-contrasting (https://imagej.net/imaging/image-intensity-processing). Scale bar is 100 µm. Fibers detection with CT-FIRE highly depends on the pixel values and is more efficient if the input data are pre-processed relevantly. CurveAlign detailed user guide is provided online by the authors at: https://eliceirilab.org/software/curvealign/.

II.3.2.2.2. CurveAlign analysis

CT-FIRE and CT-Fibers modes allow collagen fibers analysis at different levels. The first mode provides information about individual fibers, whereas the second is more suitable for bulk collagen alignment studies.

CT-FIRE-individual fiber: CT-FIRE aims to process individual fibers parameters using the CT described in the previous section. For this step, images were processed in batches (a batch corresponded to all data for one post-injury time-point). We mainly kept the default parameters of the software conceived to work with most of biological samples involving collagen fibers: minimum fiber length at 300 pixels, fiber line width at 0,5 pixels, a maximum fiber width at 15 pixels and threshold for the background intensity at 5 pixels.

The radius of the searching box was slightly moved from 8 pixels (default parameter) to 10 pixels in order to avoid the fibers over-detection, i.e., noise detected as a fiber.

The background threshold and the size of the searching box, called as “thresh_im2” and “s_xlinkbox” respectively in the software, affect the fibers extraction the most, and were tested on preliminary analyses (without background subtraction) as shown in *Figure 40*.

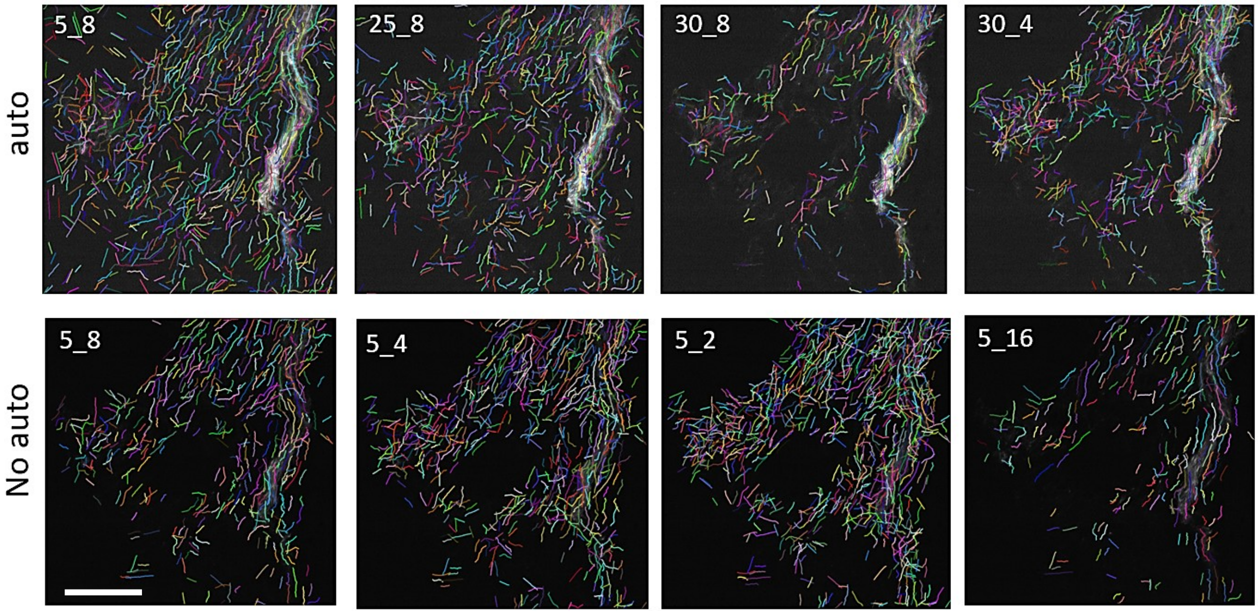

Figure 40: Example of the influence of different input parameters in the CurveAlign method for the segmentation of collagen fibers in the tissue. The background threshold (first number) and the size of the searching box (second number) were tested on SHG images with and without auto-contrasting, top and bottom images respectively. Scale bar is 100 µm. No background subtraction was applied. The default values are 5 and 8 for the ***background threshold*** *and* ***the box size****, respectively. These two parameters have been reported to affect the fibers’ detection (https://eliceirilab.org/software/ctfire/ct-fire-faq/). Increasing the background threshold decreases the number of fibers detected while decreasing the box size increases the detection.*

As a result of CT-FIRE analysis, fibers were detected and overlaid on the input image, along with histograms of various parameters such as the length, width, strength, angle of each fiber and the total number of fibers, besides an overall length and width values. *Figure 41-A* provides an example of CT-FIRE outputs. For our study, we chose to focus on the number and the length of the fibers for each polarization angle. Finally, we calculated an average of these parameters for all the polarization angles (with an estimation of the number of fibers over the area of the image, in µm² for each sample, to weight our results).

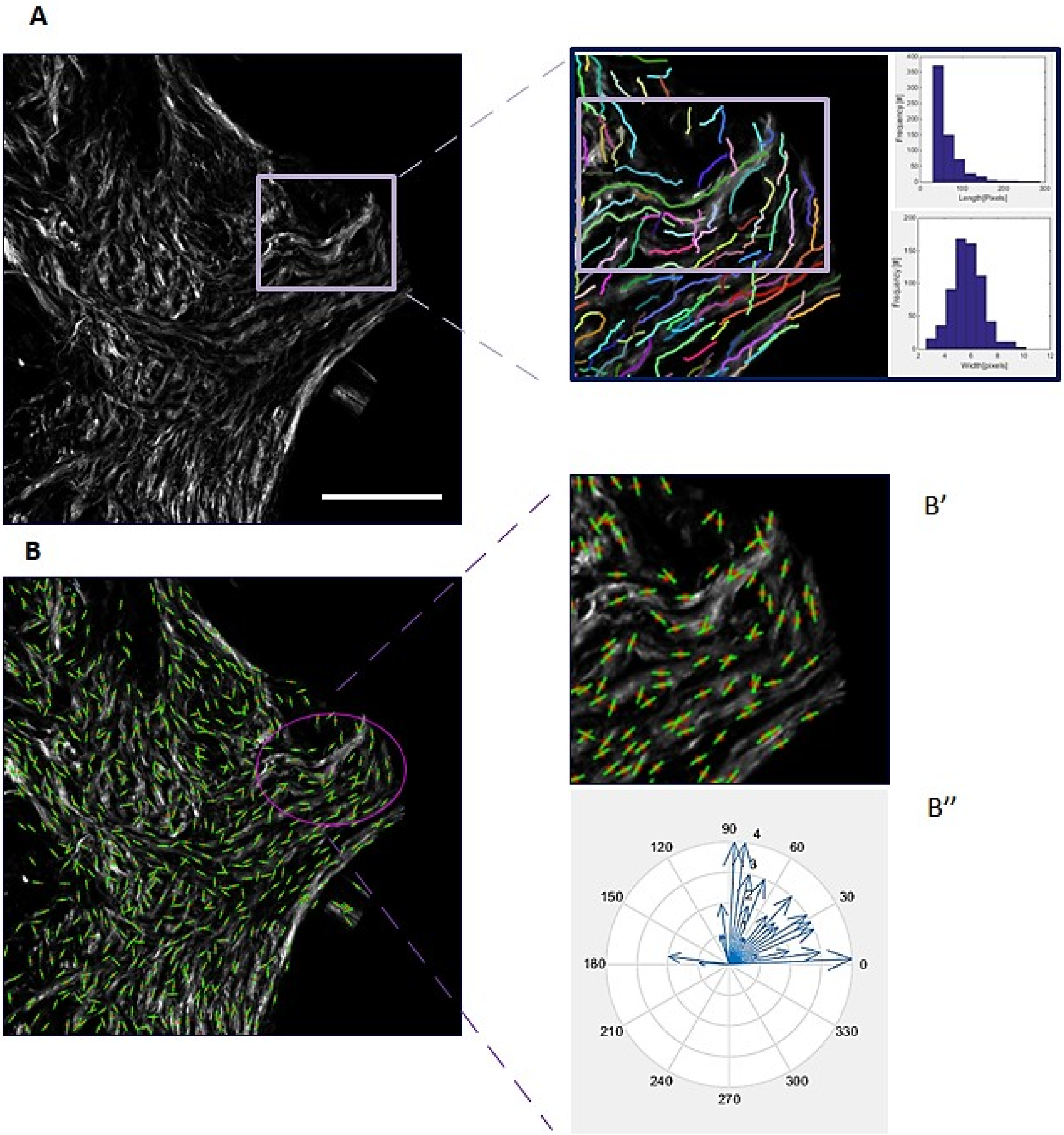

Figure 41: CT-FIRE and CT-FIRE fibers. A. Individual fiber extraction with CT-FIRE. The first step was to extract each individual fiber with CT-FIRE, based on the curvelet transform (CT). Scale bar is 100 µm. An example of fibers identification is provided from a zoomed area (violet frame) of the input data (SHG image). The outputs are fibers parameters represented in histograms (for example the frequency of the fibers length or width). B. Fibers orientation from grouped curvelets with CT-FIRE fibers in CurveAlign. CT-FIRE output was then computed in CurveAlign to provide fibers orientation information, using CT-FIRE fibers method. Each fiber was identified by an angle (green lines) and a center (red points). ROIs (violet circles, zoomed in B') could be defined and the orientation and the alignment of the fibers within each ROI can be obtained from the angle compass (B'') where the length of the blue arrows depends on the number of fibers orientated in the direction.

CT-FIRE fibers – fiber definition: The second step was to work with the CurveAlign CT-FIRE fibers mode, which is based on grouped curvelets to estimate fibers' orientation. Other modes are available in the CurveAlign software (such as CT-FIRE segments), where the CT-FIRE output is used as an input. In CT-FIRE fibers, each fiber center point of the output file corresponds to an observation in the feature set, where each center point is characterized by a unique angle (average angle of the fiber) and a position (midpoint between the fibers end points or the midpoint of the end-to-end vector). Besides, each center point is associated to a fiber length and curvature that correspond to the entire fiber. In other words, CT-FIRE fibers move the metrics generated by the CT (belonging to curvelets that form a fiber) to metrics of the entire fiber itself, defined by a specific position and angle. Alignment can then be assessed on such a fiber, considering the angle compass as illustrated in *Figure 41-B"* and the alignment factor.

Alignment For the alignment investigation, we worked first at tissue level, considering the whole image area as a single ROI. Post-analysis, based on the circular statistics methods described by Berens (Berens, 2009) provides the overall alignment of the fibers within the same ROI (one ROI in this case) by calculating the resultant vector length of all orientation vectors. Its output is an unite-less value varying from 1 to 0, indicating the distribution around the median angle in the ROI, as the fiber alignment decreases starting from a perfect alignment in the median angle direction until a random alignment (fibers are not aligned within the same ROI). The alignment factor allowed us to determine if the fibers were well aligned or not at tissue level.

We subsequently investigated the fibers alignment at a ROI-level, by drawing a series of ellipse-shaped ROIs covering the tissue (*Figure 42*). The ellipse shape allowed considering a maximum of fibers between two ROIs, including fibers that visually seemed to be aligned along the same direction. This investigation was made to corroborate visual observations we had about fibers aligned in different directions, within the same tissue. In order to control the loss of fibers detected within the ROIs (compared to the number in the whole image), we maintained a difference of 50 to 70 fibers between all the ROIs and the whole image for each sample.

Then, we classified the ROIs in four categories according the value of their alignment factors:

- cat1[75-100 %]; number of ROIs with values between 0.75 and 1, indicating a very good alignment;
- cat2]75-50] ROIs with values between 0.5 and 0.75 (excluded) indicating a good alignment;
- cat3]50-25] for values between 0.25 and 0.5 (excluded), indicating a medium alignment;
- cat4]25-0] for values under 0.25 indicating a bad alignment.

An average was done for all the polarization curves. For robust measurements, we excluded ROIs with less than 10 fibers (as recommended from CurveAlign user's manual). A final value, the alignment coefficient c_a (expressed in %) was obtained for each sample by normalizing the number of ROIs per category $ROIs_{cat}$ by the total number of ROIs used for the counting $ROIs_{tot}$:

$$c_a = \frac{ROIs_{cat}}{ROIs_{tot}} \tag{19}$$

An average of all the c_a values was finally calculated for each animal.

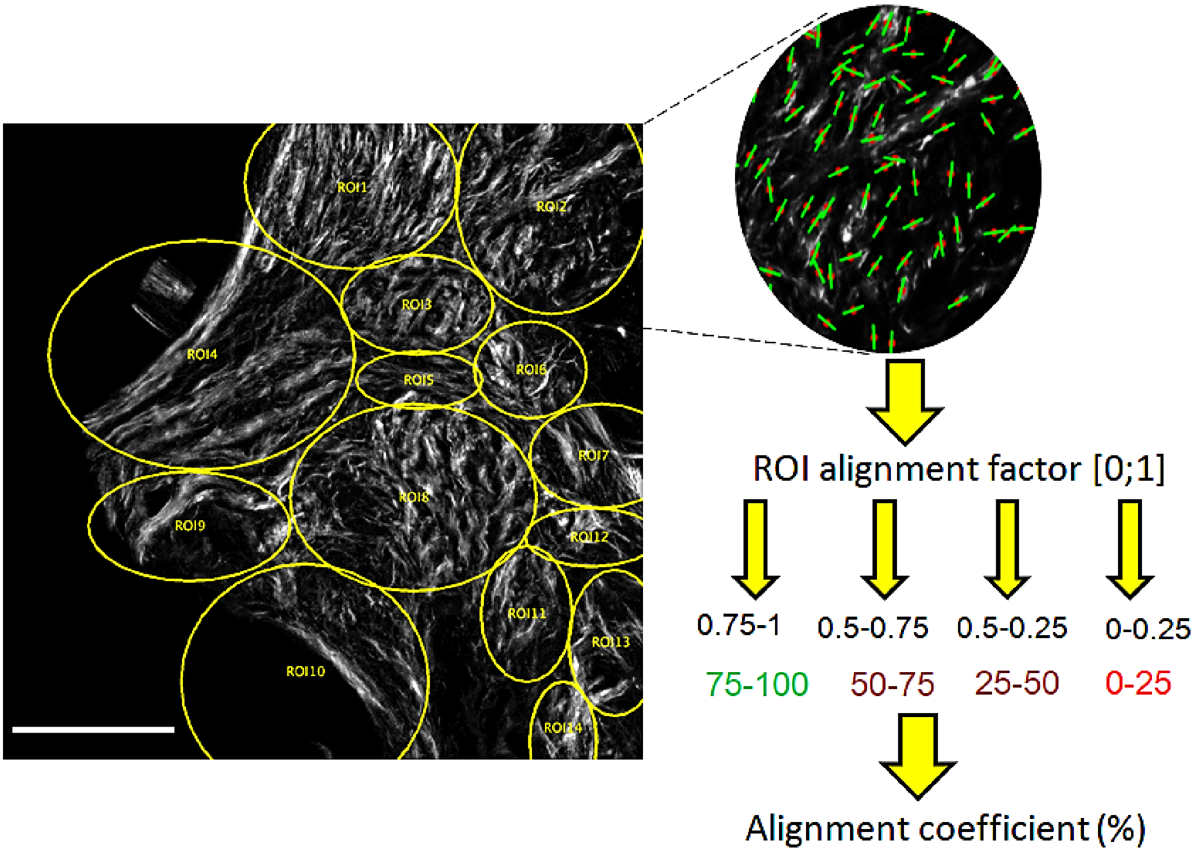

Figure 42: Alignment assessment on sub-regions. ROIs (yellow ellipses) included fibers that seemed orientated in the same direction. Scale bar is 100 µm. Fibers angle and position were extracted with CT-FIRE fibers mode and an alignment factor was obtained (value between 0 and 1) for each ROI (here for example in ROI 2). The factors were classified in four different categories indicating the good or bad alignment of the fibers within the ROI. An alignment coefficient (%) was calculated taking into account the total number of ROIs considered.

.

CT processing depends on many parameters which are hard to properly tune. The complexity of this transformation makes the software based on it complex due to the multiple parameters needing to be optimized and tuned in order to properly segregate the fibers from the microscopy images. Moreover, tissues are highly diverse and dissipative medium producing complex experimental images to characterize the collagen fibers forming after SCI.

II.3.3. Fingerprint algorithm pipeline

With the aim to improve detection of collagen fibers and to adapt it to the variability of our samples, we developed an algorithm written in MATLAB 2021a (MathWorks Inc.), based on a previously reported fingerprint enhancement algorithm FP (Kovesi, s. d.; Lin Hong et al., 1998). Data processing from the Raw SHG image to the fibers metrics extraction is explained in the following sections.

II.3.3.1. Pre-processing

The list of metadata elements were first read to take into account the number of measurements by plain and the number of plains contained in each Z-stack where P-SHG signal was recorded. The image pre-processing began by enhancing the contrast of the SHG Z-stack (sum of all 6 images per plain) using the contrast limited adaptative histogram equalization (CLAHE) method (Zuiderveld, 1994), following the same logic for fibers visualization improvement when using auto-contrasting in ImageJ. The contrast enhancement was followed by a 2D Gaussian smoothing kernel image filter for reduce the image noise. Finally, an image resizing (oversampling) is performed to increase the pixels where the fiber's border can be defined. In our data analysis, we found out that the scale-factor of 2 is a good compromise to increase the space, the noise induced by interpolation to generate more pixels and the computational time cost during further analysis (*Figure 43-A and B).*

II.3.3.2. Fingerprint algorithm

For fibers detection and quantification, we adapted an algorithm developed by Peter Kovesi for "Fingerprint Enhancement" (Kovesi, s. d.). A ridge frequency-like map (*Figure 43-C*) was processed according to the work of Hong and coworkers (Lin Hong et al., 1998). Briefly, in a local neighborhood where no singular points appear, the grey levels present in the direction perpendicular to the fibers can be modeled as a sinusoidal-shaped wave which is normal to the direction given by the principal axis of the covariance. The estimation of the weight of such sinusoidal modulation around each pixel of the image could then be used to construct frequency-like images.

Then, a binarized map of the detected fibers was created by combining a reliability map (following the work of Kovesi) with the positive-values of the ridge frequency-like map (*Figure 43-D*). The detected fibers were filtered by their size removing all detected fibers below a threshold of 1 µm² (assumed as detection noise)) before the binarized map generation.

The reliability map was obtained by finding the principal axis of variation in the image gradients as follows:

$$\nabla I_{SHG}(x,y) = \begin{bmatrix} G_x \\ G_y \end{bmatrix} = \begin{bmatrix} {\partial I_{SHG}}/{\partial x} \\ \\ {\partial I_{SHG}}/{\partial y} \end{bmatrix} \tag{20}$$

where $I_{SHG}(x,y)$ is the SHG-image, G_x and G_y are the image's partial derivate with respect to x and y, respectively. The elements of the covariance matrix are given by:

$$\begin{aligned} G_{xx} &= G_x^2 \\ G_{xy} &= G_x \cdot G_y \\ G_{yy} &= G_y^2 \end{aligned} \tag{21}$$

We diagonalized the covariance matrix to determine their principal directions. The analytic solutions of the principal directions are given by:

$$G'_{min} = \frac{G_{yy}+G_{xx}}{2} - \frac{(G_{xx}-G_{yy})}{2} \cdot cos(2\beta_r) - G_{xy} \cdot sin(2\beta_r) \tag{22}$$

$$G'_{max} = G_{yy} + G_{xx} - G'_{min} \tag{23}$$

where G'_{max} is the principal axis of the covariance, G'_{min} is the minor axis of the covariance, and β_r is the rotation angle applied to the diagonalized covariance matrix. β_r can be determined as follows:

$$sin(2\beta_r) = \frac{G_{xy}}{\sqrt{G_{xy}^2 + (G_{xx}-G_{yy})^2}} \tag{24}$$

$$cos(2\beta_r) = \frac{G_{xx}-G_{yy}}{\sqrt{G_{xy}^2 + (G_{xx}-G_{yy})^2}} \tag{25}$$

Then, a reliability map was calculated from the obtained orientations as:

$$reliability = 1 - \frac{G'_{min}}{G'_{max}} \tag{26}$$

The reliability value obtained is within [0, 1], when the reliability factor takes the value of 1 it represents a fully reliable value.

Only the values above the reliability threshold (normally defined as 0.20) were considered for obtaining the binarized map.

Finally, the skeleton map (*Figure 43-E*) of the fibers was obtained by skeletonization of the previous binarized map. This process consisted in the extraction of the central line of each feature on the binarized collagen fibers.

II.3.3.3. Untangling

As the SC tissue contained a high density of collagen fibers, some fibers were merged. To properly separate crossing fibers in the skeleton map, an untangling method was developed ((*Figure 43-F)*. First, branch-points (points connecting different fiber skeletons) and the number of participating branches were determined. Then, all the combinations of two branches were evaluated in terms of the angle (α) formed by their connection (in this context, connections with α = 90° are less likely than connections with a larger angle due to its high curvature). The combination giving the more likely connection is kept unchanged while the other connections are suppressed from the skeleton map (by setting to 0-value the closest pixel to the branch-point of the other branches). This process split some fibers but allowed computing the different metrics defined in our work (Metrics definition section).

II.3.3.4. The local orientation map

The local orientation θ_{ij} of the fibers was determined directly from the untangled skeleton map. It was estimated pixel-by-pixel based on the angle formed by its nearest neighbors in a mask of n x n pixels, which is displaced pixel-by-pixel to evaluate the local orientation following the work of Guidolin and coworkers (Guidolin et al., 2004).

Note that a larger box can define the angle with more sensitivity. However, it is also associated to an overaverage when the fiber's shape is more complex. We found n = 9 pixels/1.9 µm was a good compromise for our measurements. We decided to evaluate the local orientation by this method instead of the typical intensity's gradient since we have found artifacts related to the pixel intensity induced by light polarization when the intensity's gradient is employed. These artifacts have been reported previously in the literature (Bancelin et al., 2015; Ducourthial et al., 2019).

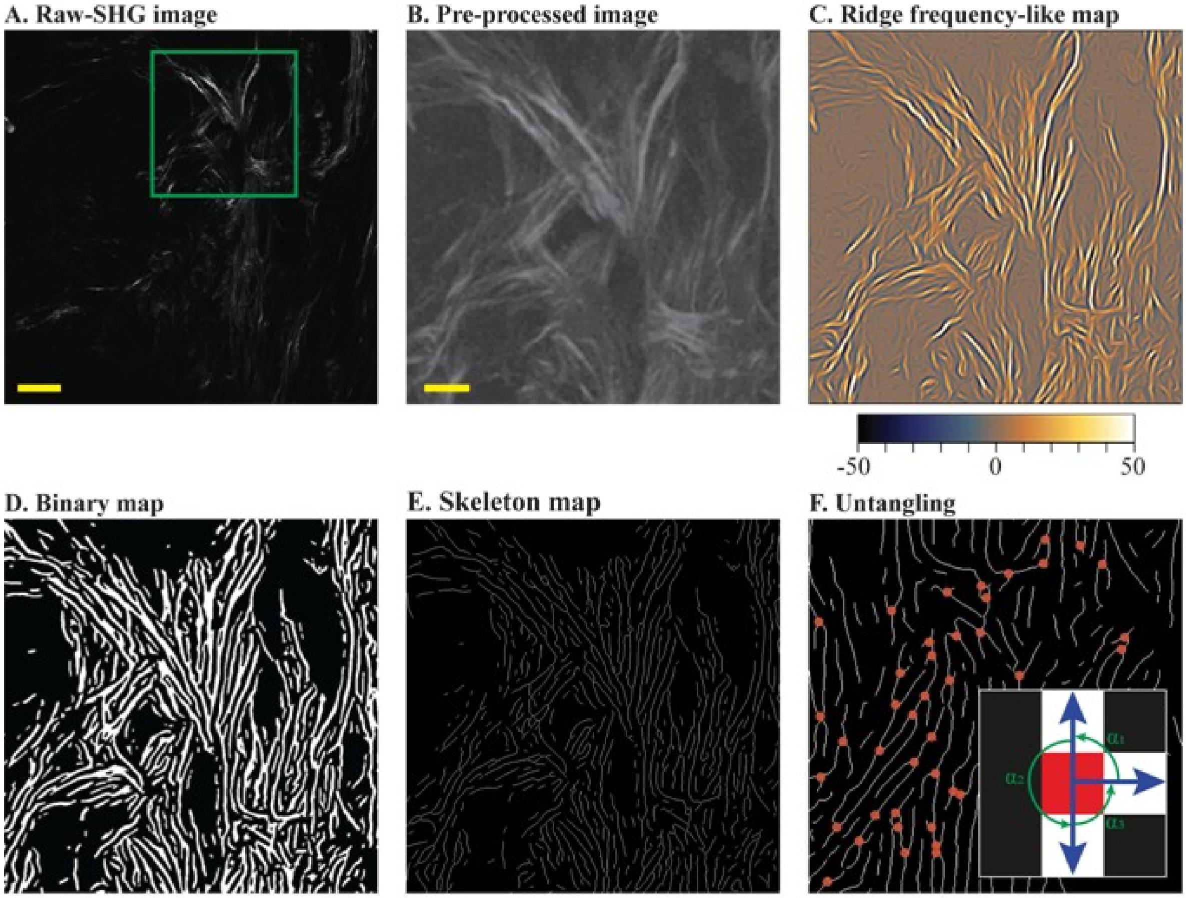

Figure 43: Pipeline of the Fingerprint enhancement-based method. ***A.*** *Raw-SHG image (scale-bar is 50 µm). The green frame shows the zoom-in displayed in the following images.* ***B.*** *Pre-processed image applying signal enhancements and oversampling (scale-bar is 20 µm).* ***C.*** *Ridge frequency-like map obtained by fingerprint enhancement method.* ***D.*** *Binary map of fibers determined by all positive values in C.* ***E.*** *Skeleton maps of fibers obtained from the binary map in D.* ***F.*** *Untangling of fibers by geometrical constraints applied on the skeleton map. Here, the branch-points were found and a sub-image of 1-pixel radius around each branch-point was analyzed to fix the fiber continuity. The most reasonable fiber continuity was stated by determining the angle (α) of each possible connection around the branch-point.*

II.3.3.5. Metrics definition

All metrics were evaluated from the skeletonized map of collagen fibers. The parameters deduced were the fibers' density, tortuosity, local alignment map of the fibers and the statistical entropy.

II.3.3.5.1. Fibers' density (ϕ)

To quantify collagen in the SC tissue we have first calculated, from the skeletonized map, the total length of the collagen fibers that was then normalized to the surface covered by the tissue extracted from the 2PEF image. Herein, we named this parameter shortly as fibers' density (ϕ):

$$\phi = \frac{F_l}{S_t} \tag{27}$$

with F_l the sum of fiber's length detected across the tissue and S_t the tissue area. S_t was determined according to the morphological thresholding of the corresponding 2PEF image as depicted in yellow in *Figure 46-B*.

II.3.3.5.2. Tortuosity

To quantify the straightness of individual fibers, we calculated the tortuosity defined as the ratio of the fiber length (L) over the fiber end-to-end distance (R) in the path length ratio method (PLR) (Shanti et al., 2014). Lower is the tortuosity straighter is the fiber (*Figure 44*).

$$Tortuosity = {}^{L}/_{R} \tag{28}$$

This method, usually employed for transport efficiency (as displacement in pore channels), is especially useful for tortuosity determination from 3D images.

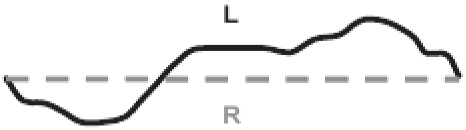

Figure 44: Schematic of a collagen fiber length (L) and end-to-end (Euclidian) length measurements for tortuosity determination. Tortuosity ≥ 1. *Adapted from (Shanti et al., 2014).*

Briefly, the L and R were measured from the coordinates of each fiber skeleton computed from the skeletonized map. R was calculated as the end-to-end fiber skeleton vector and L was calculated as the perimeter of the fiber skeleton. This procedure provided an average tortuosity of a group of fibers (single sections of fibers) along all directions.

II.3.3.5.3. Statistical entropy (S)

To evaluate the fibers' organization within the tissue, the statistical entropy *S* of the orientation distribution at pixel level was computed from the skeletonized SHG image following Ducourthial et al. (Ducourthial et al., 2019).

$$S = \frac{-1}{Ln(NB)} \sum_{\beta=-90^\circ}^{90^\circ} p(\beta) Ln\big(p(\beta)\big) \tag{29}$$

Where *NB* is the number of bins, β is the angular bin used, *p(*β*)* is the normalized number of pixels with the orientation β in the local orientation map (directly obtained from the histogram shown in *Figure 45*). To render S independent of the width of angular bins used (1˚ and 10˚ in our case), the normalization factor Ln(NB) was employed (Ducourthial et al., 2019). The entropy S provided the degree of orientation disorder. S = 1 means a fully isotropic orientation distribution, whereas small S values indicates that the orientation distribution is narrower. This approach could be related to the global alignment investigation we performed with CurveAlign considering the orientation of all the fibers within the image.

II.3.3.5.4. Local alignment of fibers, variance map

To assess fiber's alignment, we performed a circular statistical analysis for different local orientations with θ ∈ [-90°, 90°). By computing the circular variance, we evaluate the fibers local organization:

$$Var(\theta) \; = \frac{1}{N} \sum_{j=1}^{N} \big(1 - cos(2\theta_j - 2\bar{\theta})\big) \tag{30}$$

with θ_j the orientation of a pixel associated to a skeleton fiber and $\bar{\theta}$ the mean orientation which is computed as follows:

$$\bar{\theta} \; = \; arg\big\{\textstyle\sum_{j=1}^{N} e^{i2\theta_j}\big\}/2 \tag{31}$$

Var(θ)=0 for perfectly aligned fibers, and Var(θ)=1 for random (not aligned) fibers.

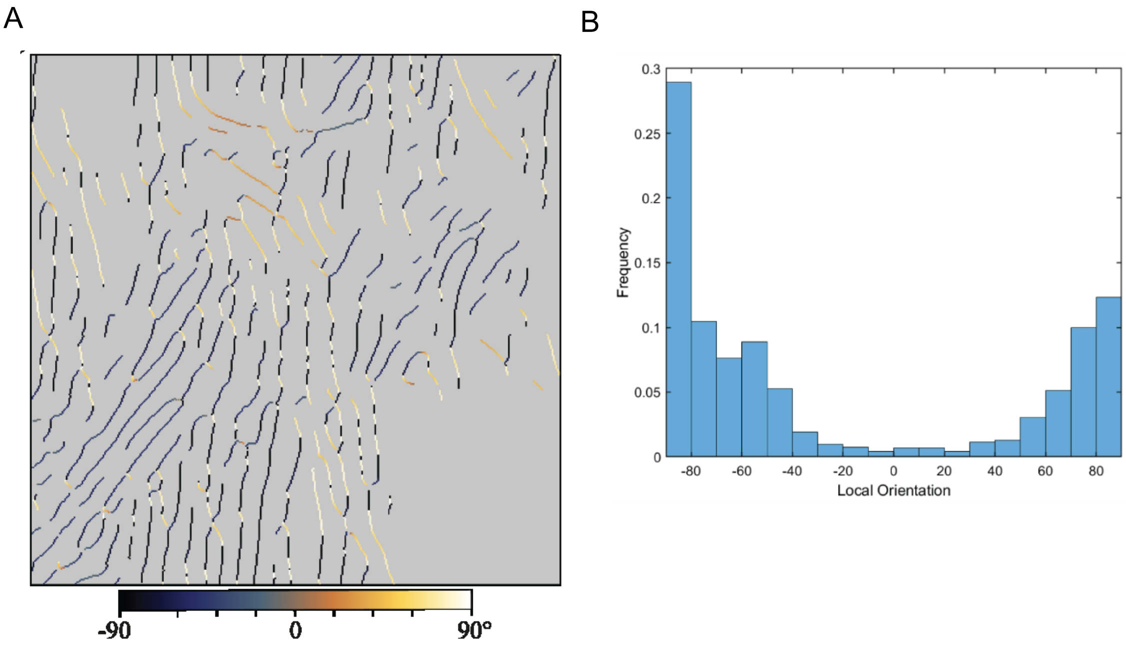

Figure 45: Local orientation distribution. In (A), the local orientation map of the fibers skeleton obtained within a box of 9x9 pixels (~1.9x1.9 µm²). The color bar indicates the orientation angle of each pixel contained in the fiber skeleton. The grey background presents no assigned orientation. In (B), the normalized histogram of the local orientation showed in (A) with a bin width of 10°.

The local alignment variance map was settled using the local orientation map. We computed the circular variance with all the θ orientations found in a window of 20x20 μm^2, with an overlap of 50%. The variance of the window was counted only when the number of local orientations θ_i was larger than 150 pixels (*Figure 46-C)*.

The degree of fibers' alignment was compared at different time-points by segmenting the Var(θ) into four different ranges of local alignment:

Var(θ) : [0, 0.25]
Var(θ) : (0.25, 0.50]
Var(θ) : (0.50, 0.75]
Var(θ) : (0.75, 1]

Lower is Var(θ), higher is the local alignment.

Circular statistics was used due to the nature of our data. Indeed, this technique is used with data on an angular scale (Berens, 2009), in contrast to linear scale (where no continuity between angles is considered). As our data range was [-90°, 90°) (and not [-180°, 180°)) we calculated the variance for 2θ (instead of θ) for correction of the space.

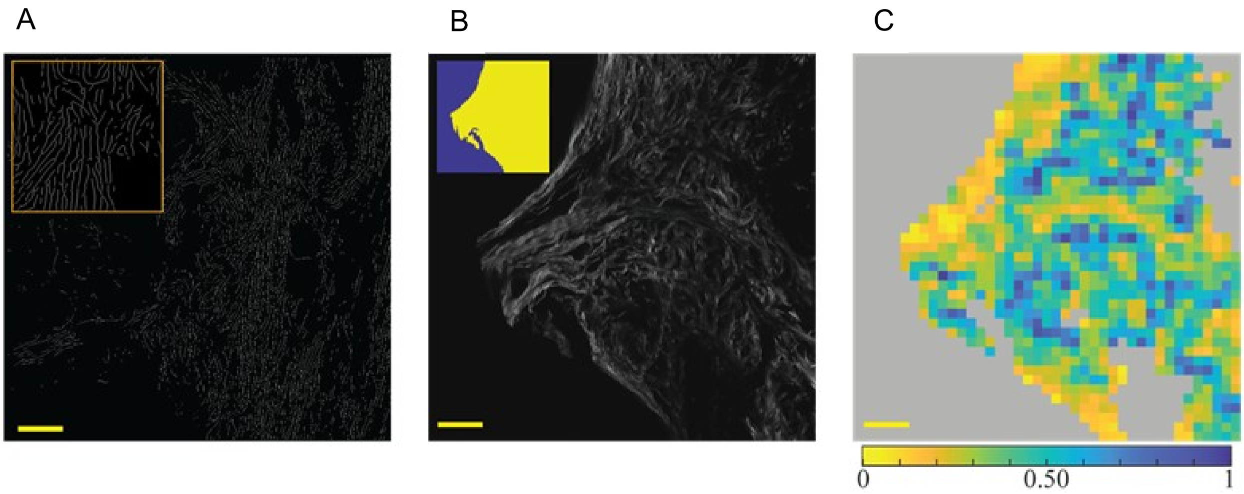

Figure 46: Fibers parameters definition. Based on the fiber skeleton map in (A), with individual fibers (zoomed area), the fibers' density was determined with the surface occupied by the tissue (inset). In (C) the local variance alignment map was generated by calculating the circular variance of the local orientation θ (0 for perfectly aligned fibers, and 1 for random/not aligned fibers). Scale bar is is 50 µm.

II.3.4. Statistical analysis

The totality of the spinal cord samples presented in Table 2 as "quantitative analyses" was considered for the statistical analysis.

1-way repeated measurements ANOVA Tukey's multiple comparisons, mixed effect model was assessed for comparison of collagen fibers metrics and Young's modulus values. Repeated measurements and the mixed effect model were necessary as the compared samples were paired and not always of the same size. Indeed, the different data obtained after varying the polarization angle (in the case of P-SHG) or varying the scanned area (in the case of AFM) were acquired on the same sample. Tukey's multiple comparisons were employed after performing normality tests for comparison of every mean with every other mean (example provided in *Figure 47*). A paired t-test with Welch's correction was used for comparing the treated group with the control one at 6wpi. 3 mice were analyzed for each condition; the number of acquisition areas is indicated in the plots. Statistical significance was set at $p \leq 0.05$.

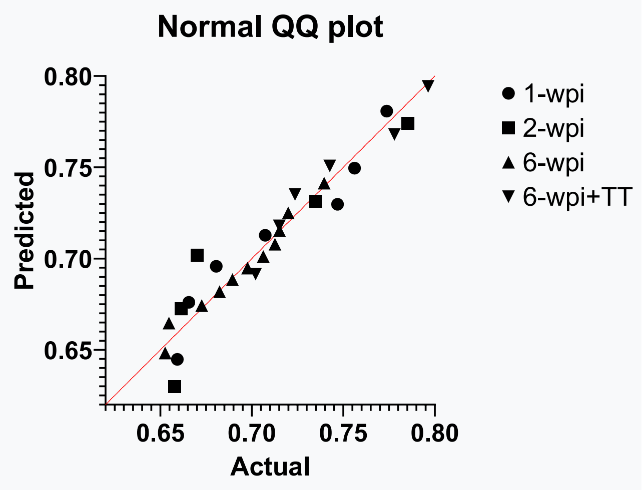

Figure 47: QQ plots for local orientation, using Shapiro-Wilk and Kolmogorov-Smirnov tests. The linearity of the points clearly suggests that the data are normally distributed. All data for collagen fiber metrics, local orientation and statistical entropy were tested for normality.

The implication of the ECM components in the formation of the glial scar and the major role of collagen in the scarring process after an injury led us to monitor with MPM the P-SHG to specifically target structural information about collagen in relation with the diseased state evolution in the fibrotic scar. The stiffness of the spinal cord has also been described as a biomarker of the injured state. AFM monitoring of the lesion could then reveal changes in the mechanical behavior of the tissue related to the fibrotic scar maturation. Overall, to address the biological problematic underlying the work, we targeted both the structural and mechanical properties of the tissue combining immunolabeling, MPM and AFM to provide a more complete description of the fibrotic scar in spinal cord injury and follow its progression in time.

CHAPTER III

-

Results and Discussion

III . Results and discussion

Imaging of spinal cord tissue has been performed with different techniques providing valuable complementary information. The fluorescence (using confocal fluorescence microscopy) and 2PEF (using MPM) signals coming from eGFP expressed in microglial are presented in green pseudo-color while IF (Alexa 594) and SHG signals coming from collagen fibers are presented in red. For the specific IF/SHG signals co-localization, IF (Alexa633) signal coming from labeled collagen I and IV is presented in green while SHG signal is presented in red.

III.1. Observations on a healthy spinal cord sample (MPM and AFM)

The bright field image of a healthy spinal cord (longitudinal section) presented in *Figure 48-A,* shows no apparent alteration of the GM and WM integrity. An example of MPM acquisition is provided in *Figure 48-B*, showing a merged image of 2PEF and SHG signals, acquired along the spinal cord width.

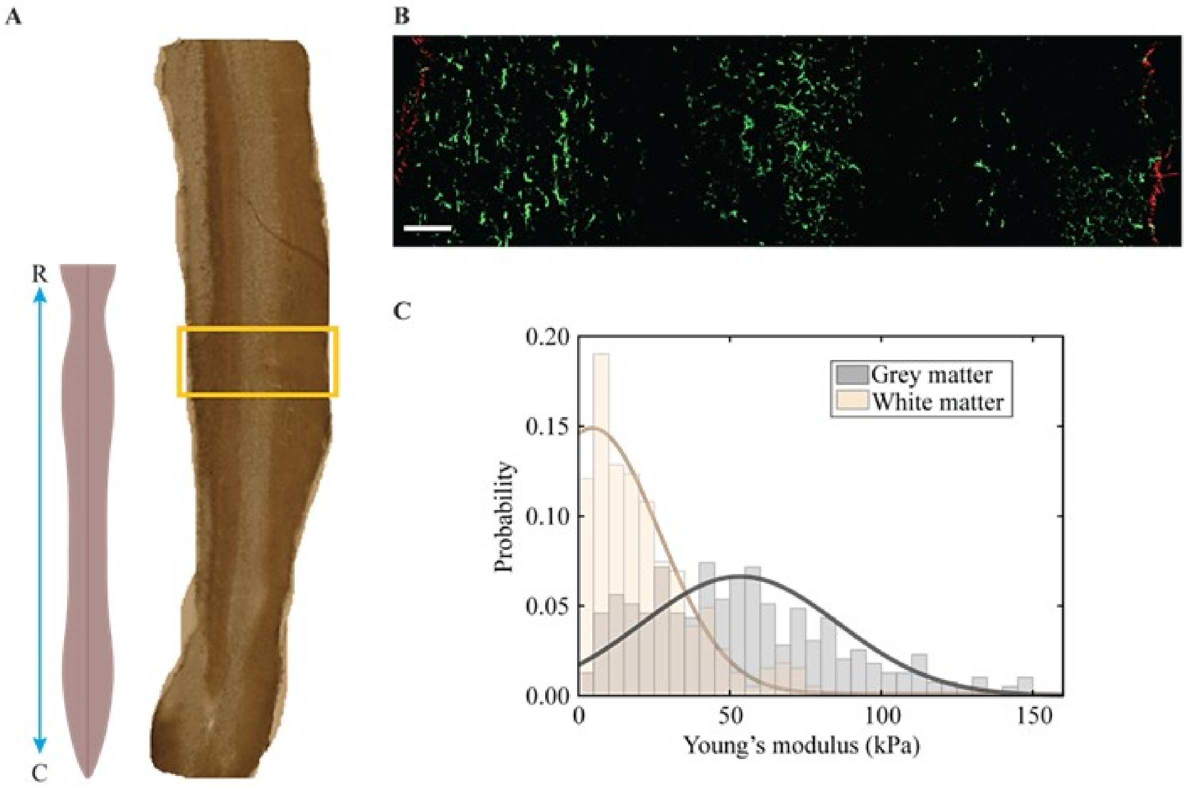

Figure 48: Structural and elastic properties of a healthy spinal cord. (A) Bright field image of a healthy spinal cord with longitudinal bands of grey matter (in the middle) and white matter showing the integrity of uninjured tissue. (B) MPM image corresponding to the yellow window merging 2PEF image (green) emitted by eGFP-microglia) and SHG image (red) emitted by collagen located only within the meninges. Scale bar is 100 µm. (C) Histograms fitted with a Gaussian distribution for GM (grey line) and WM (brown line) to obtain the mean Young's modulus value.

Microglial cells are clearly visible in their homeostatic form in all the area and no SHG signal coming from collagen is detected, except from the meninges. AFM-FS measurements provide specific histograms profiles for GM and WM (*Figure 48-C)*, with a Gaussian-like distribution. The GM appears stiffer than WM with mean E values of 54±70 µm and 10±30 µm, respectively.

III.2. Preliminary observations at 1week post injury

The first time-point we have studied for injury assessment was one week (1wpi) post-injury since the glial scar is already partly formed therefore the injured area can be clearly identified. Besides, 1wpi is considered as a key period for collagen matrix structural organization (Hermanns & Reiprich, 2001) and no collagen has been reported prior to this time-point in central nervous system in rats (Maxwell et al., 1984) or mice (Hara et al., 2017). Our first studies aimed to investigate both the axial and longitudinal sections of excised spinal cord tissue and to compare the injured and uninjured parts.

III.2.1. MPM acquisitions

III.2.1.1. Axial sections

III.2.1.1.1. Injured tissue

A bright field image of the lesion epicenter in a transversal section of a SC tissue is presented in *Figure 49*.

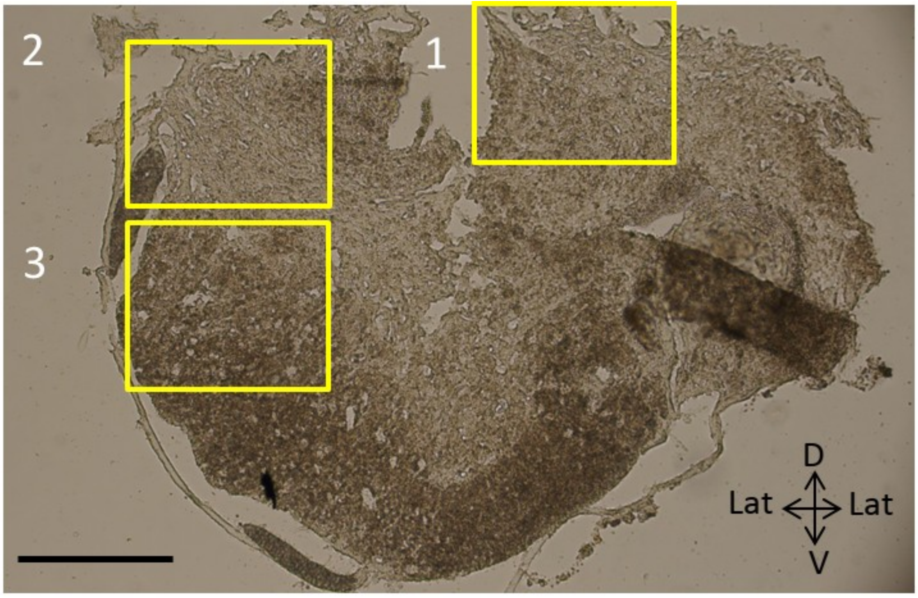

Figure 49: Bright field image at low magnification of an axial section of injured spinal cord in mice (lateral hemisection model) at 1wpi.The ipsilateral side is shown here on the right. The yellow frames, showing the MPM acquisitions areas, are located on two scarring zones in (1) and (2) as well as on the spared side (3). Grey matter (white contrast), white matter (brown contrast) are visible on (3). Scale bar is 300 µm

Consistently with a hemisection, we can observe a tissue disorganization on the ipsilateral side (no distinction between GM and WM is possible anymore) while tissue integrity is kept on the contralateral side, where spared GM and WM are identified in the center (white contrast) and surrounding (brown contrast), respectively.

MPM images were recorded on the ipsilateral side (frame 1) and in the center (frame 2) where the tissue alteration was visible, as well as on the contralateral side (frame 3). Results presented in *Figure 50* reveal first the green fluorescence emitted by eGFP- microglia cells through 2PEF.

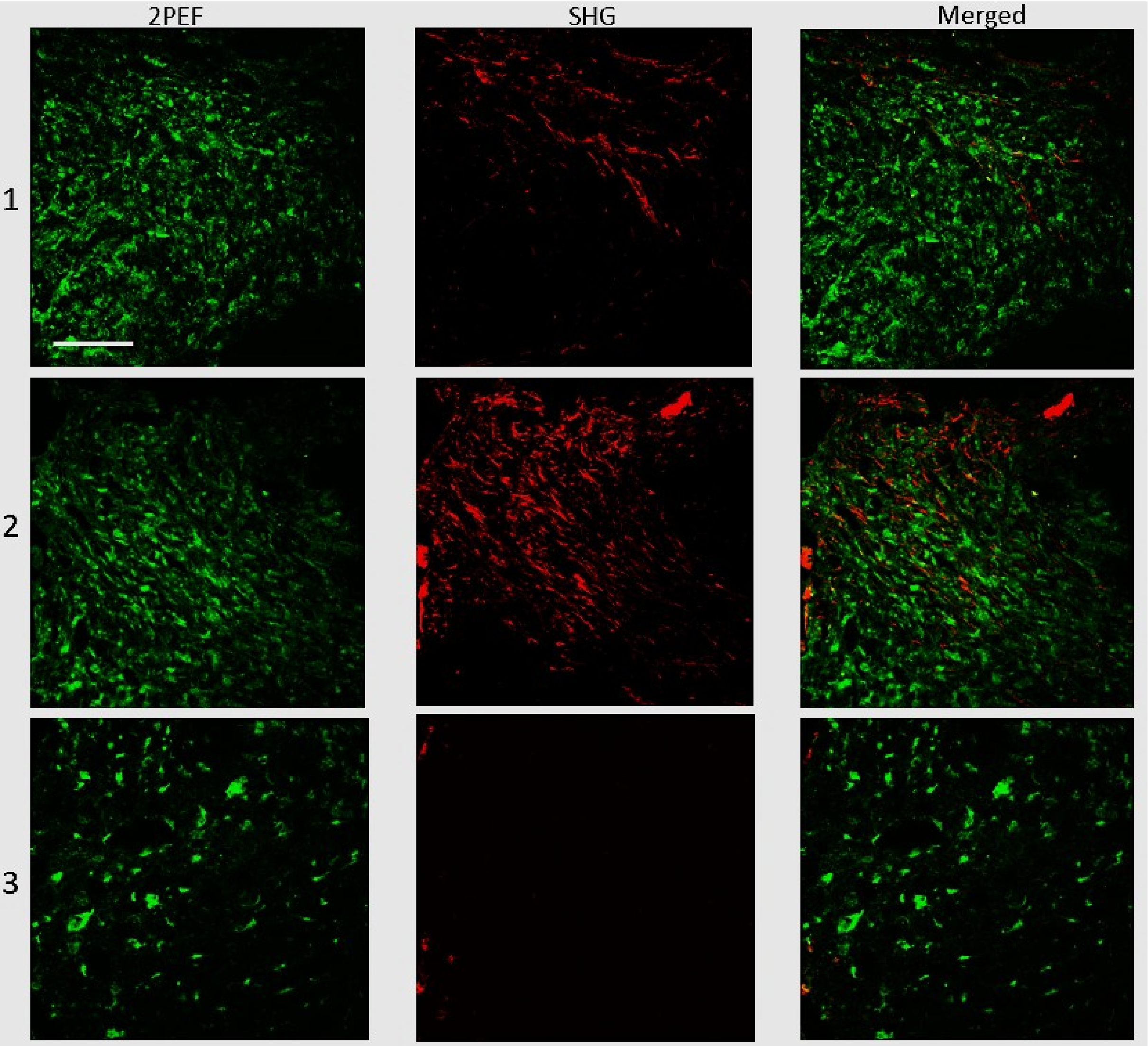

Figure 50: MPM acquisitions on axial sections of injured spinal cord at 1wpi. The images were recorded in injured (1,2) and preserved (3) areas. 2PEF signal (green) evidences the presence of activated forms of GFP microglial cells while SHG signal (red) indicated the presence of fibrillar collagen in the areas disorganized by the injury. Scale bar is 80 µm.

In the areas disorganized by the injury, a high concentration of microglial cells is visible mainly present in an activated form (i.e. amoeboid microglia with rounded shape and increased body size). In the contralateral area, the fluorescent signal is lower, this is due to the absence of microglia proliferation in the spared area. Even if few rounded and big microglia cells are still visible in this zone, we can also observe thin and elongated shapes, characteristic of homeostatic form of the cells. As previously introduced in Chapter I.1, the form and location of the microglia depend on the state of the tissue: in the case of a healthy tissue, the microglial cells are under a homeostatic form (as the ones observed in the contralateral side) while in an injured state, the cells are activated and migrate specifically to the injury site.

The second observation is that the SHG signal reveals the presence of fibrillar collagen only in areas affected by the injury and probably where a fibrotic process starts. By being specifically located in the injured zones and absent in the spared ones, fibrillar collagen could thus be a lesion biomarker. To evidence the fact that fibrillar collagen is not endogenously present in an uninjured sample, we subsequently acquired images of spared tissue.

III.2.1.1.2. Spared tissue

A bright field image of an uninjured section is presented in *Figure 51*.

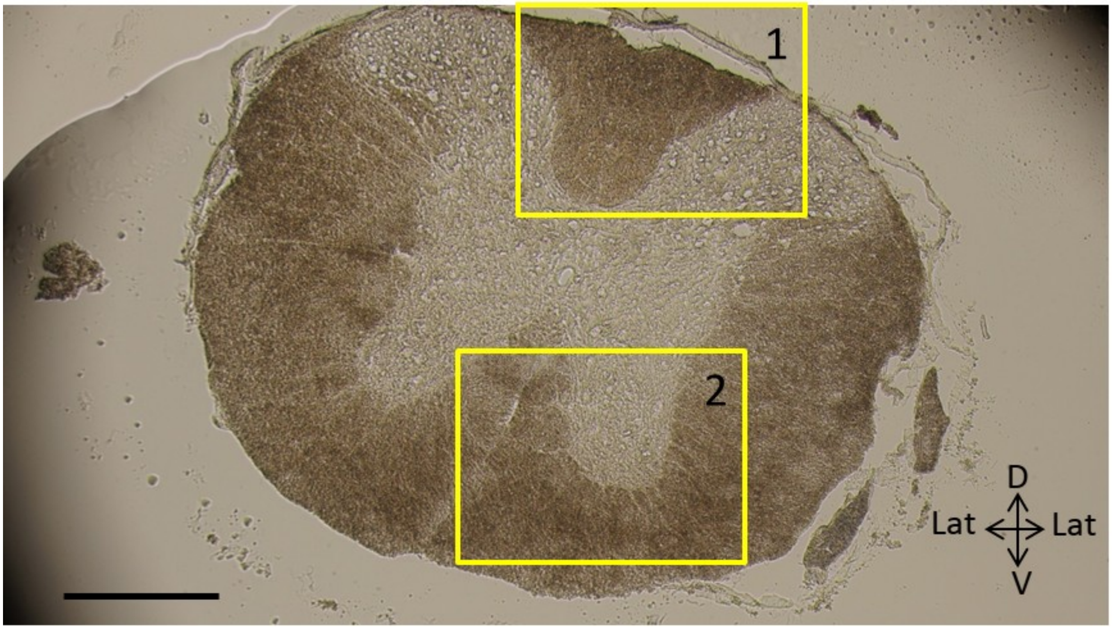

Figure 51: Bright field image at low magnification of an axial section, rostral to the lesion. Grey matter (white contrast) is located in the middle surrounded by white matter (brown contrast). The yellow frames, showing the MPM acquisitions areas, are located on the dorsal funiculus (1) and the ventral horn (2). Scale bar is 300 µm.

The uninjured samples were collected at distance from the lesion and are considered as “healthy”. Though they are not representing a proper healthy state since they do not come from a complete uninjured spinal cord, they provide information about the spinal cord state at distance from the lesion in comparison with the lesion epicenter: grey matter is clearly visible in the middle with a characteristic H or butterfly shape in axial view, surrounded by white matter. The other elements visible are the central canal in the middle of the section and the ventral medial fissure. Here, the tissue presents no disruption at any location of the spinal cord.

MPM images are presented in *Figure 52*.

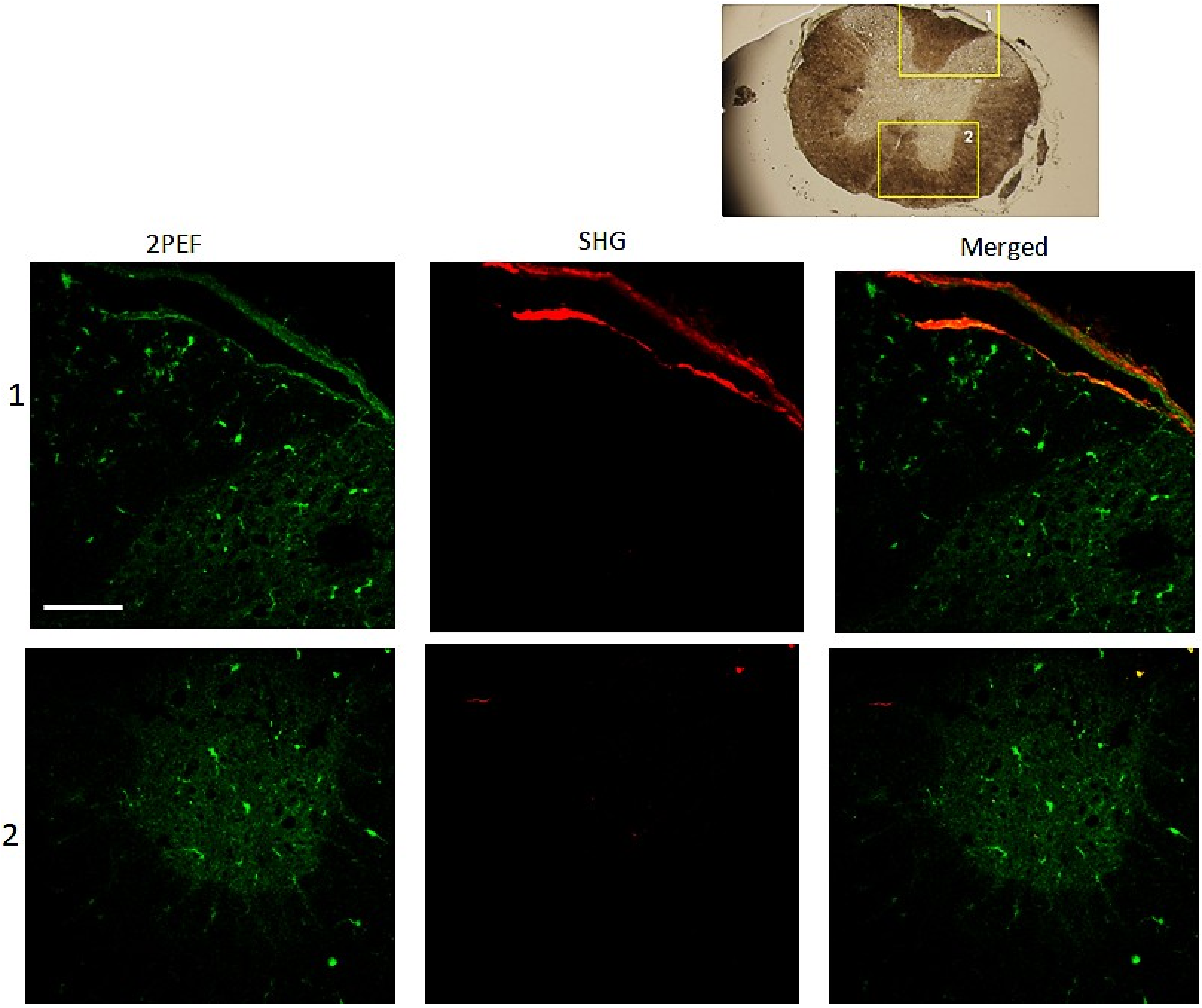

Figure 52: MPM acquisitions on axial sections of healthy spinal cord tissue. The images were recorded in the dorsal funiculus (1) and ventral horn (2) areas. 2PEF signal (green) evidences the presence of thin and elongated microglia cells while SHG signal (red) indicated the presence of fibrillar collagen in the meninges. High contrast in GM comes from tissue structure (background).Scale bar is 80 µm.

The images are dominated by the fluorescence emitted by homeostatic eGFP-microglia. The cells are thin and elongated and seem to be less aggregated than in the contralateral side of injured samples. The SHG signal is detected only in the meninges, probably emitted by the collagen contained in *dura matter*. This observation sustains that fibrillar collagen is not present elsewhere when no injury occurs.

III.2.1.1.3. Collagen extension

Further investigations carried out on sections located rostral and caudal to the lesion epicenter tend to confirm the specific presence of fibrillar collagen in injured samples. Indeed, when considering spinal cord sections collected in the rostral or in the caudal parts of the SC, SHG signal is expressed in lesioned areas and absent in spared tissue, as shown in *Figure 53*.

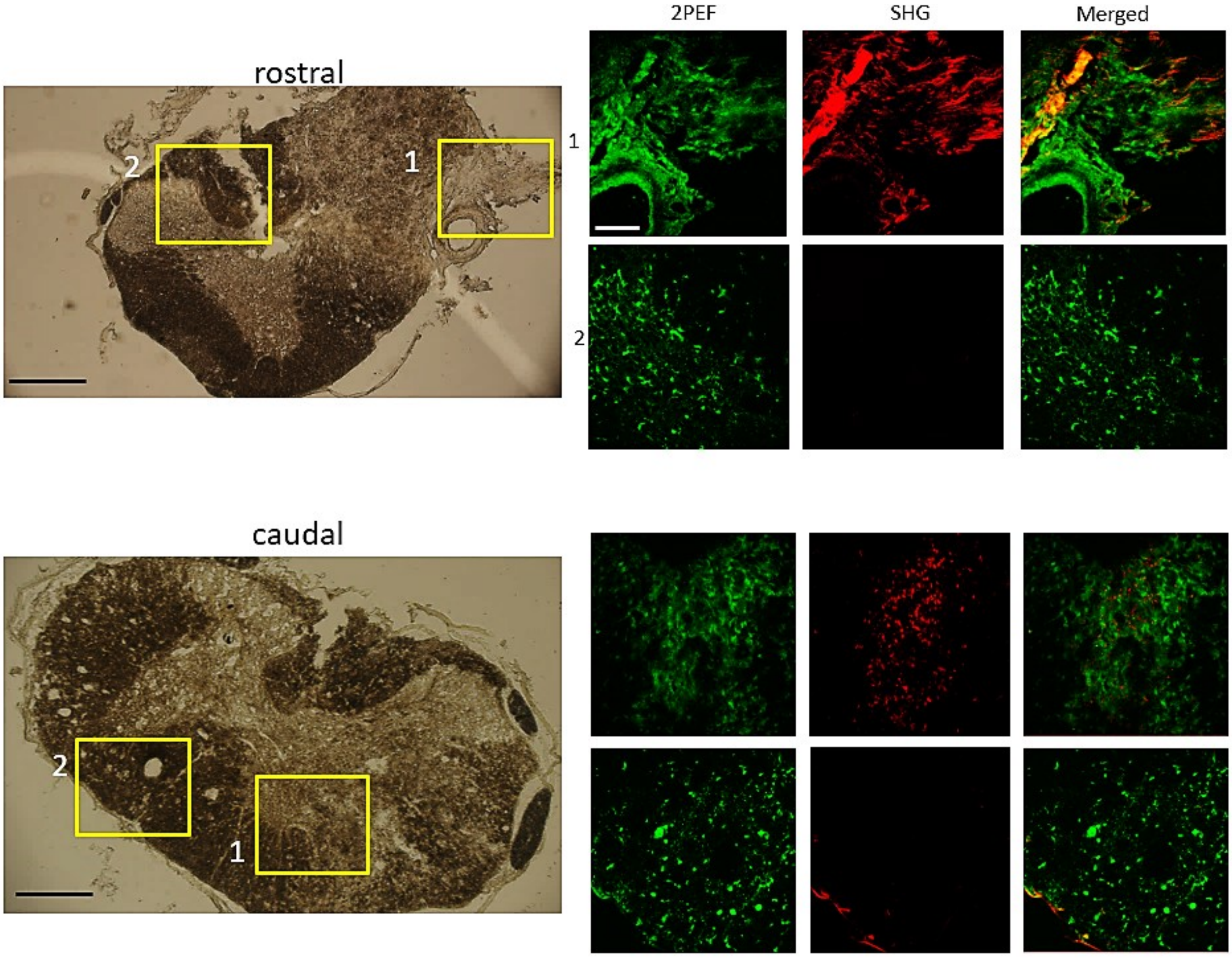

Figure 53: MPM acquisitions on axial sections at different levels. Bright field images (left) show sections collected towards rostral (up) and caudal (down) parts of the SC. The ipsilateral side is located on the right side. 2PEF signal (green) emitted by the activated microglia on the ipsilateral side and homeostatic microglia on the contralateral side. SHG signal (red) reveals the specific presence of fibrillar collagen on the ipsilateral side. Additional SHG signal is coming from collagen located in the meninges. Scale bars are 300µm for the bright field images and 80µm for the MPM data.

Collagen could also be encountered in the meninges as illustrated in the frame 2 of the caudal section imaging.

To estimate the "extension" of the collagen fibers (fibrotic process) along the rostro-caudal axis, as illustrated in *Figure 54*, we counted the number of sections where SHG signal was visible rostral and caudal to the lesion epicenter. As the distance between two consecutive sections is 630µm, we further calculated the total distance where collagen was observed. Numerical results obtained for the extension of collagen in axial sections are presented later together with extension results obtained for longitudinal sections. Note that the term "extension" used in the rest of the manuscript refers to an "area of expression" of the fibrotic process, rather than to the length of collagen fibers.

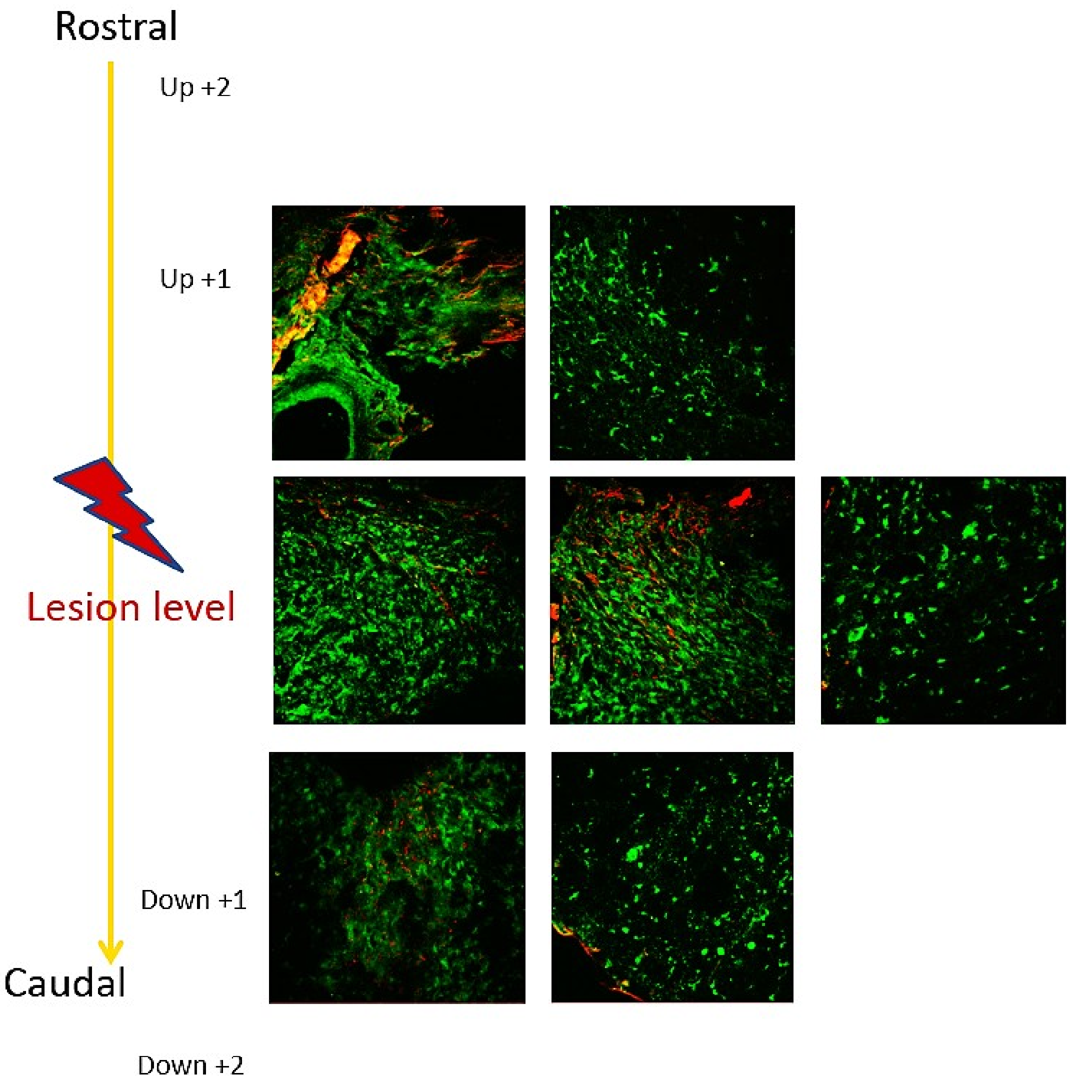

Figure 54: Estimation of fibrosis extension on axial sections of injured spinal cord at 1wpi. MPM images allow visualizing the collagen presence on the ipsilateral side through SHG signal. The extension of collagen was estimated where SHG signal was measured.

AFM measurements

AFM force spectroscopy (AFM-FS) measurements were performed on axial sections at 1wpi, including injured and uninjured spinal cord samples to address eventual modifications in the biomechanical (elasticity) behavior of the tissues.

III.2.1.1.4. Injured tissue

The Young’s modulus (E) was calculated for different spinal cord tissue areas, as shown in an example in *Figure 55* (right). These areas include: GM and WM identified in spared tissues (mainly in the contralateral side and a few in the center and the ipsilateral side) and the injured tissue identified in the ipsilateral side where no visual distinction between GM and WM was possible anymore. Histograms showing the distribution of E values reveal a matter specific profile following a Gaussian-like distribution. The maxima of these histograms indicate that the E values for GM are higher (mean of: 29.9±11.8 kPa) than for WM (mean of: 4.8±3.5 kPa), i.e. GM seems to be stiffer than WM. No apparent difference was noticed in Youngs’ modulus between GM and WM in the contralateral and ipsilateral sides. The numbers in the right image indicate the average Youngs’ moduli (in kPa) measured at different locations. An example of height maps generated for GM and WM areas, completed with the elasticity maps is shown in *Figure 55* (left).

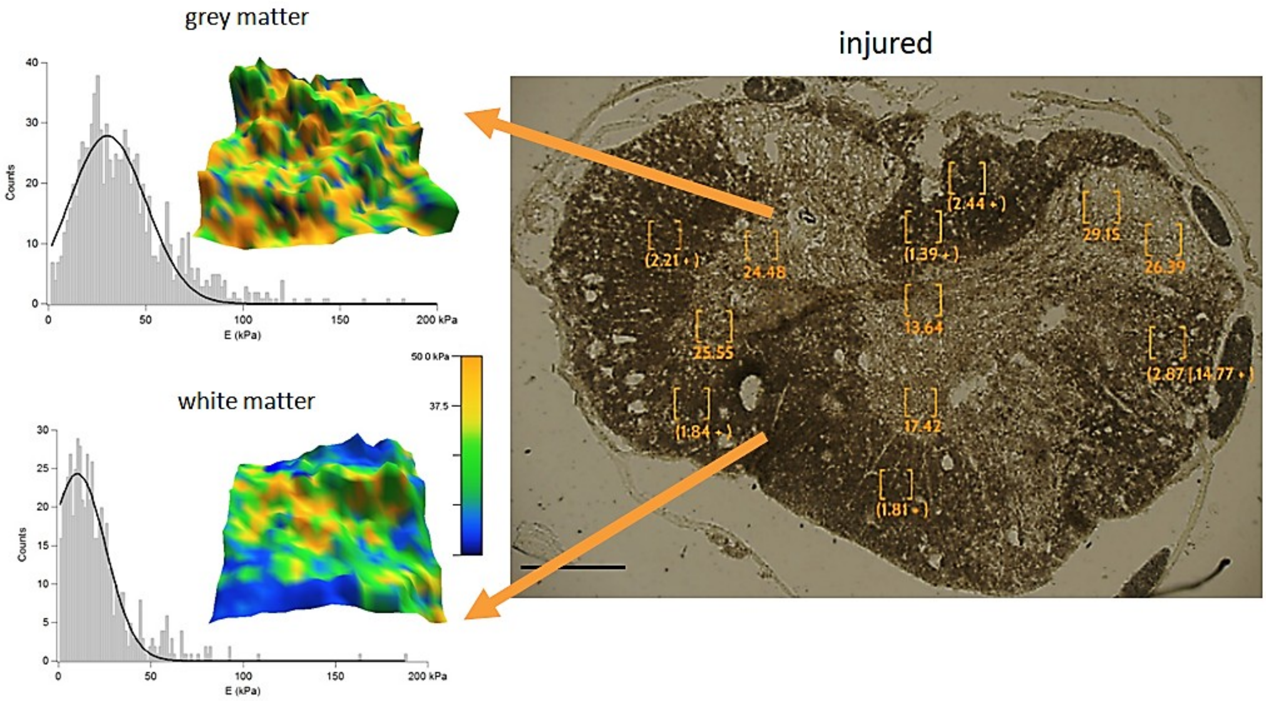

Figure 55: Elasticity assessment via AFM of an injured axial spinal cord section at 1wpi. The numbers on the bright field image indicate the area of acquisition together with the corresponding Young’s modulus (E) values (in kPa). Scale bar is 200 µm. On the left, E values distribution is shown for GM and WM, and the associated height maps with an elasticity color code (blue area: soft; yellow area: stiff).

The look-up table represents the value of E, with yellow indicating stiff zones and blue the soft ones. The mean E value obtained for the injured areas is 14.1±10.9 kPa, suggesting a lesion zone harder than the WM but softer than GM at this time point.

III.2.1.1.5. Spared tissue

An example of AFM acquisitions on an uninjured section (collected rostral to the epicenter) is presented in *Figure 56* and leads to the same observations as previously described: GM matter appears stiffer than WM with a better contrast depicted in the height maps, and histogram profiles specific to the area measured. Mean E values are 41.7±9.7 kPa and 4.4±4.0 kPa for GM and WM, respectively.

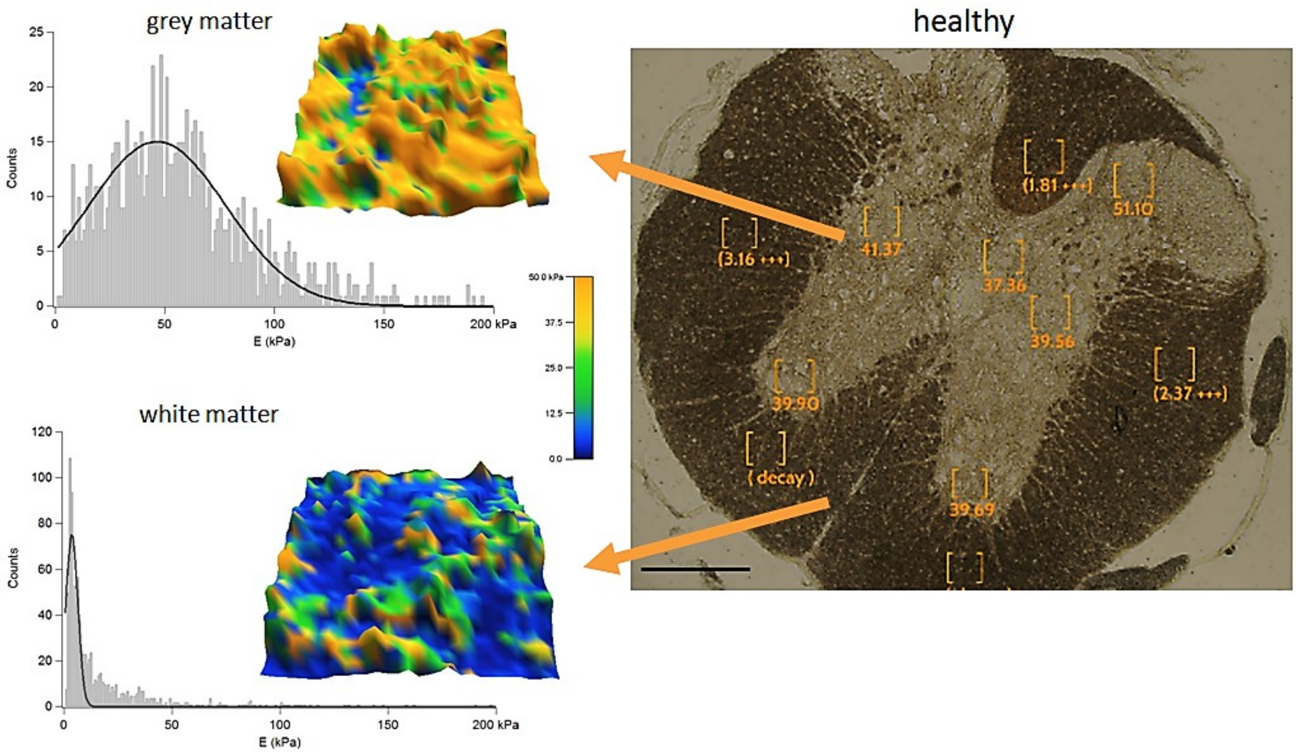

Figure 56: Elasticity assessment via AFM of axial sections of uninjured spinal cord tissues. The orange numbers indicate the area of acquisition together with the corresponding Young's modulus (E) value. On the left, an example of the E values distribution for grey matter and white. Scale bar is 200 µm.

When comparing the Young's modulus of GM and WM between spared areas (at distance from the lesion) and around the injury site, we overall observed that GM within spared tissue was higher than GM surrounding the injury (*Figure 57*). However, statistical analyses were not performed at this point to confirm this tendency of softening for GM areas close to the lesion. No evident tendency was observed for WM.

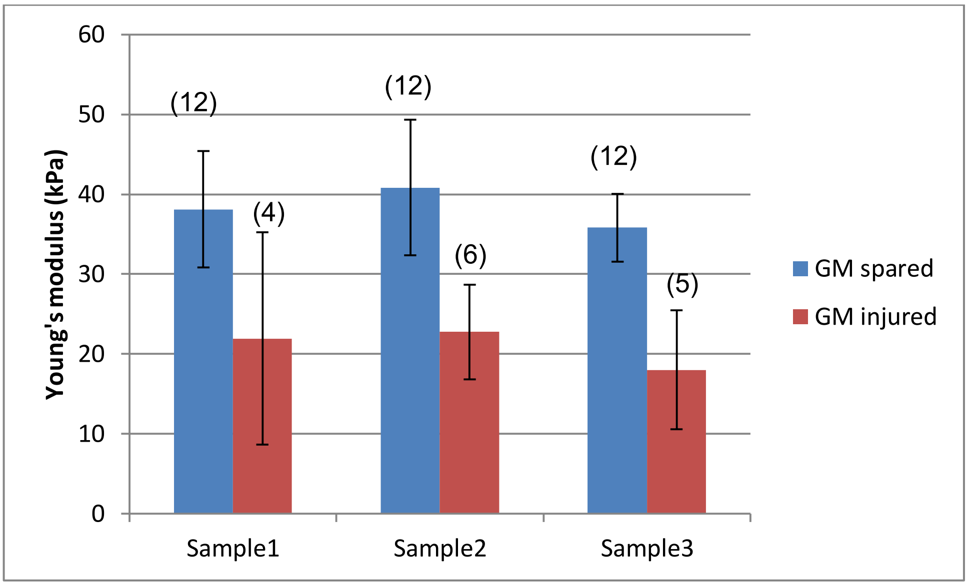

Figure 57: Young's modulus (kPa) of grey matter in spared and injured spinal cord tissue. N is indicated into brackets.

III.2.1.1.6. Area stiffness comparison

A comparison between the stiffness obtained in GM, WM and injury areas was further performed. For this analysis, we considered all the data of GM and WM acquired near and far away from the lesion. Results presented in *Figure 58* confirm the observations of GM being stiffer than WM with mean E values of 38.61±9.7 kPa (normalized: 0.56) and 4.4±4.0 kPa (normalized: 0.05), respectively. The injury (14.1±10.9 kPa; normalized: 0.20) is significantly softer than GM and harder than WM.

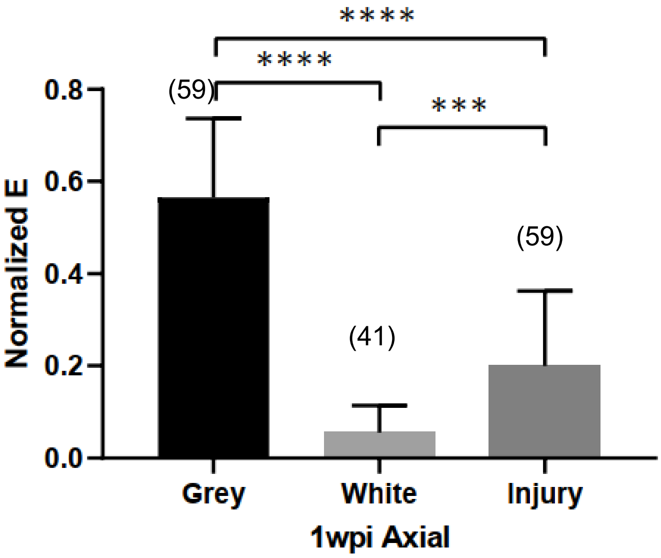

*Figure 58: Areas stiffness comparison in axial spinal cord sections at 1wpi. 1-way ANOVA for repeated measurements with a mixed effect analysis was performed. N is indicated into brackets. ****, p < 0.0001 and ***, p<0.005.*

Investigations on axial sections provided qualitative information on tissue structure in injured and spared zones and quantitative information on elastic properties of different tissue areas at 1wpi. Further we decided to work on longitudinal sections, first to evaluate the fibrosis extension from the SHG signal along the rostro-caudal axis, and secondly, longitudinal sections helped to delimitate injured tissue from spared GM and WM for AFM measurements. The identification of both injured and spared parts on the same sample subsequently eased to investigate fibrosis extension and to potentially correlate the fibrotic scar with mechanical properties changes along the spinal cord.

III.2.2. Longitudinal sections

III.2.2.1. MPM acquisitions

A bright field image of an entire longitudinal section at 1wpi is presented in *Figure 59-A.* Both GM (white contrast) and WM (brown contrast) are visible on the contralateral side, showing no alteration of tissue integrity, while tissue disorganization is observed on the ipsilateral side.

MPM acquisitions of the whole spinal cord width (yellow square in *Figure 59-A*) evidence the tissue structure in 2PEF (*Figure 59-B*) with activated eGFP-microglia on the ipsilateral side (white square on the right in *Figure 59-D,* zoomed aside down) and more elongated homeostatic cells in the contralateral side (white square on the left in *Figure 59-D,* zoomed aside up).

The SHG signal (*Figure 59-C*) specifically reveals fibrillary collagen on the ipsilateral side distinct from the tissue structure as shown in the merged picture (*Figure 59-D*). The clear location of collagen formation at the injury side and its absence in the spared tissue confirms that fibrillar collagen could be a relevant indicator of the fibrotic process occurring in the scar formation.

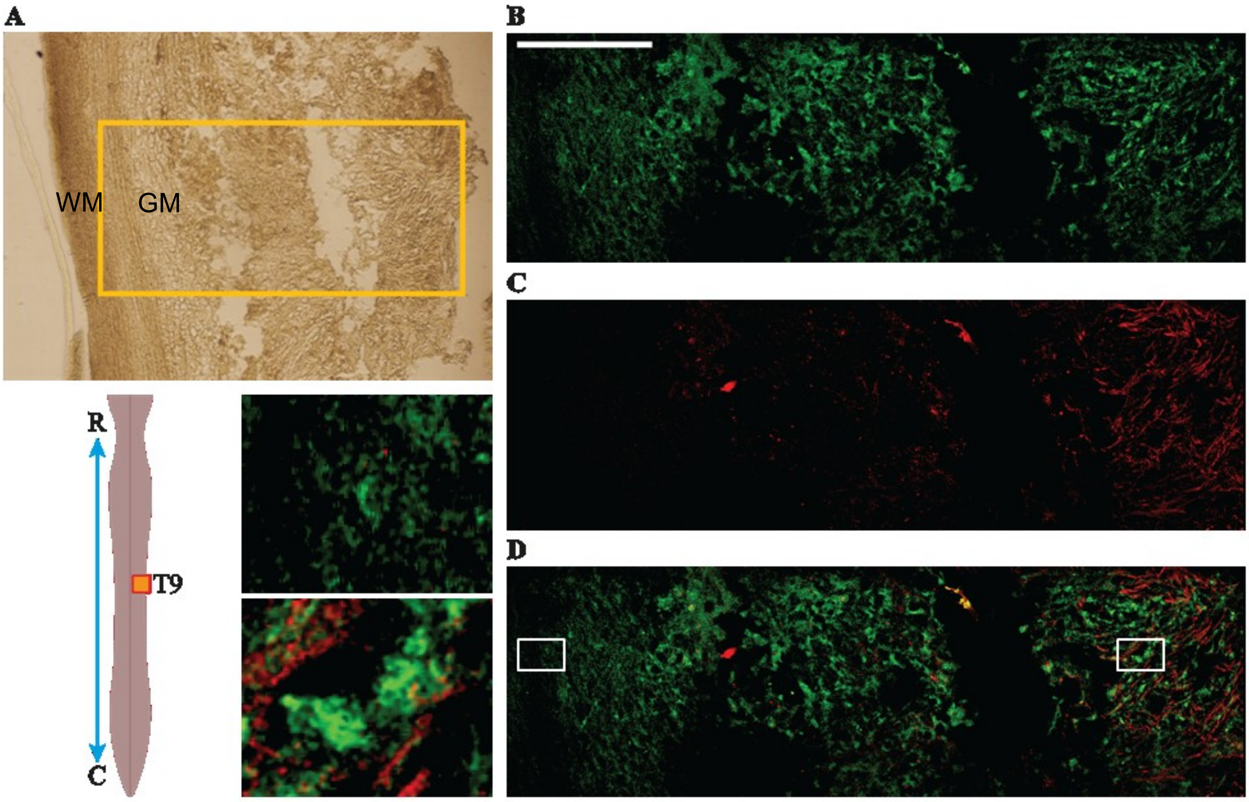

Figure 59: MPM acquisition on longitudinal sections of injured spinal cord at 1wpi. In (A) a bright field image of the entire spinal cord with the injury level located in the yellow square and zoomed aside. The ipsilateral side is presented on the right. MPM acquisition areas (yellow square: 1600x800 µm^2) show the 2PEF signal (B) emitted by fluorescent microglia and the SHG signal (C) emitted by fibrillary collagen and specifically located on the injury side. A merged picture (D) depicts both spinal cord tissue and collagen presence. White squares are zoomed on the left and present microglia cells on the spared (up) and ipsilateral side. Scale bar is 400 µm.

The stitching of MPM acquisitions performed in the rostro-caudal axis based on SHG signal detection allowed the reconstruction of the entire area where collagen was visible. We could thus estimate the fibrosis extension along the rostro-caudal axis, as illustrated in *Figure 60*. The reconstruction accuracy can be assessed by comparing the 2PEF image (green) with the bright field image on the left. In this example, even if some zones are not perfectly aligned or display different signal intensity (white arrows), the whole resulting image is sufficient to determine the extension of the SHG signal (red).

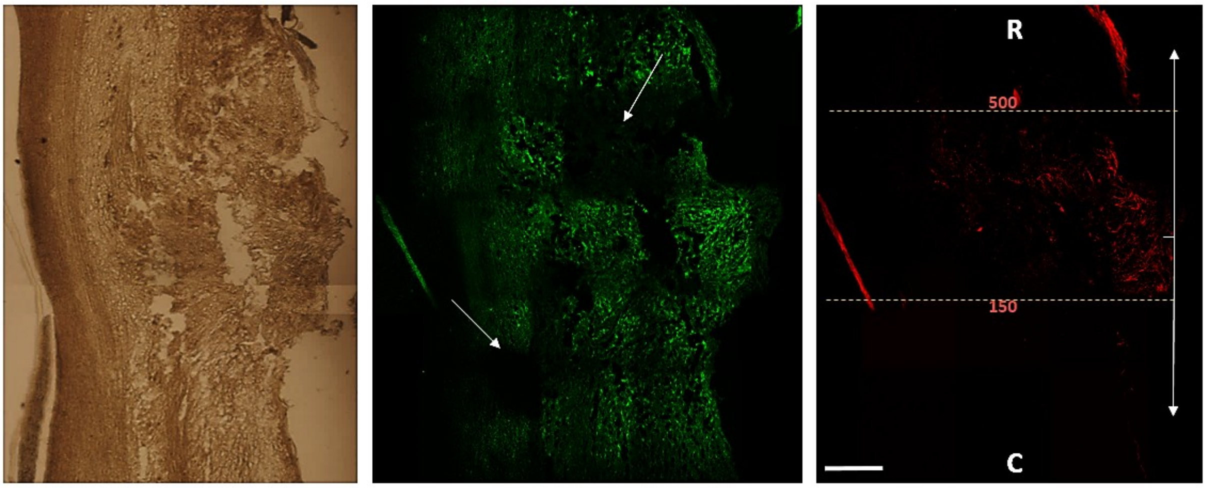

Figure 60: Collagen extension in longitudinal spinal cord sections. MPM images were stitched based on the bright field image of the sample (left) and the result can be visualized with 2PEF signal (green). SHG signal (red) extension can thus be measured starting from the injury epicenter and rostral (R) and caudal (C) to it. Scale bar is 200 µm.

In this example, the collagen extension is 500 µm and 150 µm rostral and caudal to the lesion epicenter, respectively with a total extension of 650 µm. Additionally, SHG extension covers almost half of the spinal cord width, in line with our hemisection model. A summary of the collagen extension results obtained for both longitudinal and axial sections is presented in Table 4. A maximal extension of 1500 µm has been found in longitudinal sections compared to 1890 µm in axial sections. One can note that the results from axial sections may provide higher extension estimation, due to the sections' thickness. Besides, the collagen extension is a direct measurement on the longitudinal sections contrary to quantification on axial sections that is an estimation of the spread collagen.

Table 4: Collagen extension (µm) measured in longitudinal sections (up) and estimated in axial sections (down)

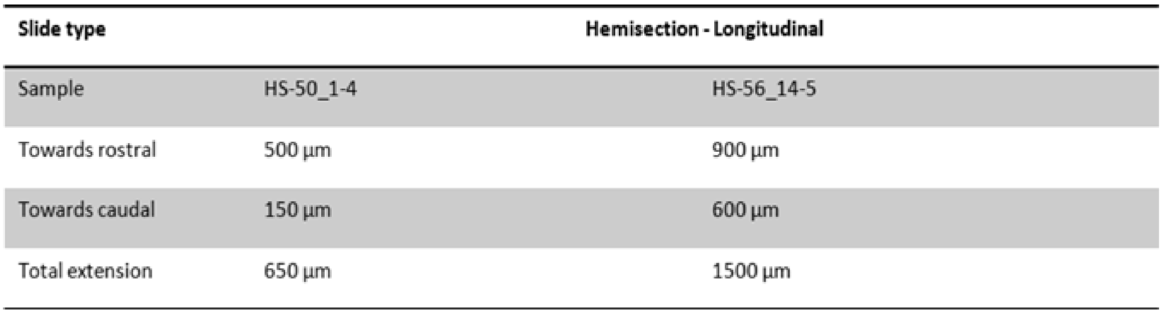

Slide type	**Hemisection - Longitudinal**	
Sample	HS-50_1-4	HS-56_14-5
Towards rostral	500 µm	900 µm
Towards caudal	150 µm	600 µm
Total extension	650 µm	1500 µm

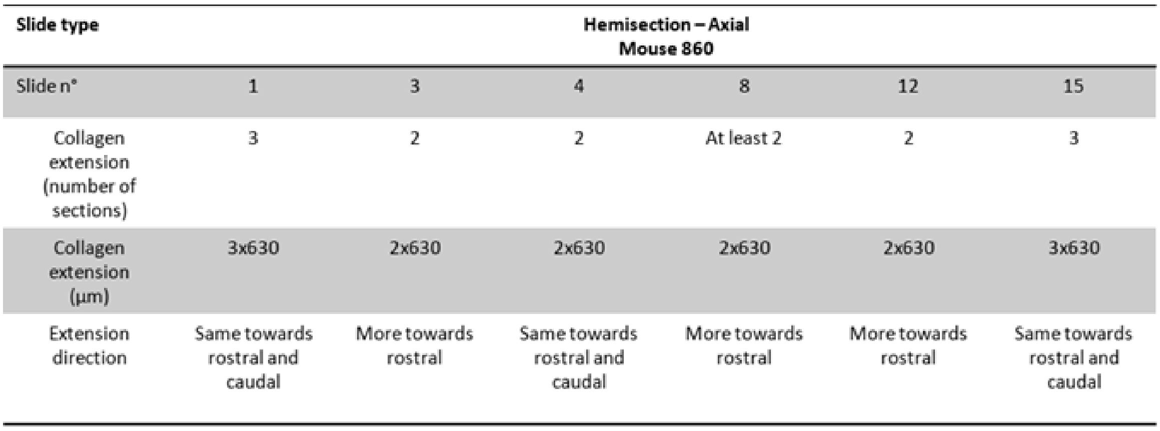

Slide type	**Hemisection – Axial Mouse 860**					
Slide n°	1	3	4	8	12	15
Collagen extension (number of sections)	3	2	2	At least 2	2	3
Collagen extension (µm)	3x630	2x630	2x630	2x630	2x630	3x630
Extension direction	Same towards rostral and caudal	More towards rostral	Same towards rostral and caudal	More towards rostral	More towards rostral	Same towards rostral and caudal

III.2.2.2. AFM measurements

AFM-FS acquisitions were carried in longitudinal sections at the injury level and on uninjured parts rostral and caudal to the injury epicenter, as presented in *Figure 61*. In this example, the ipsilateral side is presented on the left. We can first observe that E values (indicated on the locations where they were measured) for GM, in the center, are higher than the ones for WM. Besides, E values seem to increase with the distance from the lesion until reaching a stable value for the uninjured parts. Likely to the observations on axial sections, GM softens in areas close to the lesion. E values obtained for the injured area are comprised between the ones of GM and WM. Mean E values for two mice at 1wpi are: 21.0±6.03 kPa for GM, 5.8±5.01 kPa for WM and 11.4±6.33 kPa for the injury.

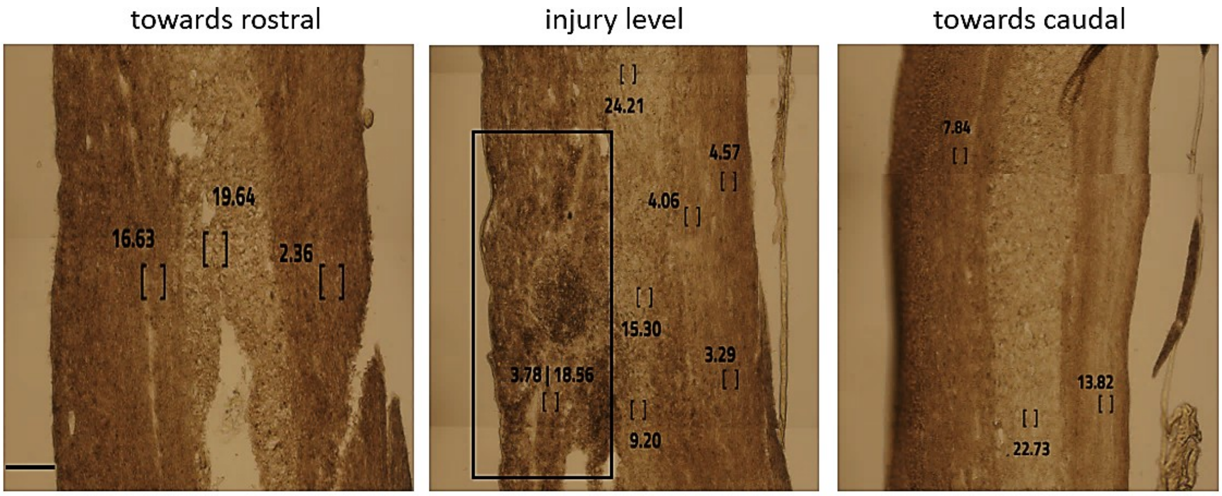

Figure 61: Elasticity assessments via AFM-FS in longitudinal spinal cord sections and at different levels (rostral, injury and caudal). The injury area is delimitated by the black square. Numbers indicate the measured Young's modulus values on the respective areas of acquisition. Scale bar is 250 µm.

III.2.3. Discussion: first highlights on the spinal cord tissue at 1 week post-injury and parameters to investigate

Our preliminary studies at 1wpi led to the following achievements: i) the imaging of both axial and longitudinal sections of injured and spared spinal cord tissue, showed a distinct SHG signal emitted by fibrillar collagen (distinct from 2PEF signal coming from homeostatic microglia in spared tissue and amoeboid microglia which migrates to the injury site) specifically located on the ipsilateral side (in injured tissues). ii) The extension of fibrosis (fibrillar collagen formation) was estimated in axial sections and measured in longitudinal sections; values obtained in the late case were between 650 and 1500 µm. iii) AFM-FS measurements revealed that GM was stiffer than WM in both uninjured and injured tissues. Injured tissue had an intermediate elasticity compared to GM and WM at 1wpi as: GM>injury>WM. GM showed a tendency of softening close to the injury level.

Though fibrillar collagen expression in the spinal cord has been poorly investigated with SHG, some studies describing healthy or spared tissues in mice (Cheng et al., 2019) or rats (Liao et al., 2019) have reported similar observations to ours, with SHG signal mainly originated from the meninges. SHG signal has been also reported from nerve fibers in rat tissues (Liao et al., 2016, 2019). In injured tissues, Huang and colleagues' (Huang et al., 2011) reported that collagen was not initially present in normal spinal cord samples (except in the meninges) but was expressed after the injury in a full transection model in rats. Also, Galli and colleagues' observations (Galli et al., 2018) on axial and longitudinal samples after hemisection in mice revealed collagen expression strictly ipsilateral to the lesion side of the spinal cord during the chronic phase, and not at 1wpi. Collagen type was not identified in previous works. Huang and colleagues attributed the SHG signal to collagen type IV, however this type of collagen does not have a non-centro-symmetric structure needed to produce SHG. Studies quantifying collagen fibers are also scarce. Galli and colleagues (Galli et al., 2018) observed SHG signal on the whole tissue area at chronic stage after SCI, but analysis was not done at earlier post-injury time-points. Routine quantifications of the lesion area are usually addressing the glial scar and are carried out by staining axial sections. The lesion extension (in mm) is estimated by counting the number of sections where injured tissue is identified. The lesion area (in %) and the lesion volume are estimated as described in Noristani et al., 2018 and (Gerber et al., 2018a)In our case, the SHG signal specific of fibrous collagen allowed to estimate the collagen expression along the rostro-caudal axis.

Controversial results for the elastic properties of the spinal cord were reported in the literature. This depends mostly on the type of sample and injury model used. However, the most encountered result is that GM is stiffer than WM (Baumann et al., 2020; Koser et al., 2015; Moeendarbary et al., 2017). In Moeendarbary and collegues's study performed on rats fresh spinal cord tissues after crush injury, the authors defined GM and WM area in 2 categories: close to the lesion (inside) or far away from the lesion (outside). No measurements were done in the injured area. Results indicated that GM is about twice as stiff than WM with median values of about 420 Pa and 117 Pa respectively. A significant softening was reported inside the lesion compared to areas outside the lesion at 1.5wpi. A global tissue softening of injured samples compared to spared ones was also reported.

Our work on axial and longitudinal sections at 1wpi provided similar observations on fibrillar collagen specific expression ipsilateral to the injury site. However, the longitudinal view was chosen for quantitative assessments since direct measurement of metrics like fibrosis extension was not possible in axial sections. As collagen appeared as a potential biomarker of the fibrotic scarring, a deeper characterization at different time-points post-injury (i.e identification of collagen type, evolution of collagen fibers formation, supramolecular and structural assessments of collagen fibers) was further performed to address the evolution of the fibrotic process after injury in mice. Elastic properties of the injury compared to spared GM and WM areas indicated important modifications at 1wpi that needed to be further assessed at other time-points.

III.3. Time-course acquisitions and treatment investigations

The evolution of collagen expression over time and in a group treated with GW2580 was monitored with both immunohistochemistry staining and SHG imaging. These experiments aimed to identify the collagen type expression after injury and to verify the specificity of the SHG method. Along with fibrillar collagen type I, collagen IV expression was also reported in the fibrotic part of the scar, though misattributed to SHG signal, as previously discussed. Therefore, in our study both types, collagen type I and collagen type IV were investigated together.

III.3.1. Labelling

III.3.1.1. Peroxidase immunostaining

Peroxidase immunostaining was performed to detect the expression of collagen types I and IV in the spinal cord after injury at different time points and following treatment at 6wpi. *Figure 62* shows the images obtained from this staining using NanoZoomer.

The expression of both collagen types I and IV is visible on the ipsilateral side from 24-hpi to 12wpi with an overall increasing up to 2wpi that most likely stabilizes after 4wpi. Fibrotic processes are clearly seen and the expression of collagens appears to become restricted over time to the lesion area and tends to decrease following transient pharmacological depletion of microglia proliferation in the treated group 6wpi + TT (decreasing tendency was observed in all 3 mice treated). These results confirm that collagen I and IV are both part of the fibrotic scar that develops after SCI.

III.3.1.2. Immunofluorescence (IF)

After evidencing collagen I and IV by immunoperoxidase staining, collagen expression using immunofluorescence (IF) was carried out to be confronted to the SHG signal. To test the specificity of our labeling, preliminary IF observations were performed using Alexa 594 secondary antibody labeling on axial and longitudinal sections at 1wpi. Collagen type IV was identified at this time-point as filaments distinct from the eGFP signal expressed by microglia, while collagen I detection required a retrieval phase to ease the antibody access to the target (see appendix for more details). IF observations using Alexa 594 were also performed on longitudinal sections at 6wpi.

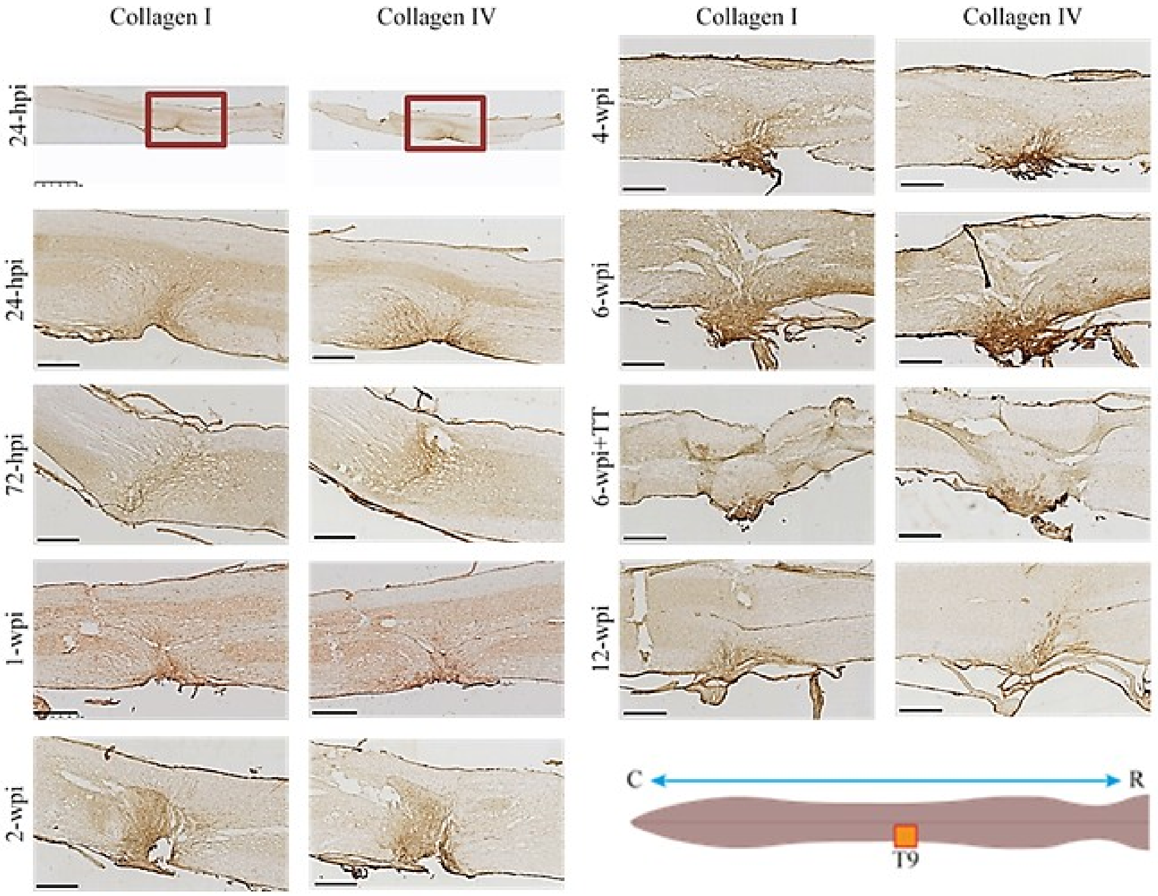

Figure 62: Collagen types I and IV at the injury site revealed by peroxidase. Optical images (NanoZoomer) of longitudinal spinal cord sections after hemisection at the thoracic 9 (T9) level (brown square: size 1.2x1.2 mm^2) are presented. Longitudinal sections were revealed by peroxidase to evidence collagen types I and IV. Spinal cord sections are presented at different time-points post-injury (24-hpi, 72-hpi, 1wpi, 2wpi, 4wpi, 6wpi and 12wpi) and with a treatment condition at 6wpi. Scale bar is 500 µm for all zoomed collagen I and IV images. IHC reveals a higher contrast at the injury site for both collagens I and IV.

A typical immunofluorescence image (confocal fluorescence microscopy) at 6wpi is illustrated in *Figure 63*, where collagen I signal (Alexa 594) is specifically emitted by fibrillar structures that do not co-localize with microglia (eGFP signal).

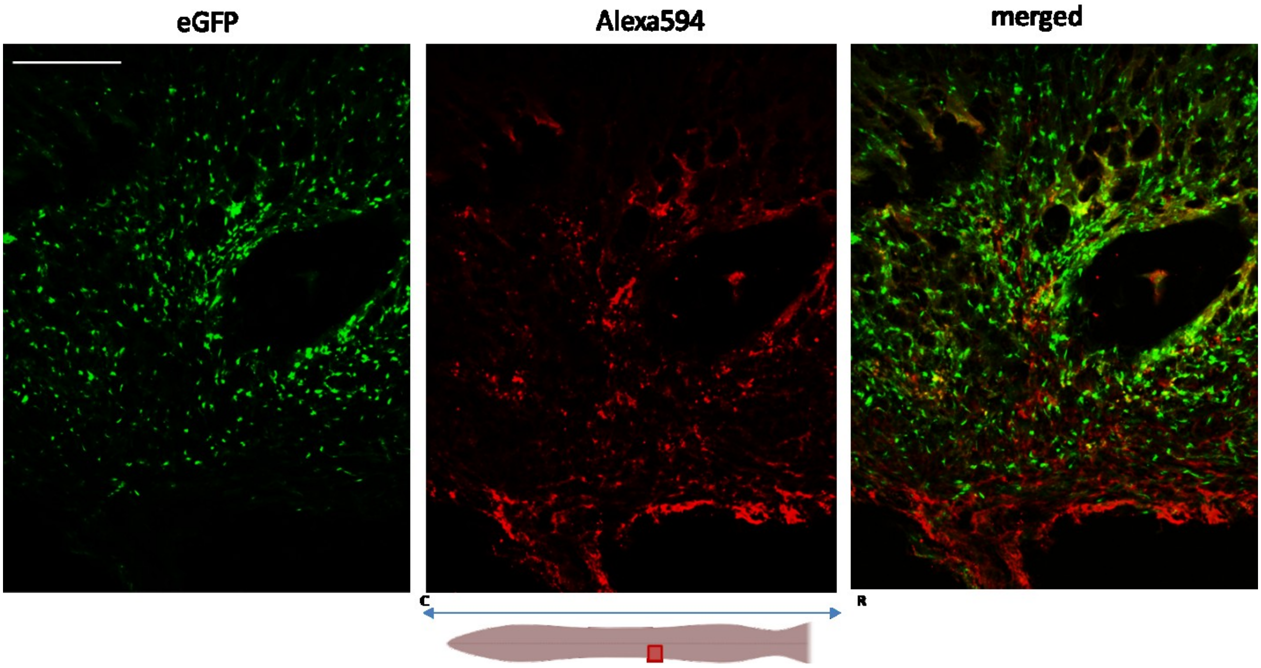

Figure 63: Immunolabeling of collagen type I in longitudinal spinal cord sections at 6wpi in mice. Collagen type I is revealed through the Alexa 594 signal (in red) as filaments specifically located on the injured side and distinct from the eGFP signal (in green) emitted by microglia. Scale bar is 160 µm.

The co-localization experiments between Alexa 633 (shown **in green** in *Figure 64*) and SHG signal (in red) at 72-hpi, 1wpi and 6wpi post-injury are presented in *Figure 64-A*). At 72-hpi, no SHG nor Alexa 633 signal is detected from any collagen type. Conversely, the immunoperoxidase staining showed a brown contrast at this time-point (*Figure 62*). At 1wpi and 6wpi, both collagen I and IV are evidenced but not clear co-localization with SHG is observed. Collagen IV is not expected to co-localize with SHG because of its centro-symmetry. The absence of co-localization is noticeable at 1wpi (white square on the right image, down) where SHG signal is visible in a large area without trace of Alexa 633.

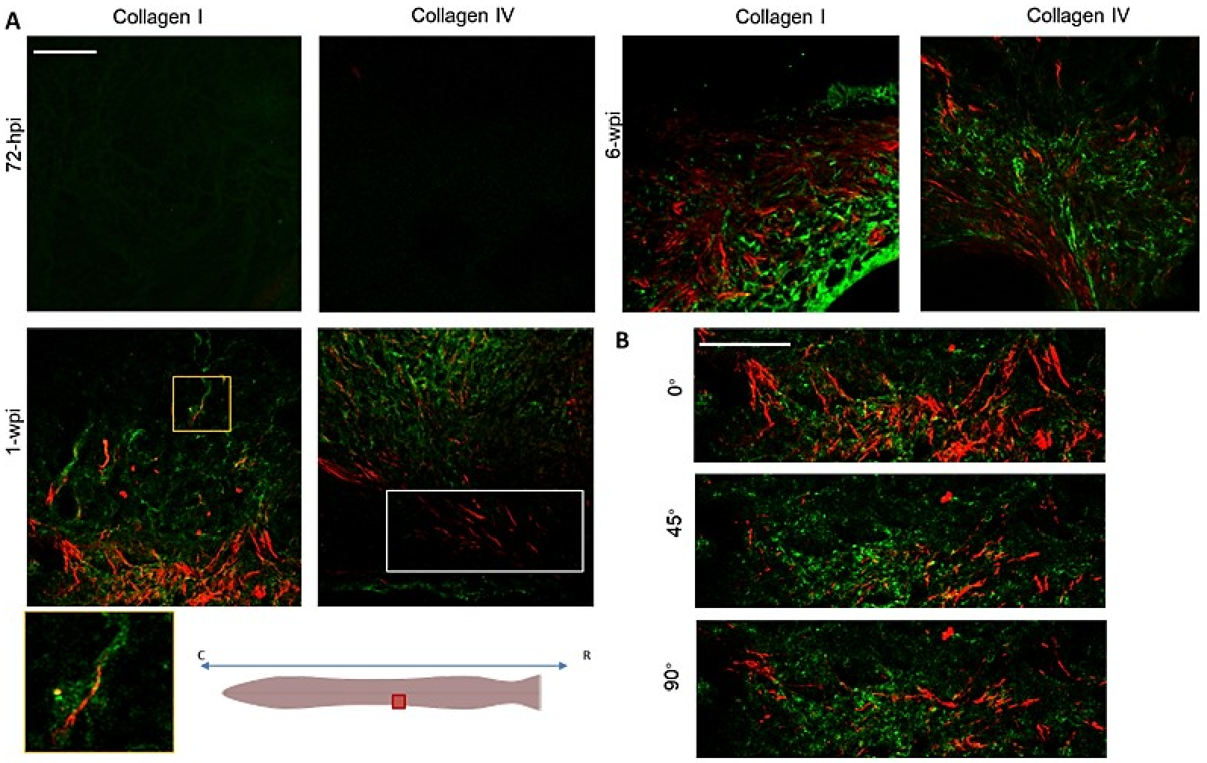

Figure 64: Immunofluorescence and SHG signal of collagen type I and IV. In (A), the Alexa 633 signal emitted by both collagens I and IV (in green) are presented together with SHG signal by fibrillar collagen (in red) at 72-hpi, 1wpi and 6wpi post-injury. A co-localization area (yellow signal) is zoomed at 1wpi (yellow square: 110x110 µm) for collagen I. No co-localization area is evidenced (white square) for collagen IV. In (B), varying polarization angles of the incident light (0°, 45 and 90°) at 1wpi confront fibers with various orientations co-detected in SHG and using immunofluorescence. Scale bar is 112 µm.

The IF signal emitted by collagen I is more superposed onto the SHG signal as compared to collagen IV and some co-localization areas are detected (as the zoomed fiber in *Figure 64-A*). By modifying the polarization angle of the incident light, it is possible to highlight fibers via their SHG signal (*Figure 64-B)* evidencing a change in fibers orientation that sometimes follows the IF signal. However, complete co-localization is never visible at the whole image-level.

In conclusion, collagen I and IV expression evolves over time after injury. Further observations of SHG signal were conducted to investigate this evolution through expression of fibrillar collagen along the rostro-caudal axis at different time-points post-injury and following treatment at 6wpi.

III.3.2. SHG acquisitions

The co-localization of IF and SHG images indicated that no collagen (type I or IV) was found prior to 1wpi. Additional SHG acquisitions performed at later time-points evidenced an increased fibrillar collagen expression over time (*Figure 65*). Contrariwise, the SHG signal seems to be decreased in the treated group (6wpi + TT) compared to the control group (6wpi). This may suggest lower collagen expression following transient depletion of microglia, consistently with the prior immunoperoxidase staining observations.

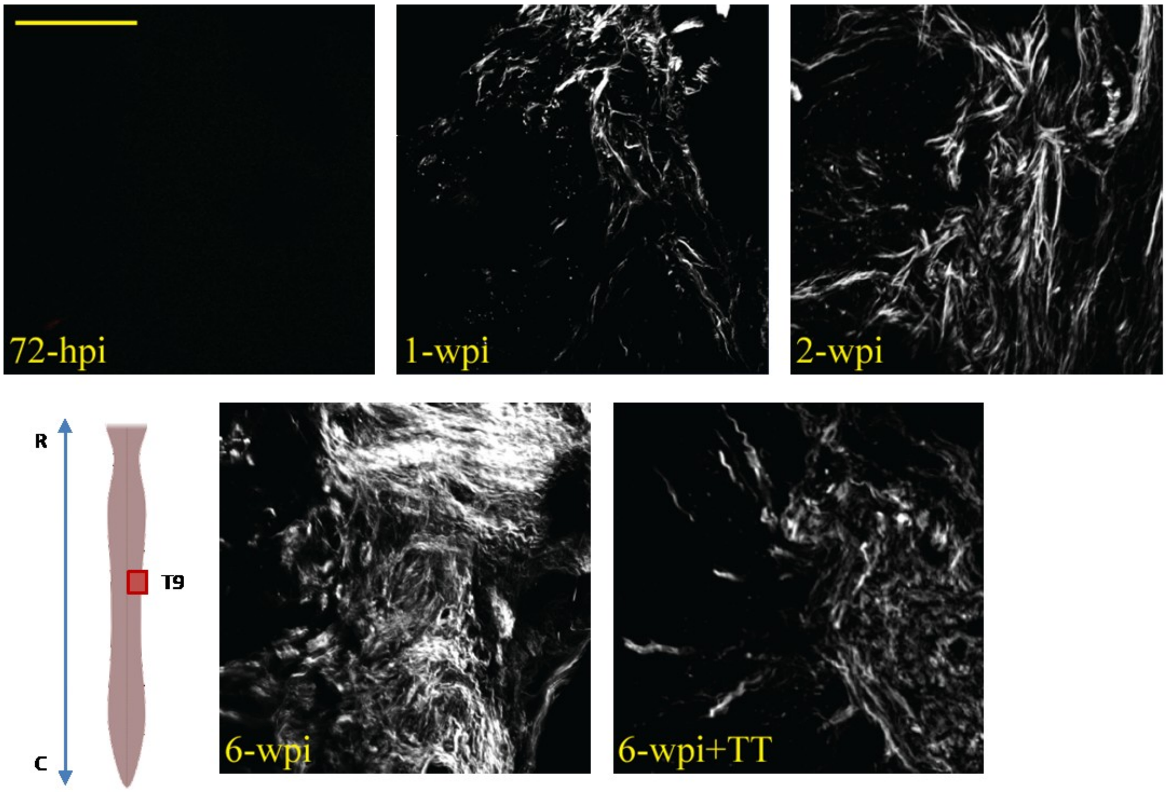

Figure 65: SHG images of the fibrotic scar over time and following treatment at 6wpi. SHG images are focused on the lesion area (where maximum SHG signal is detected) at 72-hpi, 1wpi, 2wpi, 6wpi post-injury and at 6wpi with treatment. Scale bar is 150 µm

The overall extent of collagen fibers along the rostro-caudal axis can be observed in *Figure 66 (A, B, C and D)* following a mosaic reconstruction of several MPM images. Consistently with the prior observations, fibers' extension (*Figure 66-E*) appears to increase over time reaching almost 2µm at 6wpi. Also, the extension of collagen expression in the treated group seems to decrease compared to control. Mean extension values are 867±300, 1200±400, 1800±200 and 950±250 µm at 1wpi, 2wpi, 6wpi and 6wpi + treatment, respectively.

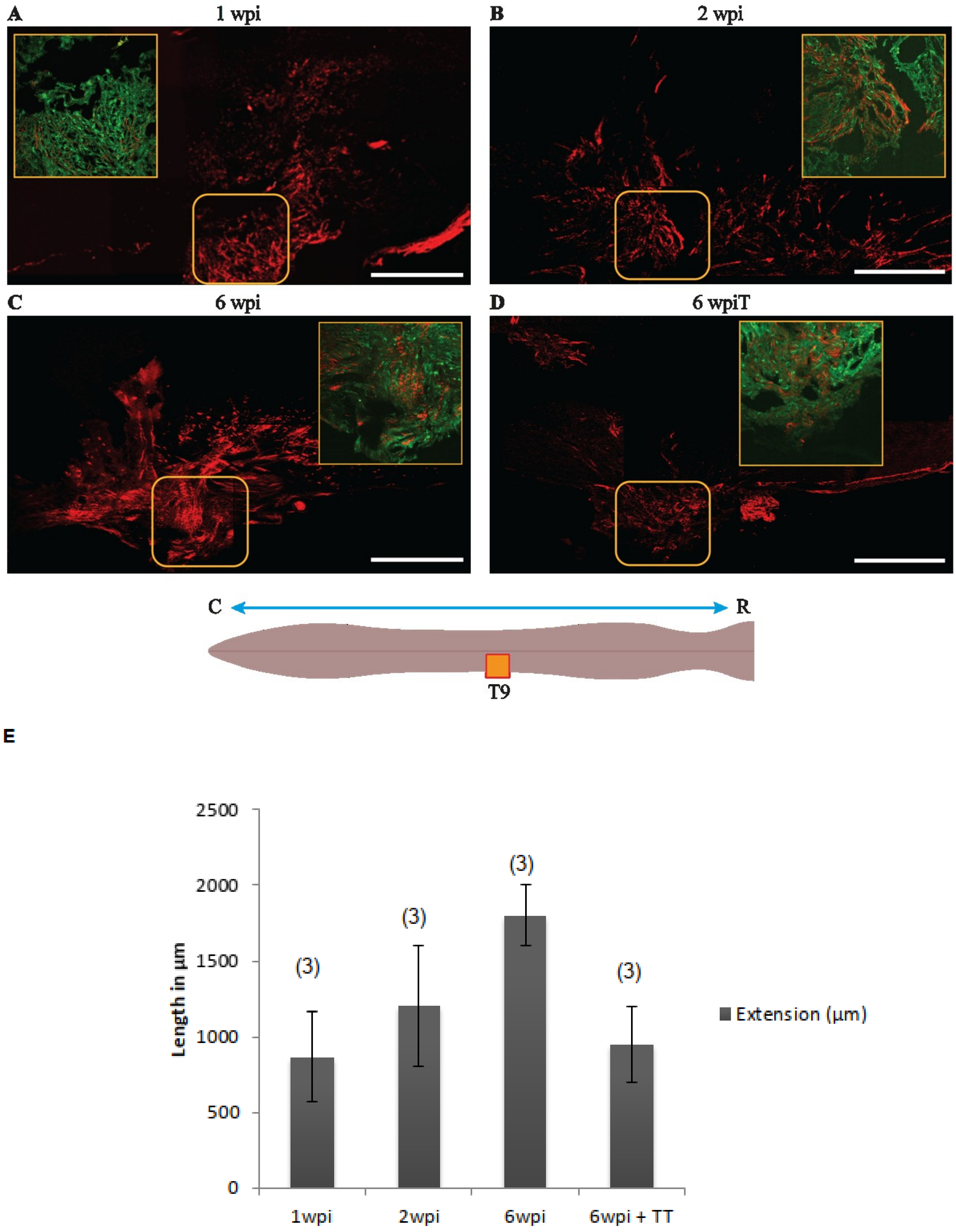

Figure 66: Collagen extension measured by SHG. Mosaic reconstruction of SHG images (signal in red) show collagen expression along the rostro-caudal axis at: (A). 1wpi, (B). 2wpi, (C). 6wpi and (D). 6wpi + treatment. The yellow squares (size: 432x432 µm^2 and zoomed aside with 2PEF in green) represent the injury border where mosaic acquisition starts. Scale bar is 400 µm for all. In (E), the mean extension length in µm with the SD error bars. N indicated in brackets.

III.3.3. Discussion: fibrillar collagen as a biomarker of the fibrotic process after lesion

The presence of collagen revealed by our IHC/IF and MPM studies indicated: i) that both collagen type IV and fibrillar collagen type I are present in the fibrotic part of the scar and their expression increases over time; ii) confronting signals emitted by labelled collagen I and SHG do not lead to a full co-localization, but only a partial one; iii) fibrillar collagen is detected with SHG from 1wpi with a tendency to increase at longer time-points post-injury iv) collagen expression shows a tendency to decrease after the treatment compared to the non-treated mice at 6wpi.

In the literature, expression of collagen IV has been described after spinal cord injury as a dense matrix meshwork of the basal lamina that composes the fibrotic part of the scar (Klapka & Müller, 2006) and widely investigated with immunolabeling (Anik et al., 2011; Hermanns & Reiprich, 2001; Loy et al., 2002; Streeter et al., 2020). As presented in the Chapter I. 3.3, collagen I and IV were rarely investigated together and at a few post-injury time-points. Klapka and Müller (Klapka & Müller, 2006) reported a higher expression of collagen IV at 4wpi compared to 1wpi after spinal cord dorsal hemisection in rats. Following contusion in rats (Okada et al., 2007) collagen type I expression was investigated in the ventral white matter through multiple approaches (immunoperoxidase and immunofluorescence , RTPCR and electron microscopy) at 1wpi, 4wpi and 8wpi. Collagen I was found at 4wpi, and further decreased at 8wpi. Another study using contusion in mice (Hara et al., 2017) performed genomic-wide expression analysis evidencing an up-regulation of the gene coding for collagen I at 2wpi. Investigations in a crush model in neonatal mice (Y. Li et al., 2020) identified collagen I expression at 3 days post injury by IHC. Discrepancy with our result may be due to the difference in the lesion models. Nevertheless, these results overall support the fact that collagen expression evolves over time after injury.

The techniques employed in previous works to target and reveal collagen I expression showed different sensitivities. For example, Okada and colleagues (Okada et al., 2007) revealed collagen I expression at 1wpi via Western-blot and RT-PCR, while IHC showed almost no signal at this time-point. In our study, both IF and SHG methods did not reveal collagen expression prior to 1wpi, while fibrotic processes are seen with peroxidase immunostaining at 24hpi and 72hpi. The sensitivity and specificity of each method needs to be considered for further interpretations. Besides, IF-collagen I and SHG signals did not co-localize. Co-localization of collagen I expression and SHG has been yet successfully achieved in renal (Strupler et al., 2007) and liver fibrotic tissues (Gailhouste et al., 2010) showing unambiguously a difference with collagen IV that did not co-localize with SHG. In these tissues, both collagen types are found even in the healthy state and are well structured in specific parts of the tissue. For example, in renal tissue, collagen type I is located in the adventitia of the artery while collagen IV is found in the basal laminae near the artery, which allows a clear discrimination between them (Strupler et al., 2007). In our case, no fibrillar collagen was found in the healthy state of the spinal cord (except in meninges). Furthermore, collagen type I and type IV detected in injured tissues did not show a distinct area of expression. Collagens expression and localization might depend on the tissue type and the scarring processes.

Other fibrillar collagens may also be present after SCI such as collagen III that has been reported in transection model in rats (Weidner et al., 1999) and in penetrant lesions in rats central nervous system together with collagen I (Maxwell et al., 1984). Though collagen I and III are known to coexist in tissues, collagen type III was reported to have a very weak SHG signal (Ranjit et al., 2015). Therefore, we first suggested that the main source of SHG signals is the fibrous collagen I. However, we cannot exclude that collagen type III is also expressed in our samples. Further IHC/IF investigations of collagen type III expression may confirm this hypothesis. Overall, considering the specificity of SHG signal produced by fibrillar collagen, we prefer to refer to the collagen observed in our samples by the general term “fibrillar” instead of stating the type of fibrillar collagen.

Concerning the increasing collagen extension we’ve observed at later time-points post-injury, additional data are needed for quantitative and statistical analyses. Studies using SHG imaging have revealed collagen I presence at 2wpi in a transection model in rats (Huang et al., 2011), in crush injury in mice (W. Wu et al., 2022) however with no quantification. Galli and colleagues compared collagen expression at 28-dpi (4wpi) and 154-dpi (22wpi) at chronic stage after a hemisection in mice (Galli et al., 2018) through the percent area covered by the SHG signal. The authors found massive deposition of collagen at the 2 time points without significant difference. This later observation differs from Okada and colleagues reporting different expression at 4wpi and 8wpi in ventral white matter through immunohistological examinations. This discrepancy may results from the difference in the injury model used, the sensitivity of the methods employed and the analyzed tissue area.

The apparent decrease of collagen in the treated 6wpi+TT group in our study requires also more quantitative analysis for a clear discussion.

Considering our preliminary studies at 1wpi and the observation of increasing collagen expression in time, the results support that fibrillar collagen has both a specific location and evolution to be a good biomarker of the fibrotic scarring.

The changes of collagen expression were further characterized at different levels and relevant fiber-related parameters were investigated to describe more accurately and quantitatively the fibrotic process as presented in the following section.

III.4. Collagen characterization at supramolecular and fiber level

III.4.1. Supramolecular level assessments

The first approach to characterize collagen fiber was through P-SHG to assess the supramolecular arrangement of the fibrils bundles. This investigation was performed at ROI level (the ROI delimitating a fiber/bundle) and not a pixel-level as previously reported (Mercatelli et al., 2020). The pixel-level approach requires a proper fiber map where the intensity of each pixel can be extracted. The perspective of these experiments is presented at the end of Chapter III.3.

The SHG intensity of each ROI was plotted in function of the polarization angle of the incident light to obtain the polarization curves. As introduced in Chapter I.2.2.3, the profile of the curve provides information about the supramolecular arrangement of the fibrils. The type of fibrils obtained at 1wpi is presented in *Figure 67*.

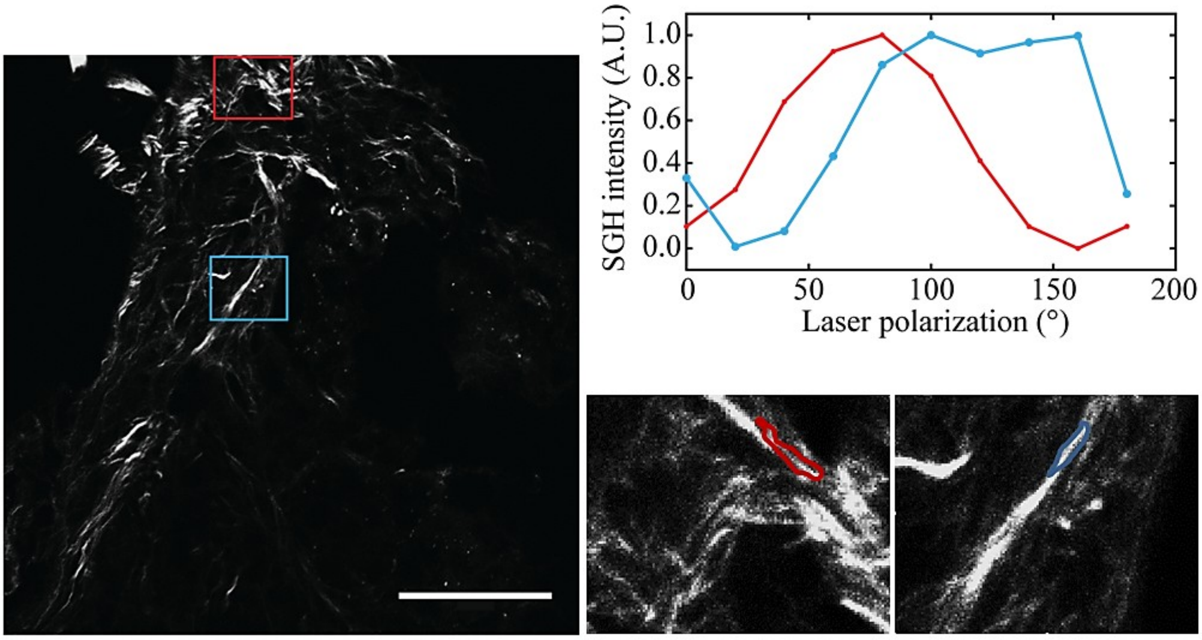

Figure 67: Fibrils profiles from Polarized-resolved Second Harmonic Generation (P-SHG). SHG image at the injury site at 1wpi is presented with zoomed areas (corresponding to the blue and red squares, 50x50 µm), showing a bundle of wavy-like fibrils (red cursor) and straight fibrils (blue cursor). The corresponding polarization curves are shown with the same colour code. Scale bar is 106 µm.

In the two selected areas, one ROI depicts a typical "single hump" profile (red frame and curve) that describes wavy-like fibrils with a trigonal symmetry. The second ROI depicts a "two-humps" profile (blue frame and curve), describing straight fibrils having a cylindrical symmetry. Overall, the polarization curve profiles showed that both straight and wavy-like fibril bundles could be encountered in the SC tissues overtime and following treatment.

Nevertheless, the estimation of different profiles (in %) based on the number of ROI with a characteristic profile (excluding the curves that did not display a “single” or “two-humps” shapes) suggests that a majority of wavy-like bundles could be encountered after 2wpi (*Figure 68-A*) as shown in the fibers profiles illustration in *Figure 68-B*.

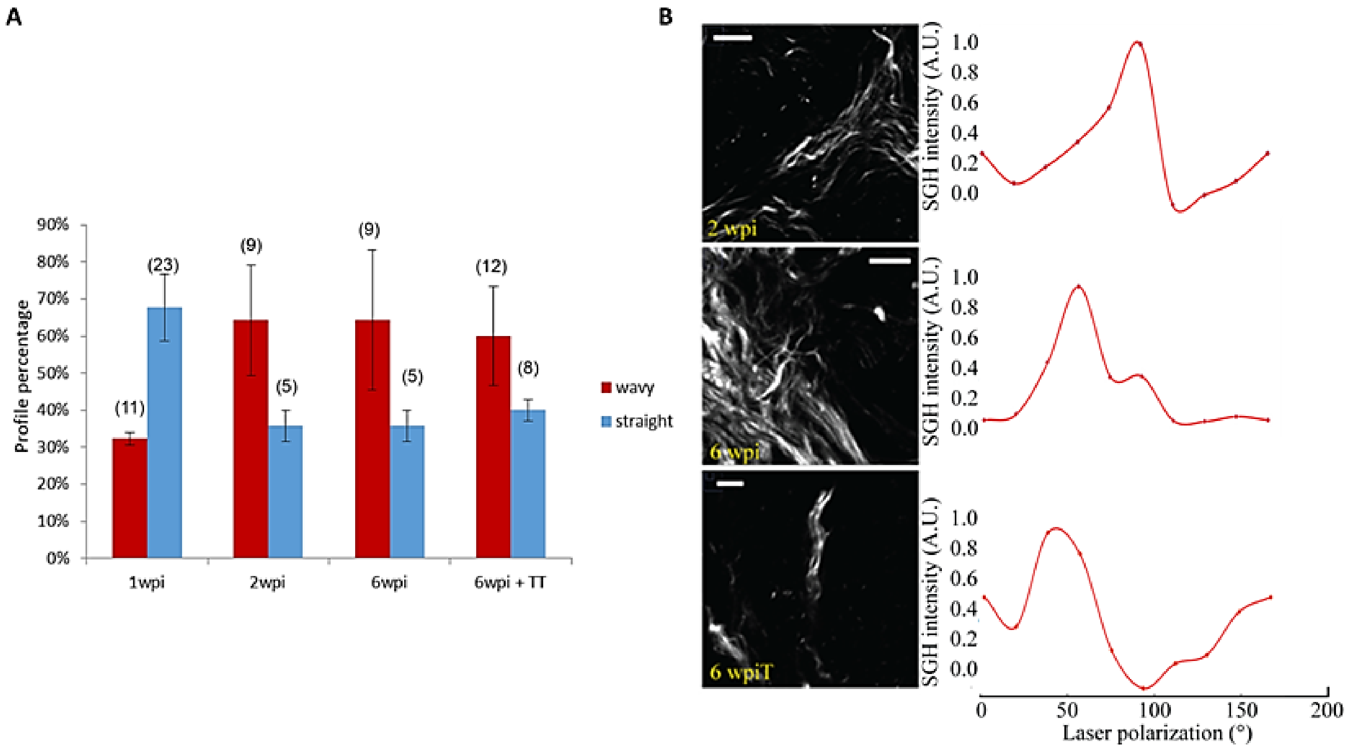

Figure 68: Estimation of fibrils profiles at different post-injury time-points. In (A) the percentage of these profiles (red for wavy and blue for straight) is presented (with SD error bars) in function of the time-point and for the treatment condition (N indicated in brackets). (B), wavy-like fibrils bundles are shown at 2wpi, 6wpi and 6wpi + TT with the associated polarization curve. Scale bars are 50 and 20 µm.

This estimation performed on a rather small data set of ROIs and, similarly to collagen extension assessments, provides valuable preliminary results that needs to be completed with statistical analysis on a larger data set.

III.4.2. Fiber-level metrics

Characterization of collagen at fiber-level requires the identification of relevant fiber metrics that can describe the evolution of the fibrotic scar in time. A first approach was performed using the software CurveAlign for assessing the number, length and orientation of the fibers.

III.4.2.1. CurveAlign results

III.4.2.1.1. Fibers quantification

The evolution in time of fibers number and length are presented in *Figure 69* .

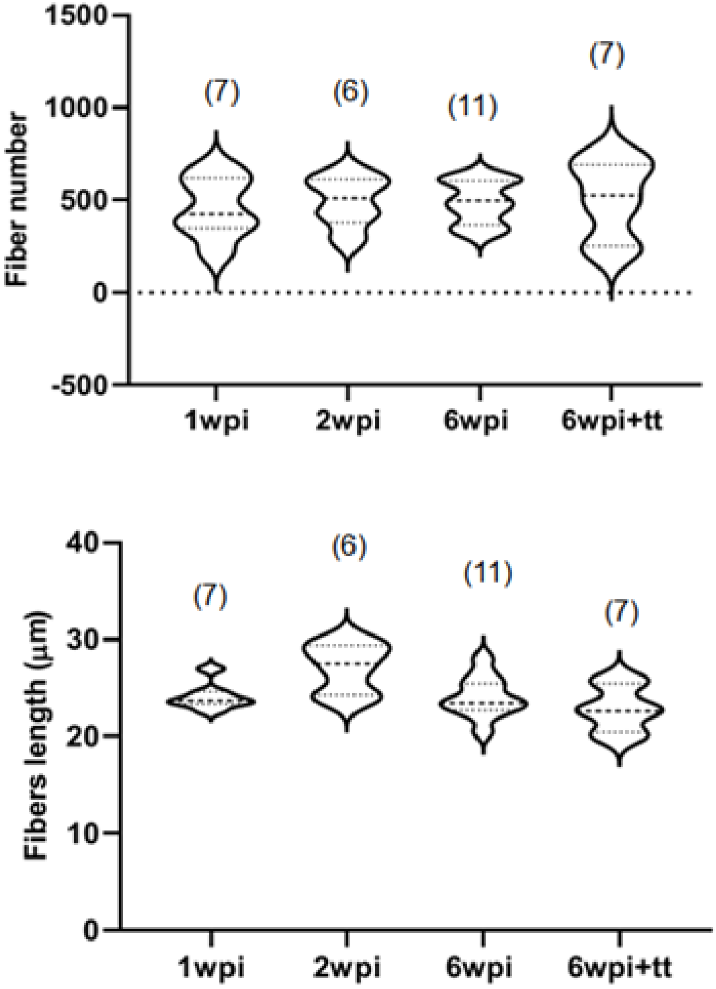

Figure 69: Fibers number and length evolution in time and following treatment at 6wpi obtained from the SHG images analyzed with CurveAlign. Means are indicated (black dash line) with SD (grey dash lines) in a violin plot. 1way ANOVA on repeated measures was performed between the time-points, and an unpaired t-test with Welch’s correction was applied to compare the treated and control group. No significant difference was found. Number of samples is indicated in brackets.

The mean values (±SD) obtained for the fibers number are: 458.4±164.77 for 1wpi, 492.7±135.17 for 2wpi, 509.9±112.77 for 6wpi and 507.3±210.50 for 6wpi with treatment. No significant difference is observed in the number of fibers at each time-point and following treatment.. Similarly, the mean length of the fibers does not depict significant difference between time-points or following treatment. The mean values (±SD) are: 24.1±1.40 µm for 1wpi, 27.1±2.55 µm for 2wpi, 23.7±1.37µm for 6wpi and 22.8±2.31 µm for the treated group.

III.4.2.1.2. Fibers orientation

III.4.2.1.2.1. ROI-level

The fibers' orientation was investigated at ROI-level (the ROI delimiting an area where the fibers seemed to have a preferential direction) through the alignment coefficient. Results showing the categories of alignment are presented in *Figure 70.*

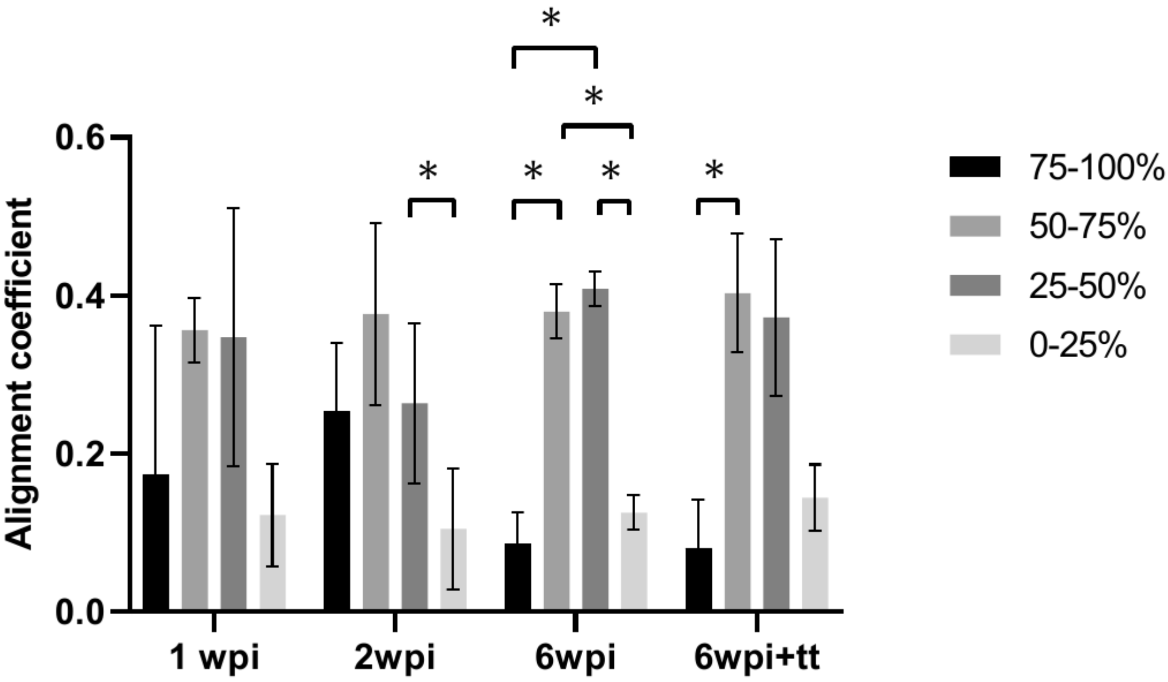

*Figure 70: Alignment coefficient. The percentage (%) of ROIs within the categories of alignment 75-100% for good, 50-75%,25-50% for medium and 0-25% for bad alignment is presented. 1way ANOVA on repeated measures was performed between the time-points, 2way ANOVA Tukey's multiple comparison on repeated measures was performed between the alignment categories for one time-point and an unpaired t-test with Welch's correction was applied to compare the treated and control group.*p<0.05. Number of data is (7) for 1wpi, (5) for 2wpi, (10) for 6wpi and (7) for 6wpi+TT.*

We note that no significant difference is seen between the time-points or following treatment. Moreover, no significant difference is found in alignment at 1wpi, suggesting that the orientation of the fibers cannot be evaluated with this method at this time-point. The results at 2wpi show a difference between 0-25% (bad alignment) and 25-50% (medium), indicating that fibers with a medium alignment are more represented than not aligned fibers. In the group which received a treatment, medium aligned fibers are more represented than well aligned fibers. The clearest result is obtained at 6wpi where medium alignment categories prevail over the other two (bad or good alignment).

Overall, no distinct alignment has been found except for 6wpi where the fibers depict a medium alignment implying no preferential orientation at this post injury time-point.

III.4.2.1.2.2. Image-level

The alignment was investigated also considering the whole image to assess the global orientation of the fibers. Typical angle compasses representing the distribution of the fiber angles at different time-points post injury are shown in *Figure 71*.

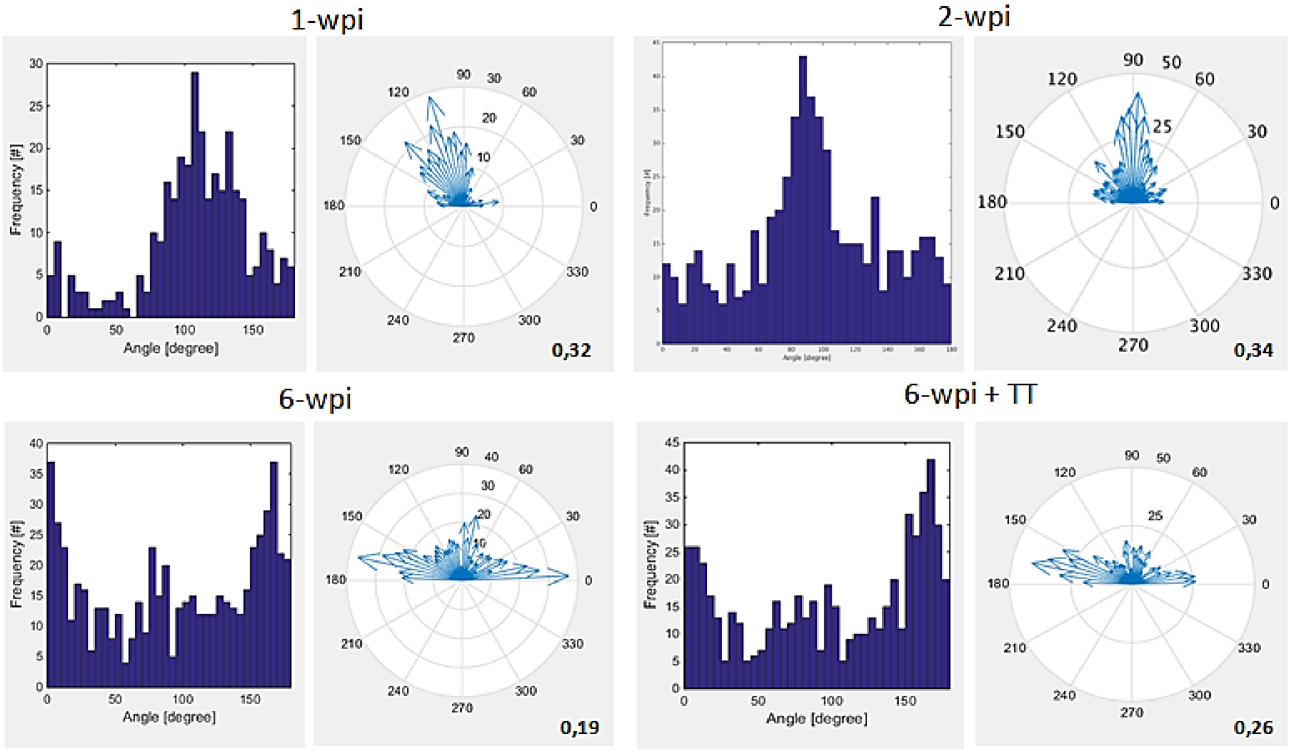

Figure 71: Fibers angles distribution at image-level. The angles frequency and orientation compass were obtained on the entire SHG image of the injury. The values in black on the compass represent the mean alignment score at each time-point post injury.

The tendency observed from the angle frequencies and orientation compasses is that at 1wpi and 2wpi some angles are more represented (the blue arrow in the compass indicates the frequency; the longer the arrow, the higher the frequency) while the angle repartition is more spread between 0 and 180° at 6wpi (without and with treatment). Means alignment values, gathered in *Figure 72*, are 0,32±0,22 for 1wpi ; 0,34±0.12 for 2wpi; 0,19±0,03 for 6wpi and 0,26±0,08 for the treated group and are. A tendency of decreasing alignment is observed at 6wpi with and without treatment, but the alignment score shows no significant difference between the time-points nor between the control and the treated group.

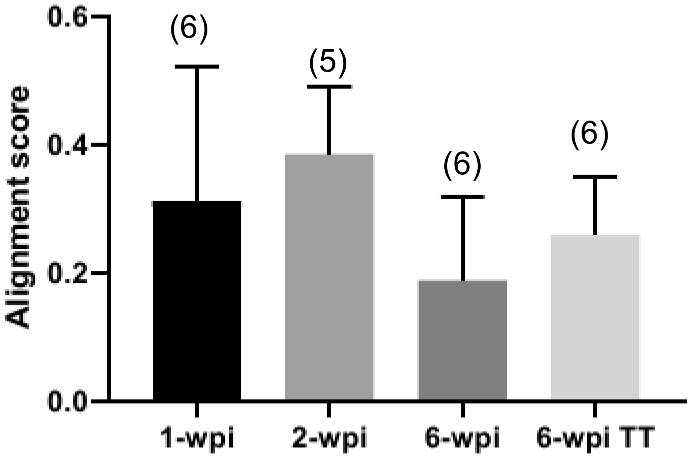

Figure 72: Fiber alignment score at image-level. The mean alignment score (with SD error bars) is presented for all time-points and following treatment at 6wpi. This score is a number between 0 for random alignment and 1 for complete alignment. 1way ANOVA on repeated measures was performed between the time-points, and an unpaired t-test with Welch's correction was applied to compare the treated and control group. N is indicated into brackets.

Overall, our fibers metrics investigation with CurveAlign did not evidence a clear evolution in fibers number, length, or orientation in function of the post-injury time. To adapt the fibers detection method to the high variability of our samples, in a tissue where collagen fibers are not present originally, but are gradually forming from 1wpi, we have developed a data analysis method based on an enhanced fingerprint algorithm. As presented in the following section, this approach permits a better control on the way fibers are detected and on definition of relevant metrics to characterize the formation of collagen fibers.

III.4.2.2. Fingerprint algorithm results

III.4.2.2.1. Fibers quantification

We first investigated the fibers number and length at 1wpi, 6wpi and following treatment at 6wpi, but no significant difference was observed between these conditions. Individual fiber metrics characterization remains hard to afford due to untangling process limitations. Nevertheless, these preliminary results are presented in *Figure 73* as they depict an interesting comparison with our first findings in CurveAlign.

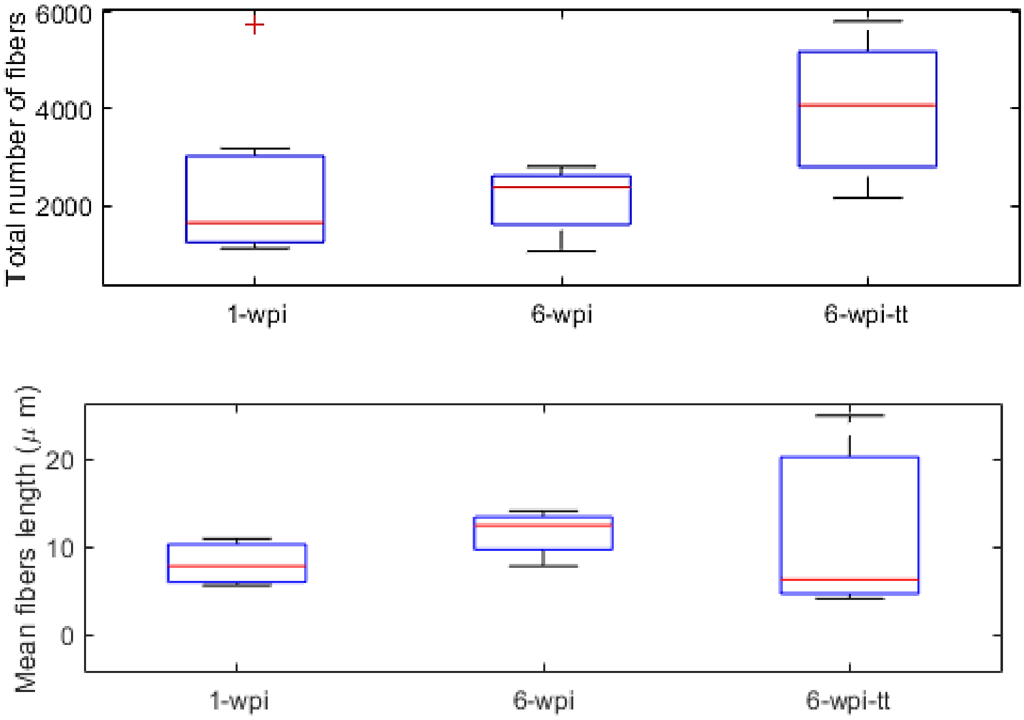

Figure 73: Fibers number and length obtained with the Fingerprint algorithm. Mean values are indicated with SD error bars.

The mean number of fibers (1500-4000 fibers) is overall higher than the mean values we found with CurveAlign (400-500 fibers). The mean fiber length is almost twice lower with values between 8 and 12 µm while the previous results showed mean lengths around 20 µm. The fibers number tendency to slightly increase between 1wpi and 6wpi is similarly observed in both methods, while the mean value following treatment seems higher in the Fingerprint than in the CurveAlign detection. Observations for the mean length are overall like our previous results, with almost no difference between the groups.

These differences are intrinsic to the fibers detection method itself. When comparing the two methods processing on the test raw image provided in *Figure 74*, a higher number of shorter fibers is clearly detected with the Fingerprint algorithm. This is certainly related to limitation in the 3D resolution when imaging tissues and to the untangling method which is crucial in separating the branches of the skeleton map into individual fibers.

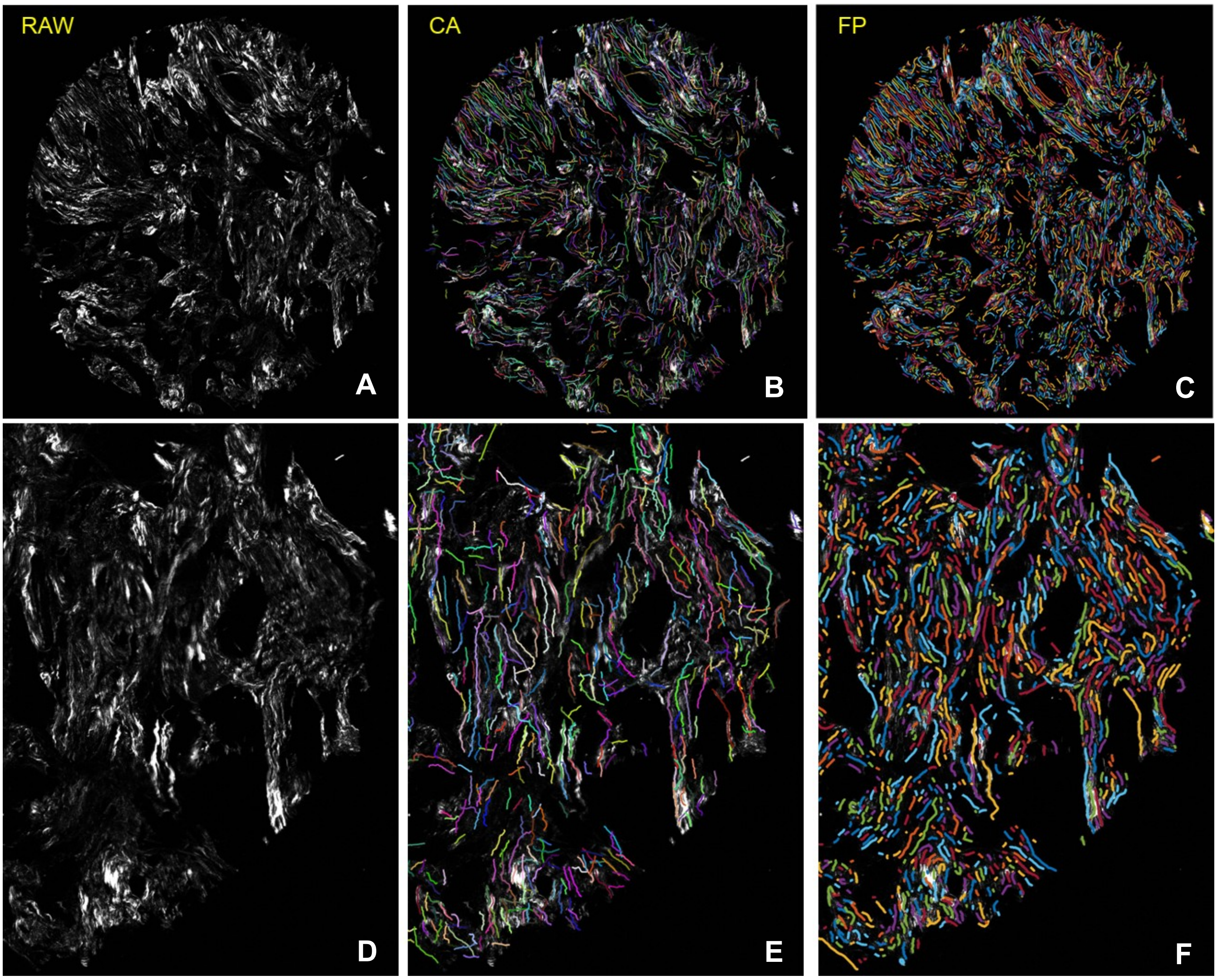

Figure 74: Comparison of the fibers detected by CurveAlign and Fingerprint methods. A. Raw-SHG image of breast cancer tissue (test image provided by CurveAlign) is analyzed by both methods, B. CurveAlign and C. Fingerprint method. A zoom-in of each top image is shown in D. E. and F.

Quantification of collagen fibers at macroscopic level was further conducted with metrics calculated from the SHG signal and presented in the following sections. Fibers were characterized in terms of fibers' density, tortuosity, local alignment and the statistical entropy. The two last parameters assessed fibers orientation at a local and global level, respectively.

The results for the fibers' density Φ (indicating the total length covered by the fibers) are presented in *Figure 75*.

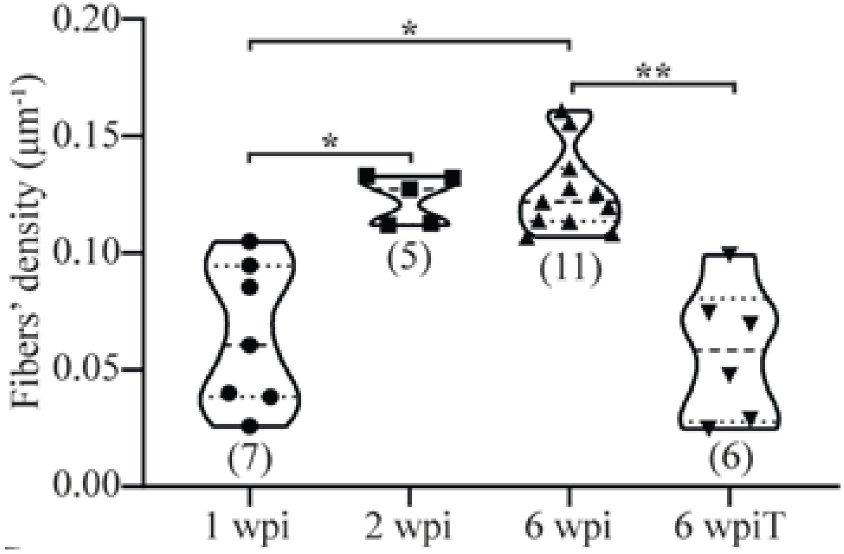

*Figure 75: Fibers density (Φ) at different post injury time-points and following treatment at 6wpi. Mean values (dashed line) are indicated together with a SD (dot lines) in the violin plot. 1way ANOVA on repeated measures was performed between the time-points and an unpaired t-test with Welch's correction was applied to compare the treated and control group. With * $p<0,05$, ** $p < 0.025$. Number of samples is indicated in brackets.*

A significant increase in the density of fibers is noticed over time: 0.06±0.03 μm^{-1} at 1wpi, 0.12±0.01 μm^{-1} at 2wpi and 0.13±0.02 μm^{-1} at 6wpi. Collagen fibers in the treated group appear to have a reduced Φ (0.06±0.03 μm^{-1}) compared to the control one.

The calculated tortuosity (*Figure 76*) shows an increasing tendency at 6wpi (1.9±0.2), compared to 1wpi (1.6±0.2) and 2wpi (1.8±0.1), suggesting that fibers became more tortuous at later time-point. A statistical significant decrease was observed between the control (6wpi) and the treated group (6wpiT) indicating that the fibers became straighter following treatment at 6wpi.

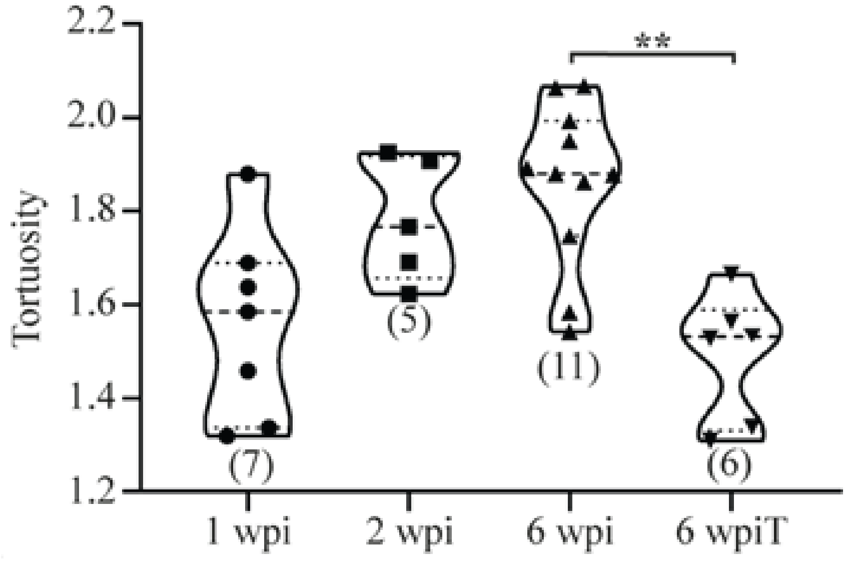

*Figure 76: Tortuosity at different post injury time-points and following treatment at 6wpi. Mean values (dashed line) are indicated together with a SD (dots lines) in the violin plot. 1way ANOVA on repeated measures was performed between the time-points and an unpaired t-test with Welch's correction was applied to compare the treated and control group. **p<0.025. Number of samples is indicated in brackets.*

III.4.2.2.2. Fibers orientation

The orientation of the fibers was assessed at two different levels: at a local level through the variance of the local orientation θ, evaluating the fibers' orientation compared to the nearest neighbor within a box of 9x9 pixels, and at a global level through the assessment of the entropy S.

III.4.2.2.2.1. Local alignment of fibers

The local alignment of fibers (Var(θ)) exhibits low values, between 0.3 and 0.5, suggesting that the fibers are rather well aligned with each other (*Figure 77-A)*. However, no significant difference is observed between the different samples. The partition of the local alignment of fibers in four groups reveals that a majority of highly aligned (Var(θ) : [0, 0.5]) fibers are observed from 1wpi to 6wpi, but they become less aligned for the treated group (*Figure 77-B)*.

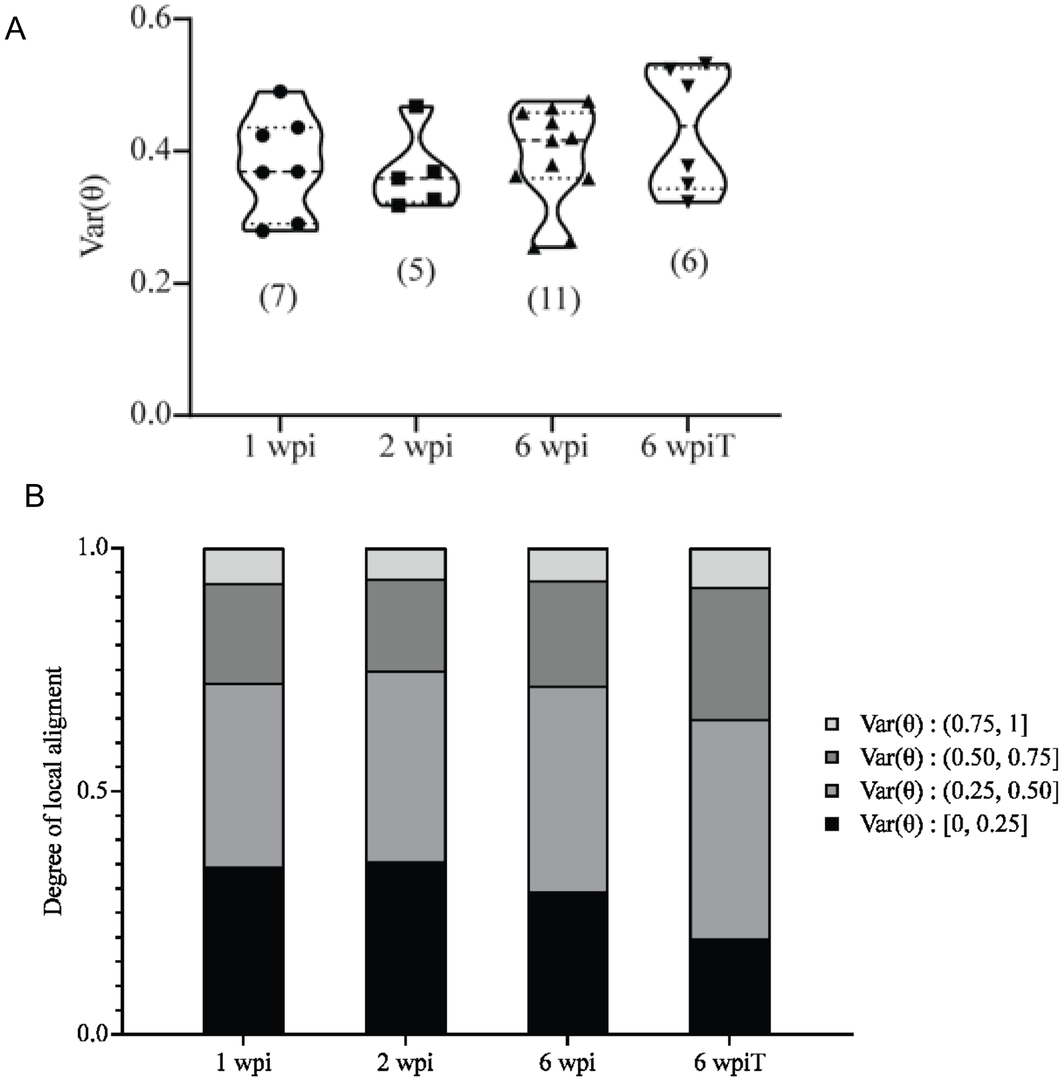

Figure 77: Local alignment of fibers at different time-points post injury and following treatment at 6wpi. A. Mean Var(θ) values (dashed line) and SD (dot lines) are presented in the violin plots. 1way ANOVA on repeated measures was performed between the time-points and an unpaired t-test with Welch's correction was applied to compare the treated and the control group. Number of samples is indicated in the brackets. B. Summary of degree of local alignment at different time-points and following treatment.

In summary these results as well as the ones obtained with CurveAlign at a ROI-level (even if the ROIs are larger than the pixel box we defined in the Fingerprint method), indicate that there is no significant modification in the local orientation of fibers in function of time. While the alignment found with CurveAlign was generally a medium one for all the samples, the local alignment defined with the Fingerprint algorithm suggested rather a good alignment. Besides, the degree of local alignment suggested less aligned fibers for the treated group, in line with CurveAlign results depicting more medium than well aligned fibers following treatment.

III.4.2.2.2.2. Global level alignment of fibers

The distribution of fibers orientation on a whole image was addressed through the calculated statistical entropy S (*Figure 78*). The entropy values were globally high (between 0.90 and 0.95) and similar for the various time-points and following treatment, meaning that no preferential orientation was detected at tissue level.

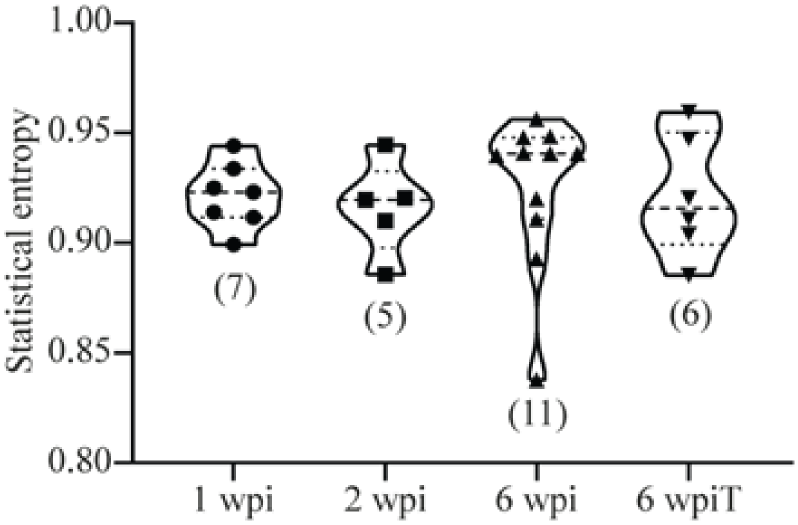

Figure 78: Statistical entropy (S). Mean S values (dashed line) and SD (dot lines) are presented in the violin plots. 1way ANOVA on repeated measures was performed between the time-points and an unpaired t-test with Welch's correction was applied to compare the treated and control group.

Similarly to CurveAlign results, the global orientation did not reveal significant change overtime, hence fibers' orientation assessments with the defined metrics were not conclusive with either of the two data analysis methods.

III.4.3. Discussion: collagen fibers metrics can describe the progression of the scarring process

Our results indicate that SHG signal assessments permitted the characterization of fibrillar collagen at different levels: the variations of SHG signal in function of polarization, monitoring the nature of collagen fibrils at a supramolecular level indicated that i) both straight and wavy fibrils were observed. Quantification of the SHG signal provided ii) two metrics suitable to monitor the fibrotic scarring process at fiber-level, the tortuosity, revealing less straight fibers at 6wpi while more straight fibers following treatment, and the fibers' density that increased with time and decreased in the treated group. iii) The orientation assessments did not exhibit any significant difference between the time-points or following treatment. iv) Investigations with CurveAlign, assessing the number, length, and orientation of the fibers did not reveal major modifications in time, but offered an interesting data analysis method of comparison and guidance for developing our home-made Fingerprint processing.

Our results can be discussed in relation with previous works, pointing out major differences in formation of collagen fibers in injured SC compared to other collagen containing tissues.

i) The supramolecular arrangement of collagen fibers was mainly investigated in cancer and no SCI studies explored this aspect. Mercatelli and colleagues (Mercatelli et al., 2020) showed that the aligned collagen bundles related to tumoral states had a cylindrical symmetry (associated with high straightness of the fibrils) while the peri-lesional tissue exhibits trigonal symmetry (associated with more waviness). In our case, there is no collagen initially present in the spinal cord but it appears after 24h, as revealed by immunochemistry and forms fiber bundles at 1wpi, as indicated by their SHG signal, gradually invading the injury site and exhibiting both straight and wavy fibrils with no evidence of spatial separation between these two configurations. Nevertheless, we observed that straight aligned fibrils are more represented at 1wpi, while wavy-like collagen structures became dominant at 2wpi and 6wpi. Collagen organization in the fibrotic scar may thus be different from cancerous fibrotic meshing.

ii) Even if no direct link can be evidenced between the tortuosity of fibers and the nature (straight or wavy) of fibrils constituting them, it may bring complementary information about the collagen organization. In our work, the profile of fibrils was characterized together with the straightness/tortuosity of the fibers: at 2wpi and 6wpi more wavy-like fibrils were estimated, together with a tendency of increasing tortuosity. Following treatment at 6wpi, more wavy-light fibrils were also estimated (with a slight higher proportion of straight profiles than in the control group), while significantly less tortuous fibers than in the control group were found.

CurveAlign also offers the possibility to calculate the straightness of the fibers, expressed as a fraction of collagen segments sharing the same orientation (Despotović et al., 2020) which is different from our approach but still worth to comment. The straightness of collagen fibers has already been explored with CurveAlign in various cancer tissues, for example, to assess healthy and cancerous states in human colon mucosa showing a significant increase in tumor (Despotović et al., 2020; Despotović & Ćosić, 2022).

The specificity of the SHG signal exhibited by collagen fibers allowed to quantify their extension along the injury over time. The fibers' density is another parameter exhibiting significance increase at later post-injury time-points. The increase in the fibers density in time could be related to the extension of collagen fibers we've measured on reconstructed mosaic SHG images increasing from 1wpi to 6wpi. After GW2580 treatment targeting the microglial proliferation and also affecting macrophages in the scar, the collagen extension appeared to be reduced. Gerber et al. (Gerber et al., 2018a) and Poulen et al. (Poulen, Aloy, et al., 2021) described that GW2580 efficiently decreased the proliferative microglia, but no effect on the lesion extension was reported. The decrease of collagen fibers' density and their apparent reduced extension in the treated group suggests inhibition of microglia proliferation directly or indirectly modulating collagen expression in the scar (Z. Li et al., 2021). Also, as discussed in the previous section, the only SCI study quantifying SHG signal of collagen at the injury site (Galli et al., 2018) was performed in a chronic stage observing no difference between 4wpi and 22wpi. Following Galli and colleagues, the total amount of collagen stabilizes between 4 wpi and 22wpi and no difference is found anymore in the chronic stage. The latest time-point we investigated with SHG so far was 6wpi, hence it is difficult to properly compare that work with our observations. Nevertheless, one could hypothesize that an increase of collagen deposition could be observed in time until stabilizing in the chronic phase.

iii) The relative orientation of fibers did not exhibit any variation up to 6wpi. Similarly, no preferential direction was reported in collagen organization in rats at 4wpi or 22wpi by Galli and colleagues (Galli et al., 2018). The authors used the Directionality tool in Fiji and expressed the direction of the highest number of fibers (performing an orientation assessment at tissue level). They found that the fibers showed large angles with respect to the longitudinal axis suggesting that the fibers were not following a preferential direction in the chronic stage. Our entropy results, where no significant differences in S over time were found, are corroborating the isotropic distribution of the fibers orientations within the injured tissue. Interesting comparisons can be done with studies exploring collagen reorganization in fibrotic diseases or cancers. Collagen fibers orientation has yet been defined as an important marker in these diseases mainly associated with highly aligned collagen bundles compared to normal state, but with converse conclusions depending on the tissue studied. In healthy skin dermis, the collagen fibers were described to be well-aligned while randomly orientated in a keloid or a diseased state (Cicchi et al., 2013). In prostate cancer tissue, however, the collagen fibers are more aligned than in healthy state (Ling et al., 2017). This observation has been generally reported for malignant tissues, where the collagen fibers reorganize into a radial alignment with respect to the tumor (Provenzano et al., 2006). Direct comparison with our results cannot be done as these studies addressed tissues containing collagen fibers in both healthy and diseased states while spinal cord tissues does not contain naïve collagen in healthy state.

iv) Another aspect to discuss is the confrontation of CurveAlign and the Fingerprint (FP) algorithms we've used for our data analysis. Both methods have obviously their advantages and drawbacks, CurveAlign being a ready-to-work and user-friendly tool to detect collagen fibers, FP algorithm allowing a finer control on fibers' definition and the metrics assessed. The images depicting the results in fibers identification and untangling (*Figure 74*) clearly show different outputs obtained with the two methods. Despite these differences, some measurements did not show significant changes overtime with both methods: the number of fibers, the mean length, and the fibers orientation. Nevertheless, different tendencies are observed in some metrics, for example in orientation assessments at global level, here measurements with CurveAlign suggested a tendency of decreasing for the alignment score at 6wpi, which was not the case for statistical entropy with FP. Overall, the FP algorithm was more adapted to our study and allowed to reveal significant changes overtime for the fibers's density. Comparison between CurveAlign and an adapted Fingerprint algorithm was reported to assess the alignment of collagen in gels (Sun et al., 2015) showing the same accuracy in the obtained results and a faster calculation time (CPU time =0.730) compared to CurveAlign (CPU time=1.680). We had similar observations in our work, where each section (10 images per section for each polarization angle) were processed within hours with CurveAlign while almost in one tenths of that time with our Fingerprint algorithm (the more time consuming is to tune the parameters in FP). Methods dedicated to collagen fibers detection have also been used together to obtain complementary information as in the work of Despotovic and colleagues (Despotović et al., 2020). Here, various specialized softwares (CT-FIRE, CurveAlign and FiberFit) were combined to characterize the collagen fibers in colon cancer, with specific assessments: CT-FIRE for straightness and width, CurveAlign for defining the alignment and FiberFit to quantify the alignment. In de Vries and colleagues' review (de Vries et al., 2023) the automated tools for quantification of fibrous networks were tested and compared in relation with the imaging techniques employed. The authors recommended, for example, OrientationJ, CurveAlign and FiberFit for fibers alignment investigations, or ER (endoplasmic reticulum) network analysis to determine the total fiber length.

III.4.4. Work in progress on collagen characterization

Complementary experiments are currently performed in the team to exploit all the data acquired at several Z-depths and different polarization angle.

For example, the Fingerprint algorithm allowed us to extract the SHG intensity of the fibers generated in the skeleton map at each Z-depth and to plot the polarization curves as presented in *Figure 79* (showing a ” single hump” profile). We can observe that the shape of the SHG intensity is mainly following the metric (total length of fibers) defined. This assessment is indeed more precise than the manually ROI-selected fibers and represents a further step towards pixel-level evaluations.

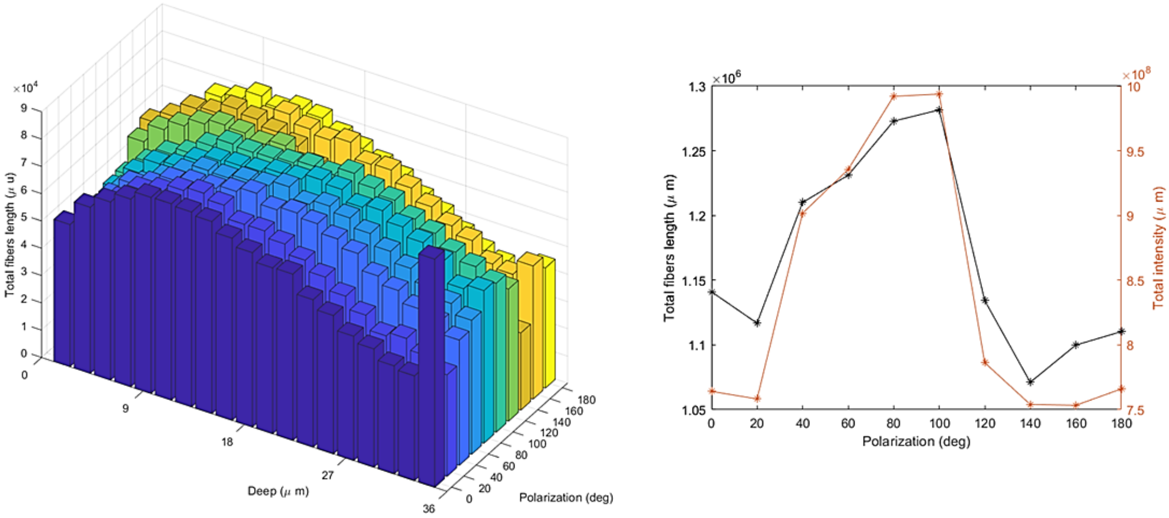

Figure 79: Fibers lenght in tissue depth. The total fibers length is presented in function of the Z-depth and the polarization angle (left). Each bar corresponds to a plane. The metric is plotted with the corresponding SHG intensity in function of the polarization angle (right).

Also, a method for better scoring of the SHG intensity and its relation to the amount of fibers could be valuable for quantitative P-SHG investigations. For that, a triangular meshing (*Figure 80*) is under test to extract the intensity in each triangle of the network, plot their frequencies and see how the mean value evolves in function of the polarization angle. A deeper understanding of how interpreting the signal distribution, together with the Z-depth effects, is necessary for relevant pipelines and metrics definition.

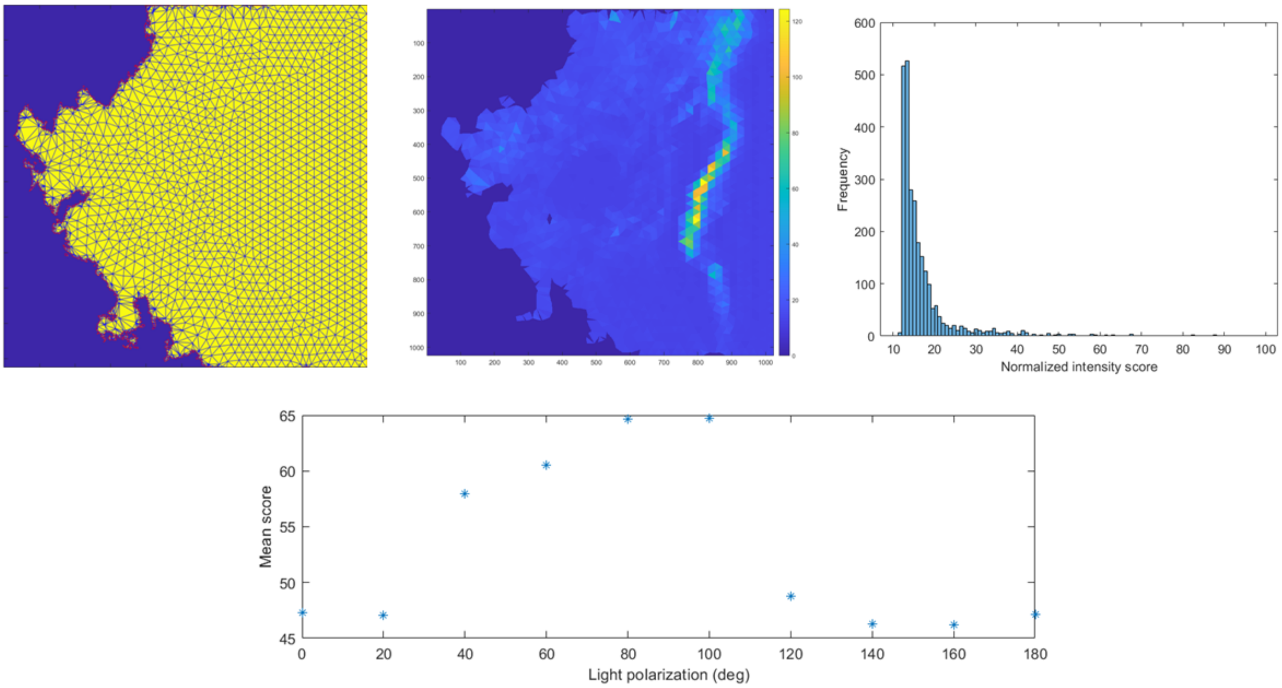

Figure 80: SHG intensity score. A triangular meshing is applied to the tissue (yellow area) and an intensity scoring is defined (color code: blue for low intensities and yellow for high ones). The distribution of the intensity score allows to extract a mean value and to plot it in function of the polarization angle.

The in-depth visualization of the fiber's skeleton might enable volumetric assessments characterizing the collagen in 3D. In *Figure 81* , the fibers appear to be differently oriented in function of the depth level at 1wpi. Interestingly, the orientation tends to harmonize between planes over time reaching almost the same orientation for all the planes at 6wpi. This observation needs to be investigated with further quantitative analyses.

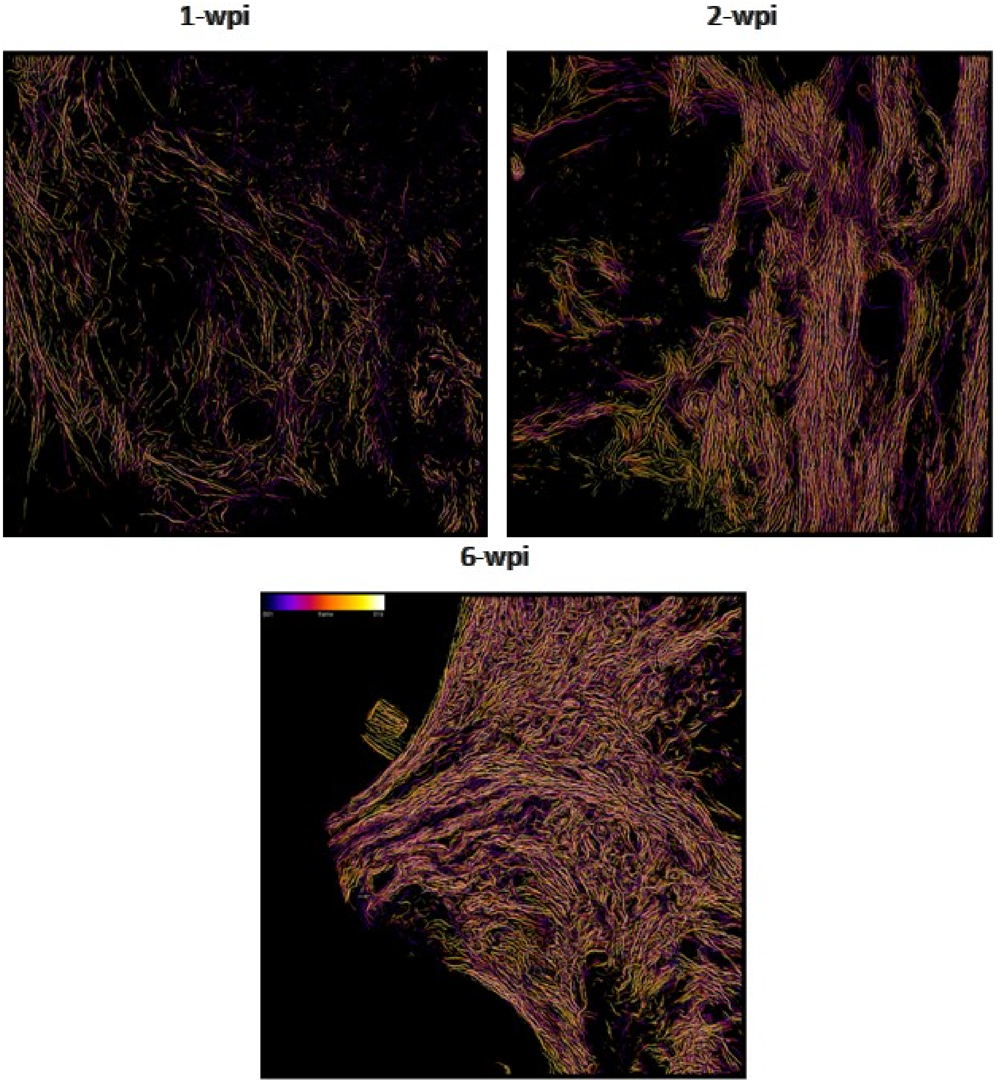

Figure 81: In-depth representation of the fibers skeleton map. The fibers are shown at different Z-depths (2 µm step) at 1wpi, 2wpi and 6wpi. Color code: violet for upper surface planes and white for deeper planes.

III.5. AFM-FS measurements time-course and treatment investigations

III.5.1. Elasticity- Height maps

Further the mechanical properties of the samples were assessed by nano-indentation measurements performed by atomic force microscopy (AFM) in force spectroscopy mode (AFM-FS). Following the structural observations of the SC tissue and characterization of collagen at the injury site, the question of the behavior of the SC tissue in terms of elasticity arose naturally. AFM-FS acquisitions were performed on three different areas of the spinal cord including GM and WM, representing spared parts where SC was not directly affected by the lesion, and the injury site, where no distinction between GM and WM was possible. After preliminary observations at 1wpi on spared and injured sections, showing stiffer GM zones than WM areas together with an injury softer than GM, we explored the elastic properties at other later post-injury time-points and following treatment at 6wpi.

The first approach was to generate height maps of the different areas, and combine them with elasticity maps (with an elasticity color code), based on the recorded Young's modulus (E) as illustrated in *Figure 82*.

The components of the different SC parts (mainly neurons bodies in GM and axons in WM) are not individually reachable by the spherical AFM tip, hence, not visible in the topography maps. Overall, the maps generated for WM show softer tissue (predominance of blue) for all time-points than the ones generated for the GM (predominance of green or yellow). High standard deviations values are reported in each case, especially in GM measurements, indicating the high variability of our measurements across the area of acquisition. Considering the differences between the time-points, E mean values for WM are similar for 72hpi, 1wpi and the treated group (2, 2 and 5 kPa, respectively) and a bit higher for 2wpi and 6wpi (26 and 10 kPa, respectively). E values for GM follow the same tendency, with a slight increase at 2wpi (81 kPa) compared to the other time-points: 38 kPa at 72hpi, 30 kPa at 1wpi and 38 kPa for 6wpi and 31 kPa for the treated group. Overall, E mean values of WM seem to be lower than for the GM at the same time-point. The injured area appears to undergo more important changes in E values over time with an increase at 2wpi, 6wpi and for the treated group (66, 42 and 37 kPa, respectively) compared to 72hpi and 1wpi (9 and 6 kPa, respectively).

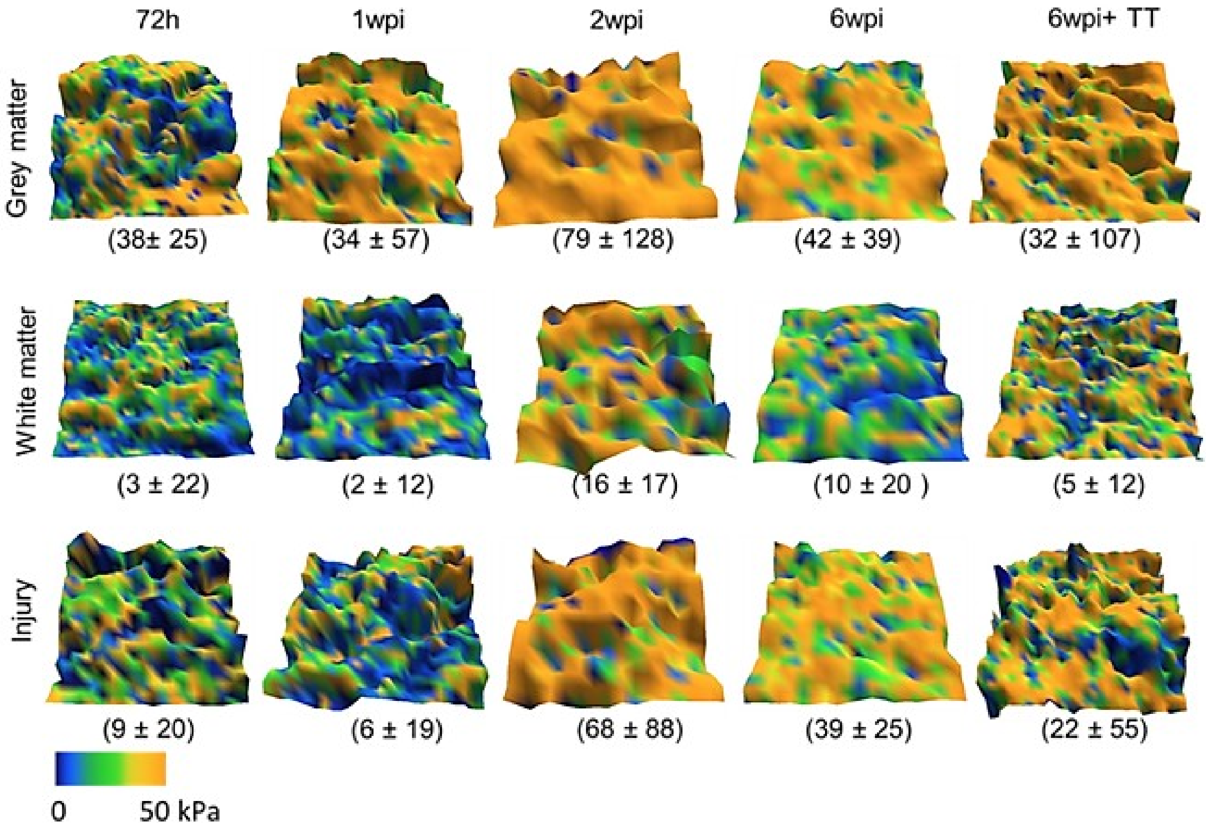

Figure 82: Combined height and elasticity map of injured mice spinal cord longitudinal sections. Young's modulus map superposed on tissue height (80 x 80 µm^2) for 72hpi, 1wpi, 2wpi, 6wpi and 6wpi + treatment (TT). Dark blue color depicts softer portions, while yellow color indicates stiffer regions. The mean Young's modulus E±SD is indicated in brackets.

III.5.2. Comparison between time-points

The statistical comparison of all the normalized E values for the GM, WM and injury at all the time-points and for the treated group is depicted in *Figure 83*. GM appears to be significantly stiffer than WM, following the tendency of the color code observed in *Figure 82*, also showing that the elasticity of GM and WM is rather stable no matter the time-point. At 72hpi (*Figure 83-A*), the injured area is significantly softer than the GM (***p<0.001) also compared to the WM, with a less significance (*p<0.05). Conversely, for the other time-points and for the treatment condition, the injured area becomes significantly stiffer than the WM, starting from 1wpi (*Figure 83-B)*, with a higher statistical significance at 6wpi without and with treatment (*Figure 83-D,E*) compared to 1wpi and 2wpi (*Figure 83-C*). Also, the injury stiffness reaches an E value close to that of GM starting at 1wpi and no significant difference is observed thereafter between them.

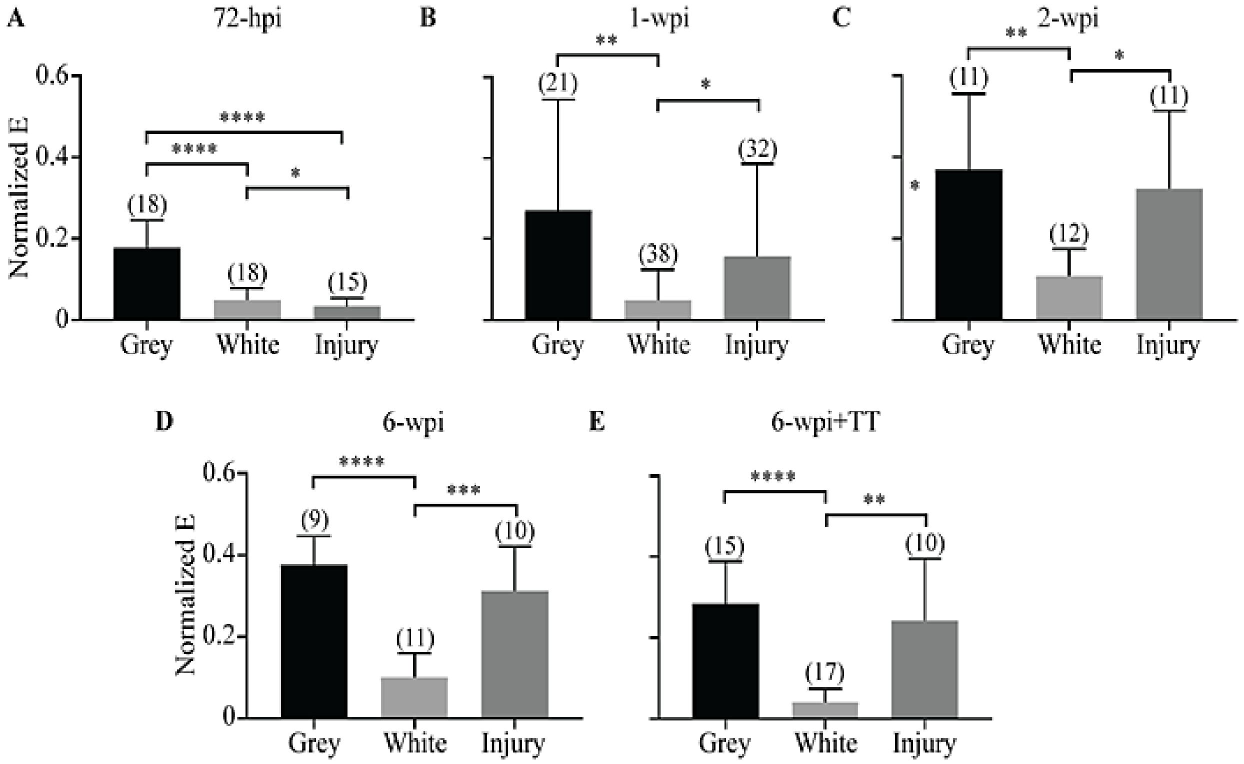

*Figure 83: Evolution of the normalized Young's modulus in time and with a treatment supplying. Comparison of Young's modulus values for grey matter, white matter and injury areas at: **A.** 72hpi, **B.** 1wpi, **C.** 2wpi, **D.** 6wpi without treatment and **E.** 6wpi with treatment supplying. 1-way ANOVA Tukey's multiple comparison mixed effect model was used to compare the area categories at each time-point (with * $p < 0.05$, **$p < 0.025$, *** $p < 0.001$ and **** $p < 0.0001$). Number of measurements is indicated in brackets.*

A closer look at the stiffness evolution of each SC area over time (*Figure 84*) highlights a more significant variation at the injury (*Figure 84-C*) between 72-hpi and the other time-points than in GM (*Figure 84-A*) or WM (*Figure 84-B*). This time-point could thus be considered as the key period for elastic properties changes at the injury site. More precisely, the initially soft injured tissue got even stiffer than the WM already at 1wpi (7±4 kPa; 0.04 normalized) reaching the elasticity value of GM at 2wpi (54±32 kPa; 0.32 normalized). The injury stiffness seems to stabilize at 2wpi as no significant difference was further found between 2wpi and 6wpi. No significant difference was reported between the elasticity of the treated and control group at 6wpi (*Figure 84-E*).

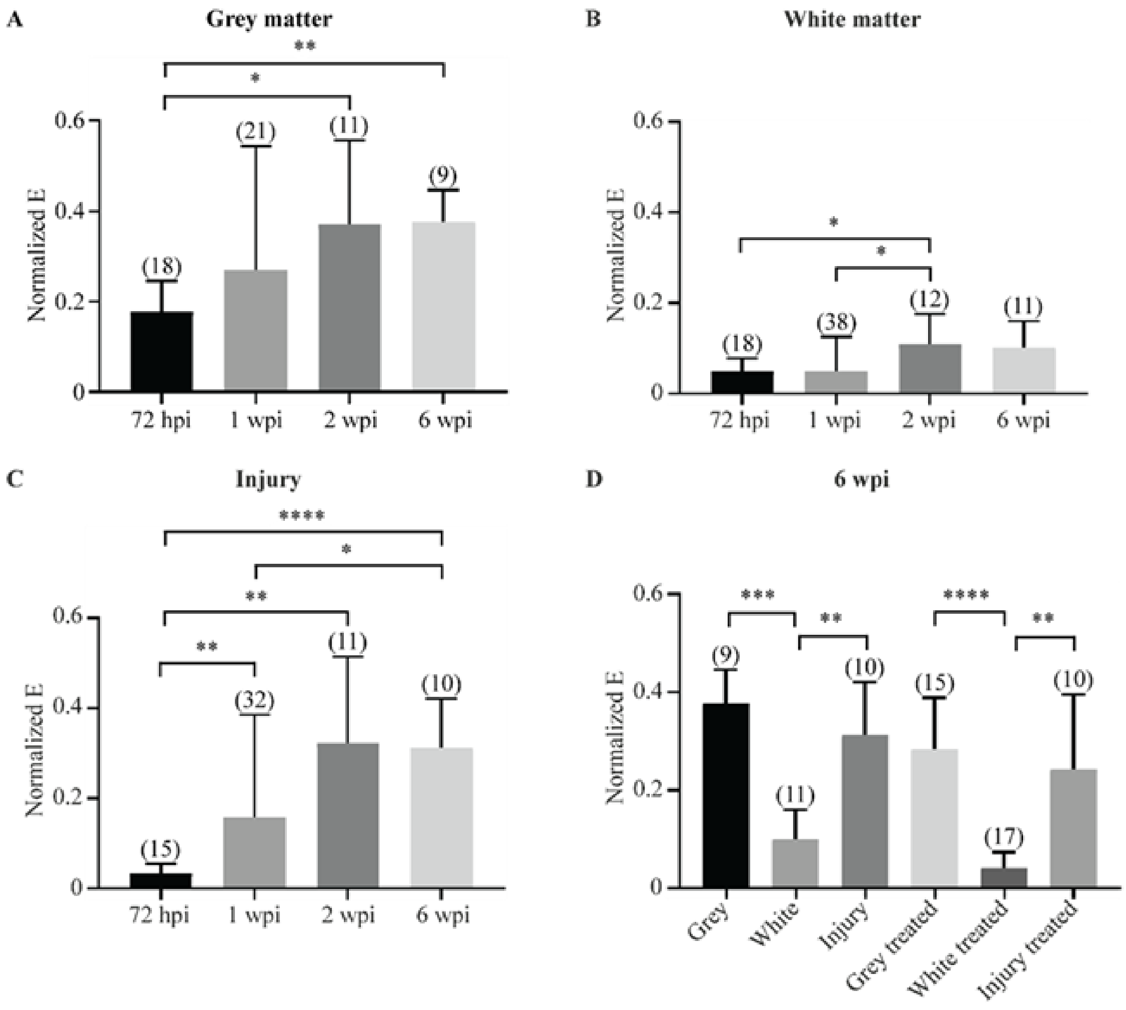

*Figure 84: Statistics of normalized Young's modulus for the three spinal cord area categories. Evolution of normalized Young's modulus values with the post-injury time-points in **A.** grey matter, **B.** white matter, **C.** injury area. **D.** Normalized E for these 3 areas at 6wpi without and with treatment supplying. Results suggest that the mechanical properties of the injury are more varying in time compared to those of grey and white matters, which are quite stable considering the samples variability. Globally, grey matter is stiffer than white matter and the injury appears to become stiffer from 1wpi. No difference is observed in the treated group compared to the control one at 6wpi (with * p < 0.05, **p< 0.025, *** p < 0.001, **** p < 0.0001). N indicated into brackets.*

Discussion: the injury site is softer than spared grey and white matter at 72hpi and hardens from 1wpi

AFM-FS measurements monitoring the elasticity modulus of GM, WM and of the injured area demonstrated that: i) GM is overall stiffer than WM, ii) the injured area is softer than the spared parts at 72-hpi, iii) but hardens from 1wpi and stabilizes at 2wpi.

Our findings can be discussed, based on a review (in Table 5) of SCI studies using AFM to evaluate the elasticity of the injured area and of spared SC parts, the GM and WM.

In a first work (Saxena et al., 2012) the authors studied the stiffness differences between healthy and injured tissues at 2wpi and 8wpi in a hemisection model in rats. Their results overall indicated that the healthy samples were significantly stiffer than those at both time-points post injury. In our work, the injury part was found almost as stiff as spared GM at 2wpi and 6 wpi and stiffer than spared WM at both time-points. Proper comparison cannot be done here since Saxena and collegues compared an entire healthy spinal cord to an entire injured one, while we worked with spared and injured tissue from the same spinal cord. Besides, we discriminated between GM and WM that could explain the discrepancy between the results. An interesting comparison would be between all the measurements we obtained on a healthy section and the measurements obtained on the entire spinal cord samples at 2wpi and 6wpi. An average softening could be obtained in line with our first observations about the tendency of softening of the GM areas located close to the lesion site. Another study on healthy and fresh spinal cords samples in mice found GM being stiffer than WM with a higher heterogeneity within GM than in WM (Koser et al., 2015). This finding is consistent with the relation we observed overtime and following treatment at 6wpi, in both axial and longitudinal sections. Moreover, as mentioned in the preliminary results part, while GM in injured parts showed a tendency of softening compared to spared areas, the behavior of WM was not so clear, probably implying the heterogeneity aspect defended by Koser and colleagues.

A work of Moeendarbary and colleagues (Moeendarbary et al., 2017) performed on fresh SC injured tissues in a crush injury model in rats, also reported that GM was stiffer than WM, and a softening of GM and WM was observed inside the lesion. In addition, this softening was positively correlated with gliosis markers such as glial intermediate filaments or ECM protein markers like collagen type IV, though, collagen I was not investigated in that context.

The stiffness at distance from the injured area was investigated in fresh tissues in a chronic hemisection model in rats (Baumann et al., 2020). A decrease in Young moduli close to the lesion was observed propagating away from the lesion core and was correlated with changes in the tissue composition.

Dominguez and colleagues (Domínguez-Bajo et al., 2019) similarly reported a softening of the injured area in a chronic cervical hemisection model in rats. However, here the injured area was referred as an “interface zone” (lesion zone located between a scaffold implant and the contralateral side).
Other mechanical properties assessments were conducted by Cooper and colleagues (Cooper et al., 2020) in a contusion model in rats at 12wpi. Interestingly, results showed that injured tissues were significantly stiffer at the lesion site than in spared tissues (including both GM and WM). The lesion site included two zones: lesion core (containing fibronectin) and lesion rim (defined as glial border). The authors hypothesized that chronic spinal cord tissue softening after SCI may be due to the presence of the fibrotic scar. They also discussed the possibility of lesion softening in the acute phase (Cooper et al., 2020)

Overall, the injury type, tissue preparation and also the anatomic plane considered (Koser et al., 2015) are various factors that could explain the discrepancy in the results previously reported. In a review focusing on the CNS mechanics (Viji Babu & Radmacher, 2019), the authors reported that cryotomed or fixed cells samples are commonly used for AFM imaging They subsequently pointed out that both methods increase the sample stiffness and that mechanical investigations on fixed samples are strongly affected by the sample preparation showing different results compared to living cells (Viji Babu and Radmacher, 2019). The authors underlined that sample preparation is challenging and they recommended agar embedment and vibratome sectioning to maintain tissue structure. The difference in elasticity of rats spinal cord tissues in function of sample preparation methods was investigated by Cooper and al. (Cooper et al., 2020). The frozen/throwing method was performed on snap frozen sham and fresh tissue preparation (based on Koser and colleagues’ work) was performed on uninjured samples. No stiffness difference was observed between GM and WM in both cases. Also, in Dominguez et al. study (Domínguez-Bajo et al., 2019), the authors performed a comparison between fresh and fixed tissues (obtained in a chronic hemisection model in rats) showing the same results, GM was stiffer than WM. Obtained values significantly increased in fixed samples (1324 Pa>269 Pa) as compared to fresh ones (275Pa>97 Pa).

Table 5: Review of AFM measurements in SCI studies

Title	Mechanical Characterization of the Injured Spinal Cord after Lateral Spinal Hemisection Injury in the Rat	CNS Cell Distribution and Axon Orientation Determine Local Spinal Cord Mechanical Properties	The soft mechanical signature of glial scars in the central nervous system
Year	2012	2015	2017
Authors	Saxena	Koser Moeendarbary Franze	Moeendarbary, Franze, Koser, Fawcett, Bradbury
Animal model	female Sprague-Dawley rats	C57BL/6 wild-type mice	12-weeks old female Lister hooded rats
N	5 ctrl 5 at 2-wpi 6 at 8-wpi	14 older than 3 months) female for indentation 7 male for creep	4 ctrl 3 at 1,5-wpi 3 at 3-wpi
GM_WM		GM>WM	GM>WM
Healthy_scar	Eu (unrelaxed elastic modulus): Healthy>scar Viscosity: 2-wpi>healthy 2-wpi > 8wpi		scar<healthy
Injury model	T9 hemisection right	Uninjured samples	Forceps crush injury
Sacrifice	2-wpi 8-wpi Deep anesthesia perfusion 1000mL PBS Dura mater kept	cervical dislocation	Euthatal i.p. cardiac perfusion with aCSF
Tissue conservation	PBS Stored 4°C	ice cold aCSF	aCSF 4°C
Sections	No section Samples were oriented rostrocaudally with the dorsal surface facing up. Spinal cords were adhered to a steel sample stage using a mildly adhesive double-sided tape	agarose cube Vibratome amplitude 1mm frequency 100 Hz speed 40µ/s Thick 500µm petri dishes coated with Cell-Tak	Agrose block vibratome 500 µm thick
AFM probe	spherical glass bead diameter 335µm Al cantilever Stepper motor	Spring cte 0,01 – 0,02N/m thermal noise Polystyrene beads diameter 37 µm	Spring cte 0,07N/m Thermal noise Polystyrene beads diameter 89µm
AFM parameters	<4h post mortem Submerged in PBS Custom microindentation system Max Force 25µN Step 400µm 100s 100Hz Indent : Healthy 140µm Scar 220µm	F/d curve every 50 µm MaxF 7nN Approach speed 10µ/s Data rate 1000Hz	Speed apporach 5-10µ/s Set F 30 nN Step 100µm
Model for fitting	modifed Standard Linear model (mSLM)	Indentation: Hertz Creep: Kelvin-Voigt	Hertz

Title	Softening of the chronic hemi-section spinal cord injury scar parallels dysregulation of cellular and extracellular matrix content	Spinal Cord Injury Results in Chronic Mechanical Stiffening Frozen-thawing process	Spinal Cord Injury Results in Chronic Mechanical Stiffening Fresh process, uninjured Compared with adjacent segments of frozen-thawing process : no difference
Year	2020	2020	
Authors	Bauman, Leipzig	Cooper et al.	
Animal model	10-weeks old female Fisher 344 rats	8-weeks-old female C57BL/6 wild-type mice	30-weeks old female C57BL/6 wild-type mice
N	3 ctrl 4 in chronic stage (15, 16, 17 and 18-wpi)	4 ctrl 4 at 12-wpi	2
GM_WM	GM>WM	GM = WM	GM = WM
Healthy_scar	scar<healthy	scar>healthy	
Injury model	T10 hemisection right	100 kdyn of impact force and a dwell time of 60 seconds severe T11 contusion SCI	Uninjured samples
Sacrifice	CO2 inhalation transcardial perfusion cold aCSF	CO2 Inhalation and perfused with 20mL ice-cold PBS	
Tissue conservation	stored in cold aCSF	snap frozen/thawing tissue embeded OCT frozen in dry-ice-cooled 2-methylbutane stored -80°C	fresh tissue embedded in 4% low melt agarose (Roche) at 37°C and kept on ice to rigidify the agarose.
Sections	Vibratome Embedding in 4% low melting point agarose sectioned in cold aCSF 500 µm Petri dish agarose secure	Cryostat Transverse 10 µm thick mounted on poly-L-lysine-coated glass slides Stored at -80C	Vibratome transverse 500 µm thick in PBS Mounted on glass slides coated with Cell-Tak adhesive
AFM probe	Spring cte 0.03N/m thermal noise 80 µm polystyrene bead	Spring cte 0,1N/m thermal tune 2.5 µm radius borosilicate sphere (Novascan)	
AFM parameters	4-8h post-mortem Speed 5 µm/s maxF20 nN Step 100 µm Avg indent 3µm Max indent 10µm	<2h ex vivo In PBS room T° 1µm indent (10 % thickness) 5–7 nN maps of 90x90-110x110 µm² (8x8 pixels; 11-15 µm space between points)	
Model for fitting	Hertz contact model	Hertz contact model	

Therefore, care should be taken to define absolute Youngs' modulus values and to compare them between various studies. Only relative variations can be addressed on similar samples recorded with the same AFM measurement and analysis pipeline. In our work, we found the same significant result of GM elasticity higher than WM elasticity, reported in many studies with unfixed samples. In any case, the softer nature of WM was likely related to myelin and other lipid-containing components (Domínguez-Bajo et al., 2019). Moreover, the hardening of the injured area overtime could be correlated with the formation of stiff collagen fibers. Therefore, we suggest that despite the fixation, the spinal cord tissue components kept their structure and show enough mechanical differences between the three areas (GM, WM, injury) to be at least relatively compared one to another.

III.5.3. Work in progress on elasticity assessments

To address the influence of tissue preparation on elasticity data, a first set of AFM-FS measurements were performed on snap frozen uninjured samples. We tested both longitudinal and axial sections for one mouse. The first results obtained are provided in the appendix section, showing no significant difference between GM and WM. Further quantitative analyses on a larger set of data are required to properly compare the results.

Other AFM-FS experiments are currently performed in the team aimed to evaluate more precisely the stiffness evolution close and at distance from the injury site in chosen areas of acquisition for all the categories (GM, WM and injury). In the results presented, measurements were carried out for one mouse at 2wpi with 12 measurements in WM, 6 in GM and 6 in the injury areas, as presented in *Figure 85*.

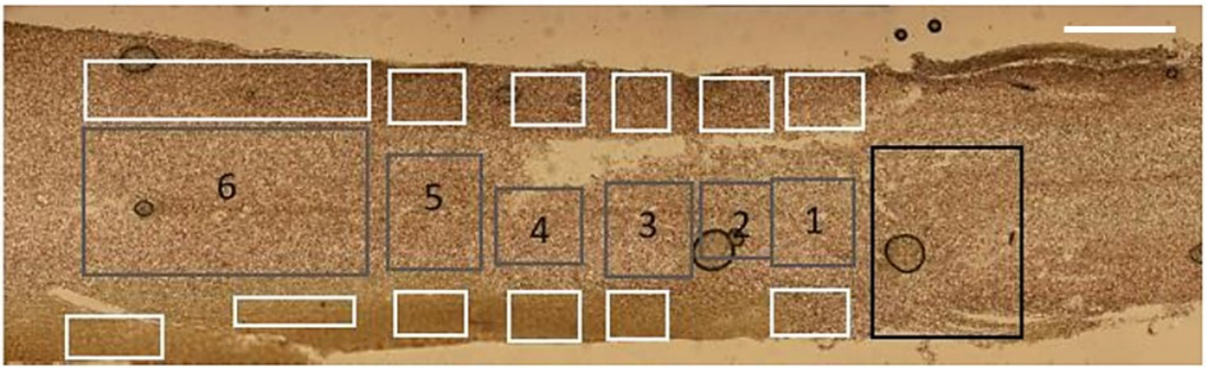

Figure 85: Acquisition areas in injured longitudinal spinal cord section in mouse at 2wpi. Grey matter areas (grey frames) are located in the sample center, white matter (white frames) on the border and the injury area is presented in the black frame. Scale bar is 500 µm.

Young's modulus comparison between the injury site and the GM and WM close and away from the lesion is shown *Figure 86*.

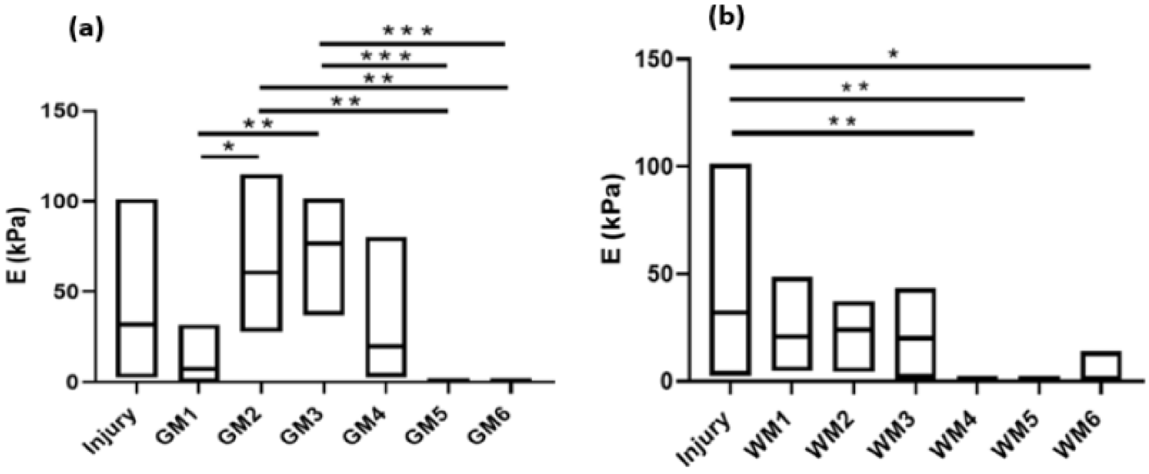

*Figure 86: Young's modulus (kPa) of the injury site at 2wpi compared to spare parts of grey matter (a) and white matter (b) located close or at distance from the injury (the number indicates an increasing distance). With * p< 0.05, **p< 0.025, *** p< 0.001.*

The injury stiffness shows no significant difference with that of GM (close or far) while is significantly stiffer than WM. This is consistent with our previous observations at 2wpi, where the injury depicted differences only with WM. To note is that these differences concern only the areas located away from the lesion. Also, a number of significant differences are observed between the GM areas located close and those away from the lesion, while no difference is evidenced for WM related to the location. GM stiffness right near the lesion site significantly increases away from the injury. The measurement performed on the furthest areas from the lesion site showed a GM softening. This could also be an interesting aspect to further investigate since it questions the tendency of softening in GM close to the injury we observed at 1wpi (that was not properly quantified).

Refining the acquisitions with AFM-FS to follow more precisely the stiffness evolution in all the areas on the spinal cord could be correlated with a more quantitative approach in collagen fibers characterization addressing the processes underlying the increased spreading of collagen in time observed in the SHG mosaic reconstructions.

III.6. Summary

To sum up the findings presented in the Results Chapter, we can state that the SHG signal, exhibited by fibrillar collagen, enabled to specifically monitor it as a marker of the spinal cord lesion. It was observed from 1wpi, specifically located at the injury site and showed a tendency of extension along the longitudinal axis in time up to 6wpi.

From the polarization dependent SHG signals, both straight and wavy-like fibril profiles were found overtime with a ROI-fiber approach that needs to be refined and conducted at pixel-level to perform quantitative analyses on an eventual profile prevailing.

At fiber-level, an increase in collagen fibers’ density together with increasing tortuosity overtime was observed with the Fingerprint algorithm. Other assessments on the fibers number, mean length or orientation, carried out with the CurveAlign software, did not exhibit any difference overtime. The accuracy in the fibers’ detection and the extraction of fibers’ metrics are intrinsic to the two methods and further studies are needed to optimize them to the specific case of spinal cord tissue where fibrillar collagen is not present in a healthy state.

Our investigations following oral GW2580 treatment at 6wpi showed that both collagen types I and IV became more restricted to the lesion site than in the control group. A lower fibers’ density was also quantified in the treated group, together with an apparent reduced fibrillar collagen extension. Less tortuous fibers were found than in the control group. The results suggested that inhibition of microglia proliferation could directly or indirectly modulate fibrillar collagen expression in the fibrotic scar. Further investigations on a larger set of data could provide complementary information about proliferative microglia and collagens roles in the scarring process.

Nano-mechanical investigations revealed a noticeable hardening of the injured area from 1wpi that is probably correlated with the apparition of fibrillar collagen. GM was found stiffer than WM, which is consistent with findings reported by other studies. However, since the tissue preparation, the lesion model or the AFM probe employed differ between works, comparison of elasticity values between works must be conducted with caution.

Altogether, our observations support the concomitance of important structural and mechanical modifications during the fibrotic scar evolution after spinal cord injury in a mouse hemisection model. Given that the supramolecular arrangement of the fibers has been reported to impact the stiffness of collagen in other tissues (Mercatelli et al., 2019), our further investigations could make a bridge between the mechanical behavior of the spinal cord injured tissue and the structure of the observed collagen fibers at supramolecular level.

The Table 6 and *Figure 87* are summarizing and illustrating our main findings.

Table 6: Qualitative and quantitative results of MPM-AFM investigations on hemisection model in mice

Aspect/metric	***Results***	***p-value****	***Comments***
Fibrillar collagen identification	Specifically revealed by SHG at the injury site from 1wpi Peroxidase staining revealed collagen I expression at all the time-points post injury.		IF-SHG co-localization not conclusive.
Fibrillar collagen formation	Apparent increasing extension in time up to 6wpi along rostro-caudal axis.		To be confronted to quantitative assessments.
GM softening at distance from lesion site	Tendency of GM softening observed near the lesion site.		Larger quantitative assessments required.
Collagen fibers supramolecular arrangement	Both straight and wavy-like fibrils profiles identified over time.		Pixel-level investigations for more relevant quantitative analyses. Relation to stiffness?
Fibers' density	Significant increase after 1wpi and significant decrease following treatment at 6wpi.	1wpi *vs* 2wpi:**0.038** 1wpi *vs* 6wpi:**0.282** Ctrl *vs* treated: **0.0102**	Could support further studies to assess collagen extension in all the Z-stacks planes.
Tortuosity	Tendency of increasing overtime and significant decrease following treatment at 6wpi.	Ctrl *vs* treated: **0.0011**	
E GM_WM	E GM> E WM for all the time-points and following treatment at 6wpi.	72-hpi: **<0.0001**; 1wpi: **0.0014**; 2wpi: **0.0023**; 6wpi: <**0.0001**	Relation to tissue preparation?

E injured_spared	Significant stiffness increase from 1wpi that stabilizes at 2wpi	72-hpi *vs* 1wpi:**0.0034** 72-hpi *vs* 2wpi:**0.0012** 72-hpi *vs* 6wpi:**<0.0001** 1wpi *vs* 2wpi:0.0686 1wpi *vs* 6wpi:**0.0215** 2wpi *vs* 6wpi:0.9994	

* significant **values in bold**

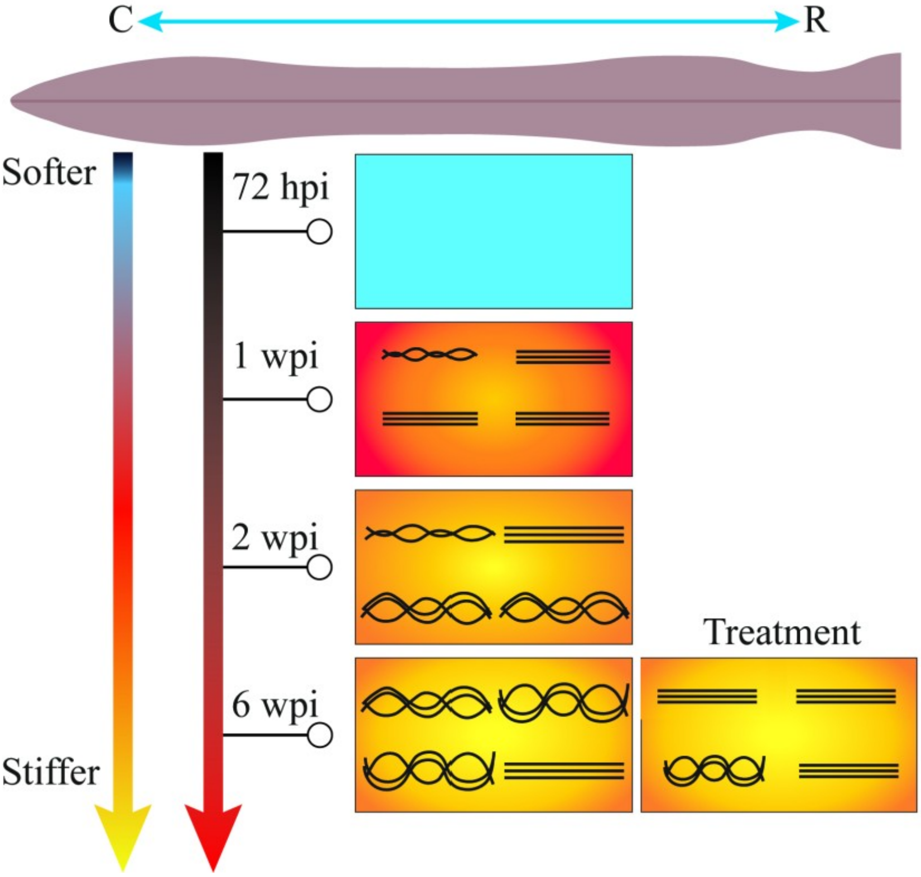

Figure 87 : Cartoon summarizing collagen fibers' organization and elastic properties of the fibrotic scar in spinal cord injury in mice. The injured area becomes stiffer over time (from blue to yellow). This could be related to the apparition of fibrillar collagen forming the fibrotic scar. Collagen fibers tended to become less straight with time and the fibers' density increased. A group treated with GW2580 was also considered at 6-wpi in which fibers were found to be more straight as in the control group, having also a lower fibers' density.

General conclusion and perspectives

The work exposed in this manuscript relied on the ability of imaging techniques in targeting and revealing specific structures or properties in a histopathology context. Moreover, the combination of various methods, (label-free or labeling) aimed to develop multimodal imaging approaches, led to a more precise and rich characterization of the spinal cord tissues depending on their state. Our multimodal approach, combining MPM (allowing both 2-PEF and SHG occurrence) and AFM as label-free techniques, completed by immunofluorescence and peroxidase immunostaining, was dedicated to the monitoring of the fibrotic scar, component of the scarring process that partially impedes the axonal regeneration after a SCI.

Chapter I presented general notions and the theoretical background to better apprehend the SCI model we employed, the techniques we combined and the data processing we developed. It started with the SCI context, a disease that despite not being so frequent is present worldwide and can lead to dramatic physics and psycho-social effects for the patients depending on the type of injury. The presentation of a healthy spinal cord state aimed to bring the sight from a naïve state, where tissue integrity is spared, towards the alteration of the homeostasis after the occurrence of a lesion. The description of the various changes following this alteration mainly in animal models highlighted the complexity of the tissular and the cellular response after a trauma. Among others, the scarring process reflects the complexity and diversity of the partners involved, such as microglial, astrocytes and fibroblasts that play both beneficial and deleterious roles. We reported in this introduction chapter a noticeable strategy related to our work that concerns the transient depletion of the proliferative part of microglia with GW2580, showing promising results in early and short–term treatment studies after spinal cord injury. An additional mention for this SCI section was the anatomical and physio-pathological difference between Human and animal models that has to be considered when investigating SCI (and more generally CNS diseases). The second part of Chapter I presented imaging techniques (label-free or through labeling) employed in SCI studies. It mainly aimed to support the methods we chose for the monitoring of the fibrotic scar. Overall, we could observe from this part that the routinely used immunolabeling and immunofluorescence are considered as important validation tools when combined with label-free techniques such as MPM. The occurrence of SHG in MPM offers considerable advantages in investigating non-centrosymmetric structures, such as the fibrillar collagen present in the fibrotic scar, together with a finer characterization of these structures with P-SHG. The last tool introduced was AFM that can be seen as a robust method in assessing mechanical properties of the tissue as long as the protocol has been adapted to the sample and that its strengths and limits have been considered for the results interpretation. It also appears from the examples mentioned that immunolabeling and AFM has been more widely employed in SCI than SHG. This aspect was further developed in the last part of Chapter I, dedicated to collagen description. The pro-collagen molecules assembly in the extracellular space is an important point to underlie in this section. It specifically defines the collagen type and is a good guidance for the collagen identification and characterization within a tissue. The other important consideration is that only fibrillar collagen can be detected by SHG. In the SCI context where collagen type IV (non fibrillar) has been more described than fibrillar collagen, monitoring SHG seems to be relevant in identifying them. The early recognition of collagen IV as a component of the fibrotic scar compared to fibrillar collagen could probably be an explanation for the scarcity of studies involving SHG to specifically target fibrillar collagen. Despite the increasing interest for SHG in SCI, only one major study properly identified and quantified fibrillar collagen type in a hemisection model in rat. This late consideration comforted us in the innovative aspect of our approach, completed with the mechanical investigation that, to our knowledge, had not been performed in combination with SHG in SCI before.

Chapter II provided methodological and technical details about our biological samples, the MPM setup, the AFM parameters and the data analysis. This chapter highlighted the potential of the proposed imaging techniques to address the biological questions also defining the sample preparation protocols. The start point focused on how the tissue were obtained: the mice (female CX3CR1$^{+/eGFP}$ expressing eGFP), the lesion model (lateral HS that have both advantages of being reproducible and of keeping intact half of the spinal cord that can be considered as a reference), the treatment (as reported in Chapter I, GW2580 was given orally just after SCI and during a short-term period starting right after the lesion and lasting 1 week), the sacrifice (at various time-points post injury to allow longitudinal analysis of the evolution of the fibrotic process through a large temporal window), the tissue preparation (ex vivo, fixed tissue). The last aspect was not optimal for AFM assessments but it was the best we could obtain in order to preserve the injury area. Snap frozen tissue, without fixation, could be obtained only for uninjured samples. Two anatomical planes were considered: the commonly used axial sections and longitudinal sections for easier collagen extension characterization. Complementary labeling techniques were employed: the peroxidase immunostaining for collagen type identification and the immunofluorescence for confrontation with SHG. The label-free imaging techniques were chosen to exploit various properties of the samples: with MPM, 2PEF aimed to reveal the eGFP expressed by microglial cells and SHG to reveal specifically fibrillar collagen in the fibrotic scar. The simultaneous acquisition of both signals enabled to visualize the different structures in the SC tissue. To reach the supramolecular arrangement of the collagen fibers with P-SHG, a combination of half-wave and quarter-wave plates was used for a fine monitoring of the incident light polarization angle, in order to obtain polarization curves profiles, related to specific symmetries of the detected structures. Finally, as a global view was required for collagen extension visualization, mosaic acquisitions were performed with circular polarization. With AFM, the measuring pipeline was defined according to the best sample preparation we had at the moment and relative elasticity (Young's modulus E) variations could be addressed this way. The probe was selected consistently with the biological samples and acquisition parameters (for optimal loading force or area scanning) were defined in line with theoretical requirements (as the indentation) and relevant mechanical assessments (comparison and evolution of GM, WM and injury elasticity). The last part of Chapter II described the data analyses we performed to extract and characterize collagen fibers at different levels. Software and metrics were chosen and defined as relevantly as possible to overcome issues related to tissue dissipative properties and to SCI samples' variation. The approach for supramolecular level investigations aimed to provide a first highlight of fibrils' nature in spinal cord injured tissues by manually selecting a set of fibrils/bundles and estimating their profiles (straight or wavy-like) overtime and following treatment at 6wpi. Larger P-SHG intensity maps are required for further quantitative analysis on pixel level. Collagen fibers were also characterized at tissue level, first with CurveAlign software, specifically dedicated to collagen fibers assessments (in cancer tissues) and allowing extraction of various fibers' metrics such as fibers' number, length, or alignment. The CT implemented in the software was a valuable (and open access) tool to identify some analysis limitations specific to our study (for example the identification of undergrowth collagen fibers in SCI tissues). It eventually led to a home-built algorithm development, based on the Fingerprint (FP) method, to refine more appropriate metrics. Our FP method generated a skeleton untangled map (for fibers identification) on which several metrics were calculated for fibers characterization: fibers' density, tortuosity, statistical entropy (global orientation) and circular variance of the local orientation.

Chapter III presented the results obtained from the structural (collagen fibers' characterization) and mechanical (E- Young's modulus relative variation) investigations performed on the fibrotic scar. A general description of the tissues (MPM and AFM studies) was first provided at 1wpi on axial and longitudinal sections, pointing out overall similar observations in both sections types, together with differences between spared and injured samples at this post injury time-point. These preliminary measurements described the specific localization of fibrillar collagen at the lesion site together with significant E variations between GM, WM and injury. It corroborated the interest on monitoring these parameters in time and following treatment. The second part of Chapter III thus focused on collagen extension evolution and explored a more precise and quantitative description of collagen fibers and of the Young's modulus. Both collagen types I and IV were identified and their extension were observed through peroxidase staining, showing gradual formation of fibrillar collagen with an increasing overtime. A reduced area of expression following treatment at 6wpi was observed. This was a qualitative observation and we did not perform quantifications using these stainings. Immunofluorescence evidenced collagen types I and IV in the injured tissues but no clear co-localization with SHG was achieved for collagen I. The main highlights for fibrillar collagen fibers were the presence of both fibrils profiles together with a significant fibers' density increase overtime while a significant fibers' density decrease was observed following treatment at 6wpi. Fibers' density measurements supported the observations done with peroxidase staining. A tendency of increasing tortuosity overtime was also observed with a significant decrease following treatment. Mechanical properties also presented changes overtime with an injury site stiffening from 1wpi which likely stabilized at 2wpi. Eventually, the increasing collagen deposition at the lesion site can be associated to the injury hardening. Overall, our imaging approaches enabled to gather valuable data at micro/nano resolution on excised spinal cord tissues. Relevant markers could be obtained, sensitive enough to assess structural and mechanical modifications of the fibrotic scar formation over time in a hemisection SCI mouse model. We reported and characterize the formation of fibrillar collagen that gradually invades the injury site from 1wpi to 6wpi. Further investigations are necessary to better understand the origin of the fibrotic process observed within the glial scar sustained by the hardening of the injured spinal cord tissue. For example measuring collagen fibers' extension along the rostro-caudal axis with smaller tills (allowing a more detailed mosaic reconstruction) could be correlated to the evolution of the tissue elasticity and thus lead to a more precise monitoring of structural and mechanical changes along the rostro-caudal axis of the injured spinal cord. Also, additional studies in other models of spinal cord injury would permit to investigate whether collagen formation depends on the type of lesion.

The current perspectives of this work relate on an additional label-free imaging technique, the Broadband Coherent Anti-stokes Raman spectroscopy (or BCARS). This imaging technique is under test in the laboratory. BCARS is an optical technique based on Raman spectroscopy, measuring the inelastic scattering of light by vibrating molecules, hence providing the chemical fingerprints of cells, tissues or biofluids (Kong et al., 2015). The high chemical specificity, minimal or lack of sample preparation and the ability to work with advanced optical technologies in the visible or near-infrared spectral range have recently led to an increased use of Raman spectroscopy in various medical diagnostic applications (Krafft & Popp, 2019; Ryzhikova et al., 2015; Wang et al., 2015). Moreover, the specific Raman signature of drugs permits their co-localisation within the cells/tissues with high precision. However, as Raman scattering efficiency is quite low, requiring relatively long acquisition times, a new technology based on BCARS (or fast Raman) was proposed (Camp Jr et al., 2014).

BCARS allows the detection of the fingerprint region of molecules (500-1500 cm-^{1}) and could probe multiple Raman transitions simultaneously, to allow imaging of biological tissues with improved molecular contrast. BCARS principle is illustrated in *Figure 88*. When compared to spontaneous Raman microscopy, BCARS microscopy provided 10- 100x faster image acquisition for quantitative and qualitative assessment of molecules at much higher spatiochemical resolution and with spectra of much higher signal-to noise ratio (Hartshorn et al., 2013).

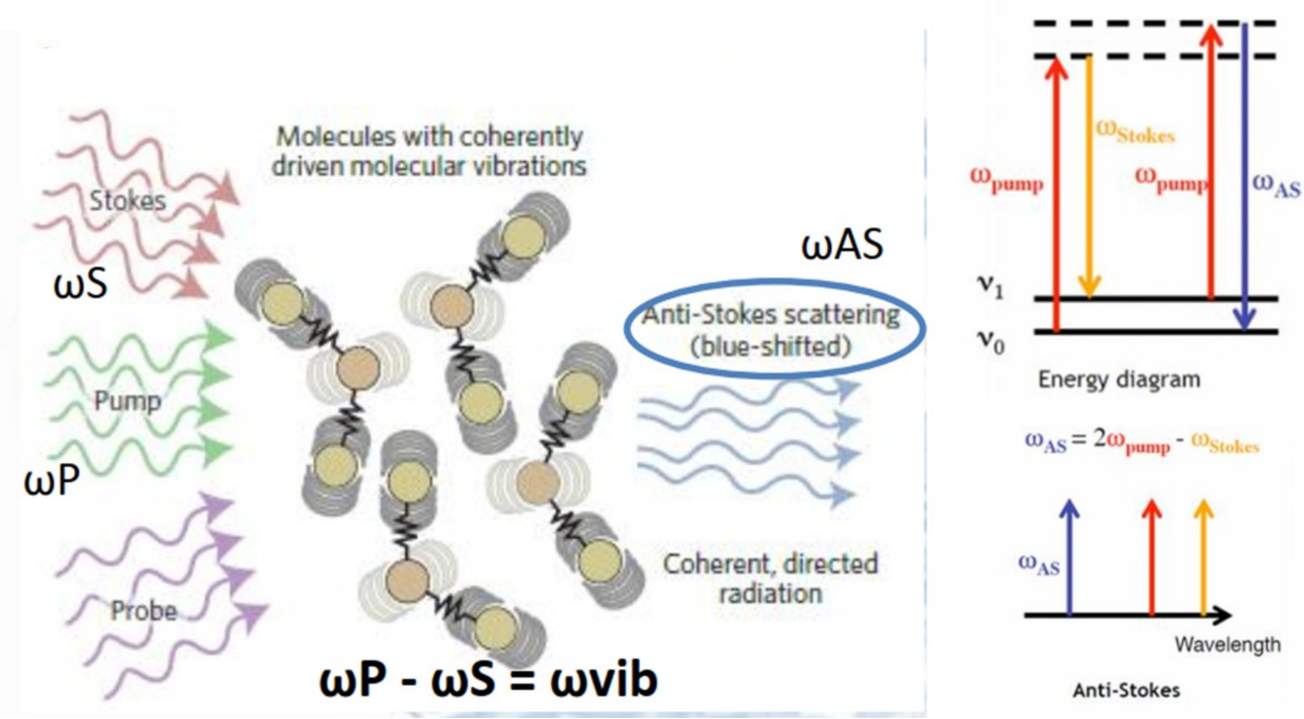

Figure 88: CARS principle (left) with the energy level diagram and excitation/emission wavelengths along the wavelength axis (right). BCARS spectra are obtained by applying a mathematical correction to CARS acquisitions in order to retrieve the fingerprint region of the molecules. Modified from (Camp Jr & Cicerone, 2015).

Raman enabled to discriminate between collagen type I and IV (Nguyen et al., 2012) and thus could be a pertinent complementary tool for instance to determine the collagen type in the fibrotic scar. In the SCI context, Raman has already been used to identify the chemical components of injured tissues in a chronic (3 weeks post injury) hemisection model in rats (Galli et al., 2012) and in a compression model in rats at different time-points post injury (J. Li et al., 2019). Typical results are presented in Table 7, summarized from Galli and colleagues work (Galli et al., 2012).

Table 7: Typical results from Raman acquisitions in SCI

Technique employed	Raman Band position [cm^{-1}]	Vibrational mode	Chemical compounds	
			Family	Species
	Healthy / SCI model			
FT-IR, Spontaneous Raman, CARS	700/(<)	sterol ring	Lipids	Cholesterol
	830-850/(>)	v(CC), v(CO), v(PO$_2^-$)	AA, Saccharides, Nucleic Acid	, , DNA
	1003/no	v(C-C)	AA	Phenylalaline
	1063/(<)	v(C-C)	Lipids	
	1130/no	v(C-C)	Lipids	
	no/1237			**Collagen zone - Fibrotic scar**
	no/1280			
	1300/(<)	d[(CH$_2$)]	Lipids	Collagen zone ?
	1440/(<)	d[(CH$_2$)]	Lipids	
	1658/	amide I	Proteins	
	1668/	v(C=C)	Lipids	
	2850	v [(CH2)] sym.	Lipids	
	2882	v[(CH3)] sym.	Lipids	
	2900	v [(CH2)] asym.	Lipids	

Similar findings could be obtained in our work to identify more accurately the chemical components within our spared and injured tissues (overtime and following treatment) and to potentially confront them to the structural and mechanical changes reported.

A last potential application of our multimodal label-free strategy is the exploration of Human spinal cord with MPM and AFM. Preliminary observations (*Figure 89* and *Figure 90*) showed a promising field of work for structural and mechanical characterization of a healthy spinal cord that could eventually enrich knowledge about spinal cord injury in humans.

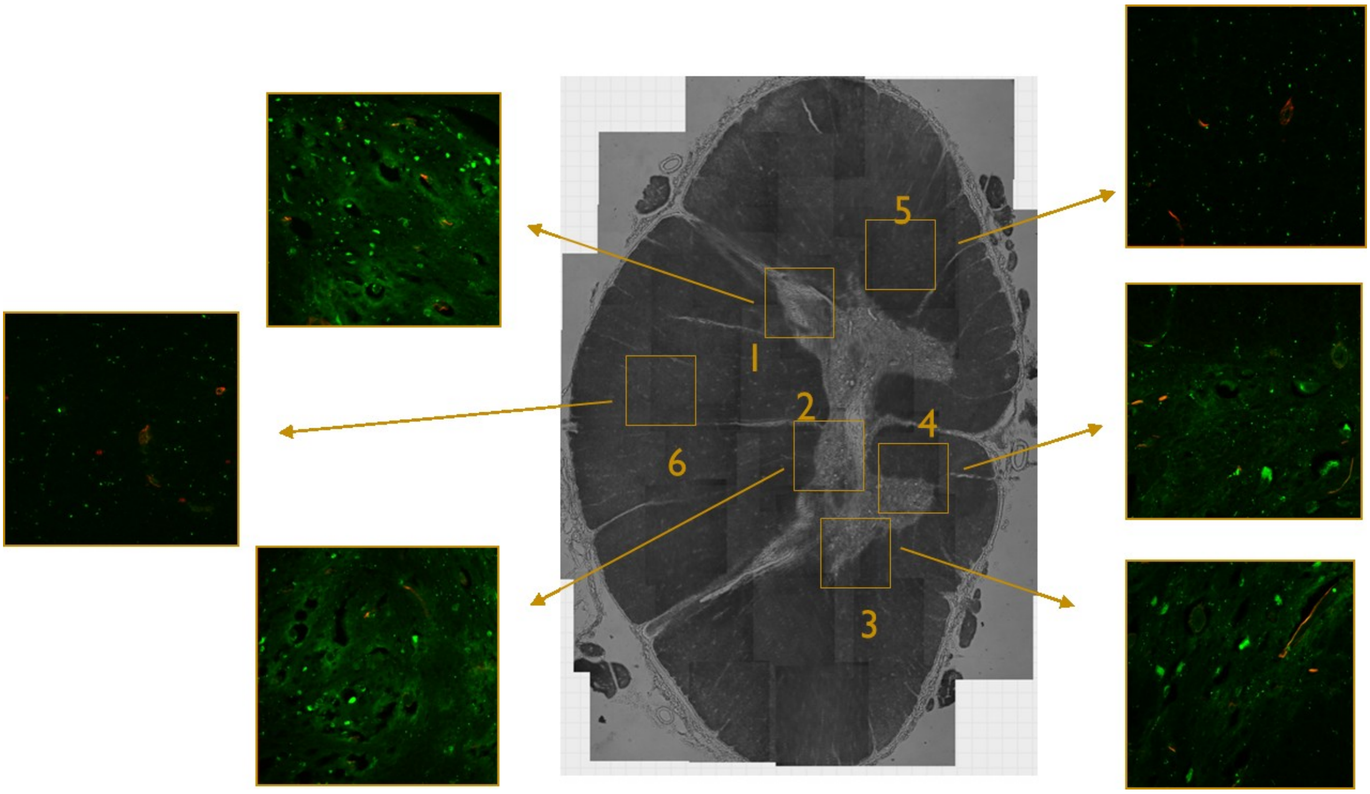

Figure 89: MPM acquisitions on various areas in healthy human spinal cord (axial section). 2PEF signal (green) emitted by autofluorescent structures (here probably mitochondria) and scarce SHG signal (red) by filaments or cell division.

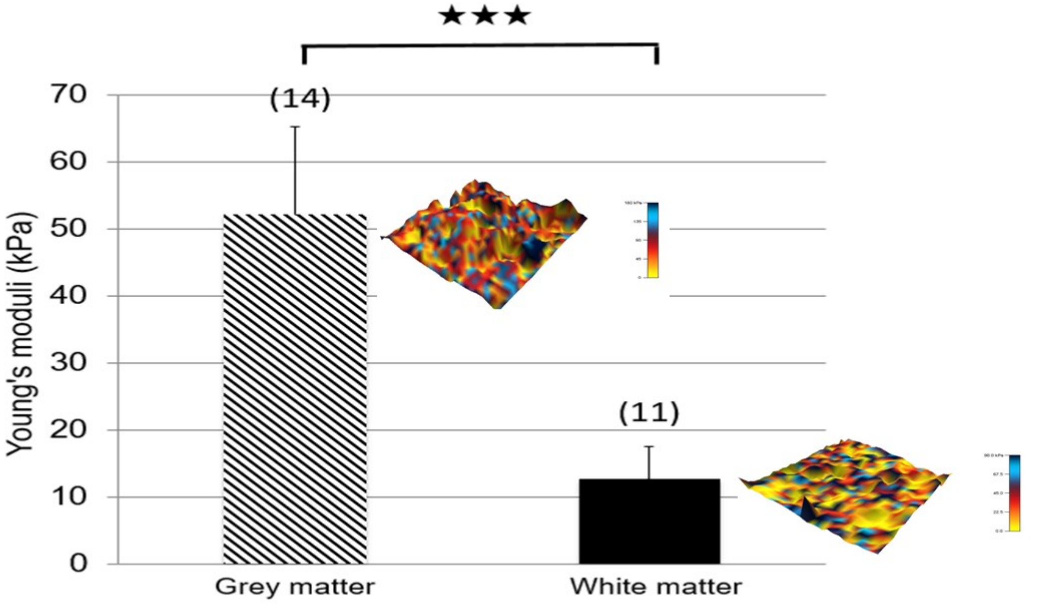

*Figure 90: Young's moduli of Grey and White matters in healthy human spinal cord with 3D height reconstruction. Color scale corresponds to Young's modulus (E) variation (blue for stiff, yellow for soft). *** $p < 0.001$, N into brackets.*

References

Ahuja, C. S., Wilson, J. R., Nori, S., Kotter, M. R. N., Druschel, C., Curt, A., & Fehlings, M. G. (2017). Traumatic spinal cord injury. *Nature Reviews Disease Primers*, *3*(1), 17018. https://doi.org/10.1038/nrdp.2017.18

Alizadeh, A., Dyck, S. M., & Karimi-Abdolrezaee, S. (2015). Myelin damage and repair in pathologic CNS: challenges and prospects. *Frontiers in Molecular Neuroscience*, *8*. https://doi.org/10.3389/fnmol.2015.00035

Alizadeh, A., Dyck, S. M., & Karimi-Abdolrezaee, S. (2019). Traumatic Spinal Cord Injury: An Overview of Pathophysiology, Models and Acute Injury Mechanisms. *Frontiers in Neurology*, *10*, 282. https://doi.org/10.3389/fneur.2019.00282

Alturkistani, H. A., Tashkandi, F. M., & Mohammedsaleh, Z. M. (2015). Histological Stains: A Literature Review and Case Study. *Global Journal of Health Science*, *8*(3), 72. https://doi.org/10.5539/gjhs.v8n3p72

Anik, I., Kokturk, S., Genc, H., Cabuk, B., Koc, K., Yavuz, S., Ceylan, S., Ceylan, S., Kamaci, L., & Anik, Y. (2011). Immunohistochemical analysis of TIMP-2 and collagen types I and IV in experimental spinal cord ischemia–reperfusion injury in rats. *The Journal of Spinal Cord Medicine*, *34*(3), 257-264. https://doi.org/10.1179/107902611X12972448729648

Aptel, F., Olivier, N., Deniset-Besseau, A., Legeais, J.-M., Plamann, K., Schanne-Klein, M.-C., & Beaurepaire, E. (2010). Multimodal Nonlinear Imaging of the Human Cornea. *Investigative Opthalmology & Visual Science*, *51*(5), 2459. https://doi.org/10.1167/iovs.09-4586

Arseni, L., Lombardi, A., & Orioli, D. (2018). From Structure to Phenotype: Impact of Collagen Alterations on Human Health. *International Journal of Molecular Sciences*, *19*(5), 1407. https://doi.org/10.3390/ijms19051407

Bancelin, S., Lynch, B., Bonod-Bidaud, C., Ducourthial, G., Psilodimitrakopoulos, S., Dokládal, P., Allain, J.-M., Schanne-Klein, M.-C., & Ruggiero, F. (2015). Ex vivo multiscale quantitation of skin biomechanics in wild-type and genetically-modified mice using multiphoton microscopy. *Scientific Reports*, *5*(1), 17635. https://doi.org/10.1038/srep17635

Baptiste, D. C., & Fehlings, M. G. (2007). Update on the treatment of spinal cord injury. In *Progress in Brain Research* (Vol. 161, p. 217-233). Elsevier. https://doi.org/10.1016/S0079-6123(06)61015-7

Basso, D. M., Fisher, L. C., Anderson, A. J., Jakeman, L. B., Mctigue, D. M., & Popovich, P. G. (2006). Basso Mouse Scale for Locomotion Detects Differences in Recovery after Spinal Cord Injury in Five Common Mouse Strains. *Journal of Neurotrauma*, *23*(5), 635-659. https://doi.org/10.1089/neu.2006.23.635

Batista, A. (2018). *Two-photon imaging of the cornea using femtosecond* [Universität des Saarlandes]. www.researchgate.net.

Baumann, H. J., Mahajan, G., Ham, T. R., Betonio, P., Kothapalli, C. R., Shriver, L. P., & Leipzig, N. D. (2020). Softening of the chronic hemi-section spinal cord injury scar parallels dysregulation of cellular and extracellular matrix content. *Journal of the Mechanical Behavior of Biomedical Materials*, *110*, 103953. https://doi.org/10.1016/j.jmbbm.2020.103953

Bellver-Landete, V., Bretheau, F., Mailhot, B., Vallières, N., Lessard, M., Janelle, M.-E., Vernoux, N., Tremblay, M.-È., Fuehrmann, T., Shoichet, M. S., & Lacroix, S. (2019). Microglia are an essential component of the neuroprotective scar that forms after spinal cord injury. *Nature Communications*, *10*(1), 518. https://doi.org/10.1038/s41467-019-08446-0

Benzina, O., Szabo, V., Lucas, O., Saab, M., Cloitre, T., Scamps, F., Gergely, C., & Martin, M. (2013). Changes induced by peripheral nerve injury in the morphology and nanomechanics of sensory neurons. *Journal of Biomedical Optics*, *18*(10), 106014. https://doi.org/10.1117/1.JBO.18.10.106014

Berens, P. (2009). CircStat : A MATLAB Toolbox for Circular Statistics. *Journal of Statistical Software*, *31*(10). https://doi.org/10.18637/jss.v031.i10

Boyd, R. W. (2008). Nonlinear optics. In *Springer Handbook of Atomic, Molecular, and Optical Physics* (Cham: Springer International Publishing, p. 1097-1110).

Bredfeldt, J. S., Liu, Y., Pehlke, C. A., Conklin, M. W., Szulczewski, J. M., Inman, D. R., Keely, P. J., Nowak, R. D., Mackie, T. R., & Eliceiri, K. W. (2014). Computational segmentation of collagen fibers from second-harmonic generation images of breast cancer. *Journal of Biomedical Optics*, *19*(1), 016007. https://doi.org/10.1117/1.JBO.19.1.016007

Brown, J. C., & Timpl, R. (1995). The Collagen Superfamily. *Int Arch Allergy Immunol*, *107*(4), 484-490. https://doi.org/10.1159/000237090

Camp Jr, C. H., & Cicerone, M. T. (2015). Chemically sensitive bioimaging with coherent Raman scattering. *Nature Photonics*, *9*(5), 295-305. https://doi.org/10.1038/nphoton.2015.60

Camp Jr, C. H., Lee, Y. J., Heddleston, J. M., Hartshorn, C. M., Walker, A. R. H., Rich, J. N., Lathia, J. D., & Cicerone, M. T. (2014). High-speed coherent Raman fingerprint imaging of biological tissues. *Nature Photonics*, *8*(8), 627-634. https://doi.org/10.1038/nphoton.2014.145

Candès, E., Demanet, L., Donoho, D., & Ying, L. (2006). Fast Discrete Curvelet Transforms. *Multiscale Modeling & Simulation*, *5*(3), 861-899. https://doi.org/10.1137/05064182X

Chen, X., Nadiarynkh, O., Plotnikov, S., & Campagnola, P. J. (2012). Second harmonic generation microscopy for quantitative analysis of collagen fibrillar structure. *Nature Protocols*, *7*(4), 654-669. https://doi.org/10.1038/nprot.2012.009

Chen, X., Wang, S., & Chen, J. (2021). Label-free imaging of spinal cords injured tissues with multiphoton microscopy. *Optics in Health Care and Biomedical Optics XI*, *11900*, 209-2013.

Chen, Y., Tang, Y., Vogel, L., & DeVivo, M. (2013). Causes of Spinal Cord Injury. *Topics in Spinal Cord Injury Rehabilitation*, *19*(1), 1-8. https://doi.org/10.1310/sci1901-1

Cheng, Y.-T., Lett, K. M., & Schaffer, C. B. (2019). Surgical preparations, labeling strategies, and optical techniques for cell-resolved, in vivo imaging in the mouse spinal cord. *Experimental Neurology*, *318*, 192-204. https://doi.org/10.1016/j.expneurol.2019.05.010

Cheriyan, T., Ryan, D. J., Weinreb, J. H., Cheriyan, J., Paul, J. C., Lafage, V., Kirsch, T., & Errico, T. J. (2014). Spinal cord injury models: a review. *Spinal Cord*, *52*(8), 588-595. https://doi.org/10.1038/sc.2014.91

Churnside, A. B., Sullan, R. M. A., Nguyen, D. M., Case, S. O., Bull, M. S., King, G. M., & Perkins, T. T. (2012). Routine and Timely Sub-picoNewton Force Stability and Precision for Biological Applications of Atomic Force Microscopy. *Nano Letters*, *12*(7), 3557-3561. https://doi.org/10.1021/nl301166w

Cicchi, R., Vogler, N., Kapsokalyvas, D., Dietzek, B., Popp, J., & Pavone, F. S. (2013). From molecular structure to tissue architecture: collagen organization probed by SHG microscopy. *Journal of Biophotonics*, *6*(2), 129-142. https://doi.org/10.1002/jbio.201200092

Cicerone, M. T., & Camp, C. H. (2018). Histological coherent Raman imaging: a prognostic review. *The Analyst*, *143*(1), 33-59. https://doi.org/10.1039/C7AN01266G

Cisek, R., Joseph, A., Harvey, M., & Tokarz, D. (2021). Polarization-Sensitive Second Harmonic Generation Microscopy for Investigations of Diseased Collagenous Tissues. *Frontiers in Physics*, *9*. https://doi.org/10.3389/fphy.2021.726996

Cooper, J. G., Sicard, D., Sharma, S., Van Gulden, S., McGuire, T. L., Cajiao, M. P., Tschumperlin, D. J., & Kessler, J. A. (2020). Spinal Cord Injury Results in Chronic Mechanical Stiffening. *Journal of Neurotrauma*, *37*(3), 494-506. https://doi.org/10.1089/neu.2019.6540

Cripps, R. A., Lee, B. B., Wing, P., Weerts, E., Mackay, J., & Brown, D. (2011). A global map for traumatic spinal cord injury epidemiology: towards a living data repository for injury prevention. *Spinal Cord*, *49*(4), 493-501. https://doi.org/10.1038/sc.2010.146

David, S., & Kroner, A. (2011). Repertoire of microglial and macrophage responses after spinal cord injury. *Nature Reviews Neuroscience*, *12*(7), 388-399. https://doi.org/10.1038/nrn3053

de Vries, J. J., Laan, D. M., Frey, F., Koenderink, G. H., & de Maat, M. P. M. (2023). A systematic review and comparison of automated tools for quantification of fibrous networks. *Acta Biomater*, *157*, 263-274. https://doi.org/10.1016/j.actbio.2022.12.009.

Despotović, S. Z., & Ćosić, M. (2022). The Morphological Analysis of the Collagen Fiber Straightness in the Healthy Uninvolved Human Colon Mucosa Away From the Cancer. *Frontiers in Physics*, *10*, 915644. https://doi.org/10.3389/fphy.2022.915644

Despotović, S. Z., Milićević, Đ. N., Krmpot, A. J., Pavlović, A. M., Živanović, V. D., Krivokapić, Z., Pavlović, V. B., Lević, S., Nikolić, G., & Rabasović, M. D. (2020). Altered organization of collagen fibers in the uninvolved human colon mucosa 10 cm and 20 cm away from the malignant tumor. *Scientific Reports*, *10*(1), 6359. https://doi.org/10.1038/s41598-020-63368-y

Dias, D. O., Kim, H., Holl, D., Werne Solnestam, B., Lundeberg, J., Carlén, M., Göritz, C., & Frisén, J. (2018). Reducing Pericyte-Derived Scarring Promotes Recovery after Spinal Cord Injury. *Cell*, *173*(1), 153-165.e22. https://doi.org/10.1016/j.cell.2018.02.004

Domínguez-Bajo, A., González-Mayorga, A., Guerrero, C. R., Palomares, F. J., García, R., López-Dolado, E., & Serrano, M. C. (2019). Myelinated axons and functional blood vessels populate mechanically compliant rGO foams in chronic cervical hemisected rats. *Biomaterials*, *192*, 461-474. https://doi.org/10.1016/j.biomaterials.2018.11.024

Ducourthial, G., Affagard, J., Schmeltz, M., Solinas, X., Lopez-Poncelas, M., Bonod-Bidaud, C., Rubio-Amador, R., Ruggiero, F., Allain, J., Beaurepaire, E., & Schanne-Klein, M. (2019). Monitoring dynamic collagen reorganization during skin stretching with fast polarization-resolved second harmonic generation imaging. *Journal of Biophotonics*, *12*(5). https://doi.org/10.1002/jbio.201800336

Duncan, G. J., Manesh, S. B., Hilton, B. J., Assinck, P., Liu, J., Moulson, A., Plemel, J. R., & Tetzlaff, W. (2018). Locomotor recovery following contusive spinal cord injury does not require oligodendrocyte remyelination. *Nature Communications*, *9*(1), 3066. https://doi.org/10.1038/s41467-018-05473-1

Fadili, J. M., & Starck, J.-L. (2009). Curvelets and Ridgelets. In *Encyclopedia of Complexity and Systems Science* (R.A. Meyers, ed., p. 1718-1738). Springer New York.

Farrar, M. J., Wise, F. W., Fetcho, J. R., & Schaffer, C. B. (2011). In Vivo Imaging of Myelin in the Vertebrate Central Nervous System Using Third Harmonic Generation Microscopy. *Biophysical Journal*, *100*(5), 1362-1371. https://doi.org/10.1016/j.bpj.2011.01.031

Forgione, N., & Fehlings, M. G. (2013). Novel insights into pathophysiology and emerging therapeutic opportunities. In M. G. Fehlings, *Critical Care in Spinal Cord Injury* (p. 22-44). Future Medicine Ltd. https://doi.org/10.2217/ebo.12.150

Frank, R., & Hargreaves, R. (2003). Clinical biomarkers in drug discovery and development. *Nature Reviews Drug Discovery*, *2*(7), 566-580. https://doi.org/10.1038/nrd1130

Fu, Y., Huff, T. B., Wang, H.-W., Cheng, J.-X., & Wang, H. (2008). Ex vivo and in vivo imaging of myelin fibers in mouse brain by coherent anti-Stokes Raman scattering microscopy. *Optics Express*, *16*(24), 19396. https://doi.org/10.1364/OE.16.019396

Gailhouste, L., Grand, Y. L., Odin, C., Guyader, D., Turlin, B., Ezan, F., Désille, Y., Guilbert, T., Bessard, A., Frémin, C., Theret, N., & Baffet, G. (2010). Fibrillar collagen scoring by second harmonic microscopy: A new tool in the assessment of liver fibrosis. *Journal of Hepatology*, *52*(3), 398-406. https://doi.org/10.1016/j.jhep.2009.12.009

Galli, R. (2018). Label-free multiphoton microscopy reveals relevant tissue changes induced by alginate hydrogel implantation in rat spinal cord injury. *SCIenTIFIC REPOrTS*, 13.

Galli, R., Sitoci-Ficici, K. H., Uckermann, O., Later, R., Marečková, M., Koch, M., Leipnitz, E., Schackert, G., Koch, E., Gelinsky, M., Steiner, G., & Kirsch, M. (2018). Label-free multiphoton microscopy reveals relevant tissue changes induced by alginate hydrogel implantation in rat spinal cord injury. *Scientific Reports*, *8*(1), 10841. https://doi.org/10.1038/s41598-018-29140-z

Galli, R., Uckermann, O., Winterhalder, M. J., Sitoci-Ficici, K. H., Geiger, K. D., Koch, E., Schackert, G., Zumbusch, A., Steiner, G., & Kirsch, M. (2012). Vibrational Spectroscopic Imaging and Multiphoton Microscopy of Spinal Cord Injury. *Analytical Chemistry*, *84*(20), 8707-8714. https://doi.org/10.1021/ac301938m

Gatto, R. G., Amin, M. Y., Deyoung, D., Hey, M., Mareci, T. H., & Magin, R. L. (2018). Ultra-High Field Diffusion MRI Reveals Early Axonal Pathology in Spinal Cord of ALS mice. *Translational Neurodegeneration*, *7*(1), 20. https://doi.org/10.1186/s40035-018-0122-z

Gavara, N. (2017). A beginner's guide to atomic force microscopy probing for cell mechanics: GAVARA. *Microscopy Research and Technique*, *80*(1), 75-84. https://doi.org/10.1002/jemt.22776

Gerber, Y. N., Saint-Martin, G. P., Bringuier, C. M., Bartolami, S., Goze-Bac, C., Noristani, H. N., & Perrin, F. E. (2018a). CSF1R Inhibition Reduces Microglia Proliferation, Promotes Tissue Preservation and Improves Motor Recovery After Spinal Cord Injury. *Frontiers in Cellular Neuroscience*, *12*. https://doi.org/10.3389/fncel.2018.00368

Gerber, Y. N., Saint-Martin, G. P., Bringuier, C. M., Bartolami, S., Goze-Bac, C., Noristani, H. N., & Perrin, F. E. (2018b). CSF1R Inhibition Reduces Microglia Proliferation, Promotes Tissue Preservation and Improves Motor Recovery After Spinal Cord Injury. *Frontiers in Cellular Neuroscience*, *12*, 368. https://doi.org/10.3389/fncel.2018.00368

Golaraei, A., Kontenis, L., Mirsanaye, K., Krouglov, S., Akens, M. K., Wilson, B. C., & Barzda, V. (2019). Complex Susceptibilities and Chiroptical Effects of Collagen Measured with Polarimetric Second-Harmonic Generation Microscopy. *Scientific Reports*, *9*(1), 12488. https://doi.org/10.1038/s41598-019-48636-w

Gong, Y., Liang, Z., Yin, Y., Song, J., Hu, X., Wang, K., He, Q., Wang, Z., Bai, J., & Wang, S. (2017). Interpreting the biochemical specificity of mouse spinal cord by confocal raman microspectral imaging. *Journal of Innovative Optical Health Sciences*, *10*(05), 1743007. https://doi.org/10.1142/S1793545817430076

Gong, Y., Wang, S., Liang, Z., Wang, Z., Zhang, X., Li, J., Song, J., Hu, X., Wang, K., He, Q., & Bai, J. (2018). Label-Free Spectral Imaging Unveils Biochemical Mechanisms of Low-Level Laser Therapy on Spinal Cord Injury. *Cellular Physiology and Biochemistry*, *49*(3), 1168-1183. https://doi.org/10.1159/000493295

Göritz, C., Dias, D. O., Tomilin, N., Barbacid, M., Shupliakov, O., & Frisén, J. (2011). A Pericyte Origin of Spinal Cord Scar Tissue. *Science*, *333*(6039), 238-242. https://doi.org/10.1126/science.1203165

Gu, Y., Yang, J., Chen, H., Li, J., Xu, M., Hua, J., Yao, J., Wang, Y., Liu, Y., & Liu, M. (2015). Different Astrocytic Activation between Adult Gekko japonicus and Rats during

Wound Healing In Vitro. *PLOS ONE*, *10*(5), e0127663. https://doi.org/10.1371/journal.pone.0127663

Guidolin, D., Nico, B., Mazzocchi, G., Vacca, A., Nussdorfer, G. G., & Ribatti, D. (2004). Order and disorder in the vascular network. *Leukemia*, *18*(11), 1745-1750. https://doi.org/10.1038/sj.leu.2403526

Gusachenko, I. (2014). Determination of collagen fibril size via absolute measurements of second-harmonic generation signals. *NATURE COMMUNICATIONS*, 8.

Hachem, L. D., Ahuja, C. S., & Fehlings, M. G. (2017). Assessment and management of acute spinal cord injury: From point of injury to rehabilitation. *The Journal of Spinal Cord Medicine*, *40*(6), 665-675. https://doi.org/10.1080/10790268.2017.1329076

Haefeli, J., Mabray, M. C., Whetstone, W. D., Dhall, S. S., Pan, J. Z., Upadhyayula, P., Manley, G. T., Bresnahan, J. C., Beattie, M. S., Ferguson, A. R., & Talbott, J. F. (2017). Multivariate Analysis of MRI Biomarkers for Predicting Neurologic Impairment in Cervical Spinal Cord Injury. *American Journal of Neuroradiology*, *38*(3), 648-655. https://doi.org/10.3174/ajnr.A5021

Hanrahan, N., Lane, S. I. R., Johnson, P., Bourdakos, K., Brereton, C., Ridley, R. A., Davies, E. R., Hosny, N. A., Spickermann, G., Forster, R., Malcolm, G., Davies, D., Jones, M. G., & Mahajan, S. (2020). *Label-free and Multimodal Second Harmonic Generation Light Sheet Microscopy* [Preprint]. Biophysics. https://doi.org/10.1101/2020.09.07.284703

Hara, M., Kobayakawa, K., Ohkawa, Y., Kumamaru, H., Yokota, K., Saito, T., Kijima, K., Yoshizaki, S., Harimaya, K., Nakashima, Y., & Okada, S. (2017). Interaction of reactive astrocytes with type I collagen induces astrocytic scar formation through the integrin–N-cadherin pathway after spinal cord injury. *Nature Medicine*, *23*(7), 818-828. https://doi.org/10.1038/nm.4354

Hartshorn, C. M., Lee, Y. J., Camp, C. H., Liu, Z., Heddleston, J., Canfield, N., Rhodes, T. A., Hight Walker, A. R., Marsac, P. J., & Cicerone, M. T. (2013). Multicomponent Chemical Imaging of Pharmaceutical Solid Dosage Forms with Broadband CARS Microscopy. *Analytical Chemistry*, *85*(17), 8102-8111. https://doi.org/10.1021/ac400671p

Hase, E., Minamikawa, T., Sato, K., Yonekura, D., Takahashi, M., & Yasui, T. (2021). Quantitative Evaluation of Both Histological and Mechanical Recovery in Injured Tendons Using Fourier-Transform Second-Harmonic-Generation Microscopy. *IEEE Journal of Selected Topics in Quantum Electronics*, *27*(4), 1-8. https://doi.org/10.1109/JSTQE.2021.3063535

Hermanns, S., & Reiprich, P. (2001). A reliable method to reduce collagen scar formation in the lesioned rat spinal cord. *Journal of Neuroscience Methods*, 6.

Hompland, T., Erikson, A., Lindgren, M., Lindmo, T., & de Lange Davies, C. (2008). Second-harmonic generation in collagen as a potential cancer diagnostic parameter. *Journal of Biomedical Optics*, *13*(5), 054050. https://doi.org/10.1117/1.2983664

Horiuchi, H., Oshima, Y., Ogata, T., Morino, T., Matsuda, S., Miura, H., & Imamura, T. (2015). Evaluation of Injured Axons Using Two-Photon Excited Fluorescence Microscopy after Spinal Cord Contusion Injury in YFP-H Line Mice. *International Journal of Molecular Sciences*, *16*(7), 15785-15799. https://doi.org/10.3390/ijms160715785

Huang, Y.-C., Chen, T.-H., Kuo, W.-C., Hsu, S.-H., Huang, Y.-Y., & Cheng, H. (2011). MULTIMODAL NONLINEAR OPTICAL IMAGING OF CELL–MATRIX INTERACTION DURING SPINAL CORD INJURY *EX VIVO*. *Biomedical Engineering: Applications, Basis and Communications*, *23*(03), 223-230. https://doi.org/10.4015/S1016237211002554

Hubertus, V., Meyer, L., Roolfs, L., Waldmann, L., Nieminen-Kelhä, M., Fehlings, M. G., & Vajkoczy, P. (2022). In vivo imaging in experimental spinal cord injury – Techniques and trends. *Brain and Spine*, *2*, 100859. https://doi.org/10.1016/j.bas.2021.100859

Hussein, I. H., & Raad, M. (2015). Once Upon a Microscopic Slide: The Story of Histology. *Journal of Cytology & Histology*, *06*(06). https://doi.org/10.4172/2157-7099.1000377

Hussell, T., Lui, S., Jagger, C., Morgan, D., & Brand, O. (2018). The consequence of matrix dysfunction on lung immunity and the microbiome in COPD. *European Respiratory Review*, *27*(148), 180032. https://doi.org/10.1183/16000617.0032-2018

Johnson, K. (1982). One Hundred Years of Hertz Contact. *Proceedings of the Institution of Mechanical Engineers.*, *196*(1), 363-378. https://doi.org/10.1243/PIME_PROC_1982_196_039_02

Jung, S., Aliberti, J., Graemmel, P., Sunshine, M. J., Kreutzberg, G. W., Sher, A., & Littman, D. R. (2000). Analysis of Fractalkine Receptor CX $_3$ CR1 Function by Targeted Deletion and Green Fluorescent Protein Reporter Gene Insertion. *Molecular and Cellular Biology*, *20*(11), 4106-4114. https://doi.org/10.1128/MCB.20.11.4106-4114.2000

Kassar-Duchossoy, L., Duchossoy, Y., Rhrich-Haddout, F., & Horvat, J.-C. (2001). Reinnervation of a denervated skeletal muscle by spinal axons regenerating through a collagen channel directly implanted into the rat spinal cord. *Brain Research*, *908*(1), 25-34. https://doi.org/10.1016/S0006-8993(01)02554-9

Khan, R. S., Ahmed, M. R., Khalid, B., Mahmood, A., & Hassan, R. (2018). Biomarker Detection of Neurological Disorders through Spectroscopy Analysis. *International Dental & Medical Journal of Advanced Research - VOLUME 2015*, *4*(1), 1-9. https://doi.org/10.15713/ins.idmjar.86

Kitano, H., Kitadai, Y., Teishima, J., Yuge, R., Shinmei, S., Goto, K., Inoue, S., Hayashi, T., Sentani, K., Yasui, W., & Matsubara, A. (2017). Combination therapy using molecular-targeted drugs modulates tumor microenvironment and impairs tumor growth in renal cell carcinoma. *Cancer Medicine*, *6*(10), 2308-2320. https://doi.org/10.1002/cam4.1124

Klapka, N., & Müller, H. W. (2006). Collagen Matrix in Spinal Cord Injury. *Journal of Neurotrauma*, *23*(3-4), 422-436. https://doi.org/10.1089/neu.2006.23.422

Kong, K., Kendall, C., Stone, N., & Notingher, I. (2015). Raman spectroscopy for medical diagnostics — From in-vitro biofluid assays to in-vivo cancer detection. *Advanced Drug Delivery Reviews*, *89*, 121-134. https://doi.org/10.1016/j.addr.2015.03.009

Koser, D. E., Moeendarbary, E., Hanne, J., Kuerten, S., & Franze, K. (2015). CNS Cell Distribution and Axon Orientation Determine Local Spinal Cord Mechanical Properties. *Biophysical Journal*, *108*(9), 2137-2147. https://doi.org/10.1016/j.bpj.2015.03.039

Kovesi, P. (s. d.). *MATLAB and Octave Functions for Computer Vision and Image Processing*. Computer Vision and Image Processing. https://www.peterkovesi.com/matlabfns/index.html

Krafft, C., & Popp, J. (2019). Medical needs for translational biophotonics with the focus on Raman-based methods. *Translational Biophotonics*, *1*(1-2), e201900018. https://doi.org/10.1002/tbio.201900018

Krieg, M., Fläschner, G., Alsteens, D., Gaub, B. M., Roos, W. H., Wuite, G. J. L., Gaub, H. E., Gerber, C., Dufrêne, Y. F., & Müller, D. J. (2019). Atomic force microscopy-based mechanobiology. *Nature Reviews Physics*, *1*(1), 41-57. https://doi.org/10.1038/s42254-018-0001-7

Kumar, V., Coluccelli, N., & Polli, D. (2018). Chapter 5 - Coherent Optical Spectroscopy/Microscopy and Applications,. In *Molecular and Laser Spectroscopy* (Elsevier, p. 87-115). V.P. Gupta. (https://www.sciencedirect.com/science/article/pii/B978012849883500005X)

Li, J., Liang, Z., Wang, S., Wang, Z., Zhang, X., Hu, X., Wang, K., He, Q., & Bai, J. (2019). Study on the pathological and biomedical characteristics of spinal cord injury by confocal Raman microspectral imaging. *Spectrochimica Acta Part A: Molecular and Biomolecular Spectroscopy*, *210*, 148-158. https://doi.org/10.1016/j.saa.2018.11.022

Li, Y., He, X., Kawaguchi, R., Zhang, Y., Wang, Q., Monavarfeshani, A., Yang, Z., Chen, B., Shi, Z., Meng, H., Zhou, S., Zhu, J., Jacobi, A., Swarup, V., Popovich, P. G., Geschwind, D. H., & He, Z. (2020). Microglia-organized scar-free spinal cord repair in neonatal mice. *Nature*, *587*(7835), 613-618. https://doi.org/10.1038/s41586-020-2795-6

Li, Z., Yu, S., Hu, X., Li, Y., You, X., Tian, D., Cheng, L., Zheng, M., & Jing, J. (2021). Fibrotic Scar After Spinal Cord Injury: Crosstalk With Other Cells, Cellular Origin, Function, and Mechanism. *Frontiers in Cellular Neuroscience*, *15*, 720938. https://doi.org/10.3389/fncel.2021.720938

Liao, C., Wang, Z., Zhou, L., Zhu, X., Liu, W., & Chen, J. (2016). Label-free imaging of rat spinal cords based on multiphoton microscopy. In Q. Luo, X. Li, Y. Gu, & Y. Tang (Éds.), *Optics in Health Care and Biomedical Optics VII* (Vol. 10024, p. 257-253). https://doi.org/10.1117/12.2245519

Liao, C., Zhu, X., Zhou, L., Wang, Z., Liu, W., & Chen, J. (2019). Visualize and quantify the structural alteration of the rat spinal cord injury based on multiphoton microscopy. *Lasers in Medical Science*, *34*(3), 561-569. https://doi.org/10.1007/s10103-018-2630-6

Lin Hong, Yifei Wan, & Jain, A. (1998). Fingerprint image enhancement: algorithm and performance evaluation. *IEEE Transactions on Pattern Analysis and Machine Intelligence*, *20*(8), 777-789. https://doi.org/10.1109/34.709565

Lin, K., Zhang, D., Macedo, M. H., Cui, W., Sarmento, B., & Shen, G. (2019). Advanced Collagen-Based Biomaterials for Regenerative Biomedicine. *Advanced Functional Materials*, *29*(3), 1804943. https://doi.org/10.1002/adfm.201804943

Ling, Y., Li, C., Feng, K., Palmer, S., Appleton, P. L., Lang, S., McGloin, D., Huang, Z., & Nabi, G. (2017). Second harmonic generation (SHG) imaging of cancer heterogeneity in ultrasound guided biopsies of prostate in men suspected with prostate cancer. *Journal of Biophotonics*, *10*(6-7), 911-918. https://doi.org/10.1002/jbio.201600090

Liu, Y., Keikhosravi, A., Mehta, G. S., Drifka, C. R., & Eliceiri, K. W. (2017). Methods for Quantifying Fibrillar Collagen Alignment. In L. Rittié (Éd.), *Fibrosis* (Vol. 1627, p. 429-451). Springer New York. https://doi.org/10.1007/978-1-4939-7113-8_28

Liu, Y., Keikhosravi, A., Pehlke, C. A., Bredfeldt, J. S., Dutson, M., Liu, H., Mehta, G. S., Claus, R., Patel, A. J., Conklin, M. W., Inman, D. R., Provenzano, P. P., Sifakis, E., Patel, J. M., & Eliceiri, K. W. (2020). Fibrillar Collagen Quantification With Curvelet Transform Based Computational Methods. *Frontiers in Bioengineering and Biotechnology*, *8*. https://doi.org/10.3389/fbioe.2020.00198

Loy, D. N., Crawford, C. H., Darnall, J. B., Burke, D. A., Onifer, S. M., & Whittemore, S. R. (2002). Temporal progression of angiogenesis and basal lamina deposition after contusive spinal cord injury in the adult rat. *The Journal of Comparative Neurology*, *445*(4), 308-324. https://doi.org/10.1002/cne.10168

Lutz, V., Sattler, M., Gallinat, S., Wenck, H., Poertner, R., & Fischer, F. (2012). Impact of collagen crosslinking on the second harmonic generation signal and the fluorescence lifetime of collagen autofluorescence: Impact of collagen crosslinking on the SHG signal. *Skin Research and Technology*, *18*(2), 168-179. https://doi.org/10.1111/j.1600-0846.2011.00549.x

Ma, J., & Plonka, G. (2010). A Review of Curvelets and Recent Applications. *IEEE Signal Processing Magazine*, *27*(2), 118-133.

Maxwell, W. L., Duance, V. C., Lehto, M., Ashurst, D. E., & Berry, M. (1984). The distribution of types I, III, IV and V collagens in penetrant lesions of the central nervous system of the rat. *Histochem J*, *16*, 1219-1229. https://doi.org/10.1007/BF01003445

Mercatelli, R., Mattana, S., Capozzoli, L., Ratto, F., Rossi, F., Pini, R., Fioretto, D., Pavone, F. S., Caponi, S., & Cicchi, R. (2019). Morpho-mechanics of human collagen superstructures revealed by all-optical correlative micro-spectroscopies. *Communications Biology*, *2*(1), 117. https://doi.org/10.1038/s42003-019-0357-y

Mercatelli, R., Triulzi, T., Pavone, F. S., Orlandi, R., & Cicchi, R. (2020). Collagen ultrastructural symmetry and its malignant alterations in human breast cancer revealed by polarization-resolved second-harmonic generation microscopy. *Journal of Biophotonics*, *13*(8). https://doi.org/10.1002/jbio.202000159

Merritt, C. H., Taylor, M. A., Yelton, C. J., & Ray, S. K. (2019). Economic impact of traumatic spinal cord injuries in the United States. *Neuroimmunology and Neuroinflammation*, *2019*. https://doi.org/10.20517/2347-8659.2019.15

Moeendarbary, E., Weber, I. P., Sheridan, G. K., Koser, D. E., Soleman, S., Haenzi, B., Bradbury, E. J., Fawcett, J., & Franze, K. (2017). The soft mechanical signature of glial scars in the central nervous system. *Nature Communications*, *8*(1), 14787. https://doi.org/10.1038/ncomms14787

Moreaux, L., Sandre, O., Blanchard-Desce, M., & Mertz, J. (2000). Membrane imaging by simultaneous second-harmonic generation and two-photon microscopy. *Optics Letters*, *25*(5), 320. https://doi.org/10.1364/OL.25.000320

Mostaço-Guidolin, L., Rosin, N., & Hackett, T.-L. (2017). Imaging Collagen in Scar Tissue: Developments in Second Harmonic Generation Microscopy for Biomedical Applications. *International Journal of Molecular Sciences*, *18*(8), 1772. https://doi.org/10.3390/ijms18081772

Muschler, J., & Streuli, C. H. (2010). Cell-Matrix Interactions in Mammary Gland Development and Breast Cancer. *Cold Spring Harbor Perspectives in Biology*, *2*(10), a003202-a003202. https://doi.org/10.1101/cshperspect.a003202

Musumeci, G. (2014). Past, present and future: overview on histology and histopathology. *Journal of Histology and Histopathology*, *1*(1), 5. https://doi.org/10.7243/2055-091X-1-5

Myllyharju, J. (2004). Collagens, modifying enzymes and their mutations in humans, flies and worms. *Trends in Genetics*, *20*(1), 33-43. https://doi.org/10.1016/j.tig.2003.11.004

Nardone, R., Florea, C., Höller, Y., Brigo, F., Versace, V., Lochner, P., Golaszewski, S., & Trinka, E. (2017). Rodent, large animal and non-human primate models of spinal cord injury. *Zoology*, *123*, 101-114. https://doi.org/10.1016/j.zool.2017.06.004

Neupert, S., Rubakhin, S. S., & Sweedler, J. V. (2012). Targeted Single-Cell Microchemical Analysis: MS-Based Peptidomics of Individual Paraformaldehyde-Fixed and Immunolabeled Neurons. *Chemistry & Biology*, *19*(8), 1010-1019. https://doi.org/10.1016/j.chembiol.2012.05.023

Nguyen, T. T., Gobinet, C., Feru, J., -Pasco, S. B., Manfait, M., & Piot, O. (2012). Characterization of Type I and IV Collagens by Raman Microspectroscopy: Identification of Spectral Markers of the Dermo-Epidermal Junction. *Spectroscopy: An International Journal*, *27*, 421-427. https://doi.org/10.1155/2012/686183

Niccolini, F., Su, P., & Politis, M. (2014). Dopamine receptor mapping with PET imaging in Parkinson's disease. *Journal of Neurology*, *261*(12), 2251-2263. https://doi.org/10.1007/s00415-014-7302-2

Nógrádi, A. (2006). *Transplantation of neural tissue into the spinal cord* (2nd ed). Georgetown, Tex. : New York, N.Y. : Landes Bioscience / Eurekah.com ; Springer Science + Business Media, c2006.

Norenberg, M. D., Smith, J., & Marcillo, A. (2004). The Pathology of Human Spinal Cord Injury: Defining the Problems. *Journal of Neurotrauma*, *21*(4), 429-440. https://doi.org/10.1089/089771504323004575

Noristani, H. N., Saint-Martin, G. P., Cardoso, M., Sidiboulenouar, R., Catteau, M., Coillot, C., Goze-Bac, C., & Perrin, F. E. (2018). Longitudinal Magnetic Resonance Imaging Analysis and Histological Characterization after Spinal Cord Injury in Two Mouse Strains with Different Functional Recovery: Gliosis as a Key Factor. *Journal of Neurotrauma*, *35*(24), 2924-2940. https://doi.org/10.1089/neu.2017.5613

Oheim, M., Beaurepaire, E., Chaigneau, E., Mertz, J., & Charpak, S. (2001). Two-photon microscopy in brain tissue: parameters influencing the imaging depth. *Journal of Neuroscience Methods*, *111*(1), 29-37. https://doi.org/10.1016/S0165-0270(01)00438-1

Okada, M., Miyamoto, O., Shibuya, S., Zhang, X., Yamamoto, T., & Itano, T. (2007). Expression and role of type I collagen in a rat spinal cord contusion injury model. *Neuroscience Research*, *58*(4), 371-377. https://doi.org/10.1016/j.neures.2007.04.009

Onose, G., Anghelescu, A., Muresanu, D. F., Padure, L., Haras, M. A., Chendreanu, C. O., Onose, L. V., Mirea, A., Ciurea, A. V., El Masri, W. S., & von Wild, K. R. H. (2009). A review of published reports on neuroprotection in spinal cord injury. *Spinal Cord*, *47*(10), 716-726. https://doi.org/10.1038/sc.2009.52

Paddison, S., & Middleton, F. (2014). Spinal cord injury. *Spinal Cord Injury*.

Pang, Q.-M., Chen, S.-Y., Xu, Q.-J., Fu, S.-P., Yang, Y.-C., Zou, W.-H., Zhang, M., Liu, J., Wan, W.-H., Peng, J.-C., & Zhang, T. (2021). Neuroinflammation and Scarring After Spinal Cord Injury: Therapeutic Roles of MSCs on Inflammation and Glial Scar. *Frontiers in Immunology*, *12*, 751021. https://doi.org/10.3389/fimmu.2021.751021

Pavone, F. S., & Campagnola, P. J. (2013). *Second harmonic generation imaging.* (Pavone, F. S., Campagnola, P. J. (Eds.). CRC Press.

Pena, A.-M. (2006). *Génération de seconde harmonique par le collagène et application à l'étude de fibroses par microscopie multiphoton.* Ecole Polytechnique.

Pena, A.-M., Boulesteix, T., Dartigalongue, T., & Schanne-Klein, M.-C. (2005). Chiroptical Effects in the Second Harmonic Signal of Collagens I and IV. *Journal of the American Chemical Society*, *127*(29), 10314-10322. https://doi.org/10.1021/ja0520969

Perez, J.-C., Gerber, Y. N., & Perrin, F. E. (2021). Dynamic Diversity of Glial Response Among Species in Spinal Cord Injury. *Frontiers in Aging Neuroscience*, *13*, 769548. https://doi.org/10.3389/fnagi.2021.769548

Piek, A., de Boer, R. A., & Silljé, H. H. W. (2016). The fibrosis-cell death axis in heart failure. *Heart Failure Reviews*, *21*(2), 199-211. https://doi.org/10.1007/s10741-016-9536-9

Pijanka, J. K., Markov, P. P., Midgett, D., Paterson, N. G., White, N., Blain, E. J., Nguyen, T. D., Quigley, H. A., & Boote, C. (2019). Quantification of collagen fiber structure using second harmonic generation imaging and two-dimensional discrete Fourier transform analysis: Application to the human optic nerve head. *Journal of Biophotonics*, *12*(5). https://doi.org/10.1002/jbio.201800376

Plumb, D. A., Dhir, V., Mironov, A., Ferrara, L., Poulsom, R., Kadler, K. E., Thornton, D. J., Briggs, M. D., & Boot-Handford, R. P. (2007). Collagen XXVII Is Developmentally Regulated and Forms Thin Fibrillar Structures Distinct from Those of Classical Vertebrate Fibrillar Collagens. *Journal of Biological Chemistry*, *282*(17), 12791-12795. https://doi.org/10.1074/jbc.C700021200

Poulen, G., Aloy, E., Bringuier, C. M., Mestre-Francés, N., Artus, E. V. F., Cardoso, M., Perez, J.-C., Goze-Bac, C., Boukhaddaoui, H., Lonjon, N., Gerber, Y. N., & Perrin, F. E. (2021). Inhibiting microglia proliferation after spinal cord injury improves recovery in mice and nonhuman primates. *Theranostics*, *11*(18), 8640-8659. https://doi.org/10.7150/thno.61833

Poulen, G., Bartolami, S., Noristani, H. N., Perrin, F. E., & Gerber, Y. N. (2021). Unlike Brief Inhibition of Microglia Proliferation after Spinal Cord Injury, Long-Term Treatment Does Not Improve Motor Recovery. *Brain Sciences*, *11*(12), 1643. https://doi.org/10.3390/brainsci11121643

Poulen, G., Gerber, Y. N., Perez, J.-C., Oubarrahou, K., Lonjon, N., Vachiery-Lahaye, F., Boukhaddaoui, H., & Perrin, F. E. (2021). Coherent Anti-Stokes Raman Scattering Microscopy: A Label-Free Method to Compare Spinal Cord Myelin in Different Species. *Frontiers in Physics*, *9*. https://doi.org/10.3389/fphy.2021.665650

Provenzano, P. P., Eliceiri, K. W., Campbell, J. M., Inman, D. R., White, J. G., & Keely, P. J. (2006). Collagen reorganization at the tumor-stromal interface facilitates local invasion. *BMC Medicine*, *4*(1), 38. https://doi.org/10.1186/1741-7015-4-38

Ranjit, S., Dvornikov, A., Stakic, M., Hong, S.-H., Levi, M., Evans, R. M., & Gratton, E. (2015). Imaging Fibrosis and Separating Collagens using Second Harmonic Generation and Phasor Approach to Fluorescence Lifetime Imaging. *Scientific Reports*, *5*(1), 13378. https://doi.org/10.1038/srep13378

Rao, R. A. R. (2012). *Quantification of collagen fiber organization in biological tissues at cellular and molecular scales using Second-harmonic generation imaging*. University of Illinois.

Reish, R. G., & Eriksson, E. (2008). Scars: A Review of Emerging and Currently Available Therapies: *Plastic and Reconstructive Surgery*, *122*(4), 1068-1078. https://doi.org/10.1097/PRS.0b013e318185d38f

Ricard-Blum, S. (2011). The Collagen Family. *Cold Spring Harbor Perspectives in Biology*, *3*(1), a004978-a004978. https://doi.org/10.1101/cshperspect.a004978

Ryzhikova, E., Kazakov, O., Halamkova, L., Celmins, D., Malone, P., Molho, E., Zimmerman, E. A., & Lednev, I. K. (2015). Raman spectroscopy of blood serum for Alzheimer's disease diagnostics: specificity relative to other types of dementia. *Journal of Biophotonics*, *8*(7), 584-596. https://doi.org/10.1002/jbio.201400060

Sami, A., Selzer, M. E., & Li, S. (2020). Advances in the Signaling Pathways Downstream of Glial-Scar Axon Growth Inhibitors. *Frontiers in Cellular Neuroscience*, *14*, 174. https://doi.org/10.3389/fncel.2020.00174

Sander, E. A., & Barocas, V. H. (2009). Comparison of 2D fiber network orientation measurement methods. *Journal of Biomedical Materials Research Part A*, *88A*(2), 322-331. https://doi.org/10.1002/jbm.a.31847

Saxena, T., Deng, B., Stelzner, D., Hasenwinkel, J., & Chaiken, J. (2011). Raman spectroscopic investigation of spinal cord injury in a rat model. *Journal of Biomedical Optics*, *16*(2), 027003. https://doi.org/10.1117/1.3549700

Saxena, T., Gilbert, J., Stelzner, D., & Hasenwinkel, J. (2012). Mechanical Characterization of the Injured Spinal Cord after Lateral Spinal Hemisection Injury in the Rat. *Journal of Neurotrauma*, *29*(9), 1747-1757. https://doi.org/10.1089/neu.2011.1818

Schindelin, J., Arganda-Carreras, I., Frise, E., Kaynig, V., Longair, M., Pietzsch, T., Preibisch, S., Rueden, C., Saalfeld, S., Schmid, B., Tinevez, J.-Y., White, D. J., Hartenstein, V., Eliceiri, K., Tomancak, P., & Cardona, A. (2012). Fiji: an open-source platform for biological-image analysis. *Nature Methods*, *9*(7), 676-682. https://doi.org/10.1038/nmeth.2019

Shanti, N. O., Chan, V. W. L., Stock, S. R., De Carlo, F., Thornton, K., & Faber, K. T. (2014). X-ray micro-computed tomography and tortuosity calculations of percolating pore networks. *Acta Materialia*, *71*, 126-135. https://doi.org/10.1016/j.actamat.2014.03.003

Shi, Y., Shi, R., Cheng, J.-X., Zhang, D., Huff, T. B., Wang, X., & Xu, X.-M. (2011). Longitudinal in vivo coherent anti-Stokes Raman scattering imaging of demyelination and remyelination in injured spinal cord. *Journal of Biomedical Optics*, *16*(10), 1. https://doi.org/10.1117/1.3641988

Soderblom, C., Luo, X., Blumenthal, E., Bray, E., Lyapichev, K., Ramos, J., Krishnan, V., Lai-Hsu, C., Park, K. K., Tsoulfas, P., & Lee, J. K. (2013). Perivascular Fibroblasts Form the Fibrotic Scar after Contusive Spinal Cord Injury. *The Journal of Neuroscience*, *33*(34), 13882-13887. https://doi.org/10.1523/JNEUROSCI.2524-13.2013

Sternberg, S. (1983). Biomedical Image Processing. *Computer*, *16*(1), 22-34. https://doi.org/10.1109/MC.1983.1654163

Stoll, G., & Müller, H. W. (2006). Nerve Injury, Axonal Degeneration and Neural Regeneration: Basic Insights. *Brain Pathology*, *9*(2), 313-325. https://doi.org/10.1111/j.1750-3639.1999.tb00229.x

Stover, S. L., De Vivo, M. J., & Go, B. K. (1999). History, implementation, and current status of the national spinal cord injury database. *Archives of Physical Medicine and Rehabilitation*, *80*(11), 1365-1371. https://doi.org/10.1016/S0003-9993(99)90246-0

Streeter, K. A., Sunshine, M. D., Brant, J. O., Sandoval, A. G. W., Maden, M., & Fuller, D. D. (2020). Molecular and histologic outcomes following spinal cord injury in spiny mice, *ACOMYS CAHIRINUS* . *Journal of Comparative Neurology*, *528*(9), 1535-1547. https://doi.org/10.1002/cne.24836

Strupler, M., Pena, A.-M., Hernest, M., Tharaux, P.-L., Martin, J.-L., Beaurepaire, E., & Schanne-Klein, M.-C. (2007). Second harmonic imaging and scoring of collagen in fibrotic tissues. *Optics Express*, *15*(7), 4054. https://doi.org/10.1364/OE.15.004054

Stylianou, A., Politopoulos, K., Kyriazi, M., & Yova, D. (2011). Combined information from AFM imaging and SHG signal analysis of collagen thin films. *Biomedical Signal Processing and Control*, *6*(3), 307-313. https://doi.org/10.1016/j.bspc.2011.02.006

Sun, M., Bloom, A. B., & Zaman, M. H. (2015). Rapid Quantification of 3D Collagen Fiber Alignment and Fiber Intersection Correlations with High Sensitivity. *PLOS ONE*, *10*(7), e0131814. https://doi.org/10.1371/journal.pone.0131814

Thomas, J. R., & Somenek, M. (2012). Scar Revision Review. *ARCH FACIAL PLAST SURG*, *14*(3).

Tonge, D. A., Golding, J. P., Edbladh, M., Kroon, M., Ekström, P. E. R., & Edström, A. (1997). Effects of Extracellular Matrix Components on Axonal Outgrowth from Peripheral Nerves of Adult Animalsin Vitro. *Experimental Neurology*, *146*(1), 81‑90. https://doi.org/10.1006/exnr.1997.6498

Toossi, A., Bergin, B., Marefatallah, M., Parhizi, B., Tyreman, N., Everaert, D. G., Rezaei, S., Seres, P., Gatenby, J. C., Perlmutter, S. I., & Mushahwar, V. K. (2021). Comparative neuroanatomy of the lumbosacral spinal cord of the rat, cat, pig, monkey, and human. *Scientific Reports*, *11*(1). https://doi.org/10.1038/s41598-021-81371-9

Vanacore, R. M., Friedman, D. B., Ham, A.-J. L., Sundaramoorthy, M., & Hudson, B. G. (2005). Identification of S-Hydroxylysyl-methionine as the Covalent Cross-link of the Noncollagenous (NC1) Hexamer of the α1α1α2 Collagen IV Network. *Journal of Biological Chemistry*, *280*(32), 29300‑29310. https://doi.org/10.1074/jbc.M502752200

Varga, B., Martin-Fernandez, M., Hilaire, C., Sanchez-Vicente, A., Areias, J., Salsac, C., Cuisinier, F. J. G., Raoul, C., Scamps, F., & Gergely, C. (2018). Myotube elasticity of an amyotrophic lateral sclerosis mouse model. *Scientific Reports*, *8*(1), 5917. https://doi.org/10.1038/s41598-018-24027-5

Verhaegen, P. D., Schouten, H. J., Tigchelaar-Gutter, W., van Marle, J., van Noorden, C. J., Middelkoop, E., & van Zuijlen, P. P. (2012). Adaptation of the dermal collagen structure of human skin and scar tissue in response to stretch: An experimental study: Collagen adaptation in response to stretch. *Wound Repair and Regeneration*, *20*(5), 658‑666. https://doi.org/10.1111/j.1524-475X.2012.00827.x

Viji Babu, P. K., & Radmacher, M. (2019). Mechanics of Brain Tissues Studied by Atomic Force Microscopy: A Perspective. *Frontiers in Neuroscience*, *13*, 600. https://doi.org/10.3389/fnins.2019.00600

Wang, W., Zhao, J., Short, M., & Zeng, H. (2015). Real-time *in vivo* cancer diagnosis using raman spectroscopy: Real-time in vivo cancer diagnosis using raman spectroscopy. *Journal of Biophotonics*, *8*(7), 527-545. https://doi.org/10.1002/jbio.201400026

Wanner, I. B., Anderson, M. A., Song, B., Levine, J., Fernandez, A., Gray-Thompson, Z., Ao, Y., & Sofroniew, M. V. (2013). Glial Scar Borders Are Formed by Newly Proliferated, Elongated Astrocytes That Interact to Corral Inflammatory and Fibrotic Cells via STAT3-Dependent Mechanisms after Spinal Cord Injury. *Journal of Neuroscience*, *33*(31), 12870-12886. https://doi.org/10.1523/JNEUROSCI.2121-13.2013

Weber-Levine, C., Hersh, A. M., Jiang, K., Routkevitch, D., Tsehay, Y., Perdomo-Pantoja, A., Judy, B. F., Kerensky, M., Liu, A., Adams, M., Izzi, J., Doloff, J. C., Manbachi, A., & Theodore, N. (2022). Porcine Model of Spinal Cord Injury: A Systematic Review. *Neurotrauma Reports*, *3*(1), 352-368. https://doi.org/10.1089/neur.2022.0038

Weidner, N., Grill, R. J., & Tuszynski, M. H. (1999). Elimination of Basal Lamina and the Collagen “Scar” after Spinal Cord Injury Fails to Augment Corticospinal Tract Regeneration. *Experimental Neurology*, *160*(1), 40-50. https://doi.org/10.1006/exnr.1999.7200

Winkler, J., Abisoye-Ogunniyan, A., Metcalf, K. J., & Werb, Z. (2020). Concepts of extracellular matrix remodelling in tumour progression and metastasis. *Nature Communications*, *11*(1). https://doi.org/10.1038/s41467-020-18794-x

Wong, D. F., Tauscher, J., & Gründer, G. (2009). The Role of Imaging in Proof of Concept for CNS Drug Discovery and Development. *Neuropsychopharmacology*, *34*(1), 187-203. https://doi.org/10.1038/npp.2008.166

Wu, J. W., Breydo, L., Isas, J. M., Lee, J., Kuznetsov, Y. G., Langen, R., & Glabe, C. (2010). Fibrillar Oligomers Nucleate the Oligomerization of Monomeric Amyloid β but Do Not Seed Fibril Formation. *Journal of Biological Chemistry*, *285*(9), 6071-6079. https://doi.org/10.1074/jbc.M109.069542

Wu, W., He, S., Wu, J., Chen, C., Li, X., Liu, K., & Qu, J. Y. (2022). Long-term in vivo imaging of mouse spinal cord through an optically cleared intervertebral window. *Nature Communications*, *13*(1). https://doi.org/10.1038/s41467-022-29496-x

Wynn, T. A. (2007). Common and unique mechanisms regulate fibrosis in various fibroproliferative diseases. *Journal of Clinical Investigation*, *117*(3), 524-529. https://doi.org/10.1172/JCI31487

Xu, C., Garutti, E., Mandai, S., & Charbon, E. (2013). Comparison of digital and analog silicon photomultiplier for positron emission tomography application. *2013 IEEE Nuclear Science Symposium and Medical Imaging Conference (2013 NSS/MIC)*, 1-7. https://doi.org/10.1109/NSSMIC.2013.6829585

Xu, P., Cox, G. C., Ramshaw, J. A. M., Lukins, P. B., & Sheppard, C. J. R. (2004). *Polarization effects in SHG of collagen* (A. Periasamy & P. T. C. So (éds.); p. 343). https://doi.org/10.1117/12.528740

Yang, T., Dai, Y., Chen, G., & Cui, S. (2020). Dissecting the Dual Role of the Glial Scar and Scar-Forming Astrocytes in Spinal Cord Injury. *Frontiers in Cellular Neuroscience*, *14*, 78. https://doi.org/10.3389/fncel.2020.00078

Yuan, Y.-M., & He, C. (2013). The glial scar in spinal cord injury and repair. *Neuroscience Bulletin*, *29*(4), 421-435. https://doi.org/10.1007/s12264-013-1358-3

Zhang, N., Fang, M., Chen, H., Gou, F., & Ding, M. (2014). Evaluation of spinal cord injury animal models. *Neural Regeneration Research*, *9*(22), 2008. https://doi.org/10.4103/1673-5374.143436

Zipfel, W. R., Williams, R. M., Christie, R., Nikitin, A. Y., Hyman, B. T., & Webb, W. W. (2003). Live tissue intrinsic emission microscopy using multiphoton-excited native fluorescence and second harmonic generation. *Proceedings of the National Academy of Sciences*, *100*(12), 7075-7080. https://doi.org/10.1073/pnas.0832308100

Zuiderveld, K. (1994). Contrast Limited Adaptive Histogram Equalization. *Graphics Gems*, 474-495. https://doi.org/doi:10.1016/B978-0-12-336156-1.50061-6*

-

Appendix

Appendix 1. Generalities - MRI images of human spinal cord

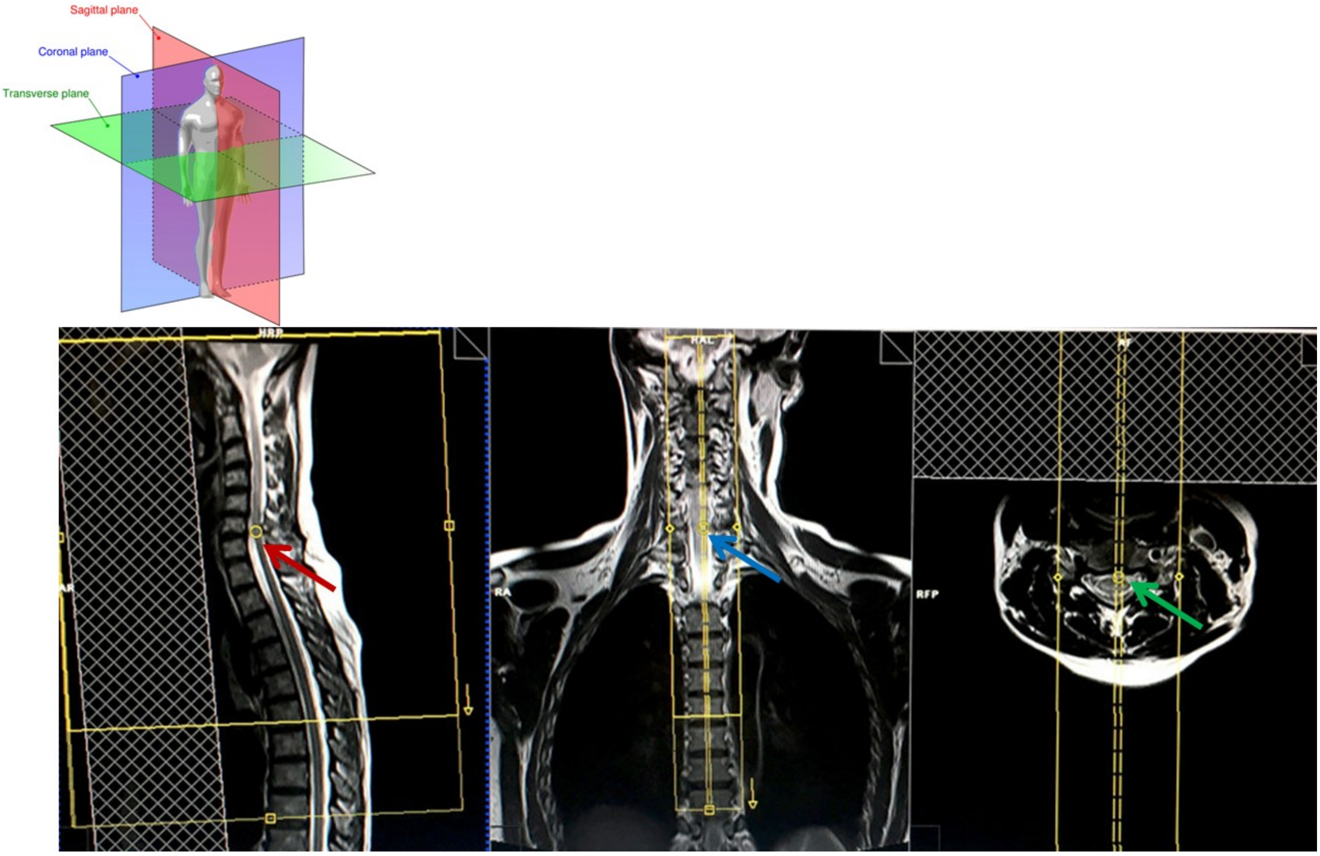

Figure 91: MRI imaging of human spinal cord. T2 sequence with spinal cord localization according to the anatomical plane (red for sagittal, blue for coronal or longitudinal and green for transverse or axial.), modified from https://mrimaster.com/PLAN spinal cord.html

Appendix 2. Material and Methods – Samples preparation and staining

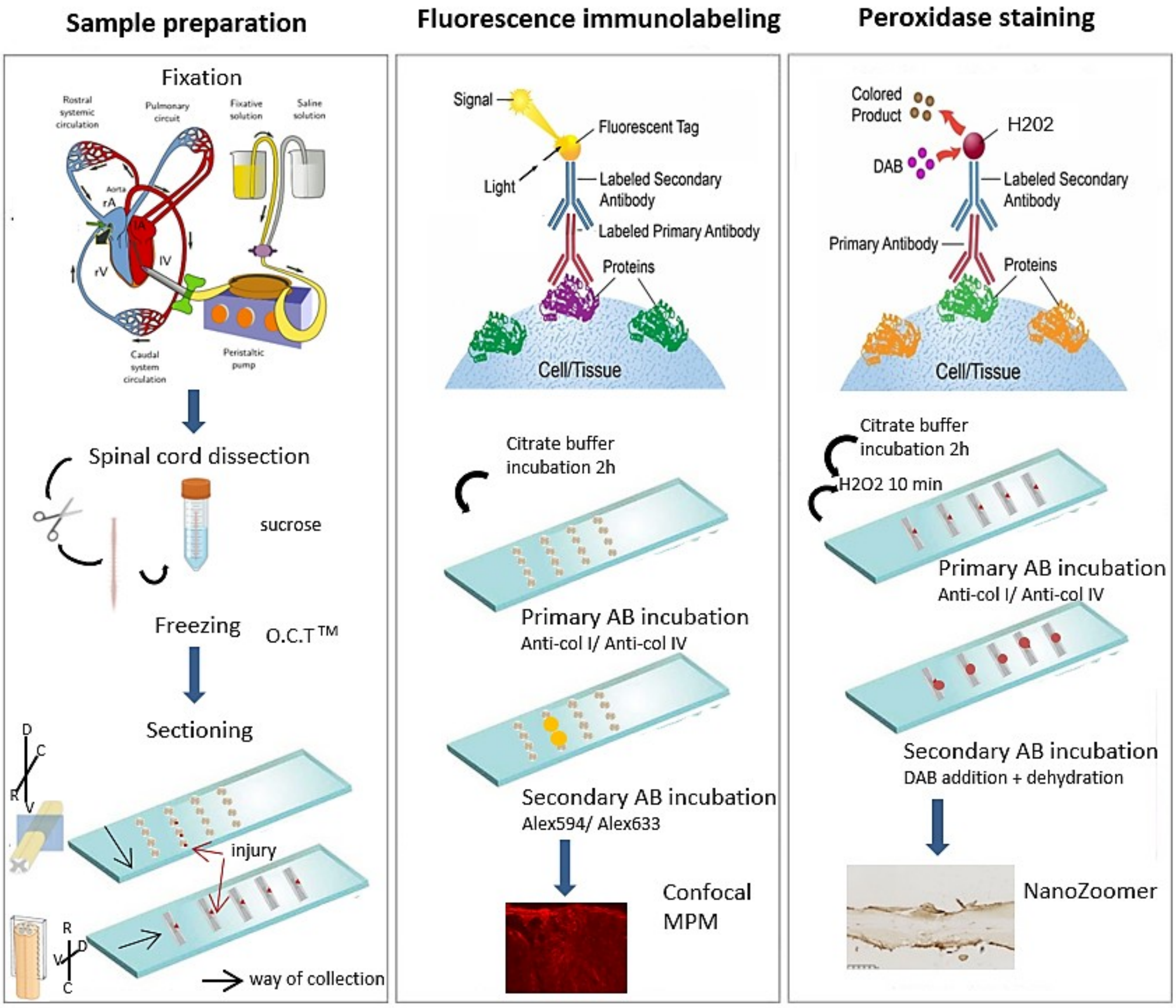

Figure 92: Spinal cord tissues preparation for ex vivo analysis. The sample preparation consists first in a fixation step through a whole body perfusion with paraformaldehyde (PFA) 4%. The spinal cord is then removed from the backbone and processed (maintained in sucrose and frozen) before the sectioning (axial and longitudinal sections) and serial collection. Immunofluorescence is performed on axial and longitudinal sections with AB I anti-collagen I and anti-collagen IV, and AB II Alexa594 (confocal microscope) and Alexa633 (MPM). Peroxidase immunostaining is also carried out on longitudinal sections for monitoring collagen I and IV at different time-points using NanoZoomer. Figure template from: (Neupert et al., 2012), and immunolabeling schemes from https://www.sigmaaldrich.com/FR/fr/applications/protein-biology/immunohistochemistry, accessed on June 25, 2022.

Appendix 3. Material and Methods – MPM software

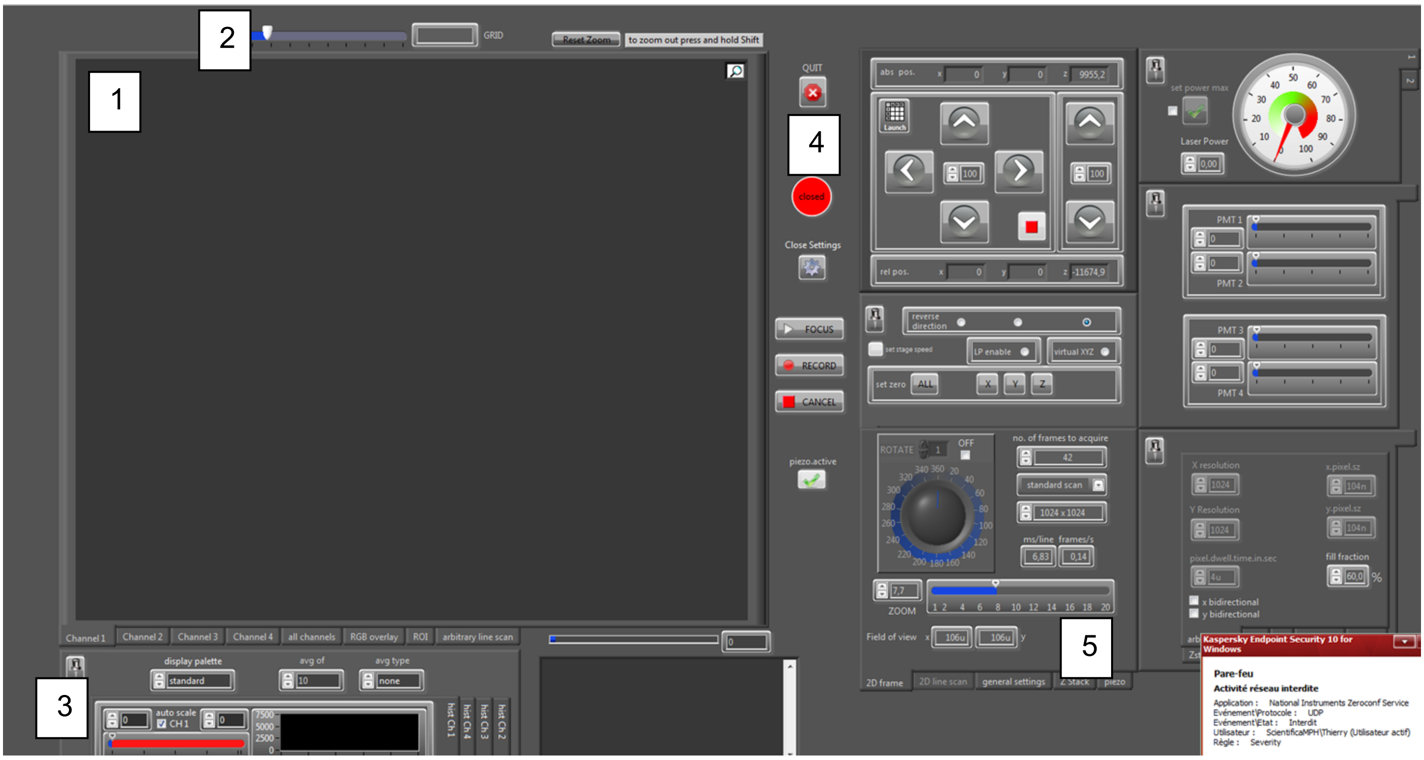

Kaspersky Endpoint Security 10 for Windows

Pare-feu

Activité réseau interdite

Application : National Instruments Zeroconf Service
Evénement\Protocole : UDP
Evénement\Etat : Interdit
Utilisateur : ScientificaMPH\Thierry (Utilisateur actif)
Règle : Severity

Figure 93: MPM software interface screenshot. 1) Imaging zone for channel's visualization. 2) Zoom scale (with grid insertion). 3) Channel characteristics (signal intensity, number of averaged images, types of averaging). 4) Focusing/imaging/lunching. 5) Acquisition type and general settings

Appendix 4. Material and Methods – AFM acquisitions

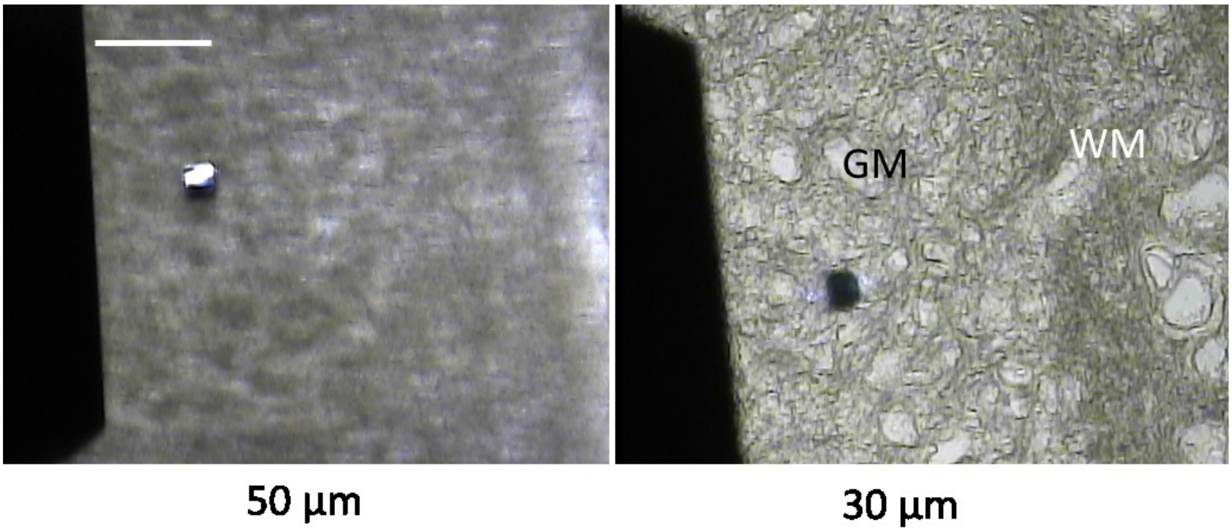

Figure 94: Sample thickness in AFM-FS acquisitions. Bright field images showing the AFM tip and the tissue with two different thicknesses. The distinction between grey (GM) and white (WM) matters is more clear with 30-µm thick tissue than with 50-µm thick. Scale bar is 80 µm.

Appendix 5. Material and Methods – Pre-processing for CurveAlign

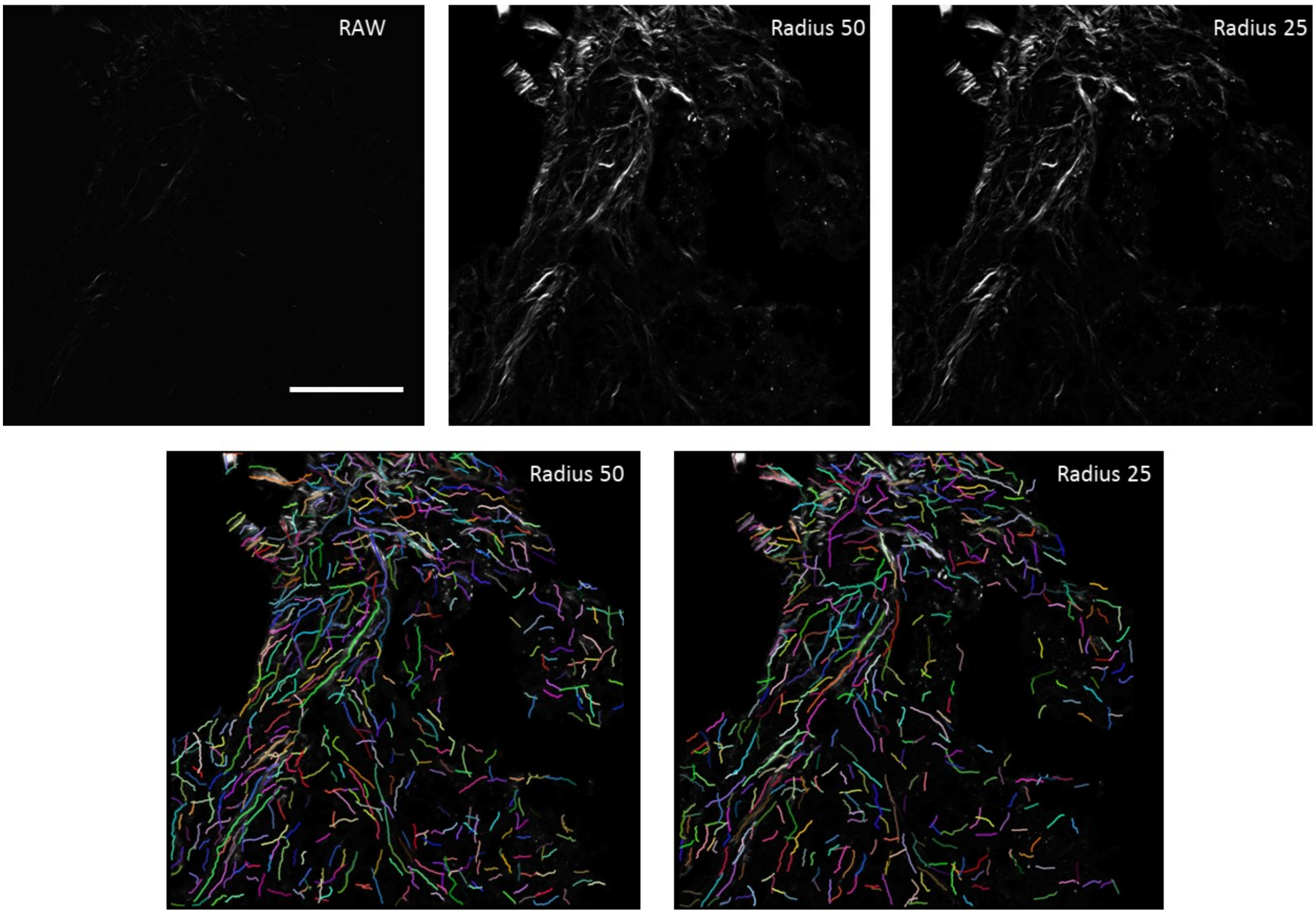

Figure 95: Background subtraction step. Images pre-processed in ImageJ with the rolling ball algorithm (https://imagej.net/plugins/rolling-ball-background-subtraction) are presented with two different radius ball of 50 and 25 (in pixels), along with the subsequent fibers detection in CurveAlign. The 50-radius pre-processing tends to overestimate the fibers detection.

Appendix 6. Results – Preliminary observations with Immunofluorescence (Alexa 594)

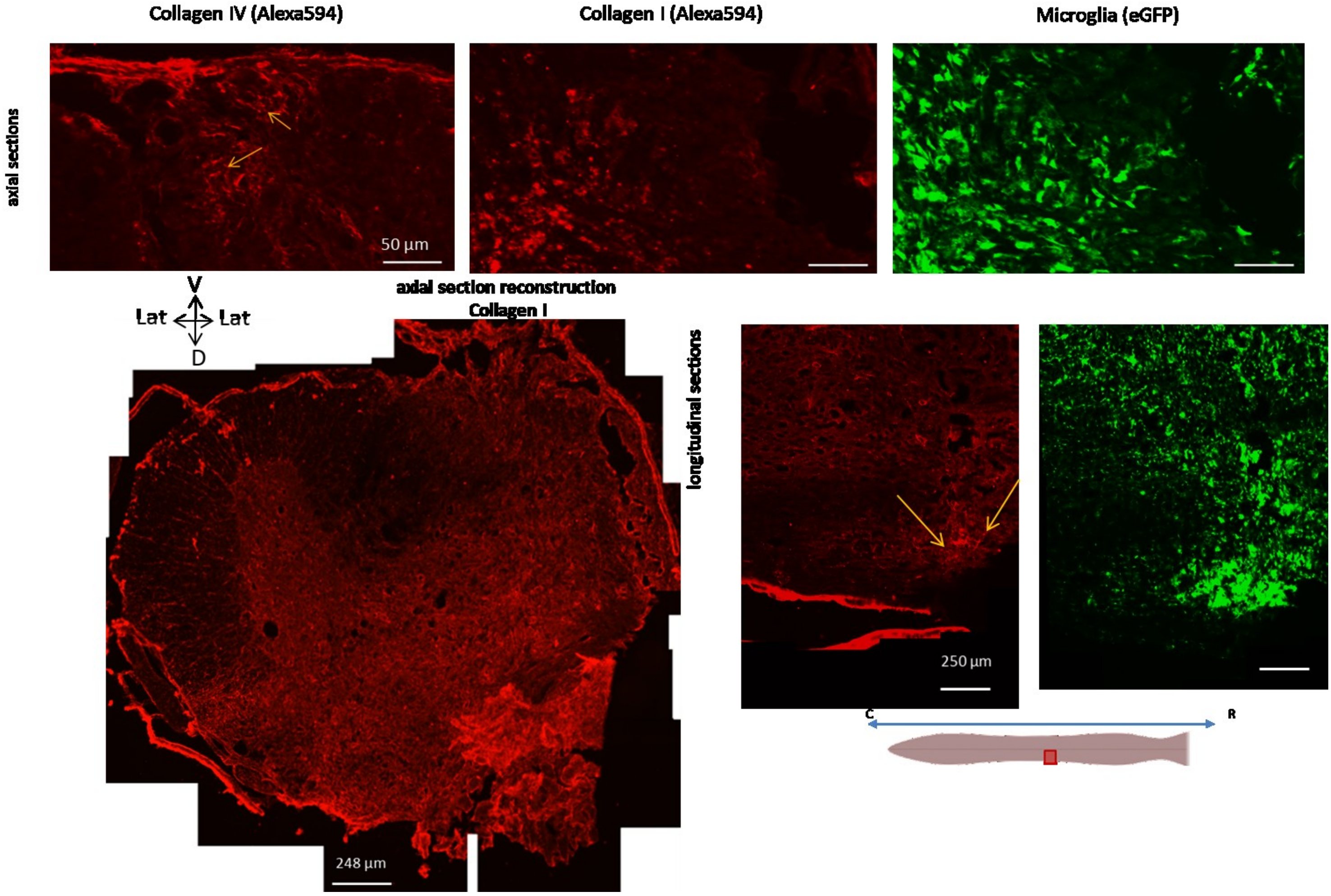

Figure 96: Preliminary IF observations in axial and longitudinal sections at 1wpi.Immunolabelling with Alexa594 to reveal collagen IV and I is observed with a confocal fluorescence microscope. In axial sections (up part), collagen IV exhibits thin stained filaments (yellow arrows) while collagen I shows non-specific structures in comparison with eGFP contrast. A reconstruction of the entire area of acquisition is presented for collagen I (down left), with the ipsilateral side shown on the right. To potentially improve collagen I targeting, retrieval phase was included in the protocol on longitudinal sections (down right). Collagen I exhibits more specific filaments (yellow arrows) distinct from the microglia in the same location.

Appendix 7. Results – Work in progress – AFM-FS on snap frozen SC tissues

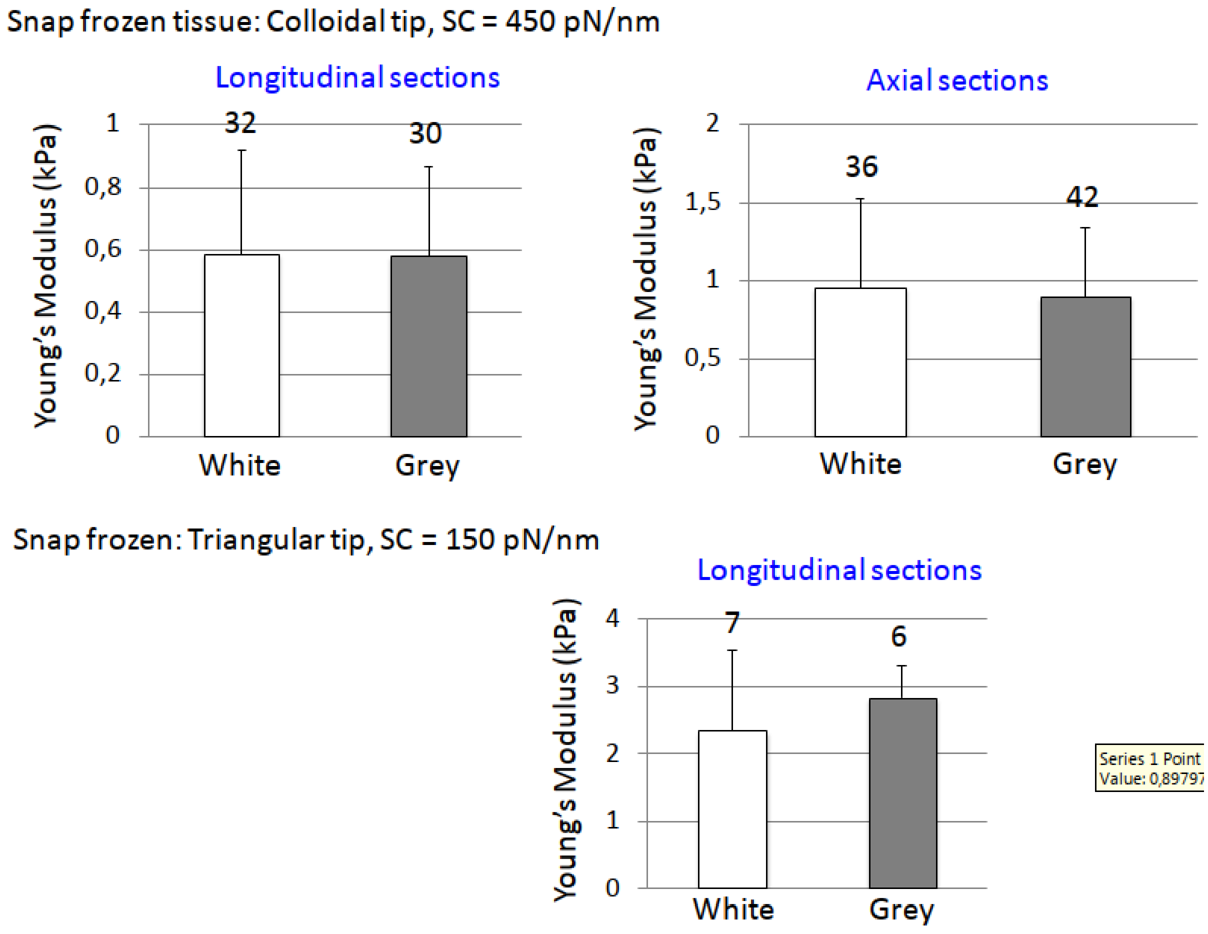

Figure 97: AFM-FS on snap frozen SC tissues. Young's moduli (in kPa) of grey and white matter obtained with a colloidal tip on snap frozen uninjured spinal cord sections are presented for longitudinal and axial sections (1 mouse for each type of section). Additional measurements were carried out on the longitudinal sections with a triangular tip. A paired t-test with Welch's correction was used for comparing the grey and white matter.

Etude photonique et nano-mécanique pour le suivi sans marquage de la cicatrice fibrotique dans les lésions de la moelle épinière chez la souris

Les lésions de la moelle épinière sont des pathologies traumatiques menant potentiellement à de sévères handicaps moteurs, sensitifs et autonomiques. Après une lésion, la formation d'une cicatrice gliale empêche partiellement la régénération axonale en formant une barrière physique et chimique. Le processus de cicatrisation implique les microglies, les astrocytes et des composants de la matrice extracellulaire, tels que le collagène, construisant la partie fibrotique de la cicatrice. Une approche multimodale combinant la microscopie multiphotonique (MMP) et la microscopie à force atomique (MFA) a été utilisée pour une imagerie sans marquage dans l'exploration spécifique du rôle du collagène. La génération de seconde harmonique (GSH) du collagène fibrillaire observable par MMP a permis son suivi dans le temps en tant que biomarqueur de la lésion. Une augmentation de la densité de collagène ainsi que la formation de fibres plus tortueuses ont été observées dans le temps après une lésion. L'étude des propriétés nano-mécaniques a révélé un durcissement notable de la zone de lésion, corrélé à la formation de fibres de collagène. Ces observations indiquent la concomitance d'importantes modifications structurales et mécaniques au cours de l'évolution de la cicatrice fibrotique.

Mots-clés : *lésion moelle épinière, collagène, génération de seconde harmonique, microscopie à force atomique, nano-mécanique.*

Photonic and nanomechanical study for label-free monitoring of the fibrotic scar in spinal cord injury in mice

Spinal cord injury is a traumatic disease potentially leading to severe motor, sensitive and autonomic impairments. After injury the axonal regeneration is partly inhibited by the glial scar, acting as a physical and chemical barrier. The scarring process involves microglia, astrocytes and extracellular matrix components, such as collagen, constructing the fibrotic component of the scar. To investigate the role of collagen, we used a multimodal label-free imaging approach combining multiphoton and atomic force microscopy. The second harmonic generation signal exhibited by fibrillar collagen enabled to specifically monitor it as a biomarker of the lesion. An increase in collagen density and the formation of more tortuous fibers over time after injury are observed. Nano-mechanical investigations revealed a noticeable hardening of the injured area, correlated with collagen fibers' formation. These observations indicate the concomitance of important structural and mechanical modifications during the fibrotic scar evolution.

Keywords : *spinal cord injury (SCI), collagen, second harmonic generation (SHG), atomic force microscopy (AFM), nano-mechanics.*